Lecture Notes in Civil Engineering

Guoxiong Mei
Zengguang Xu
Fei Zhang *Editors*

Advanced Construction Technology and Research of Deep-Sea Tunnels

OPEN ACCESS

Springer

Lecture Notes in Civil Engineering

Volume 490

Lecture Notes in Civil Engineering (LNCE) publishes the latest developments in Civil Engineering—quickly, informally and in top quality. Though original research reported in proceedings and post-proceedings represents the core of LNCE, edited volumes of exceptionally high quality and interest may also be considered for publication. Volumes published in LNCE embrace all aspects and subfields of, as well as new challenges in, Civil Engineering. Topics in the series include:

- Construction and Structural Mechanics
- Building Materials
- Concrete, Steel and Timber Structures
- Geotechnical Engineering
- Earthquake Engineering
- Coastal Engineering
- Ocean and Offshore Engineering; Ships and Floating Structures
- Hydraulics, Hydrology and Water Resources Engineering
- Environmental Engineering and Sustainability
- Structural Health and Monitoring
- Surveying and Geographical Information Systems
- Indoor Environments
- Transportation and Traffic
- Risk Analysis
- Safety and Security

To submit a proposal or request further information, please contact the appropriate Springer Editor:

– Pierpaolo Riva at pierpaolo.riva@springer.com (Europe and Americas);
– Swati Meherishi at swati.meherishi@springer.com (Asia—except China, Australia, and New Zealand);
– Wayne Hu at wayne.hu@springer.com (China).

All books in the series now indexed by Scopus and EI Compendex database!

Guoxiong Mei · Zengguang Xu · Fei Zhang
Editors

Advanced Construction Technology and Research of Deep-Sea Tunnels

Springer

Editors
Guoxiong Mei
Zhejiang University
Hangzhou, China

Zengguang Xu
Xi'an University of Technology
Xi An, China

Fei Zhang
Hohai University
Nanjing, China

ISSN 2366-2557 ISSN 2366-2565 (electronic)
Lecture Notes in Civil Engineering
ISBN 978-981-97-2416-1 ISBN 978-981-97-2417-8 (eBook)
https://doi.org/10.1007/978-981-97-2417-8

This Springer imprint is published by the registered company Springer Nature Singapore Pte Ltd.
The registered company address is: 152 Beach Road, #21-01/04 Gateway East, Singapore 189721, Singapore

Paper in this product is recyclable.

Preface

This book *Advanced Construction Technology and Research of Deep-Sea Tunnels* partly gathers selected papers accepted and presented during the 2023 5th International Conference on Civil Architecture and Urban Engineering (ICCAUE 2023), held on November 17–19, 2023 in Xiamen, China. The purpose of this compilation is to provide researchers, engineers, and enthusiasts in the field of deep-see tunnel construction with a consolidated resource that captures the forefront of knowledge and innovation in these specialized areas. By bringing together a diverse selection of contributions from renowned experts, this compilation offers a unique opportunity to explore the latest developments and challenges encountered in the deep-see tunnel construction field of marine engineering.

All papers included in the conference proceedings and published in this book were carefully reviewed by program committee members and taken into consideration the breadth and depth of the research topics.

The discipline of this book is mainly related to civil engineering and technology of construction, focusing on cutting-edge construction techniques and engineering exploration for deep-sea tunnels. And the topics include but are not limited to: (a) Deep-sea survey technology and equipment; (b) Complex load characteristics and numerical simulation technology in the marine environment; (c) Key technology of immersed tube and shield tunnel construction; (d) Deep-sea construction equipment and safety assessment method; (e) Deep-sea positioning, measurement, and control technology, etc.

Available on the latest research progress of deep-sea tunnel construction and advances in relevant engineering technologies, this book provides a detailed analysis of world-leading engineering technologies and research findings, which are expected to provide a reference for solving real-world engineering problems.

This book is intended to provide a review of studies in the field of deep-see tunnel construction for civil engineers and equip scholars in related fields of research with a deeper insight into this domain. It can also help readers bring new ideas or apply the designed approaches from the collected papers to their professional studies or vocations.

The publication of this book is believed to be beneficial to develop relevant researches and subjects!

Editor in Chief
Guoxiong Mei

Hangzhou, China
December 2023

Contents

Deep-Sea Signal Recognition and Measurement and Control Technology

Study on Hydraulic Characteristics of Horizontal and Vertical Cross Inlet

Mengzhen Zhang, Ming Chen, Jiyang Sun, Bin Wu, and Qingsheng Chen

Abstract Inlet with horizontal and vertical discharge channels, as a new type, has certain advantages in flood discharge and diversion of water conservancy and hydropower engineering, but the water flow in this inlet is more complicated and lacks relevant systematic research. In this paper, a two-dimensional hydrodynamic mathematical model is used to investigate the hydraulic characteristics such as flow rate and velocity of each channel with respect to the area and head of horizontal and vertical diversion channels. According to the results, under different head ratios, confluence ratios are proportional to head ratios; however, the Froude number of horizontal hole and shaft are inversely proportional to head ratios. When the head ratios reach a certain extent, confluence rations and the Froude number tend to be a constant. In addition, under different area ratios, as the area ratios grow, the confluence ratios and the Froude number increase.

Keywords Diversion tunnel · Horizontal and vertical cross inlet · Hydraulic characteristics

1 Introduction

As global climate changes intensify, extreme floods occurred frequently. Once the discharge capacity of diversion tunnel is insufficient, flow overflows the top of cofferdam, which has a certain impact on the construction safety of the permanent building. Therefore, horizontal and vertical cross inlet is proposed to improve the discharge capacity under a certain water head. As a new type, the inlet can not only make full use of the shaft in discharge structure during the operation period and

M. Zhang · J. Sun · Q. Chen (✉)
College of Water Conservancy and Hydropower Engineering, Hohai University, Nanjing, Jiangsu, China
e-mail: qschen-dragon@163.com

M. Chen · B. Wu
PowerChina Huadong Engineering Corporation Limited, Hangzhou, Zhejiang, China

G. Mei et al. (eds.), *Advanced Construction Technology and Research of Deep-Sea Tunnels*, Lecture Notes in Civil Engineering 490,
https://doi.org/10.1007/978-981-97-2417-8_1

the horizontal hole during the construction period as the diversion structure during the construction period, to meet the needs of the low water level and the large flow discharge, but also can be quickly converted into the flood discharge tunnel at the operation period through the blocking of the horizontal hole. When the horizontal and vertical cross inlet discharge flow, there exists the two-layer discharge characteristics distinguished by horizontal hole discharge and vertical shaft discharge, so hydraulic characteristics are more complex. Since the inlet is a new type, there is a relative lack of systematic researches in this field, and previous studies have been carried out mainly on separate horizontal inlets or shaft inlets. As for the horizontal inlets, Deng [1], for example, summarized the effects which various water flow boundary conditions and shapes of inlets had on the water surface vortex in front of the horizontal inlets, and proposed a method to improve the state of the inlet flow to overcome the vortex. Zhao et al. [2] studied the flow rate, flow regime, pressure, full flow boundary and body shape through model tests of the diversion tunnel, and proposed that V-type eddy-eliminating beam arranged in front of the inlet can effectively eliminate inlet vortex. Shi et al. [3] conducted hydraulic modeling tests aimed for steep-slope diversion tunnel and found that the head plate of the horizontal inlet was changed from the typical elliptical type to a sharp-edge form, which could eliminate the phenomenon of mixed free-surface-pressure flow in the delivery tunnel at the downstream of the inlet. Based on the Baihetan inflow model, Fu et al. [4] investigated the effect of different heights of residual cofferdam on the discharge capacity of horizontal inflow and outflow holes. Zheng [5] conducted numerical simulation of hydraulic characteristics of the spillway at low and atmospheric pressures and found that atmospheric pressure mainly affected cavitation number of the spillway. For the vertical shaft inlet, Guo et al. [6] proposed that the reasonable size of the energy dissipation well should be that the depth of the well was equal to 1.69 times the diameter of the shaft by analyzing the effect of the change of the shape on each hydraulic parameter in the energy dissipation well. Zhang [7] proposed a new internal rotational flow shaft spillway for high arch dams. The simple structured design provided not only a stable higher capacity water discharge, but also a high-energy dissipation rate and low construction costs. Guo et al. [8] proposed a new vortex drop shaft spillway, which not only improved energy dissipation, but also protected ecology and reduced investment. Liu et al. [9] proposed new shaft spillways types to generate swirling flow by using piers and circular piano-keys on the annular crest. Their findings demonstrated that the swirling flow strength in the modified spillway was several times lower when compared to that of the conventional spillway. Based on modeling tests, Kabiri-Samani et al. [10] investigated the hydraulic characteristics including head-discharge relationship, discharge coefficient, and critical submergence depths of a vertical shaft spillway with an innovative inlet (namely marguerite-shaped inlet) and derived empirical equations related to critical submergence depths and discharge coefficients of the marguerite-shaped inlet for different flow regimes. Aydin et al. [11] employed the novel labyrinth-shaft spillway which was better in terms of discharge capacity for the same weir head compared to the conventional shaft spillway. Aydin et al. [12] explored siphon-shaft spillway which could make an effective discharge through siphonic feature in dam reservoirs with narrow valleys.

To summarize, the current scholars carry out the study of the diversion tunnel basically based on the specific horizontal inlet or vertical inlet project cases, lacking systematic and regular analysis of the horizontal and vertical cross inlet. This paper utilizes Fluent, to establish the two-dimensional hydrodynamic model of the diversion tunnel, and to study the discharge characteristics of the vertical cross inlet by varying head ratio and area ratio of different horizontal inlet as well as shaft inlet.

2 Analytical Modeling and Validation

2.1 Structural Model of Inlet

The structural arrangement of the novel inlet is shown in Fig. 1. The scope of the analysis includes the reservoir area, the inlet, and the delivery tunnel. The inlet consists mainly of horizontal and shaft inlets, as well as flared and horizontal sections on the downstream of the shaft. The dimension of the inlet of the shaft are 10×17 m, and the elevation of the bottom of the shaft is lower than the floor of the horizontal hole, in order to form an energy-dissipating water cushion for the flow water from the shaft. The shaft downstream is connected with a flared section of 6 m in length, followed by a horizontal section of 5 m in length. The length of the cave of the diversion tunnel is 85 m and the slope of the bottom plate is 3.10%. In the figure, h stands for the height of the horizontal hole inlet and H means the depth of water. In addition, l represents the length of the shaft. H_V expresses the depth of water above the leading-edge of the overflow at the inlet of the shaft. CS_1 and CS_2 sections are defined as the horizontal hole and shaft inlet section respectively. CS_3 section is termed as the end of flare section (maximum average flow velocity section at the inlet).

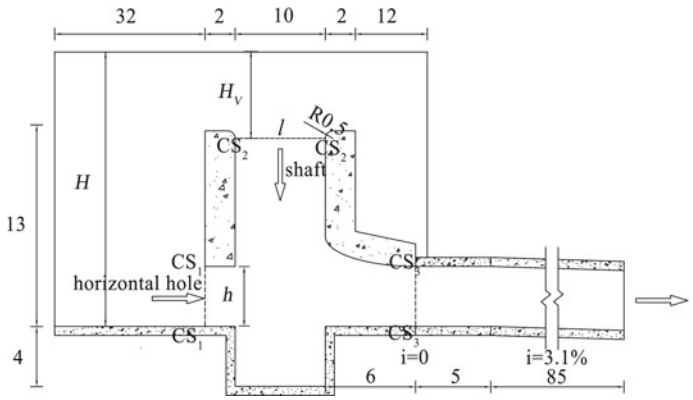

Fig. 1 Structural arrangement of the inlet and the analysed scope (unit: m)

2.2 Numerical Analysis Model

The numerical simulation is based on the SST k-omega, and the gas–liquid two-phase flow is calculated by Volume of Fluid. The control equations are discretized by the finite volume method. The control equations are as follows.

Turbulent kinetic energy:

$$\frac{\partial}{\partial t}(\rho k) + \frac{\partial}{\partial x_i}(\rho k u_i) = \frac{\partial}{\partial x_j}\left(\Gamma_k \frac{\partial k}{\partial x_j}\right) + G_k - Y_k + S_k \tag{1}$$

Turbulent dissipation rate

$$\frac{\partial}{\partial t}(\rho \omega) + \frac{\partial}{\partial x_i}(\rho \omega u_i) = \frac{\partial}{\partial x_j}\left(\Gamma_\omega \frac{\partial \omega}{\partial x_j}\right) + G_\omega - Y_\omega + D_\omega + S_\omega \tag{2}$$

In the formula: i, j are parameters of coordinate directions, i, j = 1, 2 correspond to x, y coordinate directions, respectively; x_i, x_j are the Cartesian coordinates in the i, j directions; u_i is the time-mean flow velocity in the i direction; ρ is the density; G_k is the turbulent kinetic energy which is generated by the velocity gradient of laminar flow; Γ_k and Γ_ω are the active diffusion terms of k and ω; Y_k and Y_ω are the divergent terms of k and ω; D_ω is the Orthogonal divergence term; S_k and S_ω are defined by users.

2.3 Grid Division and Solution Method

The pre-processing software Gambit is utilized to perform grid generation of the research area, and a combination of structural and non-structural grids are used for grid division. In this paper, four grid scales are used: 10, 15, 20 and 25 cm. The boundary condition of inlet and outlet are the same for the different grid scales. Grid independence analysis is performed by comparing values of flow rate and velocity at the CS_3 section for different grid scales. The grid independence results are shown in Table 1, and the results indicate that the calculation results tended to be stable. Therefore, grid scale of 15 cm is selected for numerical simulation in this paper.

The coupled algorithm is applied to deal with pressure–velocity coupling. Momentum, Turbulent kinetic energy and turbulent dissipation rate are based on

Table 1 The results of grid independence analysis

Grid scale (cm)	Grid numbers ($\times 10^4$)	Average velocity (m/s)
25	5.99	26.94
20	9.42	27.01
15	16.32	27.04
10	36.87	27.04

Table 2 Comparison of hydraulic parameters between numerical and physical models

	Flow rate (m^3/s)	Flow velocity (m/s)		
		Bottom	Middle	Surface
Experimental values	85.34	5.16	5.53	4.87
Calculated values	86.94	5.30	5.61	4.98
Error	1.87	2.71	1.45	2.26

second order upwind. Least squares cell based and PRESTO! are utilized in gradient and pressure interpolation, respectively. Standard initialization is used to set the volume fraction of water in the calculation region below the free surface to be assigned a value of 1, and the flow velocity and pressure are treated as stationary flow field. The inlet uses pressure-inlet with additional water level boundary condition. The outlet is set as pressure-outlet and average pressure of cross section was 0. The near-wall is treated with wall function and non-slip condition is adopted. The convergence criterions are set as 1×10^{-4}.

2.4 Model Verification

A physical model with a length scale of 1:50 is chosen to validate the mathematical simulation. The test results under H = 30 m and h = 4 m are used to verify the reasonableness of the established mathematical model by comparing the flow rate and velocity at the inlet and the three measuring points of the bottom, middle and surface on the perpendicular bisector in the cross sections of CS_1. Table 2 shows that the relative errors of the flow rate and flow velocity results of numerical simulation and physical model are all within 3%. Considering the influence of sidewall resistance in the physical model, it is reasonable that experimental values are smaller than the calculated values, which indicate that the accuracy of the mathematical model meet the requirements of the calculations.

3 Results Analysis

3.1 Research Program

The study program takes water depths H of 30, 35, 40 and 50 m. The height of the horizontal hole h adopts 4, 5, 6, 7 and 8 m. Therefore, there exists 20 sets of calculation conditions.

3.2 Analysis and Discussion of Results

Analysis of flow regime

For $\lambda_H = 0.75$ and $\lambda_A = 2.5$, the streamlines and flow velocity distribution profile at the inlet is shown in Fig. 2. The chart indicates that due to the deflection of flow direction in the shaft, horizontal vortex is be formed on the upstream side of the shaft, and the upstream velocity is less than the downstream velocity. In addition, the clockwise horizontal vortex is formed in the water cushion pool at the bottom of the shaft.

Analysis of discharge capacity

In terms of horizontal and vertical cross inlet, flow rates of horizontal hole and vertical shaft as well as the former two total sum are set as Q_H, Q_V and Q_T respectively. So as to explore discharge capacity of this inlet, the definitions of relevant terms in this analysis are as follows.

The head ratio of the shaft to the horizontal hole is defined as:

$$\lambda_H = \frac{H_V}{H} \tag{3}$$

The ratio of the overflow area of the shaft to the horizontal hole is normed as:

$$\lambda_A = \frac{l}{h} \tag{4}$$

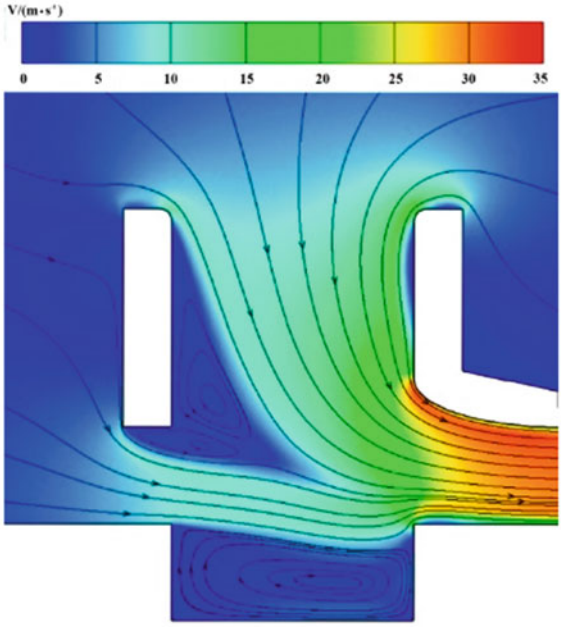

Fig. 2 Streamlines and flow velocity distribution profile at the inlet

The confluence ratio of the shaft to the horizontal hole is as:

$$\lambda_Q = \frac{Q_V}{Q_H} \tag{5}$$

Effect of head ratio on confluence ratio

In order to analyze the confluence ratios of the inlet under different head ratios, λ_A = 1.25, 1.43, 1.67, 2.00 and 2.50 are selected, and the relationship curves of λ_H and λ_Q with different area ratios are plotted, as shown in Fig. 3.

Seen from the graph, λ_Q is proportional to λ_H, which means the former increase as the latter grew; however, the increase is inversely proportional to λ_H. The bigger λ_H becomes, the stronger blocking effect of the shaft inflow on the horizontal hole discharge is, which in turn lead more water to flow into flow into the downstream delivery tunnel through the shaft. In the meantime, as λ_H increases, λ_Q is less and less affected by λ_H since the discharge capacity is mainly controlled by the shape of the delivery tunnel section, and λ_Q tends to a constant.

Effect of area ration on confluence ratio

With respect to analyze the confluence ratios of the inlet under different area ratios, this paper selects λ_H = 0.583, 0.643, 0.688 and 0.750, and plots the relationship curves between λ_A and λ_Q under different head ratios, as shown in Fig. 4.

According to the chart, λ_Q increases as λ_A inclines. In view of areas, essential factors affecting results, controlled by the CS_3 section, the total flow rates are essentially the same when head ratios of the inlet are equal, significantly varying only the confluence ratios. In addition, due to the interaction of the horizontal and vertical flow, as λ_A increases, more water enters the shaft and less water flows out of the horizontal hole, and λ_A and λ_Q show a roughly good linear relationship.

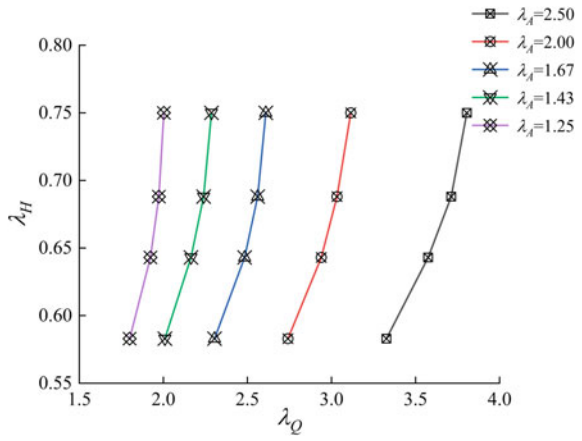

Fig. 3 Varying principles between λ_Q and λ_H under different area ratios

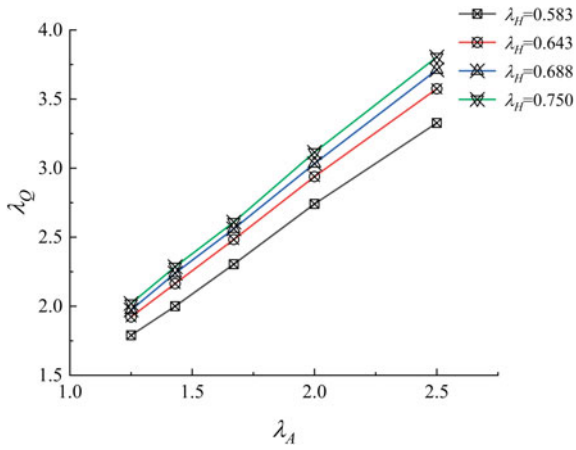

Fig. 4 Varying principles between λ_Q and λ_A under different head ratios

Analysis of the Froud number

In order to quantitatively investigate the extent, to which the horizontal hole and the shaft interact with each other when the shaft is in the regime of orifice flow for combined inlet, Fr_H and Fr_V are introduced.

The Froude Number of the horizontal hole is defined as:

$$Fr_H = \frac{v_H}{\sqrt{gH}} \tag{6}$$

The Froude Number of the inlet of the shaft is normed as:

$$Fr_V = \frac{v_V}{\sqrt{gH_V}} \tag{7}$$

In the formula: v_H and v_V are as the cross-sectional average flow rates of the horizontal hole and shaft inlet in sequence.

Effect of head ratio on the Froud number

With respect to analyze the Froud Number Fr_H and Fr_V of the inlet under head ratios, $\lambda_A = 1.25, 1.43, 1.67, 2.00$ and 2.50 are chosen, and the relationship curves between λ_H and Fr_H, λ_H and Fr_V under different area ratios are plotted, as shown in Figs. 5 and 6.

The figures reveal that Fr_H and Fr_V are inversely proportional to λ_H; however, the decreases are inversely proportional to λ_H. The relationship shows that with the increase of λ_H, the water flow in the shaft has more and more obvious blocking effect on the discharge of the horizontal hole, the role of the horizontal hole in the discharge of the flow gets smaller and smaller and with the increase of λ_H, Fr_H and Fr_V tend to a constant.

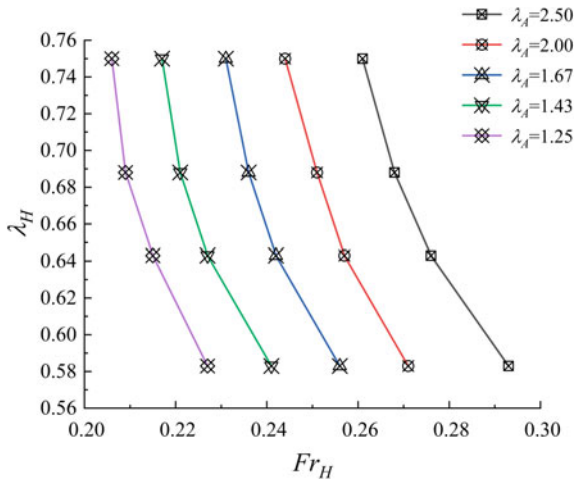

Fig. 5 Curves about the relationship between Fr_H and λ_H

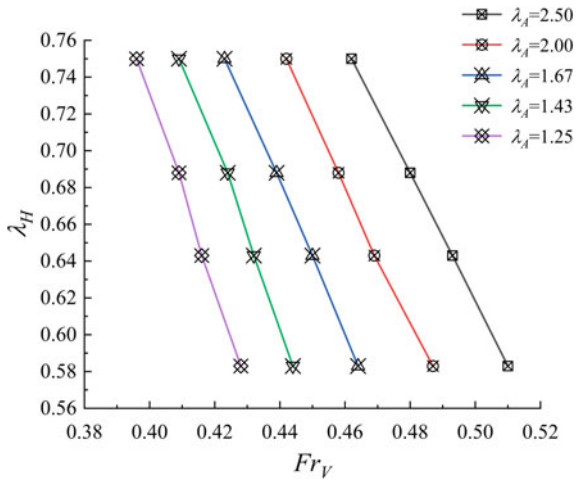

Fig. 6 Curves about the relationship between Fr_V and λ_H

Effect of area ratio on the Froud number

With respect to analyse the Froud Number Fr_H and Fr_V of horizontal and vertical cross inlet under different λ_A, in this paper, $\lambda_H = 0.583, 0.643, 0.688$ and 0.750 are selected, the relationship curves are plotted, as shown in Figs. 7 and 8.

Seen from the chat, Fr_H and Fr_V are proportional to λ_A; however, the increases are inversely proportional to λ_A.

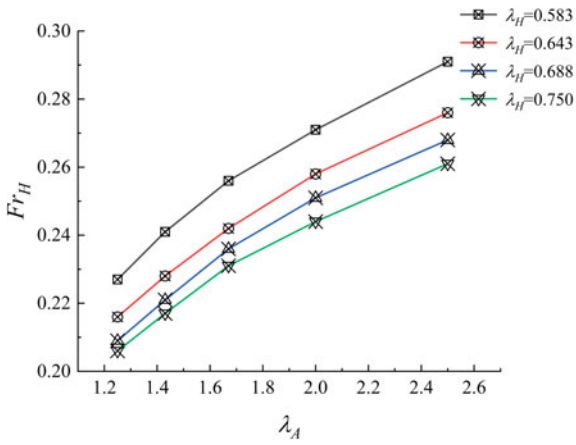

Fig. 7 Curves about the relationship between Fr_H and λ_A

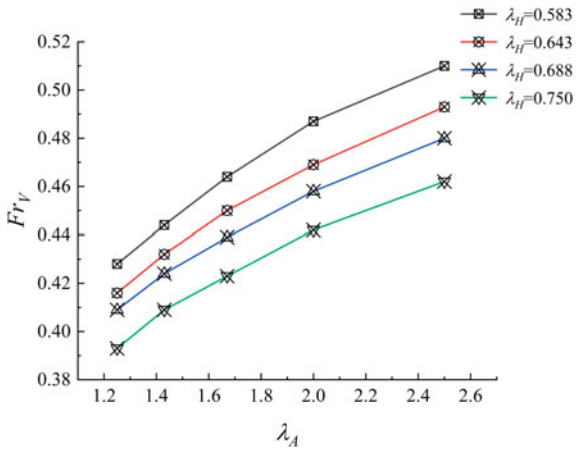

Fig. 8 Curves about the relationship between Fr_V and λ_A

4 Conclusion

Horizontal and vertical cross inlet can greatly improve the discharge capacity, and effectively solve the insufficient discharge capacity caused by extreme floods. In this paper, a two-dimensional hydrodynamic mathematical model is used to analyze the discharge characteristics such as confluence ratio and the Froud number, the conclusions are followed as.

Under different head ratios, confluence ratios are proportional to head ratios, which mean the former increases as the latter grows; however, the Froud Number of the horizontal hole and shaft are inversely proportional to head ratios. The results reveal that the increase of head ratios, the water flow in the shaft has more and more obvious blocking effect on the discharge of the horizontal hole. In addition, the head

ratios reach a certain level, the discharge capacity of the inlet is mainly controlled by the shape of the delivery tunnel.

Under different area ratios, confluence ratios and the Froud Number are proportional to area ratios. According to the results, controlled by the CS_3 section, the total flow rates are essentially the same when the head ratios of the inlet are equal, varying confluence ratios and the Froud Number.

References

1. Deng S (1986) Exploration of the formation of water surface vortex at the inlet of discharge structure and its overcoming methods. Hydro-Sci Eng 04:51–63
2. Zhao X, Zhao Y, Li S, Su X (2013) Experimental and analysis of hydraulic model of diversion tunnel of Hekou village reservoir. Water Resour Power 31:133–135
3. Shi J, Liu Y, Duan C, Shen J (2013) Research on the inlet shape of steep diversion tunnel by model test. J Yangtze River Sci Res Inst 30:37–39+53
4. Fu W, He C, Fei W, Zhou Z, Chen H (2014) Investigation of influence discharge capacity of Baihetan diversion tunnel located in inlet and outlet by residual cofferdam. Water Resour Power 32:115–118
5. Zheng X (2015) Numerical analysis on flow characteristic of RuMei hydroelectric plant spillway in high altitude region. Hohai University
6. Guo L (2007) Experimental study of bodily form optimization of the shaft spillway. Xi'an University of Technology
7. Zhang X (2015) Hydraulic characteristics of rotational flow shaft spillway for high dams. Int J Heat Technol 33:167–174
8. Guo X, Xia Q, Fu H, Yang K, Li S (2016) Numerical study on flow of newly vortex drop shaft spillway. J Hydraul Eng 47:733–741+751
9. Liu Z, Guo X, Xia Q, Fu H, Wang T, Dong X (2018) Experimental and numerical investigation of flow in a newly developed vortex drop shaft spillway. J Hydraul Eng 144:04018014
10. Kabiri-Samani A, Keihanpour M (2020) Hydraulic characteristics of swirling flow at shaft spillways with the marguerite-shaped inlets. J Hydraul Res 59:724–738
11. Aydin MC, Ulu AE (2023) Numerical investigation of labyrinth-shaft spillway. Appl Water Sci 13
12. Aydin MC, Ulu AE (2023) Developing and testing a novel pressure-controlled hydraulic profile for siphon-shaft spillways. Flow Meas Instrum 90:102332

Study on the Axial Hysteresis Performance of X Node Reinforced by Upward Grooved Ring Plate

Junwu Xia, Lingyuan Meng, Chunbo Zhou, Nianxu Yang, and Hang Xu

Abstract To address the challenge of being unable to observe damage in the main branch area with the existing reinforcement method, a new method of relocating the slotted ring flange was proposed. Through full-scale axial reciprocating loading tests, a comparative analysis of two damage modes, the ring flange corner plate and the slotted ring flange relocation reinforcement, was conducted. The study also investigated the axial hysteresis performance of the slotted ring flange's X-shaped nodes.

Keywords X-shaped square steel pipe node · Groove ring mouth plate moved up for reinforcement · Axial hysteresis performance

1 Introduction

Rectangular (square) tube sections exhibit excellent tensile, compressive, bending, and torsional properties, and they are often used in the truss structures [1]. Among these, the double-layer Vierendeel truss, characterized by the absence of diagonal members with all joints being X-type nodes, is known for its simplicity and aesthetic appearance. In steel tube trusses, complex joints are frequently reinforced locally to meet the design requirements for strong connections, ensuring the structural load-bearing capacity [2]. Steel tube joint reinforcement is typically achieved through

J. Xia · L. Meng (✉) · N. Yang · H. Xu
State Key Laboratory for Intelligent Construction and Health Operation and Maintenance, China University of Mining and Technology, Xuzhou, Jiangsu, China
e-mail: 2226092391@qq.com

J. Xia
Jiangsu Collaborative Innovation Center of Building Energy-Saving and Construction Technology, Jiangsu Vocational Institute of Architectural Technology, Xuzhou, Jiangsu, China

C. Zhou
School of Science, Qingdao University of Technology, Qingdao, Shandong, China

G. Mei et al. (eds.), *Advanced Construction Technology and Research of Deep-Sea Tunnels*, Lecture Notes in Civil Engineering 490,
https://doi.org/10.1007/978-981-97-2417-8_2

external or internal strengthening, with good reinforcement effects achieved by welding ring plates on the joint surface.

Existing research has shown that ring plates are effective in strengthening joints, but this method does not allow for the observation of joint failure modes. Therefore, building upon the concept of ring corner plates, a new method for joint reinforcement, namely, the upward movement of reinforcement plates, is proposed as slot-type ring plate upward movement. To investigate its impact on joint hysteresis performance, this study focuses on X-type joints in double-layer Vierendeel trusses. After understanding their static performance, the axial hysteresis performance of the joints is studied [3].

2 Arrangement of Axial Reciprocating Loading Test

2.1 Specimen Design

Under the action of planar bending moments, different values of β will result in different failure modes at the joint [4]. Therefore, specimens with $\beta = 0.7$ and $\beta = 1.0$ are designed as reference specimens, denoted as URX-70B and URX-100B, respectively. Specimens of joints reinforced with ring corner plates with $\beta = 0.7$ (slot-type ring plates with no upward movement) and slot-type ring plates with $\beta = 0.7$ are also designed, denoted as CPX-70-A and CPX-70-B, respectively. In these specimens, the ring corner plates are square tubes one size larger than the main pipe, with holes cut in the upper and lower flanges based on the branch pipe size. These plates are then cut along the symmetrical planes of the steel pipe's longitudinal axis and welded onto the unreinforced joint. The slot-type ring plates are also square tubes one size larger than the main pipe, with holes cut in the upper and lower flanges based on the branch pipe size. The steel pipe is cut into four symmetrical parts along two symmetric planes and then welded onto the unreinforced joint after being raised to a certain height [5]. The geometric parameters of the reinforced joints CPX-70-A and CPX-70-B are defined as shown in Fig. 1 (with the unreinforced joint as a reference), and the dimensions of each joint are listed in Table 1. The lengths of the main pipe, branch pipe, and reinforcement plate are denoted as l_0, l_1, l_p, respectively, with corresponding cross-sectional dimensions as $b_0 \times h_0 \times t_0$, $b_1 \times h_1 \times t_1$, and $b_p \times h_p \times t_p$. The upward movement height of the slot-type plate is denoted as h. All test joints are welded, with weld bead dimensions greater than or equal to 5 mm. Cold-formed hollow steel sections are used for the steel components, and the material test results are presented in Table 2.

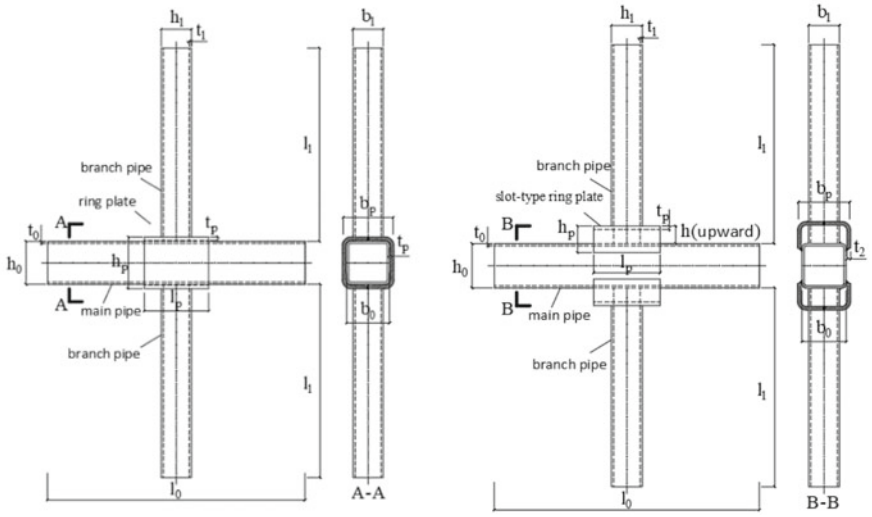

(a) CPX-70-A (b) CPX-70-B

Fig. 1 Parameter definitions of joints

Table 1 Geometries of test joints(mm)

Specimen	Main pipe				Branch pipe				Reinforcement plate				h
	b_0	h_0	t_0	l_0	b_1	h_1	t_1	l_1	b_p	hp	t_p	lp	
URX-70B	100	100	5	600	70	70	5	450	–	–	–	–	–
URX-100B	100	100	5	600	100	100	5	450	–	–	–	–	–
CPX-70-A	100	100	5	600	70	70	5	450	120	120	8	150	0
CPX-70-B	100	100	5	600	70	70	5	450	120	60	8	150	40

Table 2 Mechanical properties

Square steel tube	fy	fu	fu/fy
100 × 100 × 5	314 MPa	419 MPa	1.334
70 × 70 × 5	425 MPa	483 MPa	1.136
120 × 120 × 8	328 MPa	451 MPa	1.375

2.2 Loading Procedure

The test specimens are arranged vertically. The far end of the branch pipe is connected to the support using pin connections, while the support is connected to the self-balancing reaction frame, main pipe loading plate, and actuator using high-strength bolts. Vertical loading is applied using an MTS-100 kN servo actuator. To obtain a co-directional bending moment M at the intersection point of the branch pipe

and the main pipe, a force F is applied at the end of the main pipe, resulting in an equivalent force of 1/2F at the far end of the branch pipe, perpendicular to it. Before the formal loading, a 25% cyclic preloading is applied to ensure that all instruments and equipment are functioning properly and to eliminate installation gaps. The formal loading is initially controlled by load control, with three cycles at 50 and 75%. After that, displacement control based on yielding displacement is used, with three cycles at 1, 2, and 3% strain increments, followed by two cycles for each subsequent increment until failure of the specimen, at which point loading is stopped [6].

2.3 Measurement Plan

As shown in Fig. 2, YWC-50 displacement sensors are positioned at the axis of the lower flange of the branch pipe (50 mm from the center) to observe the corresponding angular deformations of the branch pipes. Displacement sensors are symmetrically placed on the upper side of the loading plate along the plane containing the axis of the main pipe sidewall to detect any out-of-plane deformations of the components. Strain gauges and rosettes are placed at corresponding positions on the main pipe flange and sidewall. Data collection is carried out using a DH 3816N static data acquisition system.

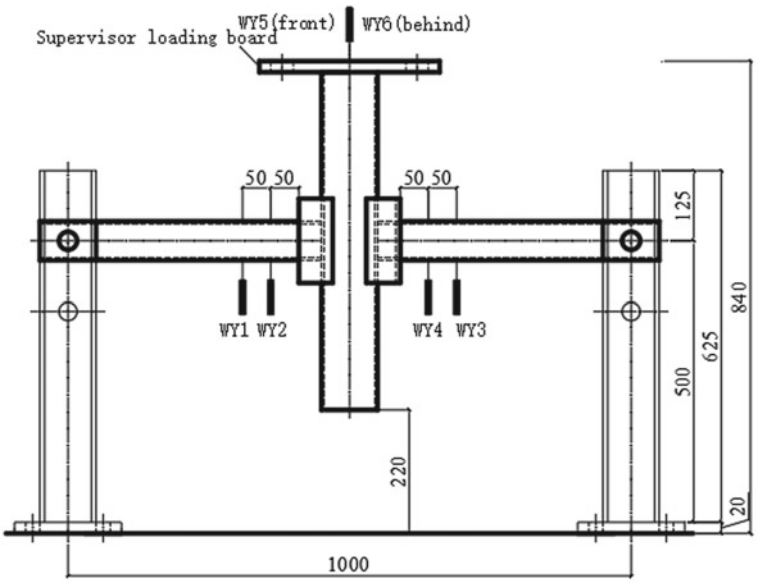

Fig. 2 Site layout plan (e.g. CPX-70-B)

3 Results and Discussion

3.1 Joint Failure Test Observations

During the loading of URX-70B, there were no significant deformations or cracking observed. In the first three levels of displacement loading, the specimen exhibited minor cracks at the weld corner of the main pipe flange (Fig. 3a), and these cracks gradually closed as compressive forces were applied to the branch pipe flange side (Fig. 3b). However, during the fourth level of displacement loading in the first cycle, cracks appeared at the weld corner of the main pipe flange (Fig. 3c). With the continued application of load, the load-carrying capacity began to decrease, and the cracks extended outward, causing deformation in the main pipe flange (Fig. 3d). Loading was stopped when the load-carrying capacity dropped below 85%. URX-100B did not exhibit significant deformation or cracking during the preloading and 50% loading phases. During the first 75% loading cycle, minor cracks appeared at the weld corner of the main pipe sidewall (Fig. 4a). In the first three levels of displacement loading, cracks on the main pipe sidewall gradually extended towards the corner (Fig. 4b), and these cracks closed gradually as compressive forces were applied to the branch pipe flange side. However, during the fourth level of displacement loading in the first cycle, significant cracking occurred at the weld corner of the main pipe sidewall (Fig. 4c). With the continued application of displacement load, the load-carrying capacity gradually decreased, and the cracks at the root of the weld on the main pipe sidewall penetrated through, resulting in deformation of the main pipe sidewall and flange (Fig. 4d). The maximum crack width reached 7 mm, and loading was stopped when the load-carrying capacity dropped below 85%.

During the loading and the first three levels of displacement cycling of CPX-70-A, there were no significant deformations or cracking observed. When loading reached the first cycle of the sixth level of displacement loading, minor cracks appeared at the weld corner of the joint (Fig. 5a). As the load was applied, cracks developed in the branch pipe at the weld corner (Fig. 5b). When loading reached the seventh level of displacement loading, cracks in the branch pipe at the weld corner became pronounced (Fig. 5c). By the eighth level of displacement loading, the cracks in the branch pipe had completely penetrated (Fig. 5d), and the joint lost its load-carrying capacity. Loading was stopped at this point. For CPX-70-B, there were no significant

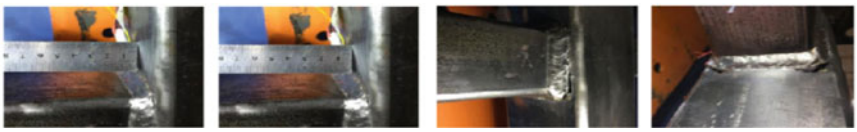

(a) minor cracks on the main pipe (b) closure of cracks in the main flange plate (c) obvious cracking of the main flange plate (d) cracking and damage of the main flange plate

Fig. 3 Performance of URX-70B

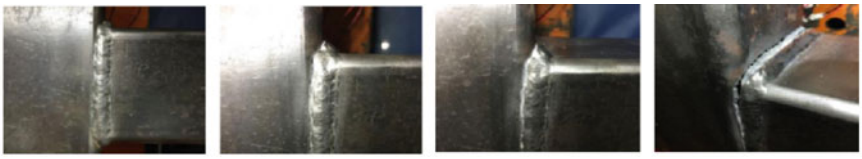

(a) minor cracks on the side wall of the mai n pipe

(b) cracks on the side wall of the supervisor spread to the corners

(c) significant cracking at the corners of the weld seam

(d) cracking and penetration failure at the root of the weld seam

Fig. 4 Performance of URX-100B

(a) minor cracks in corner branch pipe

(b) cracking of weld corner branch pipe

(c) significant cracking of the weld seam

(d) branch pipe cracking and penetration

Fig. 5 Performance of CPX-70-A

deformations or cracking during the initial loading. However, when loading reached the first cycle of the second level of displacement loading, minor cracks appeared at the root of the main pipe-branch pipe weld (Fig. 6a). As the load was applied, cracks in the branch pipe flange became more noticeable, and minor cracks also appeared at the weld corner of the slot-type ring plate-branch pipe (Fig. 6b). When loading reached the fifth level of displacement loading, cracks at the weld corner of the slot-type ring plate-branch pipe became more pronounced and extended outward (Fig. 6b). By the seventh level of displacement loading, the cracks at the weld corner of the slot-type ring plate-branch pipe had completely penetrated (Fig. 6c), and the slot-type ring plate's flange and sidewall exhibited deformation (Fig. 6d). At this point, the joint lost its load-carrying capacity, and loading was stopped. The upward movement of the reinforcement plate facilitated the observation of deformations and crack development in the main and branch pipes of the joint, but the deformations in the flange and sidewall of the slot-type ring plate were more pronounced.

3.2 The Hysteresis Loops and Skeleton Curves

Figure 7 provides the hysteresis loops and skeleton curves for each specimen. It can be observed that the hysteresis loops of all specimens are relatively full. URX-70B, CPX-70-A, and CPX-70-B exhibit no significant pinching behavior in their hysteresis loops, while URX-100B exhibits some pinching, which may be attributed to slight

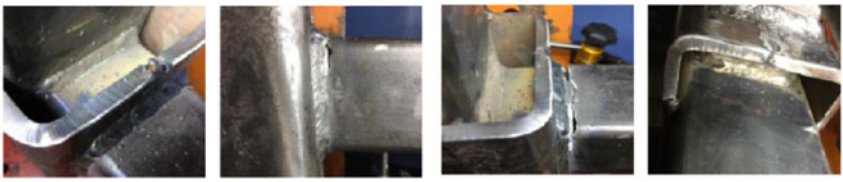

(a) minor cracks at the root of the weld seam

(b) cracking of weld corner branch pipe

(c) weld cracking and penetration

(d) concave convex deformation of the groove type ring mouth plate

Fig. 6 Performance of CPX-70-B

slippage in the loading direction during the joint loading process. Previous research has indicated that when the plastic rotation angle of a joint exceeds 0.03 radians, the joint is considered to possess strong plastic deformation capacity. The tested joints all exhibit plastic rotation angles of 0.04 radians or more, suggesting that they have good ductility [7]. The peak points of each level's first-cycle M-θ curves were used to create skeleton curves. It can be seen that the positive and negative moments of the joint are essentially symmetrical, indicating good tensile-compression symmetry.

3.3 Energy Dissipation

The equivalent viscous damping coefficient (ζeq) was used to assess the energy dissipation capacity of the joints (Fig. 8) [8]. The unreinforced joints showed an initial increase followed by a decrease in energy dissipation, while the reinforced joints did not exhibit a decreasing trend. CPX-70-A had a better ζeq compared to CPX-70-B. In comparison to URX-70B and URX-100B, specimens CPX-70-A and CPX-70-B exhibited significantly increased energy dissipation while reducing the equivalent viscous damping coefficient, but with a less pronounced reduction. Among the two reinforcement methods, the upward movement reinforcement of the slot-type ring plate had a greater efficiency in reducing the energy dissipation capacity of the joint.

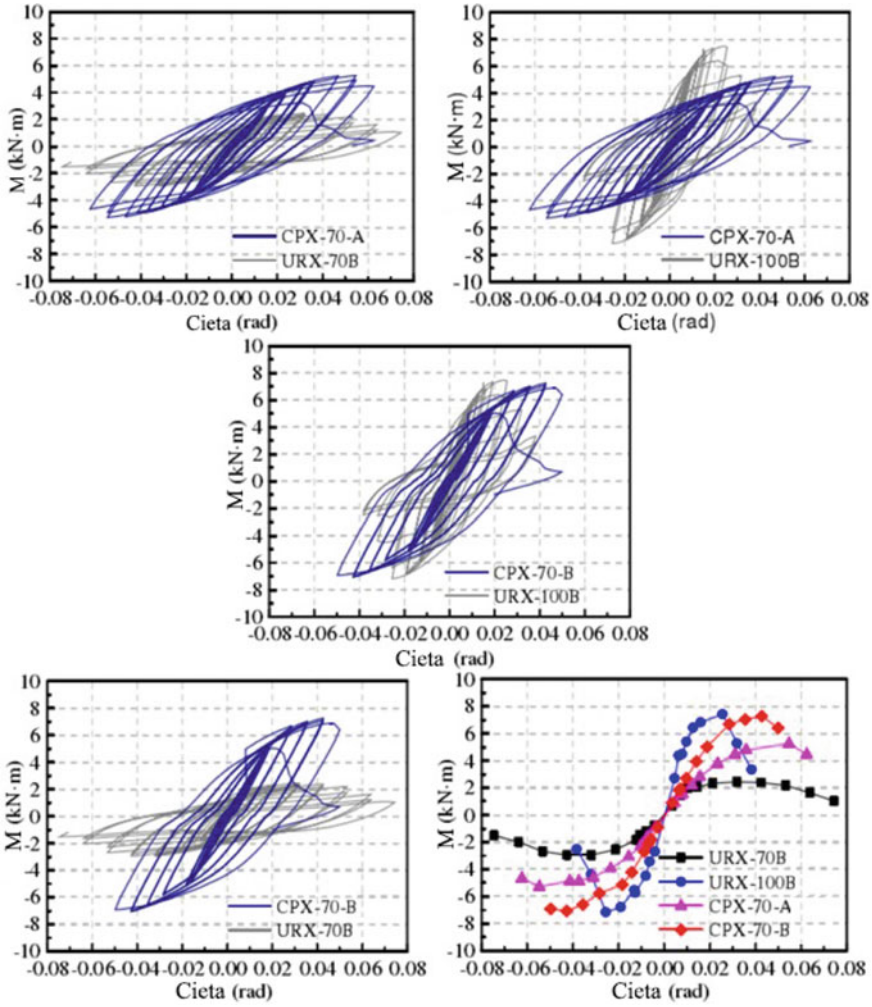

Fig. 7 The hysteresis loops and skeleton curves

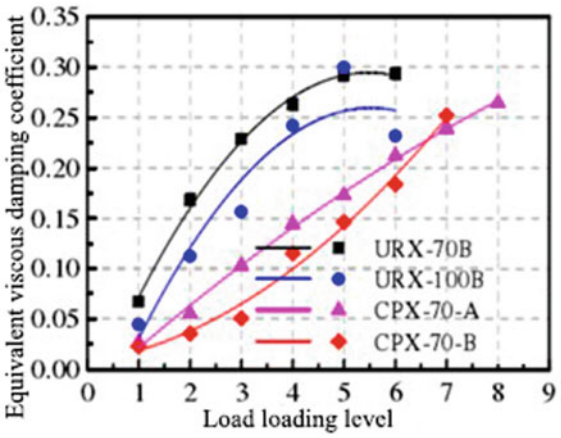

Fig. 8 ζeq of each test specimen

4 Conclusion

(1) The reinforcement of the ring flange corner plate and the relocation of the slotted ring flange can mitigate the deformation of the main pipe. The upward movement of the slotted ring flange enables effective observation of the deformation of the main pipe's flange plate and side walls, as well as the cracking in the main pipe-supporting pipe weld zone. This is highly advantageous for the timely monitoring of the deformation of the main branch pipe.

(2) Due to the upward movement, the deformation of the slotted ring flange's flange plate is more pronounced compared to the deformation of the ring flange corner plate's flange plate.

(3) The hysteresis curves for unreinforced and reinforced nodes in the plane are both relatively full. Among them, the hysteresis loop area for reinforced nodes is greater than that of unreinforced nodes.

(4) The equivalent viscous damping coefficient of reinforced nodes is smaller than that of unreinforced nodes, and node reinforcement mitigates the trend of reduced equivalent viscous damping coefficient under cyclic loads for unreinforced nodes. The reinforcement method using ring flange corner plates results in a smaller reduction in the equivalent viscous damping coefficient of nodes compared to the method involving the upward movement of slotted ring flanges.

(5) From the comparison of data, it can be seen that the mechanical properties of the two reinforcement methods are not significantly different and both meet the requirements of the specifications. However, the structural parameters for the upward movement reinforcement of the groove type annular plate were selected based on experience, and the impact of different structural parameters on its performance was not explored.

References

1. Chan TM, Gardner L, Law KH (2010) Structural design of elliptical hollow sections: a review. Proc Inst Civil Eng-Struct Build 163(6):391–402
2. Fan Z, Yang S, Luan HQ (2011) Research progress and practice of design of spatial structure joints. J Build Struct 32(12):1
3. Chang HF, Zhou LY, Hu L, Zhou J, Xia JW (2021) Research on axial hysteresis performance of T-shaped joints strengthened by square steel tube vertical insert plate. J Central South Univ (Sci Technol) 52(05):1591–1600
4. Chang HF, Luo Z, Xu W, Kong W (2018) Analysis of Axial Hysteresis performance of welded T-joints with square steel tubes. J China Univ Min Technol 47(04):913–920
5. Chang HF, Xia JW, Duan XM, Qi B (2013) Static test of T-shaped joints strengthened by square steel tube cladding and vertical insertion plate under compression. J Build Struct 34(10):57–63
6. Xu F, Ma Z, Jia Y, Li ZX (2020) Study on joint performance of energy dissipation knee braced frame. J Guangxi Univ (Nat Sci Ed) 45(01):96–104
7. Xia JW, Yu LL, Leng L, Ma RW, Gong P, Bai JB (2020) Study of seismic behavior of the new beam-column splicing outer sleeve joint. J China Univ Min Technol 49(04):627–635
8. Toscano D, Behravesh SB, Shaha SK (2020) Characterization of closed-die forged AZ31B under pure axial and pure shear loading. Int J Fatigue 139:105754

Monitoring and Prediction of Settlement in Large Diameter Slurry Shield Tunnels in Water-Rich Sand Layers

Hongxing Zhang

Abstract A major goal of the research is to find solutions to the problems caused by the unique geological features of the Large Diameter slurry shield as it tunnels through a water-rich sand stratum with sandy gravel layers. In order to improve the building process under comparable engineering conditions, the research intends to develop and test novel mud improvers as well as soil improvement methods. The investigation entails performing laboratory tests utilizing various compounds, such as xanthan gum, guar gum, and clay medium particulates, in conjunction with bentonite as the base mud. The researchers determined the optimal slurry preparation scheme by conducting tests which consists of 1% clay particles, 4% bentonite, 0.2% xanthan gum, and 0.04% soda ash. This combination is found to yield the best performance in enhancing the properties of the slurry used in tunneling, and the study concludes that xanthan gum is the most effective additive for improving slurry performance. The research provides guidance on the ideal ratio of new mud to be added to various soil types.

Keywords Slurry shield tunneling · Water-rich sand stratum · Xanthan gum

1 Introduction

Rapid growth of urban rail transportation projects, the subway shield construction has become a popular choice due to its distinct advantages [1]. During the construction of Earth Pressure Balance (EPB) shield tunnels in Beijing, the team regularly runs into difficulties due to the sandy gravel soil [2, 3]. The natural state of the excavated soil often lacks the required plastic fluidization properties [4, 5], which can lead to various issues such as excavation surface instability, pressure chamber closure [6, 7], pressure chamber caking [8], and water ingress [9]. In order to optimize the functionality of shield tunneling, the soil must possess suitable plasticity

H. Zhang (✉)
China Railway Fourth Bureau Group Fifth Engineering Co., Jiujiang 332000, Jiangxi, China
e-mail: 376906593@qq.com

G. Mei et al. (eds.), *Advanced Construction Technology and Research of Deep-Sea Tunnels*, Lecture Notes in Civil Engineering 490,
https://doi.org/10.1007/978-981-97-2417-8_3

and a low permeability [10, 11]. Muck improvement technology, a key aspect of EPB shield construction, has gained increasing attention in shield research [12]. Currently, foam agents, dispersants, clay minerals, and flocculants are the most common types of improvement additives. Clay and bentonite are frequently utilized minerals [13], which are typically used to supplement fine particles and lower the soil's internal friction angle within the pressure chamber [14]. Foam agents, made up of particular foam agents with compressed air, enhance the fluidity and impermeability of the excavated soil. Dispersants, on the other hand, dispersing material in water to generate colloidal solutions, thereby diminishing particle adhesion [15]. Many experts have studied into the types and amounts of soil improvers that affect the construction of EPB shields, primarily through indoor tests. For example, Wang [16] conducted field experiments to assess the efficacy of nano bentonite CMC as a muck improver in a tunnel project in Fuzhou. Zhu and others [17–20] assessed the earth pressure shields' stability in layers of sand and gravel, proposing measures to enhance fluidity and wear resistance using DEM modelling. Chao [21] carried out laboratory studies to find out how modified bentonite grouting affected the shield driving in layers of sand and gravel. Xu and others [22, 23] added air bubbles to soil with different moisture contents to minimize power consumption during mixing. Regardless of these insightful observations, there are still not enough theoretical methods and guidelines for analysing improver properties, matching improvers with improved soil, evaluating improver effectiveness, and understanding the connection between shield construction parameters and improvers. This lack of comprehensive guidance has led to the haphazard use of improvers in shield tunneling, potentially resulting in issues like excessive environmental pollution and material consumption.

Hence, this research conducted to develop a new kind of mud improver and studies the soil improvement techniques specific to the characteristics of Shenzhen stratum focusing on the sandy gravel stratum, drawing on lessons learned from the Shenzhen Metro Line shield tunneling project. The research involves laboratory test that uses bentonite as the mud base with several additives, including xanthan gum, guar gum, CMC, and medium particles of clay, to analyse their impact on mud performance. The research aims to identify the best-performing material for enhancing mud properties. Using two distinct varieties of mud, subsequent indoor simulated muck improvement tests are conducted, which include sliding plate tests, mixing tests, adhesion resistance tests and slump tests. The research investigates the comparative efficacy of novel and conventional mud amendments in pebble/round gravel and granular soil strata.

2 New Mud Modifier

In EPB shield construction, the excavation surface stability depends on the pressure within the enclosed cabin. Infiltration of mud into the soil results in the formation of a thin mud layer that has a low permeability. Through this mud film, the mud pressure

efficiently works on the excavation surface, maintaining stability and avoiding deformation and collapse. A significant challenge in EPB shield construction is selecting an appropriate muck modifier tailored to the engineering geological parameters. To address this, the research investigated the construction site's mud configuration plan [24]. Pure bentonite is the on-site mud with a bentonite concentration of 9%. One cubic meter of water is specifically mixed with 90–120 kg of bentonite as presented in Fig. 1 Schematic diagram of experimental steps. However, this mud exhibits high consistency and poor flowability. Even after standing, it remains highly viscous and resistant to flow [25]. Additional additives are considered in order to decrease the quantity of bentonite utilized, thereby enhancing the overall efficacy of the mud and lowering cost. The purpose of this study is the development of a unique soil amendment by combining water-soluble polymer improvement materials with mineral improvement materials. Bentonite is the major raw material that is used in the production of the mineral modifier. More precisely, red sodium bentonite is manufactured by the Shamaying Sodium Clay Factory in Weifang City, Shandong Province. This particular bentonite is identical to the material that is used on the construction site. Assemble the novel mud solution by incorporating sodium bentonite and additional components into a container containing water, while agitating at a medium speed with a mixer. If the mixture becomes thick, the mixer is stopped periodically to stir the bentonite that may have settled at the bottom, aiding in its dissolution. This stirring process continues at medium speed for approximately ten minutes. When utilizing only bentonite to prepare the slurry, a significant amount of bentonite is required, resulting in high slurry costs and difficulties in achieving the desired slurry performance for EPB shield slag improvement. Therefore, additives are introduced to optimize mud performance. The addition of soda ash significantly improves mud performance. Hence, a suitable amount of soda ash is included in the formulation to adjust the mud's PH value. In line with the objective of reducing the bentonite dosage to lower costs and enhance mud performance for EPB shield use, the preliminary bentonite dosage is set between 3 and 5%. Key parameters include plastic viscosity (PV), apparent viscosity (AV), initial shear (Gelin), dynamic shear (YP), final shear (Gel10), filtration (FL), consistency index (K), fluidity coefficient (n), and dynamic plastic ratio (YP/PV). The guar gum-augmented slurry has a low overall viscosity and a colloid rate of around 80%, suggesting a considerable quantity of water precipitation. This implies that the guar gum addition does not significantly improve the mud's properties, and there is a notable separation of water from the mixture. When CMC is added to the mud, there is a noticeable improvement in mud performance. Viscosity increases, and the filtration rate falls within the acceptable range of 20 mL/30 min, fulfilling the requirements of filtration. Furthermore, the colloid rate significantly improves, indicating a better overall performance of the mud. A significant number of insoluble materials precipitates during the production of schemes F10–F12, which contain polyacrylamide. The majority of these materials appear as white blocky colloids. The results of the API filtration test reveal that the liquid maintains a downward flow, undergoing an estimated filtration loss of 45 mL/30 min. This substantially surpasses the predetermined criteria. Consequently, the application of polyacrylamide in the mud is associated with high insolubility, and

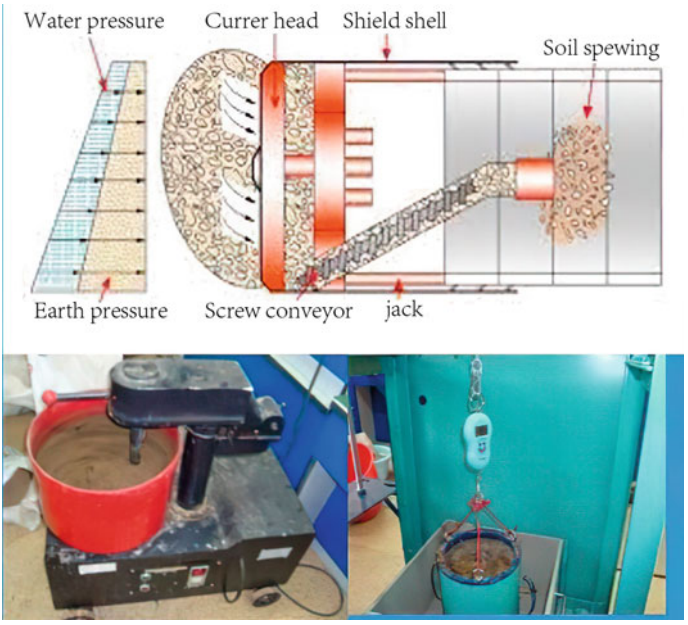

Fig. 1 Schematic diagram of experimental steps

it does not produce the desired viscosity increase in the mud. Therefore, polyacrylamide is not considered suitable for future testing. In summary, guar gum leads to lower viscosity and significant water separation, while CMC notably enhances mud performance, meeting filtration requirements and improving overall colloid properties. In contrast, polyacrylamide introduces insoluble matter and fails to achieve the desired viscosity increase, making it unsuitable for further testing.

3 Comparative Study on Mud Performance After Adding Different Additives

3.1 Viscosity Contrast

Viscosity is vital in understanding the performance of different mud formulations. Here's a breakdown of the relevant viscosity parameters: When the slurry flows, this parameter represents the friction that occurs between the solid particles, within the solid particles and the liquid phase, and as well as between liquid molecules. It quantifies the resistance to flow within the mud due to these various interactions. The ratio of shear stress to shear rate at a certain shear rate is equal to the apparent viscosity of the material. It's essentially the sum of structural and plastic viscosity. Structural

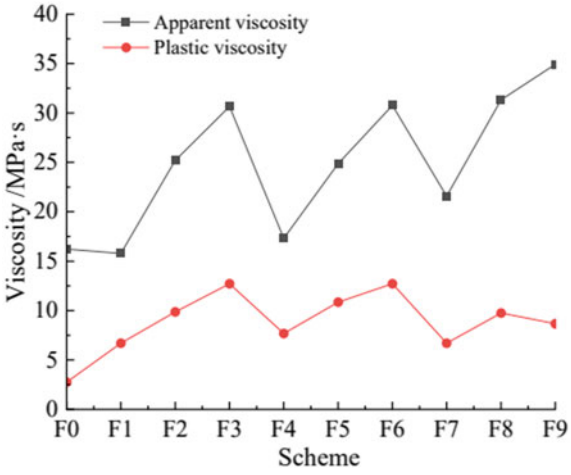

Fig. 2 Viscosity of different mud scheme

viscosity is related to the overall structure and behavior of the mud when it flows. Now, refer to Fig. 2 which displays a comparison of the viscosity of several mud schemes. With the exception of F1 and F4, the apparent viscosity of every scheme is greater than that of the building site mud (F0). However, these two schemes (F1 and F4) were both rejected because they did not meet the specifications needed for the Beijing Metro Line 10 sand gravel layer, which favors a greater slurry viscosity. One of the formulations includes the inclusion of xanthan gum, guar gum and CMC which generates the maximum apparent viscosity. This formulation has a bentonite dose of 5%. Scheme F9 stands out among them because it has the greatest apparent viscosity. This suggests that xanthan gum is preferable to CMC and guar gum when it comes to increasing the apparent viscosity of the mud. The trend in the plastic viscosity is similar to that of apparent viscosity. The addition of a viscosity enhancer improves plastic viscosity, with xanthan gum showing better performance compared to guar gum and CMC. Taking all factors into account, xanthan gum emerges as the most effective additive for improving mud viscosity, surpassing guar gum and CMC in this regard.

3.2 Dynamic Shear Force Comparison Microscopically

The response of the spatial grid structure forces between clay particles while the slurry is in motion is known as dynamic shear force. This parameter gives information on the slurry's partial capacity to move gravel and sand. Figure 3 shows the comparison of the dynamic shear force for each scheme.

When compared to the reference scheme F0, only schemes F8 and F9 show larger dynamic shear force values in the mud. This shows that xanthan gum is the only way to considerably increase mud dynamic shear force. Now, turning to the comparison

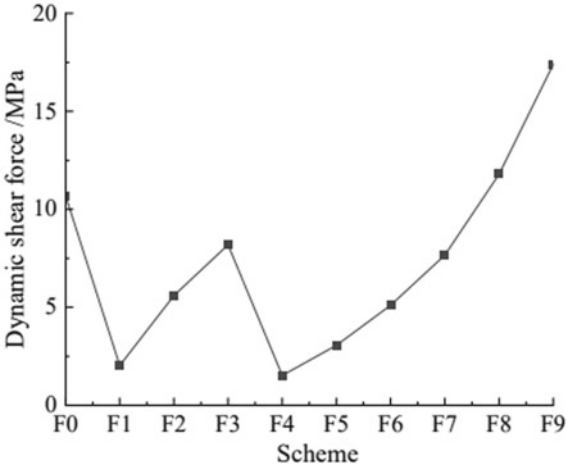

Fig. 3 Dynamic shear force of various scheme

of static shear force, which represents the strength of the internal gel network while the drilling fluid is stationary, is presented in Fig. 4.

The measurement of static shear force provides information on the drilling fluid's internal gel network structural strength at rest. The magnitude of the initial shear force plays a crucial role in lowering the shield machine's initial power consumption, so it is beneficial to keep the initial shear force at an appropriate low level. On the other hand, while working with bigger sand and pebble deposits, having a higher final shear force is advantageous for effectively suspending and transporting mud to the muck disposal area. Therefore, adjustments to the initial and final shear forces are essential based on the geological conditions.

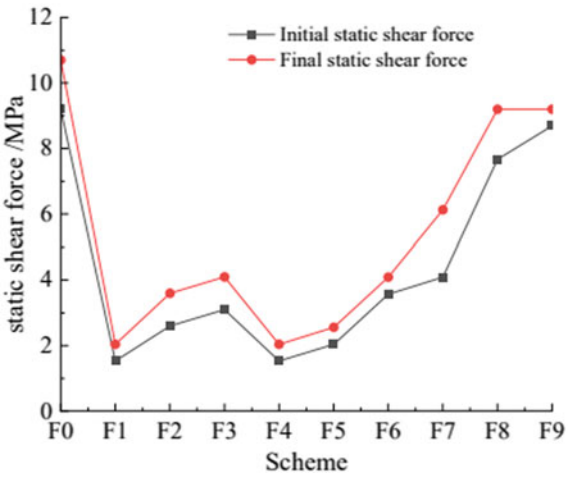

Fig. 4 Static shear force variation for several muds

With the exception of schemes F8 and F9, the results in Fig. 4 show that the static shear forces in all the schemes are not very high. This might not be good for dealing with the sandy cobble layer. For schemes F8 and F9, which involve the addition of xanthan gum, exhibit static shear forces that closely resemble those of the construction site mud. Notably, scheme F8 demonstrates adjustments in both the initial and final shear forces that are more conducive to the challenges posed by the sandy cobble stratum.

3.3 Dynamic Plastic Ratio Comparison

The dynamic plastic ratio (τd/ηp) is a key measure for figuring out how shear dilution works in mud. In the context of shield soil improvement materials, it is essential to maintain an optimum dynamic plastic ratio in order to prevent the accumulation and settling of excavated soil at the bottom of the earth ballast tank. To ensure that the mud has an adequate capacity to carry solid particles, a recommended dynamic plastic ratio range of 0.5–1.5 Pa/MPa · s has been established for this test. Analyzing Fig. 5, several observations can be made: The dynamic-plastic ratio (τd/ηp) of the mud scheme (F0) used on the building site is excessively high. This high dynamic-plastic ratio is not conducive to effective mud pumping. However, schemes F1–F6 have excessively low mud dynamic-plastic ratios. This lower dynamic-plastic ratio is not favorable for the efficient transport of cuttings and solid particles. In summary, maintaining an appropriate dynamic plastic ratio is essential to ensure effective mud pumping and the transport of cuttings and solid particles during shield soil improvement. On the construction site, the mud scheme used had a dynamic-plastic ratio that was too high, while schemes F1–F6 had dynamic-plastic ratios that were too low, indicating the need for adjustments to achieve the desired balance.

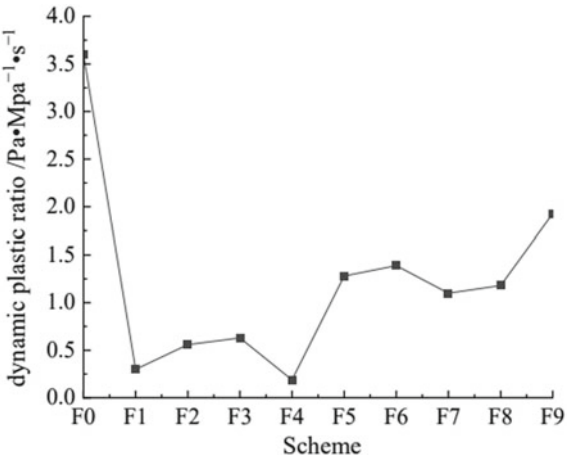

Fig. 5 Variation in the dynamic-plastic ratio across various schemes

3.4 Flowability Index and Consistency

The fluidity index, denoted as "n," reflects a fluid's non-Newtonian behavior within a certain range of flow velocities and serves as an indicator of the fluid's overall flow characteristics. An ideal popularity index "n" in the context of drilling fluids is approximately 0.5 and is typically less than 1. A smaller value of "n" indicates higher fluidity.

On the other hand, the consistency coefficient, denoted as "k," represents the fluid's viscosity under a 1 s^{-1} flow velocity gradient. A fluid with a greater consistency coefficient is thicker and more viscous. The best range for the consistency coefficient "k" of the EPB shield, while dealing with bigger sand and pebble formations, is 1.5–2.

Examining Fig. 6, which illustrates the consistency coefficient and fluidity index for each mud scheme:

The construction site (F0) mud scheme has a fluidity index of 0.17, which is exceptionally low. Such a low value can hinder the effectiveness of mud in transporting gravel. Conversely, if the consistency coefficient is excessively high, it can negatively impact the pumpability of the slurry.

In schemes F2–F7, the consistency coefficients are all less than 1. These values are more suitable for the desired flow characteristics of the EPB shield in the presence of larger and pebble and sand formations. Taking both the consistency coefficient and fluidity index into account, schemes F2–F7 exhibit more favorable properties for the intended application.

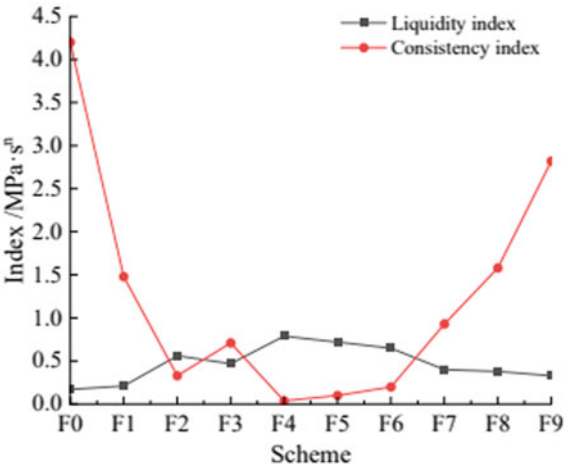

Fig. 6 Fluidity index and consistency changes for various schemes

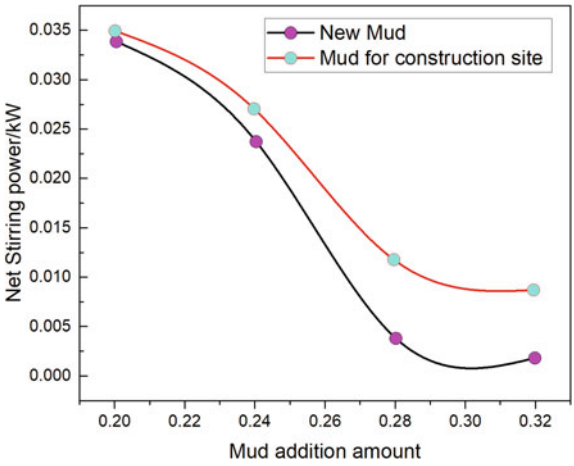

Fig. 7 Two kinds of mud comparison using net power of pebble/round gravel

3.5 API Filtration Loss

It is essential to compare the mud filtration in each scheme in order to assess the stability of the mud. The amount of filtration loss is a measure of the mud stability. A minimal quantity of water filtration by the sediment contributes to the maintenance of a consistent pore water pressure close to the excavation face. The production of the mud film is vital for maintaining the stability of the excavation surface, and this stability guarantees that the excavation face's effective mud-water pressure stays constant following the formation of the mud film.

In essence, a smaller water loss during filtration is indicative of better mud performance. Please refer to Fig. 7 for a visual representation of the comparison of each scheme's mud filtration.

4 Conclusions

Laboratory tests evaluated the impact of different additives, including xanthan gum, guar gum, CMC and polyacrylamide, on slurry performance using bentonite as the base slurry. Tests included viscosity comparisons, dynamic shear force comparisons, dynamic plasticity ratio comparisons, flowability index comparisons and API filtration losses. The findings revealed that best material for slurry performance is xanthan gum. The optimal slurry composition is determined to be 1% clay particles, 0.2% xanthan gum, 4% bentonite, and 0.04% soda ash. This slurry ratio has better performance and is more appropriate for enhancing the soil characteristics of the water-rich sand layer.

Acknowledgements This research was funded by the National Natural Science Foundation of China (52078418), Key R & D plan of Shaanxi Province (2021GY-273, 2021SF-520), the National Post-Doctoral Science Foundation (No. 2019M653645), Project of strategic planning department of Ministry of science and technology (HXJC2019FG/072HZ), Shaanxi four main bodies and one united Soil Engineering Technology Research Center (2022ZY2-CXJD-09), Science and technology project of Yulin (CityCXY-2020-046), Joint research center for future urban construction and management innovation (20211177-ZKT14), Heyang Jinqiao Coal Co., Ltd (20210571)

References

1. Li P, Dai Z, Huang D, Cai W, Fang T (2021) Impact analysis for safety prevention and control of special-shaped shield construction closely crossing multiple operational metro tunnels in shallow overburden. Geotech Geol Eng 1–18
2. Powell JP, Fraszczyk A, Cheong CN, Yeung HK (2016) Potential benefits and obstacles of implementing driverless train operation on the Tyne and wear metro: a simulation exercise. Urban Rail Transit 2:114–127
3. Yang X, Huang M, Lin F (2019) Research strategies on new prefabricated technology for underground metro stations. Urban Rail Transit 5(3):145–154
4. Chen Z-L, Chen J-Y, Liu H, Zhang Z-F (2018) Present status and development trends of underground space in Chinese cities: evaluation and analysis. Tunnel Underground Space Technol 71:253–270
5. Liu Q (2021) Key technologies of metro construction in hard rock stratum. World Scientific
6. Liao S-M, Liu J-H, Wang R-L, Li Z-M (2009) Shield tunneling and environment protection in Shanghai soft ground. Tunnel Underground Space Technol 24(4):454–465
7. Xiahou X, Tang L, Yuan J, Zuo J, Li Q (2022) Exploring social impacts of urban rail transit PPP projects: towards dynamic social change from the stakeholder perspective. Environ Impact Assess Rev 93:106700
8. Min F, Du J, Zhang N, Chen X, Lv H, Liu L, Yu C (2019) Experimental study on property change of slurry and filter cake of slurry shield under seawater intrusion. Tunnel Underground Space Technol 88:290–299
9. Annis M, Monaghan P (1962) Differential pressure sticking-laboratory studies of friction between steel and mud filter cake. J Petrol Technol 14(05):537–543
10. Pan Y, Zhang L (2022) Mitigating tunnel-induced damages using deep neural networks. Autom Constr 138:104219
11. Wang X, Lai J, He S, Garnes RS, Zhang Y (2020) Karst geology and mitigation measures for hazards during metro system construction in Wuhan, China. Nat Hazards 103:2905–2927
12. Girnau G, Blennemann F (1989) Cost-benefits in underground urban public transportation. Tunnel Underground Space Technol 4(1):23–30
13. Sun Y, Zhao D (2022) Research and experimental application of new slurry proportioning for slag improvement of EPB shield crossing sand and gravel layer. Coatings 12(12):1961
14. Zhao J, Tan Z, Yu R, Jia A, Qu C (2022) Study on the mix of slurry membrane for soil conditioning of EPB shield and its application effect in water-rich gravel strata. Adv Civil Eng
15. Qian Y, Min F, Mo Z, Fan X (2020) Experimental study of the influence of excavation surface stability and sand flowability caused by dense slurry-earth pressure balance shield tunneling in silty sand stratum. Adv Civil Eng 2020:1–14
16. Wang S, Lu X, Wang X, He C, Xia X, Ruan L, Jian Y (2019) Soil improvement of EPBS construction in high water pressure and high permeability sand stratum. Adv Civil Eng
17. Lee H, Choi H, Choi S-W, Chang S-H, Kang T-H, Lee C (2021) Numerical simulation of EPB shield tunneling with TBM operational condition control using coupled DEM–FDM. Appl Sci 11(6):2551

18. Liu B, Li T, Han Y, Li D, He L, Fu C, Zhang G (2022) DEM-continuum mechanics coupling simulation of cutting reinforced concrete pile by shield machine. Comput Geotech 152:105036
19. Wu L, Qu F-Z (2009) Discrete element simulation of mechanical characteristic of conditioned sands in earth pressure balance shield tunneling. J Cent South Univ Technol 16(6):1028–1033
20. Zhu H, Panpan C, Xiaoying Z, Yuanhai L, Peinan L (2020) Assessment and structural improvement on the performance of soil chamber system of EPB shield assisted with DEM modeling. Tunnel Underground Space Technol 96:103092
21. Chao X, Li-xin T, Ren-peng C, Zhi-quan Z, Jun-sheng Y (2019) Dynamic coupling simulation of shield construction mechanics considering characteristics of soils. Chinese J Geotech Eng 41(6):1108–1115
22. Li L, Sun S, Wang J, Yang W, Song S, Fang Z (2020) Experimental study of the precursor information of the water inrush in shield tunnels due to the proximity of a water-filled cave. Int J Rock Mech Min Sci 130:104320
23. Xu Q, Zhang L, Zhu H, Gong Z, Liu J, Zhu Y (2020) Laboratory tests on conditioning the sandy cobble soil for EPB shield tunneling and its field application. Tunnel Underground Space Technol 105:103512
24. Nguyen TT, Indraratna B, Kelly R, Phan NM, Haryono F (2019) Mud pumping under railtracks: mechanisms, assessments and solutions. Aust Geomech J 54(4):59–80
25. Cengeloglu Y, Tor A, Ersoz M, Arslan G (2006) Removal of nitrate from aqueous solution by using red mud. Sep Purif Technol 51(3):374–378

Integrate the Methods of Linear Full Resonance with Quarter-Wavelength into Strong Motion Synthesis

Zhiguo Tao, Shiyao Liu, Zhengru Tao, and Zhaoyue Zhang

Abstract The local site condition plays a crucial role in the study of strong ground motion, and much effort has been expended. The most common theoretical methods are linear full resonance (FR), quarter-wavelength (QWL), equivalent linear and nonlinear. We compare the site response from these two methods and the combination of them for the mainshock of the 2016 Kumamoto earthquake. The surface-borehole recordings at a far-field station FKOH01 and a near-fault station KMMH03 are selected as benchmark. Horizontal ground motions at these two borehole stations are simulated. The site effect is evaluated by three methods of FR, QWL and the combination QWL × FR. At FKOH01, PGAs from QWL × FR are larger than those from QWL and FR; at KMMH03, PGAs from QWL are larger than those from QWL × FR, and the latter are close to those from FR. A similar trend is observed in the comparison of response spectra. Compared with the records, QWL × FR can be adopted to evaluate the site response.

Keywords Linear full resonance · Quarter-wavelength · Site response · Strong motion synthesis

1 Introduction

Local site conditions influence the characteristics of strong ground motion strongly. The early investigations can be traced to [1–3], as old as earthquake engineering [4]. Attempts to evaluate the effect of soil column, named as site response [5], have a long history, and much effort has been expended, from both theoretical and experimental points of view. The most common theoretical methods are linear full resonance (FR), quarter-wavelength (QWL), equivalent linear and nonlinear [6]. Pioneer works

Z. Tao · S. Liu · Z. Tao (✉) · Z. Zhang
Key Laboratory of Earthquake Engineering and Engineering Vibration, Institute of Engineering Mechanics, China Earthquake Administration; Key Laboratory of Earthquake Disaster Mitigation, Ministry of Emergency Management, Harbin, Heilongjiang 150080, China
e-mail: taozr@iem.ac.cn

G. Mei et al. (eds.), *Advanced Construction Technology and Research of Deep-Sea Tunnels*, Lecture Notes in Civil Engineering 490,
https://doi.org/10.1007/978-981-97-2417-8_4

appeared in the first half of the twentieth century [7, 8]. Following these, lots of works came up [9–13].

FR and QWL are widely used, the former is the theoretical prediction of site amplification that accounts for the constructive and destructive interference of all reverberations in layered media, and the latter is an approximation. A few comparisons of QWL amplifications and FR amplifications have appeared [5, 14]. In the case of the mainshock of the 2016 Kumamoto earthquake, we compare the site response from these two methods and the combination of them. With the help of the pairs of borehole and surface strong-motion records at two KiK-net stations, we compare synthetic and observed ground motions on the surface, by inputting our synthetic ground motions on buried bedrock using EXSIM [15].

2 Method for Ground Motion Synthesis

On April 14, 2016, an M_{JMA}6.5 earthquake occurred in the Kumamoto area of Japan (32.74°N, 130.81°E), with the focal depth of 11 km, and caused Japan Meteorological Agency (JMA) intensity 7 in Mashiki. 28 h later, the M_{JMA}7.3 mainshock (32.75°N, 130.76°E) occurred, with the focal depth of 12 km, and caused JMA intensity 7 in Mashiki and Nishihara [16]. The Headquarters for Earthquake Research Promotion judged that the M_{JMA}6.5 earthquake occurred on Takano-Shirahata section of the Hinagu fault zone, while the mainshock occurred on the Futagawa section of the Futagawa fault zone [16]. During the M_{JMA}6.5 event, strong ground motions on surface and in the borehole were recorded at 146 KiK-net stations, PGAs larger than 500gal were observed around the epicentre and the maximum PGA of 1580gal was recorded at KMMH16 station with the epicentral distance of 7 km; for the mainshock, KiK-net obtained strong ground motion data at 328 stations on surface and in the borehole, and the maximum PGA of 1362gal was recorded at KMMH16 station [17].

After this event, several rupture processes of the mainshock were provided [18–23]. We borrow the source model from [20], which is divided into 21 subfaults along the strike direction and 9 subfaults along the dip direction, each with a size of approximately 2 × 2 km. Stress drop is set as 70bars, κ_0 is 0.05 s [24], the other parameters used in synthesis are from [25].

Surface-borehole records at a far-field station FKOH01 and a near-fault station KMMH03 from the mainshock are collected. The processed data, using baseline correction and 0.1–25 Hz band-pass filter with a fourth-order Butterworth filter. Horizontal ground motions at these two borehole stations are synthesized by EXSIM [15]. Density of soil layers is calculated by the relation between density and P-wave velocity [26], as Eq. (1).

$$\rho = 0.23 V_P^{0.25} \tag{1}$$

Observed and synthetic full wave A_{full} on the buried bedrock is transmitted to upward wave A_{up} by Eq. (2), which is the relationship between the acceleration

Fourier amplitude spectra.

$$\frac{A_{\text{up}}}{A_{\text{full}}} = \frac{E_N}{E_N + F_N} = \frac{e_N}{e_N + f_N} \tag{2}$$

where, E_N and F_N are the amplitude coefficients of upward and downward waves on the buried bedrock. A_{up} is the input on the buried bedrock to evaluate the site response.

We consider the site response in three ways. The first one is to multiply the input Fourier spectra by FR from the bottom to the ground surface. The second one is to multiply the input Fourier spectra by the amplification spectra from the bottom to the ground surface, which are calculated by QWL approximation initially proposed by [12]. We propose to apply QWL for the amplification from hard rock surface to engineering rock surface, and FR for the amplification of ground motion in soil layers. The input Fourier spectra are multiplied by the product of QWL amplification spectra and FR (QWL × FR), the QWL amplification spectra are from the bottom to −13 m and −80 m for two station respectively, and the FR are from −13 m to −80 m to the ground surface. The input position is consistent with the depth of the buried bedrock surface, and the detailed velocity structure of site is involved.

3 Ground Motion Synthesis at Two KiK-Net Stations

When we input the transmitted upward waves from synthetic and observed borehole full waves, the surface ground motions at station FKOH01 are shown in Fig. 1a–c and Fig. 2, respectively, compared with the observed surface ground motions in two horizontal directions as Fig. 1d and e.

In Fig. 1, the waveforms of synthetic and observed motions on surface are difference; the durations of strong motion are close; the PGAs from FR in Fig. 1a, QWL in Fig. 1b and QWL × FR in Fig. 1c are 45.6 gal, 45.6 gal and 50.9 gal, the observed

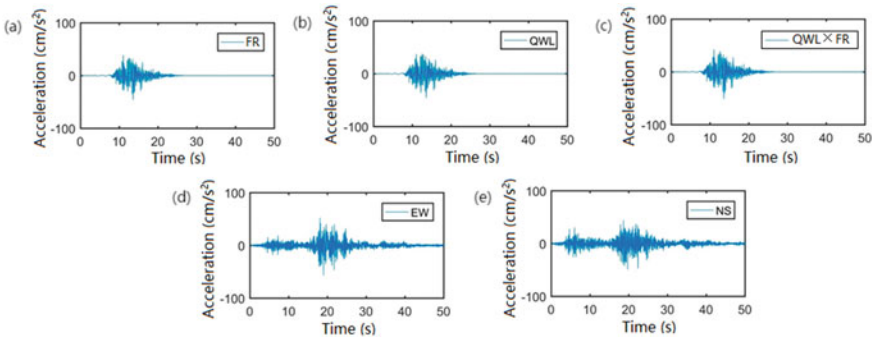

Fig. 1 Ground motions at FKOH01 surface station, inputted by synthetic ground motions

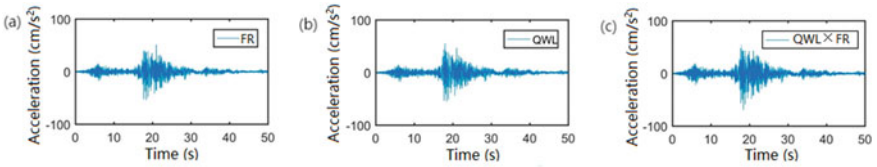

Fig. 2 Ground motions at FKOH01 surface station, inputted by observed borehole ground motions

PGAs in two horizontal directions are 56.6 gal and 49.0 gal. In Fig. 2, the waveforms are similar, especially in EW direction; the PGAs from FR in Fig. 2a, QWL in Fig. 2b and QWL × FR in Fig. 2c are 53.5 gal, 55.2 gal and 68.7 gal.

The results at station KMMH03 are shown in Fig. 3 and Fig. 4, respectively.

The surface waveforms inputted by the upward waves of synthetic motions (Fig. 3a–c) are difference with those inputted by observed motions (Fig. 4a–c); the durations of synthetic motions are shorter; the PGAs from FR in Fig. 3a, QWL in Fig. 3b and QWL × FR in Fig. 3c are 363.2 gal, 399.8 gal and 365.5 gal, the observed PGAs in two horizontal directions are 227.6 gal in Fig. 3d and 786.6 gal in Fig. 3e. In Fig. 4, the waveforms are close and the durations of strong motions are similar; the PGAs from FR in Fig. 4a, QWL in Fig. 4b and QWL × FR in Fig. 4c are 217.5 gal, 262.2 gal and 215.6 gal.

The 5% damped acceleration response spectra, from the three methods of FR, QWL and QWL × FR, are compared with those of records on these two surface

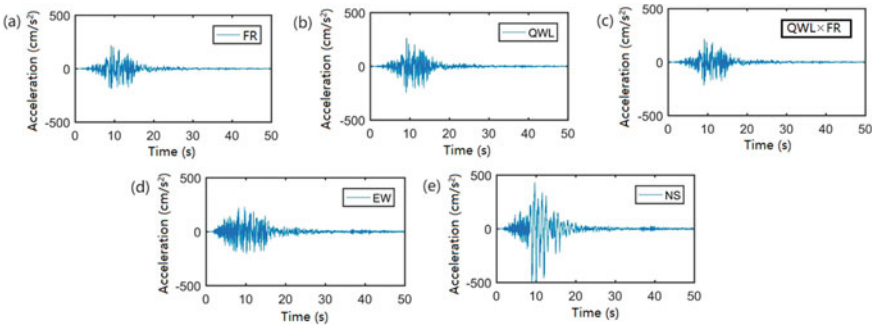

Fig. 3 Ground motions at KMMH03 surface station, inputted by synthetic ground motions

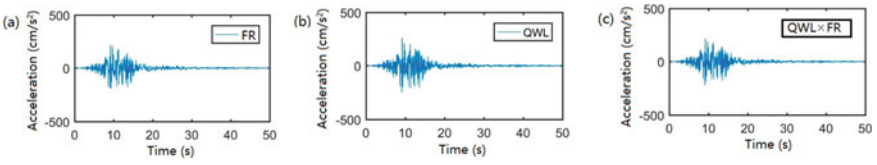

Fig. 4 Ground motions at KMMH03 surface station, inputted by observed borehole ground motions

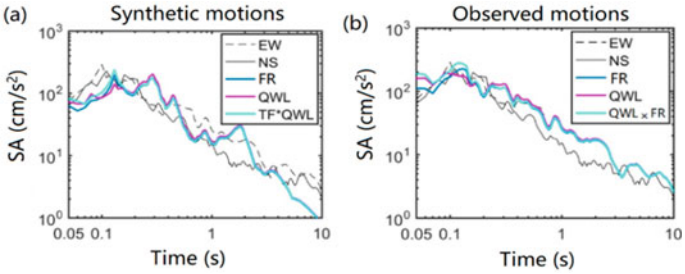

Fig. 5 Acceleration response spectra at FKOH01 surface station

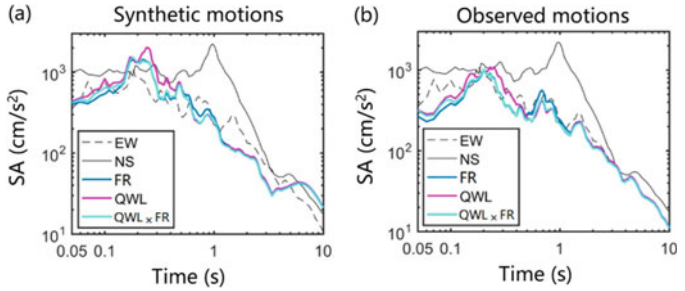

Fig. 6 Acceleration response spectra at KMMH03 surface station

stations, as shown in Figs. 5 and 6, corresponding to the upward-wave inputs of synthetic and observed ground motions.

In Fig. 5a, the response spectral amplitudes from the three methods are close to the records at periods 0.15–5 s. In Fig. 5b, the results from the three methods are closer to the records, especially at periods higher than 0.5 s, which implies that all three ways to consider site effect is feasible. In Fig. 6, the difference between the two-horizontal spectra is large, our results fit with the EW spectrum. The spectra are close at periods lower than 1.5 s in Fig. 6a, the spectral amplitudes from three methods are lower at periods 1.5–4 s, while those are higher at periods 7–10 s; in Fig. 6b, the spectra fit well at periods higher than 0.5 s, while the spectral amplitudes from three methods are lower at periods less than 0.2 s.

4 Conclusions

Ground motions at two KiK-net stations, FKOH01 and KMMH03, in the mainshock of 2016 Kumamoto Earthquake, are synthesized, in which borehole ground motions are from EXSIM and site response is considered by three methods of FR, QWL and QWL × FR. Our results are compared with both the borehole and the surface records in two horizontal directions to illustrate the feasible of the three methods.

By inputting the upward waves of synthetic borehole motions, the surface motions from these three methods are different; the durations of strong motion are close. By inputting the upward waves of observed motions, the waveforms are close and the durations of strong motions are similar. Further comparison shows that PGAs from QWL × FR are larger than those from QWL, which are larger than that from FR, at FKOH01, the relative error is 3.2–28.3%; at KMMH03, PGAs from QWL are larger than those from QWL × FR, and the latter are close to those from FR, the relative error is 0.9–20.5%. A similar trend is observed in the comparison of response spectra.

Acknowledgements This work was financially supported by Scientific Research Fund of Institute of Engineering Mechanics, China Earthquake Administration (Grant No. 2020B02) and National Natural Science Foundation of China (51678540 and 51478443).

References

1. Carey EP (1906) The great fault of California and the San Francisco earthquake. J Geogr 5(7):289–301
2. Lawson AC, Gilbert GK, Reid HF, Branner JC, Fairbanks HW, Wood HO, Hayford JF, Baldwin AL, Omori F, Leuschner AO, Davidson G, Matthes FE, Anderson R, Louderback GD, Holway RS, Eakle AS, Crandall R, Hoffman GF, Warring GA, Hughes E, Rogers FJ, Baird A, many others. (1969) Isoseismals: distribution of apparent intensity—the California earthquake of April 18, 1906. Cabnegie Institution of Washington, USA
3. Reid HF (1910) The influence of the foundation on the apparent intensity—the California earthquake of April 18, 1906. Cabnegie Institution of Washington, USA
4. Trifunac MD (2009) The nature of site response during earthquakes. Springer Science+Business Media B.V, Netherlands
5. Boore DM (2013) The uses and limitations of the square-root—impedance method for computing site amplification. Bull Seismol Soc Am 103(4):2356–2368
6. Carpenter NS, Wang Z, Woolery EW (2020) An evaluation of linear site-response parameters in the Central and Eastern United States and the importance of empirical site-response estimations. Bull Seismol Soc Am 110(2):489–507
7. Sezawa K (1927) On the decay of waves in visco-elastic solid bodies. Bull Earthq Res Inst 3:43–53
8. Kanai K (1950) The effect of solid viscosity of surface layer on the earthquake movements. Bull Earthq Res Inst 28:31–35
9. Idriss IM, Seed HB (1968) Seismic response of horizontal soil layers. J Soil Mech Found Div 94(4):1003–1031
10. Seed HB, Idriss IM (1970) Soil moduli and damping factors for dynamic response analysis. University of California, USA
11. Joyner WB, Chen ATF (1975) Calculation of nonlinear ground response in earthquakes. Bull Seismol Soc Am 65(5):1315–1336
12. Joyner WB, Warrick RE, Fumal TE (1981) The effect of quaternary alluvium on strong ground motion in the Coyote lake, California, earthquake of 1979. Open-file report 81–353
13. Day SM (1996) RMS response of a one-dimensional half space to SH. Bull Seismol Soc Am 86:363–370
14. Boore DM, Joyner WB (1991) Estimation of ground motion at deep-soil sites in Eastern North America. Bull Seismol Soc Am 81(6):2167–2185
15. Motazedian D, Atkinson GM (2005) Stochastic finite-fault modeling based on a dynamic corner frequency. Bull Seismol Soc Am 95:995–1010

16. Japan Meteorological Agency (2018) Report on the 2016 Kumamoto Earthquake. Technical Report of the Japan Meteorological Agency. http://www.kyoshin.bosai.go.jp., No. 135
17. Suzuki W, Aoi S, Kunugi T, Kubo H, Morikawa N, Nakamura H, Kimura T, Fujiwara H (2017) Strong motions observed by K-NET and KiK-net during the 2016 Kumamoto earthquake sequence. Earth Planets Space 69:19
18. Nozu A, Nagasaka Y (2017) Rupture process of the main shock of the 2016 Kumamoto earthquake with special reference to damaging ground motions: waveform inversion with empirical Green's functions. Earth Planets Space 69:22
19. Kubo H, Suzuki W, Aoi S, Sekiguchi H (2016) Source rupture processes of the 2016 Kumamoto, Japan, earthquakes estimated from strong-motion waveforms. Earth Planets Space 68:161
20. Asano K, Iwata T (2016) Source rupture processes of the foreshock and mainshock in the 2016 Kumamoto earthquake sequence estimated from the kinematic waveform inversion of strong motion data. Earth Planets Space 68:147
21. Yagi Y, Kuwaki RO, Enescu B, Kasahara A, Miyakawa A, Otsubo M (2016) Rupture process of the 2016 Kumamoto earthquake in relation to the thermal structure around Aso volcano. Earth Planets Space 68:118
22. Yarai H, Kobayashi T, Morishita Y, Fujiwara S, Hiyama Y, Kawamoto S, Ueshiba H, Miura Y, Miyahara B (2016) Source fault models of the 2016 Kumamoto Earthquake inverted from crustal deformation. Bull Geospat Inf Auth Jpn 128:169–176
23. Kobayashi H, Koketsu K, Miyake H (2017) Rupture processes of the 2016 Kumamoto earthquake sequence: causes for extreme ground motions. Geophys Res Lett 44:6002–6010
24. Zhang L, Chen G, Wu Y, Jiang H (2016) Stochastic ground-motion simulations for the 2016 Kumamoto, Japan, earthquake. Earth Planets Space 68:184
25. Atkinson GM, Assatourians K (2015) Implementation and validation of EXSIM (a stochastic finite-fault ground-motion simulation algorithm) on the SCEC broadband platform. Seismol Res Lett 86(1):48–60
26. Gardner GHF, Gardner LW, Gregory AR (1974) Formation velocity and density-the diagnostic basics for stratigraphic traps. Geophysics 39(6):770–780

Comparative Study on Chinese and Foreign Earth Pressure Calculation Methods for Pipe-Sheet Composite Wharf Structure

Hongwei Chen, Jinghong Zhang, Taotao Mei, and Fei Niu

Abstract Pipe-sheet combination structure is a novel form of wharf structure, which utilizes steel pipe piles with better performance as the main stress components to withstand lateral pressures such as water pressure and earth pressure, and low-cost steel sheet piles as the linking structure to form a pipe-sheet combination wall, which to a certain extent can take into account both the performance and the cost issues, but whether the pipe-sheet combination structure can be adapted to the design and use of the large-scale berths of the wharf under the deep-water environment has always been a controversial issue in the engineering field. However, it has been controversial in the engineering community. Therefore, it is necessary to analyze and research more deeply the actual force situation of the pipe-sheet combination structure and the applicable calculation method. In this paper, based on the field measurement data, the active earth pressure calculation of the back side of the pipe-sheet composite pile is compared and analyzed, and the results show that the earth pressure calculation formulas used in China and the United States for the sheet pile structure are much closer to the actual results compared to the calculation method of the Japanese specification in the calculation of the earth pressure of the back side of the pipe-sheet composite structure; the numerical simulation can be used to set up the pipe-sheet composite pile structure into an equivalent cross-section of the sheet pile module, which can effectively avoid the data of the sheet pile module, and can also be used in the numerical simulation. When numerical simulation is used, the pipe-sheet composite structure can be set up as a plate pile module with equivalent cross-section, which can effectively avoid the problems of aberration and stress concentration in the data calculation, and the calculation results can better respond to the actual stress situation in the field.

H. Chen (✉)
Guangzhou Port Company Limited, Guangzhou 510230, China
e-mail: chenhongwei@gzport.com

J. Zhang · T. Mei · F. Niu
CCCC Fourth Harbor Engineering Institute Co. Ltd, Guangzhou 510230, China

G. Mei et al. (eds.), *Advanced Construction Technology and Research of Deep-Sea Tunnels*, Lecture Notes in Civil Engineering 490,
https://doi.org/10.1007/978-981-97-2417-8_5

Keywords Pipe-sheet combination wharf structure · Earth pressure · Calculation methods

1 Introduction

Pipe-sheet composite wharf structure can be made of steel pipe pile with high stiffness and steel sheet pile with low price to form pipe sheet composite wall [1, 2]. The pipe pile is used as the main force component to withstand lateral pressure such as water pressure and earth pressure, and the sheet pile between pipe piles is used as the soil retaining and linking structure. This new form not only has the advantages of low price of steel sheet pile, but also improves the stiffness of the overall section by using steel pipe pile with large stiffness, which greatly reduces the deformation of the composite wall, and has good force transmission and interlocking through special latch connection. As a new type of sheet pile structure, steel pipe composite sheet pile structure has not been applied in large-scale deepwater wharf. As a new type of wharf structure, the calculation method of pipe-sheet composite structure is not mature, and the calculation method of earth pressure behind it has not been given in the current specification. In terms of calculation and research of pipe-sheet composite structure, Fuqiang and Li [3] proposed through research that the lock in pipe-sheet composite system structure plays a role in transferring load. Since the stiffness of steel sheet pile is far less than that of steel pipe pile, it can be ignored in the force study, and the force of steel pipe pile should be mainly calculated during calculation. Zhang [4] confirmed that pipe-sheet composite piles can be loaded by using the vertical elastic foundation beam method through practical engineering verification. In the past, numerical simulation is often used in the calculation of pipe-sheet composite pile structure, due to the lack of relevant actual monitoring data, if the calculation result is small, it may cause the instability of the structure, and if the value of the safety coefficient is large, it may cause the actual cost to be high. This paper adopts the method of comparing the actual engineering monitoring and the calculation of national norms to confirm the distribution and calculation method of the rear earth pressure of the new type of pipe-plate combination structure, which makes the calculation of the rear earth pressure more close to the actual situation, ensures the stability of the structure and reduces the cost as much as possible, and can provide a reference for the same type of dock structure engineering.

2 Calculation Method of Earth Pressure

2.1 Method in China Standard

As the calculation method of earth pressure in pipe-sheet composite pile structure has not been provided in the Design Code for Wharf Structures (JTS 167-2018), when the ground surface is horizontal and the wall back is vertical, the standard value of active earth pressure horizontal strength generated by the soil itself and the wharf surface under uniform load can be calculated according to the following formula [5]:

$$p_{ax} = \left(\sum \gamma_i h_i\right) K_a \cos\delta - 2c\frac{\cos\varnothing\cos\delta}{1+\sin(\varnothing+\delta)} \tag{1}$$

$$e_{aqx} = qK_a\cos\delta \tag{2}$$

The standard value of passive earth pressure level strength generated by the soil itself in front of the wall is calculated as follows:

$$p_{px} = \left(\sum \gamma_i h_i\right) K_a \cos\delta + 2c\frac{\cos\varnothing\cos\delta}{1-\sin(\varnothing+\delta)} \tag{3}$$

In this equation, Ka and Kp have active and passive earth pressure coefficients according to Eqs. (4) and (5) respectively, where ϕ is the effective internal friction Angle of the soil, θ is the Angle between the wall and the plumb line, and β is the slope of the ground. The pipe-sheet composite pile is vertically placed on the ground, and $\theta = \beta = 0°$ is taken. δ is the wall friction Angle, take 1/3 ∅ for sandy soil and 2/3 ∅ for cohesive soil.

$$K_a = \frac{\cos^2(\varnothing-\theta)}{\cos^2\theta\cos(\delta+\theta)\left[1+\sqrt{\frac{\sin(\varnothing+\delta)\sin(\varnothing-\delta)}{\cos(\delta+\theta)\cos(\beta-\theta)}}\right]^2} \tag{4}$$

$$K_p = \frac{\cos^2(\varnothing+\theta)}{\cos^2\theta\cos(\delta-\theta)\left[1-\sqrt{\frac{\sin(\varnothing+\delta)\sin(\varnothing+\delta)}{\cos(\delta-\theta)\cos(\beta-\theta)}}\right]^2} \tag{5}$$

2.2 Method in America Standard

The port engineering design standard system in the United States is different from that in China. There is no special national, departmental or local design standard, and the relevant design method is provided by the departments engaged in relevant engineering. This paper takes the Design of sheet pile walls (EM 1110-2-2504)

as reference. Active earth pressure and passive earth pressure can be calculated according to the following formula [6]:

$$P_a = p_v K_a - 2c\sqrt{K_a} \tag{6}$$

$$P_p = p_v K_p + 2c\sqrt{K_p} \tag{7}$$

where, Ka and Kp are the coefficients of active earth pressure and passive earth pressure respectively, which are the same as the Chinese specification and are calculated according to Eqs. (4) and (5) respectively, where δ is the wall friction Angle and there is no clear rule. Generally, 1/2 ∅ is taken and pv is the effective vertical earth pressure at the depth of Z. The valid values of ϕ and c are calculated according to the following formula:

$$\tan\varnothing_{eff} = \frac{\tan\varnothing}{\text{FSP(FSA)}} \tag{8}$$

$$c_{eff} = \frac{c}{\text{FSP(FSA)}} \tag{9}$$

Among them, FSP is the passive earth pressure safety factor, which is generally 1.5 under normal conditions of wharf structure, and FSA is the main dynamic earth pressure safety factor, which is 1.0 in most cases.

2.3 Method in Japan Standard

According to the Japanese code, the earth pressure acting on the building should be calculated according to the soil, sandy soil, clay soil, the type of the building and the state of the force, active, passive, normal force and earthquake force, etc. The active earth pressure and passive earth pressure of sandy soil acting on the wall are calculated according to the following formula [7, 8]:

$$P_a = K_a\left[\sum \gamma_i h_i + \frac{w\cos\theta}{\cos(\theta - \beta)}\right]\cos\theta \tag{10}$$

$$P_p = K_p\left[\sum \gamma_i h_i + \frac{w\cos\theta}{\cos(\theta - \beta)}\right]\cos\theta \tag{11}$$

Among them, the active upward pressure coefficient Ka and passive earth pressure coefficient Kp are calculated according to Eqs. (4) and (5) respectively (δ direction is not considered when calculating the passive earth pressure coefficient), δ is the wall friction Angle, the backfill soil has $\phi/2$, generally within the range of ±15–20°, and w is the wharf surface load. For cohesive soil, the Japanese code stipulates that

the active earth pressure and passive earth pressure strength acting on the wall are calculated according to the following formula.

$$P_a = \sum \gamma_i h_i + w - 2c \tag{12}$$

$$P_p = \sum \gamma_i h_i + w + 2c \tag{13}$$

where c is the cohesion of the soil. When the active earth pressure of cohesive soil is calculated by the formula, the negative earth pressure is not considered. When the earth pressure is negative, it can be calculated by 0. For clay, the friction Angle δ between the soil and the wall is not considered, that is, $\delta = 0°$.

2.4 Contrastive Analysis

This paper lists the active earth pressure calculation formulas used in the design of sheet pile piers in China, the United States and Japan. From the formulas, it can be seen that the same active and passive earth pressure coefficients are used in the calculation of earth pressure in all countries. Under the calculation conditions of wharf structure, the earth pressure coefficients are only slightly different in the value of wall friction Angle. In the calculation of earth pressure, Japan gives different calculation formulas for sandy soil and cohesive soil according to the soil quality, while the Chinese and American methods do not consider the soil quality, and use the same formula to calculate the earth pressure of different soil. The safety factor method is used to calculate the internal friction Angle ϕ and cohesion force c of passive earth pressure in the United States, which is relatively more conservative.

3 Information of Project

3.1 Project Introduction

The shoreline length of a container terminal project in Guangzhou is 1460 m, and the dock structure is designed according to the berthing of 100,000 ton container ships, the design bottom elevation is −16.0 m, and the width of the berthing water area at the front of the wharf is 92 m. The new type pipe-sheet composite structure of wharf hydraulic structure has a design service life of 50 years, and the structural safety grade is Class II. In order to study the size and distribution form of earth pressure behind the pipe-sheet composite structure, the earth pressure behind the pipe-sheet composite structure is calculated, and the test instrument is buried in the field for

Table 1 Physical and mechanical property indexes of main rock and soil layers

Soil layer	Moisure content	Degree	Void ratio	Direct shear test		Consolidation shear test		Modulus	Unconfined compressive strength
	w	ρ	e	c	φ	c	φ	$Es_{1\text{-}2}$	q_u
	(%)	(g/cm^3)		(kPa)	(°)	(kPa)	(°)	(MPa)	(kPa)
②$_1$Mud	63.5	1.61	1.735	5.6	2.5	4.4	17.5	2.489	9.9
②$_2$ Silt	61.2	1.64	1.688	6.6	1.5	7.6	15.7	2.169	16.1
②$_3$Mucky soil	55.1	1.68	1.512	13.9	1.9	11.9	15.7	2.521	28.7
③$_1$Clay	28	1.85	0.794	30.3	4.5	22.8	17.6	6.158	58.4
④$_2$Clayey soil	32.9	1.88	0.934	22.7	6.1	18.8	16.9	5.167	37.9
⑥$_2$Clayey soil with sand	38.9	1.81	1.012	27.6	4.8	24.5	15.5	4.54	53.0

verification, which provides a basis and reference for the earth pressure calculation behind the new pipe-sheet composite structure.

3.2 Geological Conditions

The project is located at the intersection of rivers and oceans in the estuary of the Pearl River Delta. Its basement is a deep metamorphic regional metamorphic rock in the Lower Paleozoic, which is covered with strata formed in different Quaternary periods and of different origin. According to the drilling data, there are mainly terrestrial alluvial strata, estuarine alluvial sedimentary strata, terrestrial alluvial sedimentary strata, sea-land interaction sedimentary strata and artificial fill soil layers from the bottom up. The project is mainly for soft soil layer, and the geotechnical parameters are calculated according to the recommended values of geotechnical parameters given in the investigation report, the measured values of standard penetration number and the experience of related projects, as shown in the following Table 1.

3.3 Structure Condition

The berth of this project is designed according to the berthing of 100,000 ton container ships,, as shown in the following Fig. 1. and the design bottom elevation is −16.0 m. The single anchor sheet pile scheme with pipe-sheet composite pile at the front wall is adopted. The combination of Φ2032mm steel pipe pile with 24 mm wall thickness

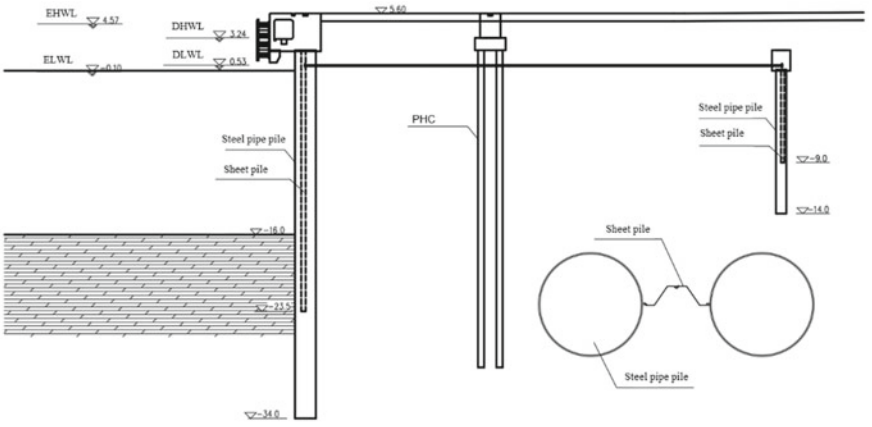

Fig. 1 Pipe-sheet composite wharf structure

and Z-shaped steel sheet pile is adopted at the front wall. The material of steel pipe pile is Q420B, the material of steel sheet pile is S430GP, and the pile top elevation is +2.0 m. The superstructure of composite sheet pile is cast-in-place C40 reinforced concrete parapet with a width of 5.0 m. The yield strength of the tie rod steel is not less than 550 MPa, the tensile strength is not less than 750 MPa, the spacing is 3.35 m, the installation elevation is 0.5 m, and the diameter is Φ140mm. The anchoring structure adopts 1.0 m steel pipe pile combined Z steel sheet pile structure, the top of the pile is set with C40 concrete guide beam, the top elevation is +2.0 m, and the bottom elevation of the anchoring pile is −14.0 m.

3.4 Monitoring Scheme

During the construction period and trial operation stage, a monitoring section is arranged along the shoreline of the pipe-sheet composite structure, and the active and passive earth pressure of the steel pipe pile and steel sheet pile are respectively dynamically monitored and the monitoring frequency is once a week.

4 Monitoring Results and Comparative Analysis

4.1 Comparative Analysis of Measured Results and Theoretical Calculations

According to the relevant calculation formulas, as shown in Fig. 2, the earth pressure calculation methods adopted by China, the United States and Japan in the calculation of pipe-sheet composite piles are all based on the coulomb earth pressure formula, and are modified on this basis. The Chinese and American codes take into account both the cohesion and the influence of the friction Angle on the wall, and the calculation formulas and calculation methods are roughly the same. There are only some differences in the values of some parameters, while the Japanese standard considers clayey soil and non-clayey soil, and there are some differences in the calculation method of the active earth pressure of clayey soil. When calculating active earth pressure, the Japanese method does not use the Coulomb coefficient for corresponding reduction, and the calculation result of active earth pressure is larger and more conservative than that of China and the United States. When calculating passive earth pressure, the American standard will reduce the safety factor of soil parameters, and the calculation result is smaller and more conservative. In terms of earth pressure calculation, China's standard is more radical than other countries, and the calculated dynamic earth pressure is small, and the passive earth pressure is large.

The in-situ earth pressure monitoring results show that the earth pressure on the pipe pile and sheet pile increases gradually from shallow to deep, and the size and distribution law of the earth pressure distribution on the pipe pile and sheet pile are relatively consistent, and no obvious earth pressure redistribution phenomenon occurs. There is still a large earth pressure on the rear side of the sheet pile. Therefore, when the structural stress calculation is carried out subsequently, the calculation of the sheet pile should not only consider its soil retaining effect, but also need to carry out the structural strength and stability check to ensure the safety and stability of the structure. In terms of active earth pressure calculation, the active earth pressure calculation methods and results in China and the United States are basically the same, and are closer to the actual test results. When the subsequent stress calculation is performed, considering uncertainties such as sudden changes in the soil stratum and construction deviations, a suitable safety factor can be selected according to the actual engineering conditions to ensure that the calculated earth pressure is greater than the actual earth pressure and to ensure the stability of the structure. The calculation results obtained by the Japanese calculation method are relatively more conservative, and the calculation results are obviously larger than the measured results. The adoption of this calculation method may lead to a greater depth of the structural piles into the ground for subsequent stress calculations, and the demand for the structural parameters of the piles, such as strength and stiffness, is also greater, which corresponds to the related project cost will also be higher. In terms of passive earth pressure, the results of passive earth pressure calculations in China and Japan are basically the same and significantly larger than those calculated by the U.S. specification using

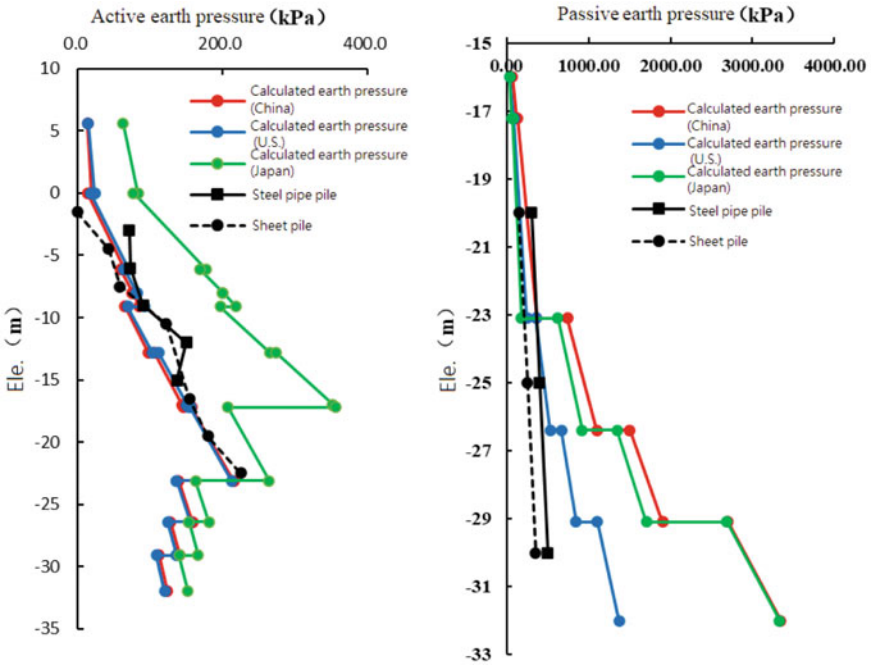

a) Active earth pressure b) Passive earth pressure

Fig. 2 Comparison between calculated earth pressure and measured earth pressure

a safety factor discount. According to the measured passive earth pressure is small, mainly concentrated in the toe of the wall in contact with the soil, mainly because the actual displacement of the combined pipe and sheet pile in this project is small, and the passive earth pressure required to resist the displacement is also small. And the passive earth pressure on the front side of the steel pipe pile is obviously large compared with that on the front side of the steel sheet pile, which is mainly related to the fact that the steel pipe pile mainly bears stress and the soil deformation on its front side is relatively large. Therefore, when calculating the passive earth pressure, the passive earth pressure of the soil within 10 m of the top of the passive zone should be mainly considered, and the passive earth pressure below the depth of 10 m should be appropriately discounted in the calculation to reduce the safety risk. The discount factor of steel sheet pile and steel pipe pile should be considered separately in the calculation of subsequent structural stress and stability by using the calculation of passive earth pressure to reduce the safety risk.

To sum up, when the American code is used to calculate the relevant earth pressure of pipe-plate composite structure, the calculated results have a high consistency with the field measured results, and the American code standards can be selected for calculation and analysis.

4.2 *Comparative Analysis of Measured Results and Numerical Calculation*

The numerical modeling software was used to simulate the earth pressure behind the pipe-sheet composite structure, and the results were shown in Fig. 3. It can be seen that when the pipe pile and sheet pile were modeled respectively, due to problems such as the finite element module division of the model, distortion often occurred at the junction of soil layer and the junction of structure, and the calculated value of earth pressure was abnormally large. Therefore, the equivalent section replacement method should be used to calculate this situation. The soil pressure distribution behind the pipe-sheet composite pile structure can be well calculated by using the numerical simulation method, and the equivalent conversion method of section parameters can be used to simplify the pipe-sheet composite pile into sheet pile structure during setting, which can simplify the model to avoid distortion and stress concentration. The correct earth pressure results can also be calculated.

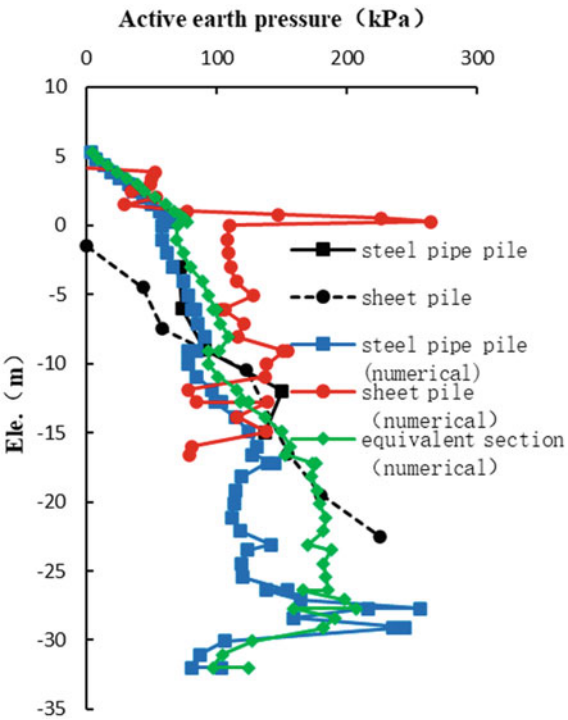

Fig. 3 Comparison between numerical simulated earth pressure and measured earth pressure

5 Conclusions

By comparing with theoretical calculation and field monitoring, this paper calculates and analyzes the distribution and magnitude of earth pressure behind the new pipe-sheet composite pile structure, and the following conclusions can be drawn.

(1) Behind the pipe-sheet composite pile structure, earth pressure is exerted on both pipe pile and sheet pile at the same time, and the magnitude and distribution of earth pressure on pipe pile and sheet pile are consistent, and no obvious earth pressure redistribution phenomenon occurs. There is still a large earth pressure on the rear side of the sheet pile. Therefore, when the structural stress calculation is carried out subsequently, the calculation of the sheet pile should not only consider its soil retaining effect, but also need to carry out the structural strength and stability check to ensure the safety and stability of the structure.
(2) The calculation methods and results of active earth pressure in China and the United States are basically the same and closer to the actual test results. The calculation results obtained by the Japanese calculation method are relatively more conservative. The passive earth pressure calculation results in China and Japan are basically the same, but larger than the actual test results, the U.S. specification for the calculation of passive earth pressure using the safety factor method, the calculation results are smaller and closer to the actual results. Comprehensive comparison, the U.S. standard calculation of earth pressure is more in line with the actual, the subsequent calculation of related projects can be prioritized to consider the use of U.S. standards.
(3) The method of numerical simulation can effectively calculate the soil pressure distribution behind the pipe-sheet composite pile structure, and the method of equivalent conversion of cross-section parameters can be used to simplify the pipe-sheet composite pile into the sheet pile structure, which can simplify the model to avoid aberration and make the calculation results closer to the actual results.
(4) The soil body at the rear side of the pipe pile of tube-sheet combination structure will have a certain degree of soil pressure redistribution due to the arch shape of the pipe pile, and the calculation formulas do not consider the influence of the form of retaining structure at the front side, which can be further investigated in the subsequent study to further refine the calculation results with a view to reducing the cost of the project.

References

1. Rens KL, Liu R, Foltz SD (2013) Sustainable approach for optimal steel sheet pile structure assessment, maintenance, and rehabilitation. J Perform Constructed Facilities 27(2):181(10)
2. Isobe K, Kimura M, Ohtsuka S (2014) Design approach to a method for reinforcing existing caisson foundations using steel pipe sheet piles. Soils and Foundations 54(2):141–154

3. Fuqiang W, Li T (2010) Feature and application of steel pipe-sheet pile structure in deepwater berth. Port Eng 47(06):24–26
4. Zhang L (2016) The structure of the steel sheet pile design calculation and construction technology research. Shanghai Jiao Tong University
5. Code for design and construction for quay wall of sheet pile (JTS167-2010) (2010) Ministry of Transport of the People's Republic of China. China Communications Press
6. Department of the Army (EM 1110-2-2504) (1994) U.S. Army Corps of Engineers CECW-ED Washington, D.C.
7. Technical standards and commentaries for port and harbour facilites in japan ports and harbours bureau, Ministry of land, infrastructure, transport and tourism (MLIT) (2009) The Overseas Coastal Area Development Institute of Japan, Tokyo, Japan
8. Design and construction of steel pipe pile and bolt plate foundation (1997) Japan road association

A Signal Processing Approach for Fracture Inversion Technique Utilizing Acoustic Emission Signal in Shale Hydraulic Fracturing Experiment

Qiyang Yao, Sheng Wang, Yao Chen, Yanchao Shao, and Xiaokun Fan

Abstract In order to detect the fracture information inside the material, solve the problem of static flaw detection and dynamic monitoring of the material, this paper studies the processing method of acoustic emission signal based on the active excitation signal of shale surface and the data output from hydraulic fracturing test. Event detection is the preliminary signal processing, to obtain the event information conveyed by acoustic emission signal and capture the information of shale internal materials carried in signal transmission. Sound source location is calculated by dividing the unit and fitting the signal source position. Both spectrum analysis and tomography are used to locate static natural fractures. Through the analysis of signal data, the positioning situation of different methods is compared. Based on experimental data from laboratory shale hydraulic fracturing, this study uses Julia language to construct a processing model for acoustic emission signals. Through the research context of this paper, we hope to provide reference for Julia language in the field of acoustic emission signal processing.

Keywords Acoustic emission technology · Shale hydraulic fracturing · Crack signal processing

Q. Yao (✉) · Y. Shao · X. Fan
Central Research Institute of Building and Construction Co., Ltd., MCC Group, Beijing 100088, China
e-mail: qiyang_yao@tongji.edu.cn

S. Wang
Dongcheng District, China Minmetals Corporation, TowerA Minmetals Plaza, No.3 Chao Yangmen North Avenue, Beijing 100010, China

Y. Chen
China Metallurgical Group Corporation, No. 28, Shuguang Xili, Chaoyang District, Beijing 100028, China

G. Mei et al. (eds.), *Advanced Construction Technology and Research of Deep-Sea Tunnels*, Lecture Notes in Civil Engineering 490,
https://doi.org/10.1007/978-981-97-2417-8_6

1 Introduction

Solid materials are subjected to external conditions such as mechanical and temperature loads, which generate local stress concentrations within them [1]. In this process, the strain energy is rapidly released in the form of waves, and this release process is known as acoustic emission [2]. Kaiser found in tests of the acoustic emission properties of metals that the acoustic emission of metal specimens subjected to unidirectional stretching began to be noticeable when the internal stress reached the maximum prior stress to which the material was subjected [3]. Goodman found in compression tests of rocks that the Kaiser effect still applied to rocks. Mogi [4] and Boyce experimentally derived the relationship be-tween the magnitude of rock acoustic emission activity and loading. Since then, more scientific research and technical applications have contributed to the development of AE techniques, which have been applied to various engineering problems [5].

Shales have ultra-low permeability properties and store significant hydrocarbon resources beneath them [6]. Laboratory-based hydraulic fracturing experiments have advantages over onsite microseismical monitoring experiments. Firstly, the laboratory can control the stress loading and injection pressure; secondly, the laboratory hydraulic fracturing experiments can accurately simulate the hydraulic process and obtain data with high signal-to-noise ratio [7–9]. The experimental shale itself has a large fracture, and the natural fracture has a strong influence on the growth direction of the newly formed fracture [10].

2 Experimental Details

2.1 Experimental Parameters

Sample size: 710 × 710 × 914 mm. A 530 mm deep borehole was drilled in the vertical laminar surface of the specimen, a high strength steel pipe with 25 mm outer diameter and 19 mm inner diameter was fixed, and a 100 mm wide slit was symmetrically cut at 405 ~ 505 mm depth to serve as a water pressure channel. In view of the complexity of shale fracture morphology, the method of 6-side average layout is adopted. As shown in Fig. 1.

2.2 Experimental Procedure

The Hydraulic fracturing experiment is divided into two stages. In the first stage, the active acoustic emission signal scheme is adopted. By tapping each sensor to transmit the signal, other sensors are used to capture the event and locate the active tapping position. The second stage of work is to hydraulically pressurize, crack the hole wall,

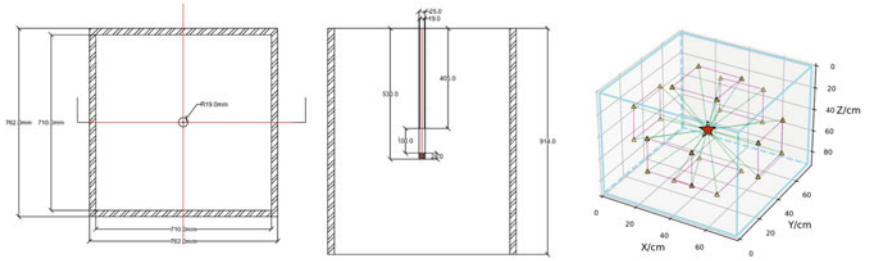

Fig. 1 Rock sample size and sensor coordinate space

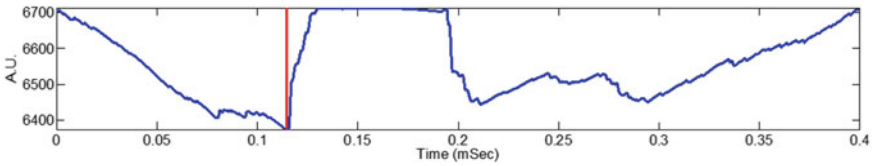

Fig. 2 AIC method capture event start time diagram

capture the event with the sensor, and apply the code analysis results validated in the first stage.

3 Methodology

3.1 Event Detection

AIC method uses the concepts of entropy and variance. The calculation is based on Eq. 1, and the result is shown in Fig. 2.

$$AIC(t_w) = t_w * \log(\text{var}(R_w(t_w, 1))) + (T_w - t_w - 1) * \log(\text{var}(R_w(1 + t_w, T_w))) \quad (1)$$

3.2 Signal Location

The method of cell meshing is used to locate the active excitation signal of the test rock sample. The assumption of uniformity is made inside the rock, and the theoretical calculation time is obtained by the path/velocity integral. Then the theoretical time

and t_obs output in the event detection are fitted to locate the actual unit position of the sound source. ($t_{obs} = tpick\_all[:, i]. - tpick\_all[i, i]$).

The theoretical time needs to be calculated by path/velocity integral and further fitted with t_obs. The theoretical formulas needed are as follows:

$$f(x) = \frac{\left|\left|g_{(x)} - d\right|\right|}{2}, \ d_i = t_{obs}^i \tag{2}$$

$$g_i = \frac{1}{v} * \sqrt{\left(x_r^i - x_s\right)^2 + \left(y_r^i - y_s\right)^2 + \left(z_r^i - z_s\right)^2} \tag{3}$$

$$t_{nobs}^i = g_i\left(x_r^i\right) + e, \ e \sim \mathrm{N}\left(0, \sum e\right) \tag{4}$$

Formula (2) is the fitting of theoretical time and actual time, Formula (3) is the theoretical method to calculate theoretical time, and the path integral is done on the known linear path, and formula (4) is the noise e added considering the instrument error, which is determined in the fitting of the calculation time and observation time.

3.3 Spectrum Analysis

The Fourier transform, which can represent complex functions as trigonometric functions or linear combinations of their integrals, is widely used in digital signal processing [11].

$$F(\omega) = F(f(t)) = \int f(t) \cdot e^{-i\omega t} dt \tag{5}$$

[ω is the frequency, t is the time, $e^{-i\omega t}$ is the complex function].

3.4 Tomography

Tomography is widely used in seismic waveform analysis. After the focal location is completed, the change of seismic wave transmission is analysed with the given distribution of seismic receiving stations and focal points. If the seismic wave travels through an abnormally low velocity region, the time of its arrival at the seismic station and the theoretical velocity calculation model will have a large error.

In addition, the signal received by the receiver also carries a lot of information inside the transmission material, through the full use of these information can improve the resolution of the tomography.

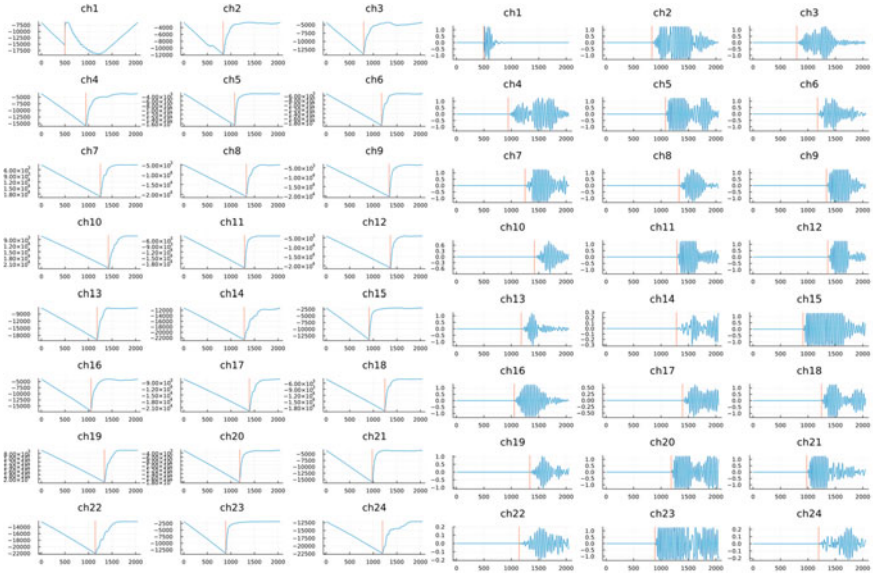

Fig. 3 AIC method result output

4 Results and Discussion

4.1 Event Detection

Figure 3 shows the Akaike information criterion method for detecting the start time of an event.

4.2 Signal Location

As shown in the Fig. 4, take e = 60 ms by calculation.

The localization results are shown in Figs. 5 and 6. Ignoring the localised areas on the surface, the localised points in the interior marked by red lines are the more concentrated areas of acoustic signal emission. It roughly shows the acoustic signal emission during the hydraulic fracturing phase within the rock, demonstrating that although there are more marginal events, it is still possible to roughly identify the area of event occurrence.

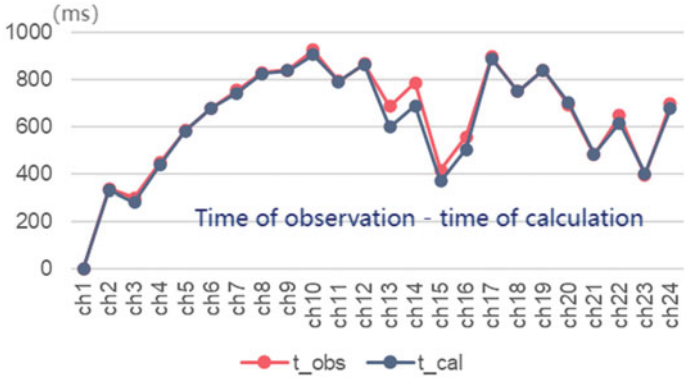

Fig. 4 Calculated time versus observed time

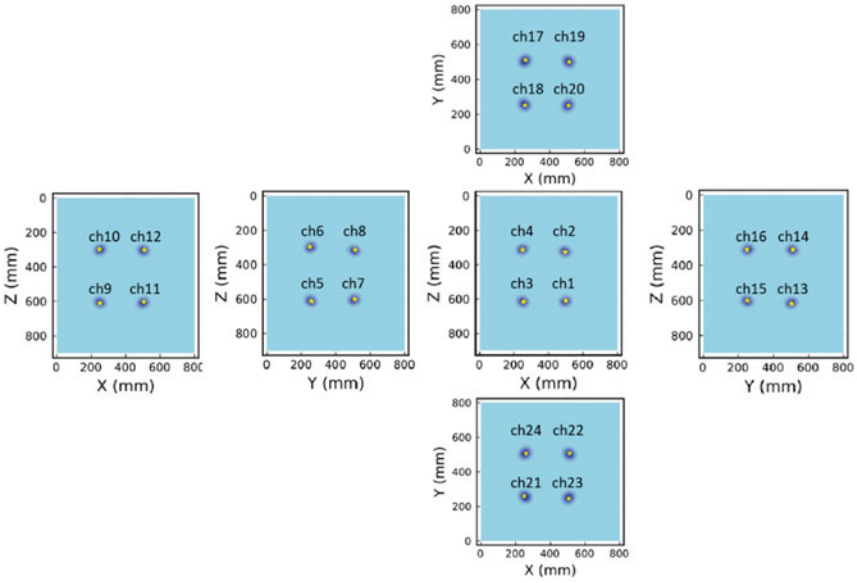

Fig. 5 Location results (active)

4.3 Spectrum Analysis

Take the first event(active) as an example for spectral analysis, and the result is shown in Fig. 7.

It can be found from the pictures that these lost band points are basically after the Y = 40 cm plane, with the absence of high frequencies in the X = 0 plane not obvious, and only in sensor 6, near Y = 20 cm, where there is an absence near X = 70 cm and a missing signal across the upper and lower bottom surfaces.

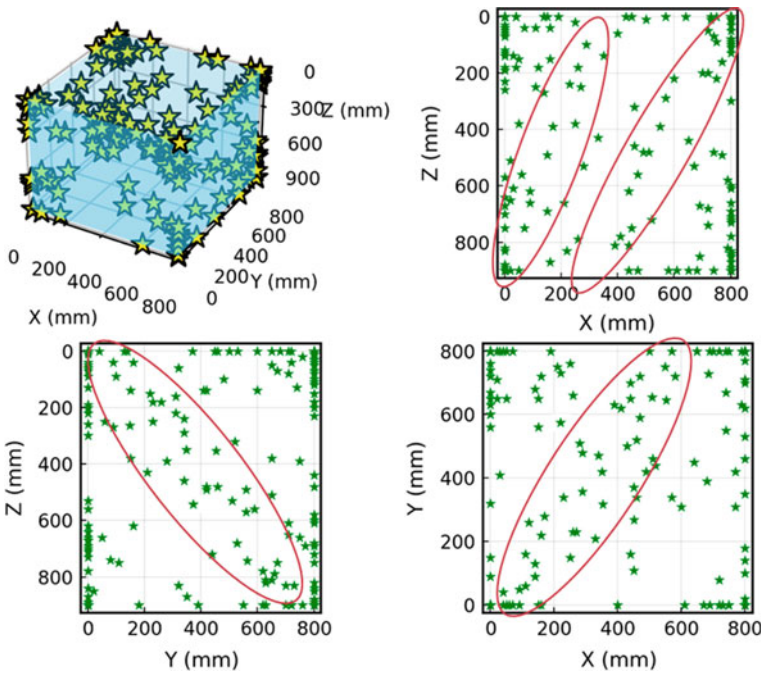

Fig. 6 Location results (passive)

It can therefore be roughly guessed that a fracture surface exists near X = 70 cm at Y = 40 cm and runs through the upper and lower bottom surfaces. The progression from the X = 70 cm surface towards the interior of the rock progresses towards the fracture surface in a progressive negative direction on the Y axis until it extends to the vicinity of sensor 6.

4.4 Tomography

To simplify the calculation process, six sections can be cut out of the rock cube, each containing eight sensors. To perform in-plane chromatographic imaging of the intercepted plane.

Through several iterations, a 4 × 5 division was determined. As shown in Fig. 8.

Approximating the transfer path straight line, the path length of the signal transmission path for any two sensors is calculated for all velocity cells and the data is stored in the path matrix (28 × 20).

From $[\frac{1}{v}] = [L^T * L + \lambda * I] \backslash [L^T * T]$, The distribution of calculated speeds is shown in Table 1.

Reduction of the velocity distribution to the section divider.

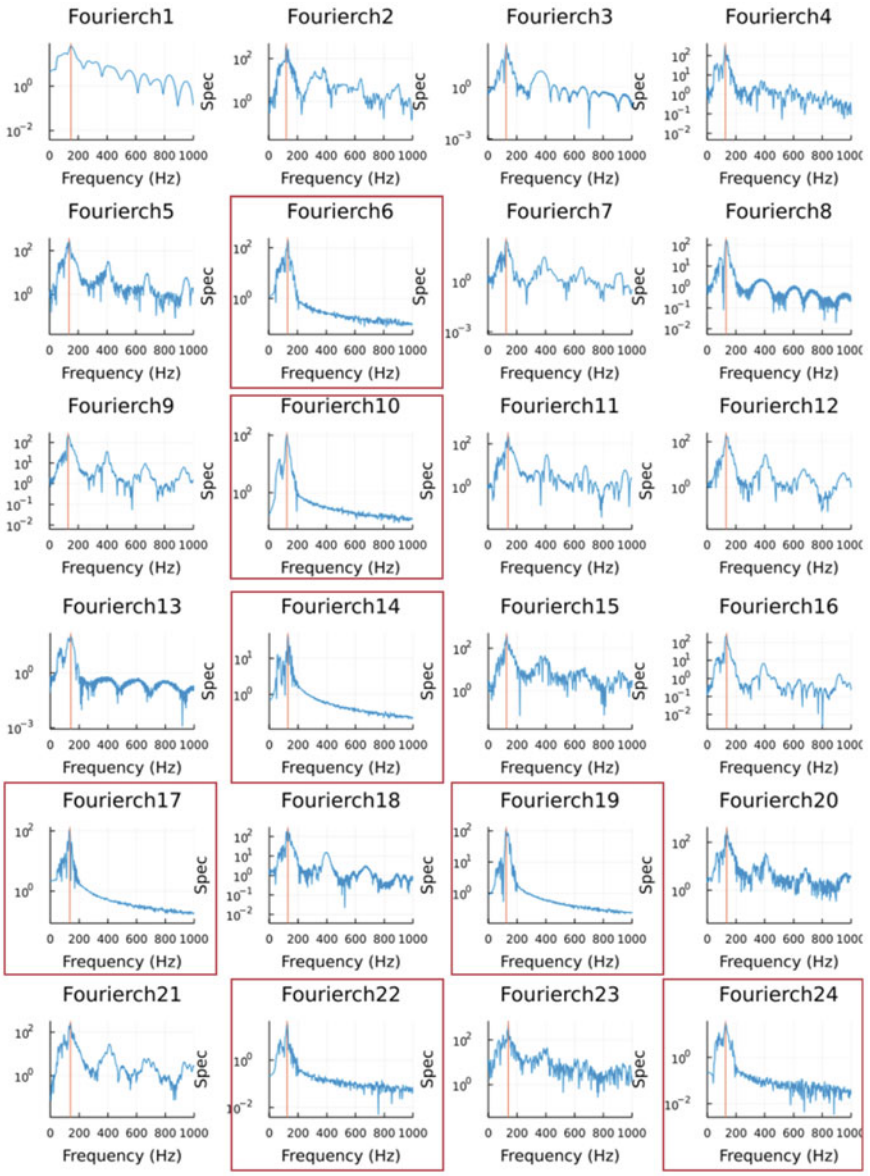

Fig. 7 High frequency missing signal propagation paths

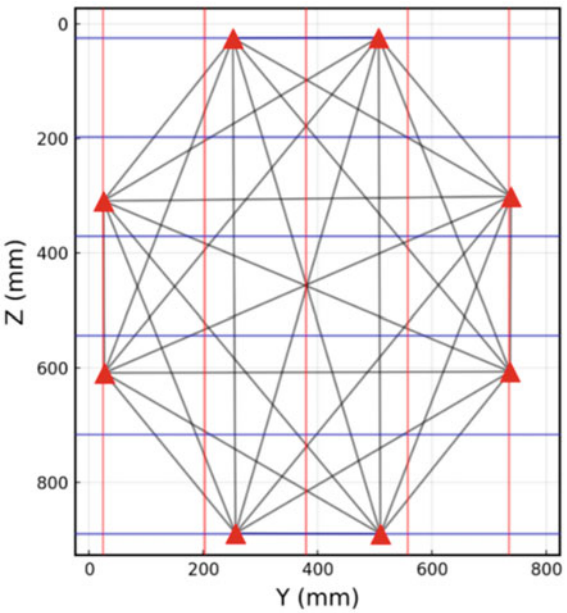

Fig. 8 Tomography meshing

Table 1 Speed distribution data

·	Calculated speed values	Number	Calculated speed values
1	979.842842	11	4301.567425
2	839.540217	12	1155.078139
3	645.799202	13	766.9197312
4	2171.25934	14	1286.622887
5	917.30248	15	755.6646747
6	1547.317	16	890.1983908
7	840.038423	17	1070.043079
8	714.423366	18	961.8436737
9	951.923935	19	748.209758
10	550.725555	20	896.2802467

Calculation by objective data sensor 2 with sensor 4:
$v = l/t = 713 \times 10^{-3} m/806 \times 10^{-6} s = 885 \text{m/s}$.
As shown in Fig. 9, the data in red is below average speed (885 m/s).

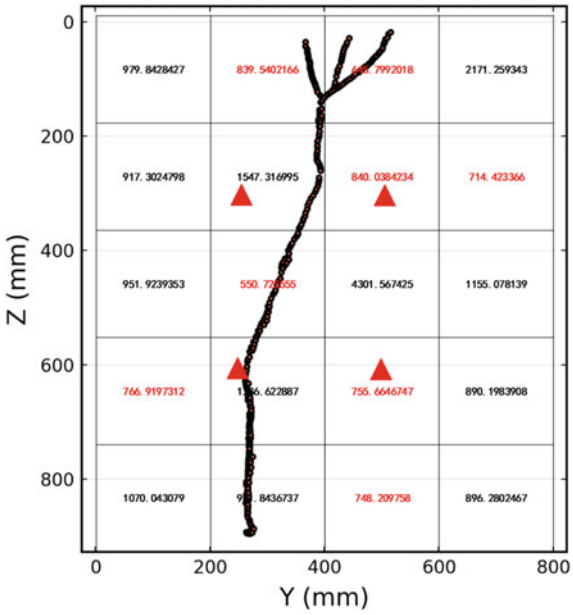

Fig. 9 Comparison of chromatography results

5 Conclusion

The findings of this paper are as follows.

Experimental results of hydraulic fracturing acting on shales with primary natural fractures were investigated. Under pressure, new fractures develop more along the primary fractures. When the stress on the rock reaches a prior maximum stress, close to rupture, an acoustic signal is emitted from inside the rock, which is captured by externally placed sensors.

Exploration of signal processing. By mastering the principles of analysis, constructing a code system for signal processing, completing a series of tasks such as detection, localization, spectral analysis and laminar imaging, the entire state of the rock sample before and after the test was analysed and calculated. Reference is provided to further promote the application of acoustic emission technology.

This study focuses on laboratory shale hydraulic fracturing and analyses the fracture condition of cracks through data from 24 sensors. The signal processing method in the data model is also verified. Systematic ideas are also presented for work in the field of structural health monitoring in the civil engineering industry, particularly in the area of crack acoustic emission signal localization.

Acknowledgements This work was financially supported by Beijing Nova Program 20220484088, 20230484402, Major Research Projects of MCC Group YCC2021Kt01.

References

1. Zacharia T (1994) Dynamic stresses in weld metal hot cracking. Welding J Including Welding Res Suppl 73(7):164–172
2. Hazzard JF, Young RP (2000) Simulating acoustic emissions in bonded-particle models of rock. Int J Rock Mech Min Sci 37(5):867–872
3. Huandong P, Fuxing J, Xingmin Z (2004) The role of shear stress in the acoustic emission of defective bodies. J Geotech Eng 26(6):824–827
4. Mogi K (1962) Study of elastic shocks caused by the fracture of inhomogeneous materials and its relations to earthquake phenomena. Bull Earthq Res Inst 40(6):831–853
5. Gu C, Mok U, Marzouk YM, Prieto GA, Sheibani F, Evans JB, Hager BH (2020) Bayesian waveform-based calibration of high-pressure acoustic emission systems with ball drop measurements. Geophys J Int 221(1)
6. Ju YW, Bu HL, Wang GC (2014) Main characteristics of shale gas reservoirs and their impact on reservoir modification. Adv Earth Sci 29(4):492
7. Josh M, Esteban L, Delle Piane C, Sarout J, Dewhurst DN, Clennell MB (2012) Laboratory characterisation of shale properties. J Petrol Sci Eng 88–89, 107–124. <Go to ISI>://WOS:000307151400013
8. Lei X, Ma S (2014) Laboratory acoustic emission study for earthquake generation process. Earthq Sci 27(6):627–646
9. Li Y, Yang S, Zhao W, Li W, Zhang J (2018) Experimental of hydraulic fracture propagation using fixed-point multistage fracturing in a vertical well in tight sandstone reservoir. J Petrol Sci Eng 171:704–713
10. Zhai H, Chang X, Wang Y, Lei X, Xue Z (2020) Analysis of acoustic emission events induced during stress unloading of a hydraulic fractured Longmaxi shale sample. J Petrol Sci Eng 189.https://doi.org/10.1016/j.petrol.2020.106990
11. Putra TE, Asrina D, Dirhamsyah M (2020) The ability of the fast Fourier transform to de-noise a strain signal. IOP Conf Ser: Mater Sci Eng 931(1)

A New Bayesian Method for Dynamic System Identification Using FFT Data

Jiahua Yang and En-Jie Meng

Abstract Dynamic system identification is an important field of research focused on identifying accurate system models of structures for predicting dynamic behaviors. This field finds widespread application in downstream research such as response prediction, structural failure and reliability analysis, and related areas of structural health monitoring. Conventional methods update structural finite element models (FEMs) using experimental modal parameters, because excitations are difficult to measure for full-scale structures and measured responses cannot be used as data in model updating. One challenge of conventional methods is thus that additional time is required for modal analysis, and by packing response data into modal parameters, original information in response data may be lost and cannot be used for model updating. Concerning this issue, this paper develops a dynamical system identification method to directly update an FEM using experimental fast Fourier transform (FFT) data following a Bayesian approach. The modeling of FFTs combing FEM and an efficient algorithm for processing the large amount of FFTs are not available for conventional methods. In this paper, the posterior probability density function (PDF) of the model parameters is derived assuming that FFTs at different frequency. instances follow independent and identically distributed complex Gaussian distributions under the long-data condition. One contribution of this work is that the sub-structure FEM analysis is integrated into the formulation of the posterior PDF to make the direct use of FFT data possible, and increase computational efficiency. The most probable values (MPVs) of the model parameters are obtained by maximizing the posterior PDF. By making use of the special mathematical structure of the posterior PDF, a novel algorithm that iterates among the model parameters is developed to efficiently search parameter space for the maximization. A numerical case has demonstrated that the proposed method can accurately identify the FEM of

J. Yang · E.-J. Meng (✉)
School of Civil Engineering and Architecture, Guangxi University, Nanning 530000, Guangxi, China
e-mail: 1015942989@qq.com

J. Yang
National Engineering Research Center of High-Speed Railway Construction Technology, Changsha 410075, China

G. Mei et al. (eds.), *Advanced Construction Technology and Research of Deep-Sea Tunnels*, Lecture Notes in Civil Engineering 490,
https://doi.org/10.1007/978-981-97-2417-8_7

the target structure together with the unmeasured excitation parameters and damping ratios.

Keywords Bayesian identification · Fast Fourier transform · Long data · Sub-structure analysis

1 Introduction

Bayesian modal identification and model updating based on ambient vibration data have garnered increasing attention among engineers and researchers working in the field of structural health monitoring (SHM) [1–3]. Since there is a one-to-one correspondence between the time-domain data and its FFT, transforming responses into the frequency domain signals enables the full utilization of well-separated modal information [4]. Modeling FFT of response using modal parameters make it convenient to construct the covariance matrix of FFT [5], and thus its PDF [6, 7]. It is practical to assume that around a peak of the plot of response auto-power spectral densities (PSDs) only one structural mode is dominant [8]. In this situation, it is convenient to model FFTs around a spectral peak, and FFTs around different spectral peaks contain main dynamic information of a structure, so only the FFTs around the spectral peaks of interest are used as data for Bayesian inference in this work. The modal parameters calculated by a FEM are used to construct the PDF of FFTs. Model updating needs modal parameters calculated with different sets of FEM parameters, which means many times of finite element analysis. The excitation data is challenging to measure directly, for large structures with thousands of degrees of freedom (DOFs), this will consume a substantial amount of computational resources. To alleviate computational burden, the sub-structure method is employed in this study to reduce FEMs. This method has been widely used for dynamic analysis [9]. By integrating the sub-structure method into the formulas of Bayesian model updating [10–12], the computation time is reduced.

This paper proposes a new method to update dynamic system models of structures using FFTs of responses data without measuring excitations. This approach bypasses modal analysis, allowing for the direct update of the finite element model of a full-scale structure.

2 Methodology

2.1 Posterior PDF

The FFTs of measured acceleration data $\hat{\mathbf{x}}_j \in R^n$ at n measurement channels are defined as:

$$\mathcal{F}_k = \mathbf{F}_\mathrm{k} + \mathbf{i}\mathbf{G}_\mathrm{k} = \sqrt{\frac{2\Delta t}{N}} \sum_{j=1}^{N} \hat{\mathbf{x}}_j \exp\{-2\pi \mathbf{i}[(k-1)(j-1)/N]\} \tag{1}$$

where $\mathbf{F}_k$ and $\mathbf{G}_k$ represent the real and imaginary parts of the FFTs, respectively; Δt is the sampling time interval; $k = 2, 3, \ldots, N_q$ is the frequency index; N_q is the FFT ordinate at the Nyquist frequency; $j = 1, 2, \ldots, N$ is the time index; N is the total number of samples.

Let an augmented vector $\mathbf{Z}_k = \left[\mathbf{F}_k^\mathrm{T}, \mathbf{G}_k^\mathrm{T}\right] \in R^{2n}$, denotes the measured data. It has been proven that $\{\mathbf{Z}_k\}$ asymptotically follows a zero-mean Gaussian distribution when the number of response data points is large enough, which is easy to fulfill in practice for measurement with a high sampling rate and long duration. This result can be used to formulate the posterior PDF of the uncertain model parameters θ conditional on the experimental FFTs. Assuming that the prior PDF is a uniform PDF, according to Bayes' theorem, the posterior PDF $p(\boldsymbol{\theta}|\{\mathbf{Z}_k\})$ is proportional to the likelihood function $p(\{\mathbf{Z}_k\}|\boldsymbol{\theta})$:

$$p(\boldsymbol{\theta}|\{\mathbf{Z}_k\}) \propto p(\{\mathbf{Z}_k\}|\boldsymbol{\theta}) \tag{2}$$

where the uncertain parameters $\boldsymbol{\theta} = \left\{\boldsymbol{\alpha}, \{S_m, \zeta_m :, m = 1, 2, \cdots, N_m\}, \sigma^2\right\}$ include the stiffness parameters $\boldsymbol{\alpha}$ for FEM, PSD of modal excitation S_m and damping ratio ζ_m of the m-th mode for N_m modes, and PSD of prediction error σ^2. Using the result that FFTs at different frequency instances follow independent and identically distributed complex Gaussian distributions, the likelihood function can be constructed as:

$$\begin{aligned} &p(\{\mathbf{Z}_k\}|\boldsymbol{\theta}) \\ &= \prod_{m=1}^{N_m} \prod_{k=2}^{N_{q,m}} (2\pi)^{-\frac{N_{q,m}-1}{2}} \det\left(\mathbf{C}_{k,m}(\boldsymbol{\theta})\right)^{\frac{1}{2}} \exp\left(-\frac{1}{2} \sum_{k=2}^{N_{q,m}} \mathbf{Z}_k^T \mathbf{C}_{k,m}(\boldsymbol{\theta})^{-1} \mathbf{Z}_k\right) \end{aligned} \tag{3}$$

where the covariance matrix can be constructed using the modal parameters calculated by FEM:

$$\begin{aligned} \mathbf{C}_{k,m}(\boldsymbol{\theta}) &= \left(\frac{S_m D_{k,m}}{2}\right) \begin{bmatrix} \varphi_m \varphi_m^\mathrm{T} & 0 \\ 0 & \varphi_m \varphi_m^\mathrm{T} \end{bmatrix} + \left(\frac{\sigma^2}{2}\right) \mathbf{I}_{2n} \\ &= \frac{1}{2} \begin{bmatrix} \mathbf{E}_{k,m} & 0 \\ 0 & \mathbf{E}_{k,m} \end{bmatrix} \end{aligned} \tag{4}$$

where it has been assumed that around each spectral peak only one mode is dominant $\mathbf{E}_{k,m} = S_m D_{k,m} \varphi_m \varphi_m^\mathrm{T} + \sigma^2 \mathbf{I}_n$ represents the power spectral density (PSD) of the response data, $D_{k,m} = \left[\left(\beta_{k,m}^2 - 1\right)^2 + \left(2\zeta_m \beta_{k,m}\right)^2\right]^{-1}$ is the dynamic amplification factor where $\beta_k = f_m / f_k$; f_m and φ_m are the natural frequency and mode shape of the m-th mode calculated by FEM; $f_k = (k-1)/(N\Delta t)$.

The most probable value of $\boldsymbol{\theta}$ is obtained by maximizing the posterior PDF, which is equivalent to minimize the negative logarithmic likelihood function (NLLF) as follows:

$$L(\boldsymbol{\theta}) = -nN_f \ln 2 + (n-1)N_f \ln\sigma^2 + \sum_{m=1}^{N_m}\sum_{k} \ln\left(S_m D_{k,m} + \sigma^2\right) + \sigma^{-2}\left(d - \varphi_m^{\mathrm{T}} \mathbf{A}_m \varphi_m\right) \tag{5}$$

where $\mathbf{A}_m = \sum_k \left[1 + S_m / S_m D_{k,m}\right]^{-1} \mathbf{D}_k$; $\mathbf{D}_k = \mathbf{F}_k \mathbf{F}_k^{\mathrm{T}} + \mathbf{G}_k \mathbf{G}_k^{\mathrm{T}}$.

It is known from the above equation that the natural frequencies needed for $D_{k,m}$ and mode shapes can be obtained from FEM. A new iterative algorithm was developed. To facilitate the iteration among different model parameters, analytical formulations of S_m and σ^2 were derived with the assumption of high signal-to-noise ratio for asymptotic approximation. Given each stiffness parameter $\boldsymbol{\alpha}$, minimization is done separately for S_m and σ^2 with their analytical formulations as the initial values. Minimization is also done for damping ratios. Iteration is conducted among S_m, σ^2 and ζ_m until convergence. We minimize the NLLF until the difference between two iteration steps $L(\boldsymbol{\theta}_i)$ and $L(\boldsymbol{\theta}_{i-1})$ is small enough.

2.2 Sub-Structure Finite Element Analysis

Repeated finite element analysis is needed for minimizing the NLLF. This could be computationally intensive if a full FEM is used. We propose to reduce the order of FEM with the sub-structure method. With an FEM divided into s sub-structures, the mass matrix $\mathbf{M}^s$ and stiffness matrix $\mathbf{K}^s$ for sub-structure s are partitioned as

$$\mathbf{M}^s = \begin{bmatrix} \mathbf{M}_{ii}^s & \mathbf{M}_{ib}^s \\ \mathbf{M}_{bi}^s & \mathbf{M}_{bb}^s \end{bmatrix} \in R^{n^s \times n^s}, \mathbf{K}^s = \begin{bmatrix} \mathbf{K}_{ii}^s & \mathbf{K}_{ib}^s \\ \mathbf{K}_{bi}^s & \mathbf{K}_{bb}^s \end{bmatrix} \in R^{n^s \times n^s}, s = 1, \ldots, N_s \tag{6}$$

where n^s represents the number of DOFs of sub-structure s; N_s denotes the number of sub-structures; the subscripts i and b represents internal and boundary DOFs, respectively. The coordinate set for internal and boundary DOFs is denoted as $\mathbf{u}_i^s(t) \in R^{n_i^s}$ and $\mathbf{u}_b^s(t) \in R^{n_b^s}$, respectively. Consequently, the physical coordinates of sub-structure s are expressed as $\mathbf{u}^s(t) = \mathbf{u}_i^s(t) + \mathbf{u}_b^s(t) \in R^{n^s \times 1}$, where $n^s = n_i^s + n_b^s$.

According to the Craig–Bampton fixed-interface mode method, the Ritz coordinate transformation matrix can be used for reduction and is expressed as:[11]

$$\boldsymbol{\Psi}^s = \begin{bmatrix} \boldsymbol{\Phi}_{ik}^s & \boldsymbol{\Psi}_{ib}^s \\ 0_{bk}^s & \mathbf{I}_{bb}^s \end{bmatrix} \in R^{n^s \times \hat{n}^s} \tag{7}$$

where $\hat{n}^s = n_{ik}^s + n_b^s$ and $\boldsymbol{\Phi}_{ik}^s \in R^{n^s \times n_{ik}^s}$ represents the low-order dominant mode shapes ($n_{ik}^s < n_i^s$) of the internal DOFs in each sub-structure. $\boldsymbol{\Psi}^s$ that is comprised of the k-th mode coordinates of internal DOFs and all physical coordinates at interface DOFs is used to convert the physical coordinates into the generalized coordinates. The mass and stiffness matrix of the reduced sub-structure s are represented as

$$\hat{\mathbf{M}}^s = \boldsymbol{\Psi}^{s\mathrm{T}} \mathbf{M}^s \boldsymbol{\Psi}^s \in R^{\hat{n}^s \times \hat{n}^s}, \hat{\mathbf{K}}^s = \boldsymbol{\Psi}^{s\mathrm{T}} \mathbf{K}^s \boldsymbol{\Psi}^s \in R^{\hat{n}^s \times \hat{n}^s} \tag{8}$$

Finally, the mass matrix and stiffness matrix of the reduced model are assembled through all reduced sub-structure, denoted as $\hat{\mathbf{M}}$ and $\hat{\mathbf{K}}$, respectively.

2.3 *Parameterization of Model Updating Based on Sub-Structure Finite Element Analysis*

The Craig-Bampton transformation can be done separately [11]. Therefore, the parameterization of the reduced-order FEM can be achieved conveniently using the reduced-order matrices of sub-structures:

$$\hat{\mathbf{K}}(\mathbf{x}) = \hat{\mathbf{K}}^0 + \sum_{s=1}^{N_s - 1} \hat{\mathbf{K}}^s \mathrm{x}_s \tag{9}$$

where the superscript '^' denotes the reduced-order stiffness matrix of the FEM. Consequently, the frequencies and mode shapes can be computed by solving the eigenvalue problem:

$$\left(\hat{\mathbf{K}}(\mathbf{x}) - \omega_n(\mathbf{x})^2 \hat{\mathbf{M}}\right) \varphi_n(\mathbf{x}) = 0 \tag{10}$$

where $\omega_n(\mathbf{x})$ and $\varphi_n(\mathbf{x})$ represent nth modal frequency and mode shape, respectively. By continuously updating the stiffness coefficients x_s of the sub-structures, the natural frequencies and mode shapes can be updated.

3 Case Study

A simulated 12-story building structure shown in Fig. 1 is used to validate the proposed method. Each two stories (eight columns and two floors) were considered as one sub-structure, so there are six sub-structures in this case. Accelerations were measured along the x direction at 6 stories, i.e., story 2, 4, 6, …, 12. Table 1 lists the basic information of the structure.

Accelerations of the structure were simulated with the PSD of modal excitation $0.25^2 \mathrm{N}^2/\mathrm{Hz}$ and the PSD of prediction error $10^{-10}\left(\mathrm{m}/s^2\right)^2/\mathrm{Hz}$. The sampling

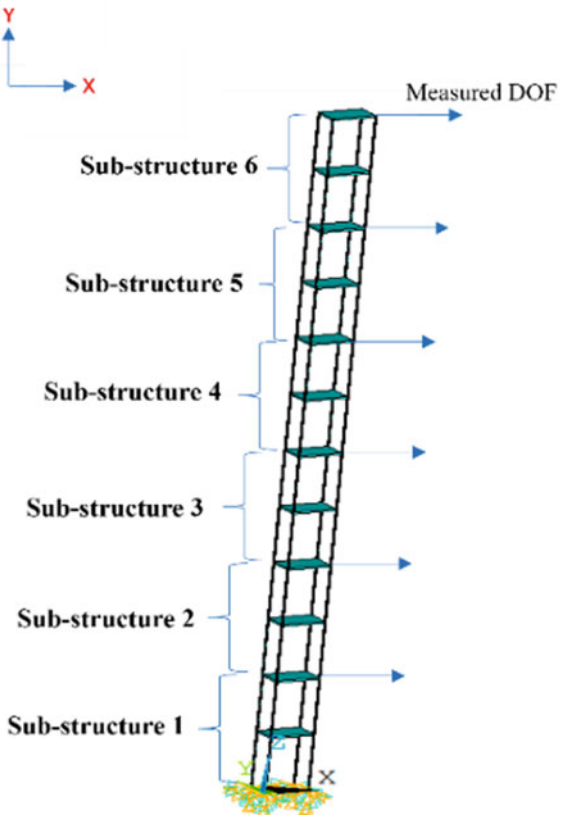

Fig. 1 The 12-story shear building

Table 1 The basic information of the structure

Column	Width (m)	0.025
	Thickness (m)	0.005
Floor slab	Length (m)	0.45
	Width (m)	0.28
	Thickness (m)	0.025
Floor height (m)		0.8
Density of mass (kg/m^3)		7850

frequency is 200 Hz and of the length of data is 300 s. The singular value (SV) spectrum is depicted in Fig. 2. The FFT data around the four peaks marked in the graph were used for updating the FEM.

The MPVs of the model parameters were identified. The MPVs of the stiffness parameters were input the FEM to calculate the natural frequencies and mode shapes. The calculated mode shapes are compared with the exact ones in Fig. 3. The errors between the calculated and exact natural frequencies are also shown above each

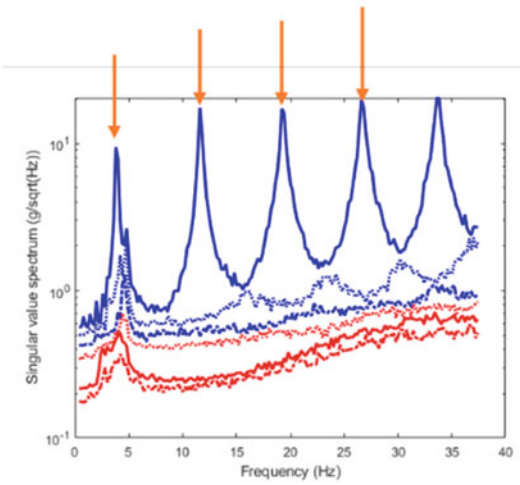

Fig. 2 The SV spectrum of response data

sub-plot. Figure 3a shows the comparison for the four modes whose FFT data were included in model updating, i.e., the four selected spectral peaks correspond to these four modes. It is seen that the calculated and exact modal parameters match well. Figure 3b and c show the comparison for the modes whose FFT data were not included for model updating. The calculated modal parameters by the updated FEM can still well match with the exact ones. These results verify the feasibility of the proposed method.

The successful validation of this method provides an efficient and accurate approach for dynamic system identification of full-scale structures. It yields a model that accurately predicts the dynamic behaviors of the structure under different conditions, while the identified results also provide reasonably accurate modal excitations. The proposed method can be used to continuously update the structural model when monitoring data are continuously measured, and the continuously updated model can be used to assess the structural performance in a timely fashion. This evaluation is crucial for ensuring the safety and stability of structures, and it plays an important role in SHM by enhancing the accuracy of analysis and design.

4 Conclusions

A new Bayesian method for dynamic system identification has been developed. The proposed method can use the original FFTs of measured responses to update the FEM of a target structure and statistical properties of modal excitations without measuring excitations. System identification is achieved by identifying the posterior PDF of uncertain model parameters conditional experimental FFT data. The posterior PDF is constructed using the fact that FFT at each frequency instance asymptotically

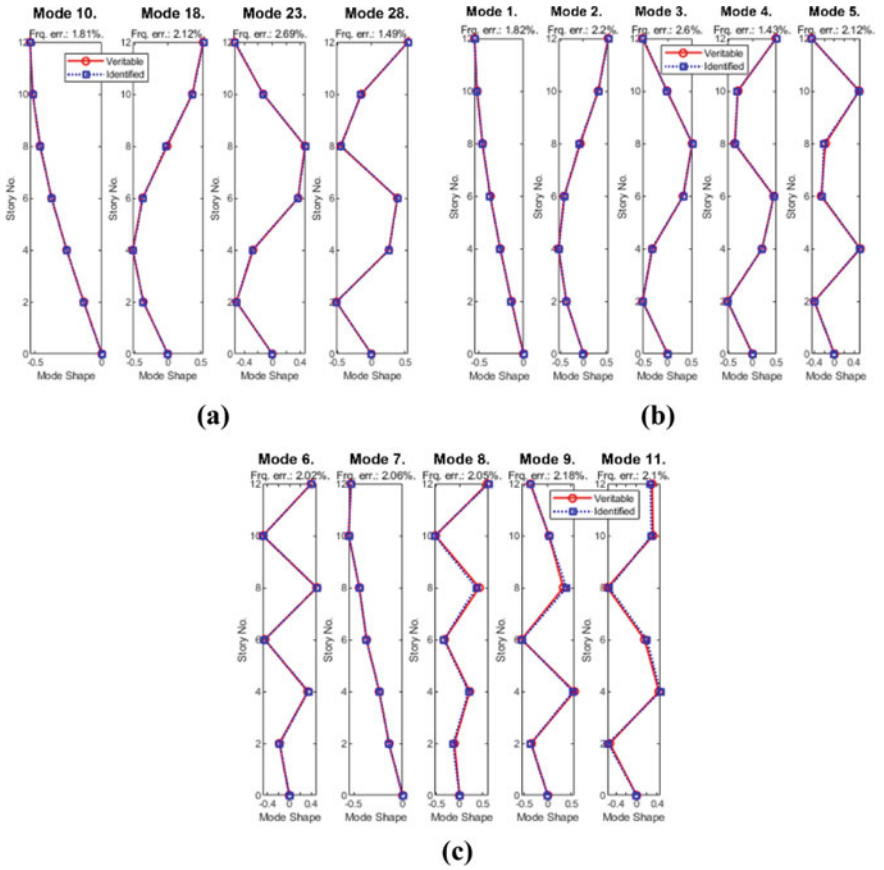

Fig. 3 The comparison of the calculated and exact modal parameters

follows a complex Gaussian distribution. Sub-structural finite element analysis is integrated into the formulation of the posterior PDF. By utilizing the Craig-Bampton transformation matrix for reducing the full FEM, convenient parameterization can be done. The sub-structure method also eliminates the need for re-analysis of fixed-interface orthogonal modes and interface constraint modes. A new iteration algorithm has been developed to efficiently search one local area of the parameter space at a time. The proposed method was verified numerically by 12-story building structure. The updated FEM could accurately predict the modal parameters, even for the ones whose experimental information was not included for model updating.

Acknowledgements The financial support from Science and Technology Base and Talent Program of Guangxi (Grant No. GuikeAD21220031), Open Foundation of National Engineering Research Center of High-speed Railway Construction Technology (Grant No. HSR202108), and National Key Research and Development Program of China (Grant No. 2022YFC3005300) is greatly acknowledged.

References

1. Rosati I, Fabbrocino G, Rainieri C (2022) A discussion about the Douglas-Reid model updating method and its prospective application to continuous vibration-based SHM of a historical building. Eng Struct 273(115058)
2. Kamariotis A, Chatzi E, Straub D (2022) Value of information from vibration-based structural health monitoring extracted via Bayesian model updating. Mechan Syst Signal Proc 166(108465)
3. Zhu YM, Sun Q, Zhao C et al. (2023) Operational modal analysis of two typical UHV transmission towers: A comparative study by fast Bayesian FFT method. Eng Struct 277(115425)
4. Yuen KV, Katafygiotis LS (2003) Bayesian fast fourier transform approach for modal updating using ambient data. Adv Struct Eng 6(2):81–95
5. Ni YC, Zhang FL (2021) Uncertainty quantification in fast Bayesian modal identification using forced vibration data considering the ambient effect. Mechan Syst Signal Proc 148(107078)
6. Au SK (2011) Fast Bayesian ambient modal identification in the frequency domain, Part I: Posterior most probable value. Mech Syst Signal Process 26:60–75
7. Au SK (2011) Fast Bayesian ambient modal identification in the frequency domain, Part II: Posterior uncertainty. Mech Syst Signal Process 26:76–90
8. Au SK (2011) Fast Bayesian FFT method for ambient modal identification with separated modes. J Eng Mech 137(3):214–226
9. Craig RR Jr, Bampton MC (1968) Coupling of substructures for dynamic analyses. AIAA J 6(7):1313–1319
10. Li YW, Tian K, Hao P et al. (2020) Finite element model updating for repeated eigenvalue structures via the reduced-order model using incomplete measured modes. Mechan Syst Signal Proc 142(106748)
11. Papadimitriou C, Papadioti DC (2013) Component mode synthesis techniques for finite element model updating. Comput Struct 126:15–28
12. Zhu HP, Li JJ, Tian W et al. (2021) An enhanced substructure-based response sensitivity method for finite element model updating of large-scale structures. Mechan Syst Signal Proc 154(107359)

Quantifying Uncertainties in Model Updating Following Bayesian Approach Using a Parameter Space-Search Algorithm

Jiahua Yang and Yi Zheng

Abstract Model updating aims to provide accurate models to reveal possible structural damage information for structural health monitoring (SHM). Uncertainties always exist in model updating due to incomplete information in measurement and modeling. These uncertainties usually cause the problem of non-uniqueness, i.e., multiple equivalent models can fit the experimental data the same well. Locating all these equivalent models and including them for representing structural dynamics is a challenging task. This work employs a Bayesian probabilistic framework for model updating, so that the uncertainties can be quantified, and thus all of the multiple equivalent models can be considered naturally. A parameter space-search algorithm is proposed to systematically locate all the equivalent models. A transmission tower under laboratory conditions with limited modal parameters was used to valid the proposed method.

Keywords Model updating · Bayesian probabilistic framework · Parameter · Space-search algorithm

J. Yang
School of Civil Engineering and Architecture, Guangxi University, Nanning, Guangxi, China

National Engineering Research Center of High-Speed Railway Construction Technology, Changsha 410075, China

J. Yang
e-mail: cnjavayang@gxu.edu.cn

Y. Zheng (✉)
School of Civil Engineering and Architecture, Guangxi University, Nanning, Guangxi, China
e-mail: YiZheng@st.gxu.edu

G. Mei et al. (eds.), *Advanced Construction Technology and Research of Deep-Sea Tunnels*, Lecture Notes in Civil Engineering 490,
https://doi.org/10.1007/978-981-97-2417-8_8

1 Introduction

Model updating is an important research topic, because it is useful in downstream research of structural health monitoring. The updated models can be used to determine damage location and intensity of structures. Model updating has successfully assisted monitoring the fatigue, corrosion and earthquake effects of bridges, large-scale building structures and aerospace structures [1-3]. Therefore, A great deal of research has aimed at establishing efficient local and global model updating methods for structural health monitoring in the past four decades. Despite of numerous methods developed, technical challenges still remain and effective model updating methods for complex structures have not yet been established.

One classical idea of model updating is to match the model-predicted modal parameters with the experimental ones, i.e., the experimental natural frequencies and mode shapes identified using measured structural responses. Model updating is to solve the inverse problem of determining structural parameters given some modal data [4, 5]. The hypothesis is that the change in model parameters related to different structural parts causes the change in model-predicted modal parameters, so theoretically adjusting model parameters can make the model-predicted modal parameters match with the experimental ones, giving the updated model that can reflect actual structural behaviors. Most of the deterministic methods pinpoint one model, even though there may be other equivalent models. The problem is the lack of theoretical basis for considering all the equivalent models.

There are inherent difficulties in model updating of complex structures in practice. The solution of the inverse problem is uncertain and not unique due to incomplete information, e.g., measurement noise and modeling errors. Meanwhile, how to incorporate all the equivalent models to represent the actual structure is difficult. This paper follows the Bayesian probability framework for quantifying the uncertainties in model updating [6-10], so that multiple models can be considered with a theoretical basis. An improved parameter space-search algorithm [11, 12] is developed to locate all the equivalent models.

2 Method

2.1 Bayesian Probabilistic Framework

According to Bayes' theorem, the posterior probability density function (PDF) of the model parameters $\boldsymbol{\theta}$ given some measured data $\mathbf{D}$ can be expressed as follows:

$$p(\boldsymbol{\theta}|\mathbf{D}) = \frac{p(\boldsymbol{\theta})p(\mathbf{D}|\boldsymbol{\theta})}{p(\mathbf{D})} \tag{1}$$

Here, $p(\boldsymbol{\theta})$ is the prior PDF of model parameters, $p(\mathbf{D})$ is a normalizing constant, and $p(\mathbf{D}|\boldsymbol{\theta})$ is the likelihood function that need to be determined. When the prior PDF is considered as a uniform PDF, the posterior PDF can be rewritten as:

$$p(\boldsymbol{\theta}|\mathbf{D}) = cexp(-L(\boldsymbol{\theta})) \tag{2}$$

where c is constant and $L(\boldsymbol{\theta})$ is the negative log likelihood function.

$$L(\boldsymbol{\theta}) = -lnp(\mathbf{D}|\boldsymbol{\theta}) = N_d \ln\left(2\pi\sigma^2\right) + \frac{J_0(\boldsymbol{\theta})}{2\sigma^2} \tag{3}$$

where $J_0(\boldsymbol{\theta})$ is the error function between calculated and measured responses and can be expressed in the following formula:

$$J_0(\boldsymbol{\theta}) = \sum_{n=1}^{N_d} \left(\left(\frac{\omega_n(\boldsymbol{\theta}) - \hat{\omega}_n}{\hat{\omega}_n} \right)^2 + \left(1 - \left| \varphi_n^T(\boldsymbol{\theta}) \hat{\varphi}_n \right|^2 \right) \right) \tag{4}$$

where the ω_n is calculated frequency and $\hat{\omega}_n$ is measured frequency, similarly, the φ_n is calculated mode shape and $\hat{\varphi}_n$ is measured mode shape.

However, the posterior PDF of model parameters is usually unknown. The second-order Taylor series expansion is adopted to approximate the posterior PDF where the negative log likelihood function $L(\boldsymbol{\theta})$ can be rewritten as:

$$L(\boldsymbol{\theta}) \approx L\left(\hat{\theta}_i\right) + \frac{1}{2}\left(\boldsymbol{\theta} - \hat{\theta}_i\right)^T H\left(\hat{\theta}_i\right)\left(\boldsymbol{\theta} - \hat{\theta}_i\right) \tag{5}$$

where $\hat{\theta}_i$ is an optimal parameter of $\boldsymbol{\theta}$ such that the first derivation of $L(\boldsymbol{\theta})$ with respect to $\boldsymbol{\theta}$ is equal to 0 and omitted, and $\mathbf{H}\left(\hat{\theta}_i\right)$ is the Hessian matrix of $L(\boldsymbol{\theta})$ evaluated at $\hat{\theta}_i$.

Then, one Gaussian PDF can be used to approximate the posterior PDF centered at each optimum $\hat{\theta}_i$:

$$p(\boldsymbol{\theta}|D) \approx \sum_{i=1}^{N_d} \omega_i \mathcal{N}\left(\boldsymbol{\theta}; \hat{\theta}_i, \mathbf{H}^{-1}\left(\hat{\theta}_i\right)\right) \tag{6}$$

Here ω_i is the normalized weight of $\hat{\theta}_i$ that can be calculated as:

$$\omega_i = \frac{\omega_i'}{\sum \omega_i'}, \omega_i' = p\left(\hat{\theta}_i\right)\left|\mathbf{H}\left(\hat{\theta}_i\right)\right|^{\frac{1}{2}} \tag{7}$$

2.2 The Parameters Space-Search Algorithm

It is difficult to find the multiple optimums of $L(\boldsymbol{\theta})$ since when the known information for identification is limited, there is a series of structural models

(equivalent models) that can output the same modal parameters, i.e., natural frequency $\boldsymbol{\Phi}^1(\boldsymbol{\theta}) = \left[\omega_1(\boldsymbol{\theta}), \omega_2(\boldsymbol{\theta}), \omega_3(\boldsymbol{\theta}), \ldots, \omega_{N_d}(\boldsymbol{\theta})\right]$ and mode shape $\boldsymbol{\Phi}^2(\boldsymbol{\theta}) = \left[\varphi_1(\boldsymbol{\theta}), \varphi_2(\boldsymbol{\theta}), \varphi_3(\boldsymbol{\theta}), \ldots, \varphi_{N_d}(\boldsymbol{\theta})\right]$. In order to find those equivalent models $S(\boldsymbol{\theta})$ with different model parameters $\{\boldsymbol{\theta}_s : s = 1, 2, 3, \ldots, N_s\}$, the parameters space-search algorithm is adopted and its strategy is to search lower-dimensional manifolds in the parameter space, i.e., curves, that are subset of the parameter space of interest. More specifically, it minimizes $L(\boldsymbol{\theta})$ along different curves by generating a sequence of points. Defining $C_k\left(\boldsymbol{\theta}; \tilde{\theta}\right)$ that passes through an optimal point $\tilde{\theta}$ as a curve in the parameter space of interest, and the curve satisfies that all of the modal frequencies remain unchanged except the k^{th} modal frequency. By iteratively searching on these curves, minimization of $L(\boldsymbol{\theta})$ is achieved such that the target equivalent models $S(\boldsymbol{\theta})$ can be found: $S(\boldsymbol{\theta}) = C_1\left(\boldsymbol{\theta}; \tilde{\theta}\right) \cap C_2\left(\boldsymbol{\theta}; \tilde{\theta}\right), \ldots, C_{N_d}\left(\boldsymbol{\theta}; \tilde{\theta}\right) = \bigcap_{k=1}^{N_d} C_k\left(\boldsymbol{\theta}; \tilde{\theta}\right)$where $C_k\left(\boldsymbol{\theta}; \tilde{\theta}\right) = \left\{\boldsymbol{\theta} : \omega_r(\boldsymbol{\theta}) = \omega_r\left(\tilde{\theta}\right), r = 1, 2, \ldots, k-1, k+1, \ldots, N_d\right\}$;

Minimization along the current curve $C_k\left(\boldsymbol{\theta}; \tilde{\theta}\right)$ passing through $\tilde{\theta}$ is done by searching from the start point $\boldsymbol{\theta}^1 = \tilde{\theta}$. Given the current point $\boldsymbol{\theta}^i$, the next point $\boldsymbol{\theta}^{i+1}$ will be generated by the following steps.

$$\boldsymbol{\theta}^{i+1} = \boldsymbol{\theta}^i + \delta\boldsymbol{\theta}^i \tag{8}$$

where vector $\delta\boldsymbol{\theta}^i$ is calculated by following linear algebra system.

$$\nabla\omega\left(\boldsymbol{\theta}^i\right)\delta\boldsymbol{\theta}^i = \delta\boldsymbol{\omega}^i \tag{9}$$

where $\nabla\boldsymbol{\omega}\left(\boldsymbol{\theta}^i\right)$ is the first derivative of ω at $\boldsymbol{\theta}^i$; $\delta\boldsymbol{\omega}^i$ is also a vector and the k^{th} element of $\delta\boldsymbol{\omega}^i$ is calculated by Eq. (10), and other elements are calculated by Eq. (11).

$$\delta\omega_k^i = \gamma\alpha\omega_k\left(\tilde{\theta}\right) \tag{10}$$

$$\delta\omega_j^i = \omega_j\left(\tilde{\theta}\right) - \omega_j\left(\boldsymbol{\theta}^i\right);\ j = 1, \ldots, k-1, k+1, \ldots, N_d \tag{11}$$

where the γ is direction parameter that takes 1 or -1 to decide the iteration direction, and α is the fractional step. After that $\delta\boldsymbol{\theta}^i$ is calculated, the following condition need to be checked.

$$\left(\delta\boldsymbol{\theta}^i\right)^T\delta\boldsymbol{\theta}^{i-1} > 0 \tag{12}$$

This constraint helps avoid an undesired change in the iteration along curve C_k. And if the condition is not satisfied, then $\delta\boldsymbol{\theta}^i$ is set equal to $-\delta\boldsymbol{\theta}^i$ and the sign of γ is also changed. After $\delta\boldsymbol{\theta}^i$ satisfying Eq. (12), the candidate $\boldsymbol{\theta}^{i+1}$ is calculated by Eq. (8). Next, it is checked if $\boldsymbol{\theta}^{i+1}$ satisfies the constraints imposed by Eq. (13).

$$\left|\frac{\omega_j\left(\boldsymbol{\theta}^{i+1}\right) - \omega_j\left(\tilde{\theta}\right)}{\omega_j\left(\tilde{\theta}\right)}\right| < \varepsilon;\ j = 1, 2, \ldots k-1, k+1, \ldots N_d \tag{13}$$

where the ε is a tolerance. If Eq. (13) in not satisfied, which mean $\boldsymbol{\theta}^{i+1}$ is not close enough to the curve, set $\boldsymbol{\theta}^{i+1}$ to a new start point and do the internal iterations with the same procedure until the above condition is satisfied.

Following the curves, the released natural frequency $\omega_k(\boldsymbol{\theta})$ is checked for the following equation.

$$\left(\omega_j\left(\boldsymbol{\theta}^{i+1}\right) - \omega_k\left(\tilde{\theta}\right)\right)\left(\omega_j\left(\boldsymbol{\theta}^{i}\right) - \omega_k\left(\tilde{\theta}\right)\right) < 0,\ j = 1, \ldots, k-1, k+1, \ldots, N_d \tag{14}$$

When the Eq. (14) is satisfied, it indicates that there is a new point $\hat{\theta}^{i+1} \in S(\boldsymbol{\theta})$ lies between $\boldsymbol{\theta}^{i}$ and $\boldsymbol{\theta}^{i+1}$. The algorithm needs to search the curve between $\boldsymbol{\theta}^{i}$ and $\boldsymbol{\theta}^{i+1}$ with reduced steps until another point is found.

Ensure all the curves $C_k\left(\boldsymbol{\theta}; \tilde{\theta}\right), k = 1, \ldots, N_d$ are searched. For target set $S(\boldsymbol{\theta})$, all the points will be checked the condition:

$$\frac{\left|\varphi_j\left(\tilde{\theta}\right) - \varphi_j(\boldsymbol{\theta})\right|}{\left|\varphi_j\left(\tilde{\theta}\right)\right|} < \in;\ j = 1, 2, \ldots k-1, k+1, \ldots, N_d \tag{15}$$

If this condition satisfied, it indicates that the model at $\boldsymbol{\theta}$ has equivalent mode shapes and natural frequencies, so the point $\boldsymbol{\theta}$ belongs to the target set $S(\boldsymbol{\theta})$. Finally, all the output equivalent points are found.

3 Results and Discussion

A transmission tower model is used to validate the proposed method numerically. The structure is shown in Fig. 1 and the material information is shown in Table1. We treated each floor as a substructure such that in total 8 sub-structures with 8 independent stiffness parameters are used for parameterization in model updating.

Using measured natural frequencies and mode shapes of 5 modes of this tower as the experimental data for model updating. Then, model updating was conducted with the stiffness of the 8 sub-structures treated unknown. To conduct model updating, the parameter-space search algorithm started from an initial model parameters and finally located 7 equivalent sets of model parameters, i.e., input any set of these identified parameters to the finite element model of the transmission tower can produce the model-predicted modal parameters that can fit the experimental ones the same well. The error between the calculated frequencies from initial parameter and measured modal frequencies is shown in Table2. And the Fig. 2 comparing the calculated and experimental mode shapes. The results of the search algorithm by the searching that starts from one optimum are shown in Table 3**.**

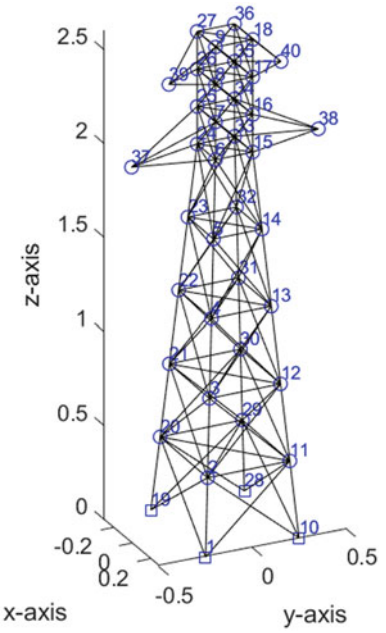

Fig. 1 Transmission tower model

Table 1 Material information

	$A(cm^2)$	$\rho(Kg/m^3)$	$E(Pa)$	υ
Columns	3.8e-5	7800	200e9	0.3
Cross-arms	3.2e-8	7800	200e9	0.3
Braces	3.6e-5	2700	69e9	0.3

Table 2 The error of frequencies between calculated from initial parameter and measured

Mode no	Measured frequencies (Hz)	Calculated frequencies (Hz)	Error (%)
1	35.31	32.97	6.63
2	40.60	38.28	5.72
3	68.39	62.77	8.22
4	120.90	123.87	–2.45
5	127.01	136.13	–7.19

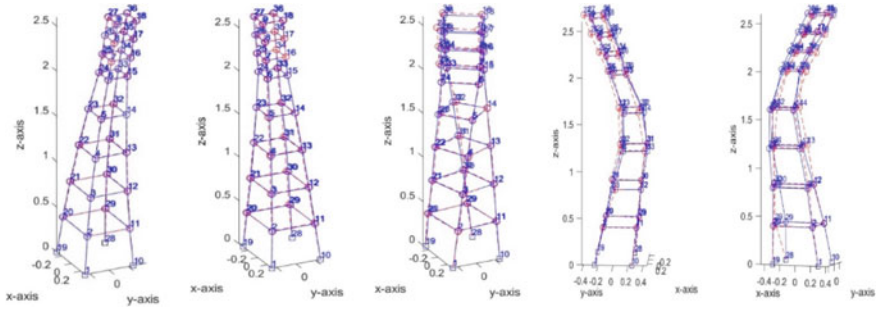

Fig. 2 The comparing between the initial parameter calculated and experimental mode shapes

Table 3 The search results of parameters space-search algorithm

Parameter no	θ_1	θ_2	θ_3	θ_4	θ_5	θ_6	θ_7	θ_8
Initial Parameter	0.4896	0.4964	0.4554	0.4865	0.4926	0.3829	0.4391	0.1907
1	0.4913	0.4886	0.4694	0.4709	0.4991	0.3688	0.3978	0.4608
2	0.4843	0.5112	0.4432	0.4871	0.4941	0.3637	0.4819	0.4631
3	0.4957	0.4725	0.4907	0.4554	0.5007	0.3629	0.5105	0.4039
4	0.4906	0.4904	0.4683	0.4701	0.4997	0.3670	0.3701	0.9153
5	0.4856	0.5073	0.4475	0.4845	0.4927	0.3713	0.5606	0.2134
6	0.4909	0.4894	0.4692	0.4699	0.4997	0.3672	0.3785	0.7241

4 Conclusions

This paper proposed an improved parameters space-search algorithm for Bayesian model updating, considering the non-uniqueness and uncertainty in model updating. The advantages of this algorithm are verified by the example of a transmission tower. The algorithm located all the output-equivalent models for the transmission tower, and all the equivalent models can be considered following the proposed Bayesian farmwork. Complex problems for full-scale structures caused by incomplete information can be solved using the proposed method.

Acknowledgements The financial support from Science and Technology Base and Talent Program of Guangxi (Grant No. GuikeAD21220031), Open Foundation of National Engineering Research Center of High-speed Railway Construction Technology (Grant No. HSR202108), and National Key Research and Development Program of China (Grant No. 2022YFC3005300) is greatly acknowledged.

References

1. Aktan AE, Farhey DN, Helmicki AJ, Brown DL, Hunt VJ, Lee KL, Levi A (1997) Structural identification for condition assessment: experimental arts. J Struct Eng 123(12):1674–1684
2. Girardi M, Padovani C, Pellegrini D, Robol L (2021) A finite element model updating method based on global optimization. Mech Syst Signal Process 152:107372
3. Yu TH, Johnson EA, Brewick PT, Christenson RE, Sato E (2023) Modeling and model updating of a full-scale experimental base-isolated building. Eng Struct 280:114216
4. Mottershead JE, Friswell MI (1993) Model updating in structural dynamics: a survey. J Sound Vib 167(2):347–375
5. Sanayei M, McClain JAS, Wadia-Fascetti S, Santini EM (1999) Parameter estimation incorporating modal data and boundary conditions. J Struct Eng 125(9):1048–1055
6. Nabiyan M, Ebrahimina H, Moavevi B, Papadimitriou C (2022) Adaptive Bayesian inference framework for joint model and noise identification. J Eng Mech 148(3):04021165
7. Beck JL, Katafygiotis, LS (1998) Updating models and their uncertainties. I: Bayesian statistical framework. J Eng Mechan 124(4):455–461
8. Beck JL, Au SK, Vanik MW (2001) Monitoring structural health using a probabilistic measure. Comp-Aided Civil Infrastruct Eng 16(1):1–11
9. Chen Y, Patelli E, Edwards B, Beer M (2023) A Bayesian augmented-learning framework for spectral uncertainty quantification of incomplete records of stochastic processes. Mech Syst Signal Process 200:110573
10. Fang C, Liu HJ, Lam HF, Adeagbo MO, Peng HY (2022) Practical model updating of the Ting Kau Bridge through the MCMC-based Bayesian algorithm utilizing measured modal parameters. Eng Struct 254:119839
11. Beck JL, Katafygiotis LS (1998) Updating models and their uncertainties. II: model identifiability. J Eng Mechan 124(4):463–467
12. Yang JH, Lam HF, An YH (2022) Development of a two-phase adaptive MCMC method for efficient Bayesian model updating of complex dynamic systems. Eng Struct 270:114836

Fatigue Response Analysis of Steel Pipe Piles with Super Length to Diameter Ratio Under Adverse Sea Conditions

Bo Zhang, Shuhui Lv, Jiaqi Wu, and Shiding Su

Abstract As an important component of seaport structures, steel pipe piles are subjected to cyclic loads over long periods of time in marine environments, especially when steel pipe piles are subjected to large bending moments, where the weld position is susceptible to fatigue damage. Based on an engineering example, a load-pile-soil triaxial fatigue analysis model was established to study the fatigue response rule of steel pipe piles under wave load, and the following conclusions were obtained: Regardless of whether the factor of weld is considered, the wave load with the wave height below 3.5 m will not cause fatigue damage to the steel pipe pile with the pile diameter of 1.2 m and wall thickness of 20 mm. The increased wave load will reinforce the effect of the weld on the steel pipe piles, resulting in a rapid reduction in the fatigue life of the steel pipe piles and a larger range of fatigue damage.

Keywords Steel pipe pile · Wave load · Weld · Fatigue response

B. Zhang · S. Lv (✉) · J. Wu · S. Su
CCCC Fourth Harbor Engineering Institute Co., Ltd., Guangzhou, China
e-mail: lshuhui@cccc4.com

Key Laboratory of Environment and Safety Technology of Transportation Infrastructure Engineering, CCCC, Ltd., Guangzhou, China

B. Zhang
e-mail: zbo7@cccc4.com

J. Wu
e-mail: wjiaqi2@cccc4.com

S. Su
e-mail: sshiding@cccc4.com

G. Mei et al. (eds.), *Advanced Construction Technology and Research of Deep-Sea Tunnels*, Lecture Notes in Civil Engineering 490,
https://doi.org/10.1007/978-981-97-2417-8_9

1 Introduction

Fatigue analysis is a key part of the quality and safety control of steel structure foundation [1–3]. At present, classification societies of various countries use the method of fatigue cumulative damage analysis based on S–N curve to evaluate Marine engineering structures, and carry out the fatigue check of Marine pile foundation [4, 5].

As an essential part of the seaport's structure, the steel pipe piles are subject to environmental loads and long working loads. As wave is a cyclic load with random changes in environmental loads, the internal stress of steel pipe piles will change under such alternating loads, and fatigue damage of steel pipe piles will be caused as the number of cycles increases [6, 7]. In particular, steel pipe piles are prone to fatigue failure when subjected to large bending moments, so it is crucial to study the fatigue response of steel pipe piles under wave load in combination with realistic parameters from field engineering.

2 Project Overview

A pier is located in deep offshore water without cover and 222 steel pipe piles made of Q345B are under construction. The construction area is characterized by frequent typhoons and strong monsoon winds. Refer to the "Steel Structure Design Standard" (GB50017-2017) [8], when the material is Q345B, the wall thickness is 16 mm < φ < 40 mm, the design value of yield stress at the mud surface of steel pipe pile is 335 MPa, and the minimum limit tensile strength is 470 MPa.

Under the reciprocal action of wind and wave, steel pipe piles are prone to induce alternating stresses in the local structure [9, 10]. The pile foundation constructed in a wharf has a total pile length of 56 m and a pile diameter of 1.2 m, which belongs to the steel pipe with super length to diameter ratio. The length of the pile below the designed low water level is 49 m. The wind load on the pile foundation is much smaller than the wave load, so only the effect of the wave load on the pile foundation is considered.

3 Natural Conditions and Calculation of Pile Foundation Load

Due to the uncertainty of waves, it is difficult to obtain the structural stress response under the action of random waves, and it is also difficult to obtain the maximum and minimum stress under the action of random waves. In this paper, conditions with greater risk of causing alternating loads are selected according to experience or trial calculation, and the maximum wave elements in the monsoon period and the

Table 1 Wave load on pile foundation

Period	Maximum total wave force Pmax (kN)	Maximum total bending force Mmax (kN · m)	The distance from the action point to the mud surface (m)
Monsoon period	51.2	742.4	14.5
Typhoon period	116.5	2170.9	18.6

Table 2 Soil layer material parameters

Soil layer	Thickness t (m)	Density ρ (g/cm3)	Compression modulus Es (MPa)	Internal friction angle Φ (°)	Cohesive force c (kPa)
Silt mix	2.9	0.6	4.866	17.3	3.5
Silty fine sand	1.3	0.25	12.0	24	18.8
Silty soil	7.2	0.74	3.580	2.1	16.2
Clay	4.1	0.92	10.379	4.0	61.2
Silty fine sand	1	0.25	12.0	24	18.8
Fully weathered granite	4	0.88	11.045	28.5	21.7
Heavily weathered granite	5	0.87	9.393	26.7	31.8

wave elements in the H4% typhoon period, which occur once every five years, are selected for calculation. Due to the large ratio of wave height to water depth, wave load has strong nonlinearity, so the wave load on pile foundation can be calculated using Stokes fifth-order wave theory and Morison equation [11], as shown in Table 1, and soil parameters are shown in Table 2.

4 Natural Conditions and Calculation of Pile Foundation Load

The contact properties of the pile-soil interface were defined in the form of Mohr–Coulomb friction function to simulate the shear transfer and relative displacement between pile-soil. The master–slave contact algorithm was adopted, and the pile with large stiffness was selected as the master surface and the soil surface as the slave surface. The finite element calculation model established between the steel pipe pile and soil was established by using 6-hedral and 8-node linear scaling integral solid elements. The load-pile-soil ternary fatigue analysis model combined with soil

constitutive model is established. In order to eliminate the influence of boundary on the calculation results, the test results show that the influence of boundary on the calculation results can be basically eliminated when the soil base is fully constrained, the lateral displacement is constrained, and the soil diameter of the straight pile is 10 times of the pile diameter.

In order to verify the reliability of the calculated results of the finite element model, two single pile foundations with displacement monitoring data were taken as an example to verify the reliability of the finite element model. As for the external force on the pile foundation, the wave load calculated by the wave parameters at that time is applied, and the pile foundation of the wharf without pile stabilization measures is simulated. The horizontal displacement of the pile foundation in the harsh Marine environment is shown in Fig. 1.

5 Numerical Simulation Analysis of Fatigue Response of Steel Pipe Pile

When fatigue analysis of steel pipe piles is performed with finite element software, the load type is loaded using the load ratio method, and the stress lifetime of a single S–N curve of a steel pipe pile material is corrected using Soderberg theory. Fatigue life analysis and safety factor analysis of steel pipe piles under 1×10^9 cyclic load revealed the fatigue damage law of steel pipe piles under wave load.

Under different sea conditions, the fatigue damage degree of steel pipe pile is different, especially the stress concentration is easy at the weld, which aggravates the fatigue damage. In addition, the pile foundation soil parameters also have some influence on the fatigue damage of steel pipe piles. In this paper, the fatigue analysis and calculation conditions of steel pipe piles are determined by comprehensively considering the sea condition, pile weld and soil layer parameters, as shown in Table 3.

The fatigue analysis of the pile foundations under wave load during monsoon and typhoon periods, without taking into account the welds, is shown in Figs. 2, 3. The analysis of the fatigue response of the pile foundations under wave load during monsoon and typhoon periods, taking into account the welds, is shown in Figs. 4, 5. The analysis of the fatigue response of the steel pipe piles at the maximum wave load during the typhoon is shown in Fig. 6, after taking into account the welds and increasing the riprap by 5m.

The finite element numerical analysis of fatigue response of steel pipe pile shows that there is no fatigue damage in the whole steel pipe pile during the monsoon period after 1×10^6 cyclic loading. When the influence of the weld is considered, the minimum safety factor is reduced from 2.44 to 2.16, which indicates that after the wave load increases to 2.16 times during the monsoon period, the steel pipe piles with welded seams will suffer fatigue failure within the range of 3m below the sand surface to 10m above the mud surface after 1×10^9 cycle load.

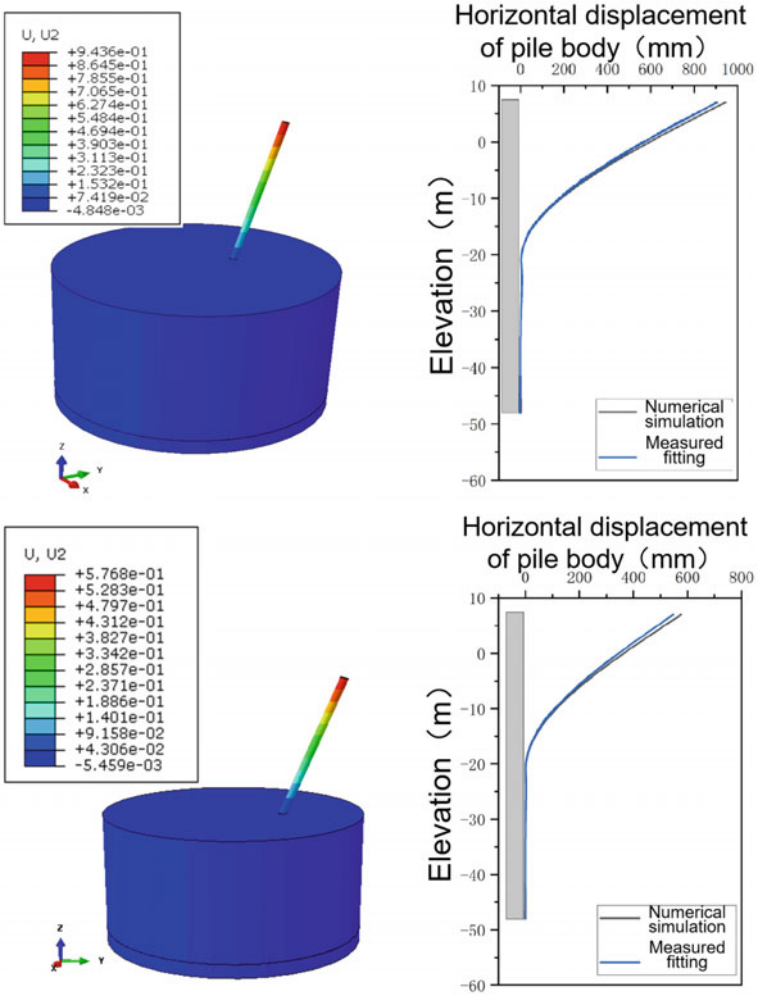

Fig. 1 Model verification

When the influence of weld is not considered, fatigue failure occurs within the range of 1.8 m below the mud surface to 3.2 m above the mud surface after 3×10^5 cyclic loading. When considering the influence of welding seam, fatigue damage occurs in the welding area after the steel pipe pile is subjected to 1.7105 cyclic load, and the minimum safety factor decreases from 0.81 to 0.72, indicating that after the wave load is reduced to 0.72 times during the typhoon period, after 1×10^9 cyclic loading, steel pipe piles with welded seams will suffer fatigue failure within the range of 1.7 m below the sand surface to 3.6 m above the sand surface, resulting in pile foundation instability failure.

Table 3 Fatigue analysis of steel pipe piles to calculate working conditions

Calculated working condition	Period	Weld position	Riprap thickness(m)
1	Monsoon period	Nil	Nil
2	Typhoon period	Nil	Nil
3	Monsoon period	The weld is 0.5 m on the surface of sand and mud	Nil
4	Typhoon period	The weld is 0.5 m on the surface of sand and mud	Nil
5	Typhoon period	The weld is 0.5 m on the riprap surface	Riprap 5 m

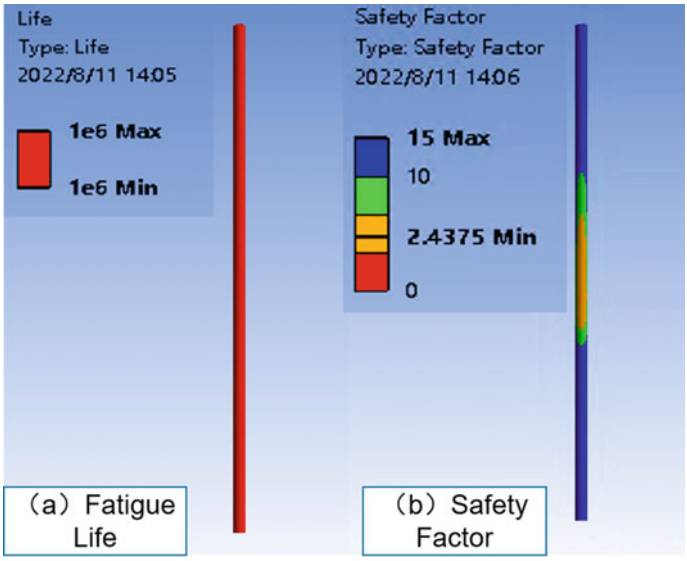

Fig. 2 Monsoon fatigue analysis diagram

The numerical simulation results of fatigue response analysis of steel pipe pile after 5 m thick ripolite is added above the original seabed mud surface show that, considering the influence of weld seam, steel pipe pile fatigue failure occurs in the welding area after 9.4×10^5 cyclic load during typhoon period, and the minimum safety factor is 0.99, which means that after the wave load is reduced to 0.99 times during typhoon period, the steel pipe pile fatigue failure occurs in the welding area. After 1×10^9 cyclic loading, fatigue failure of steel pipe piles with welded seams will occur within the range of 7.8 m below the riprap surface to 10.7 m above the riprap surface, resulting in pile foundation failure. The results show that the fatigue resistance of the pile foundation can be increased after the riprap stabilizing pile treatment. However, it is difficult to carry out underwater construction with 5m thick

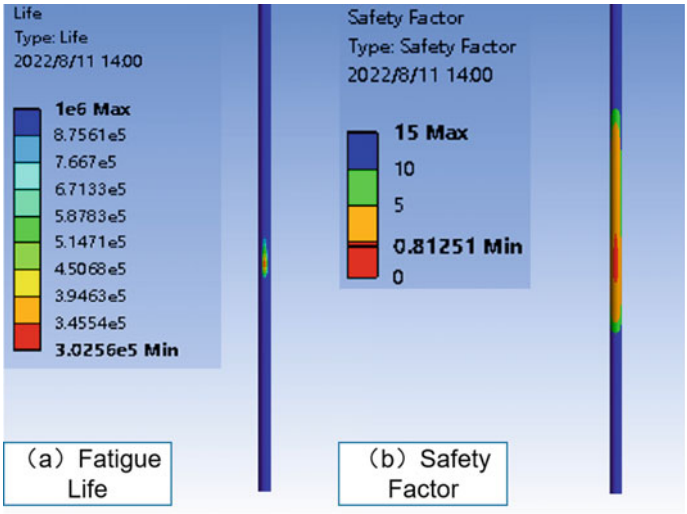

Fig. 3 Typhoon fatigue analysis diagram

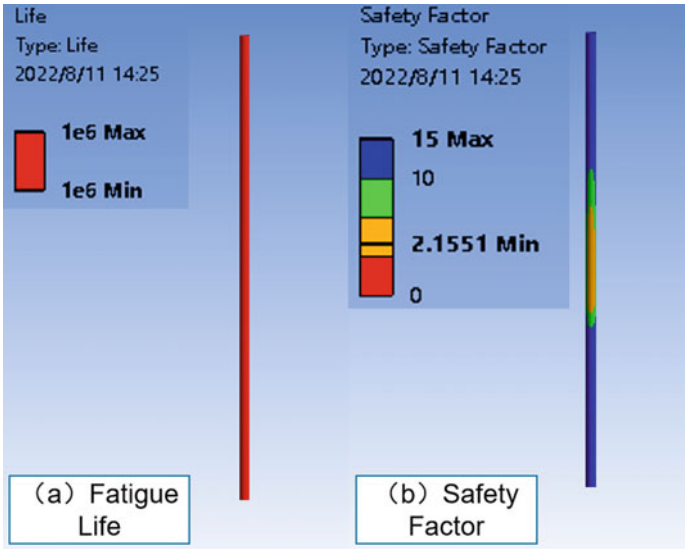

Fig. 4 Considering the fatigue analysis diagram of the weld seam during the monsoon period

underwater rubble. When conditions are poor, the quality of construction may not be guaranteed and it is difficult to form artificial foundation sections.

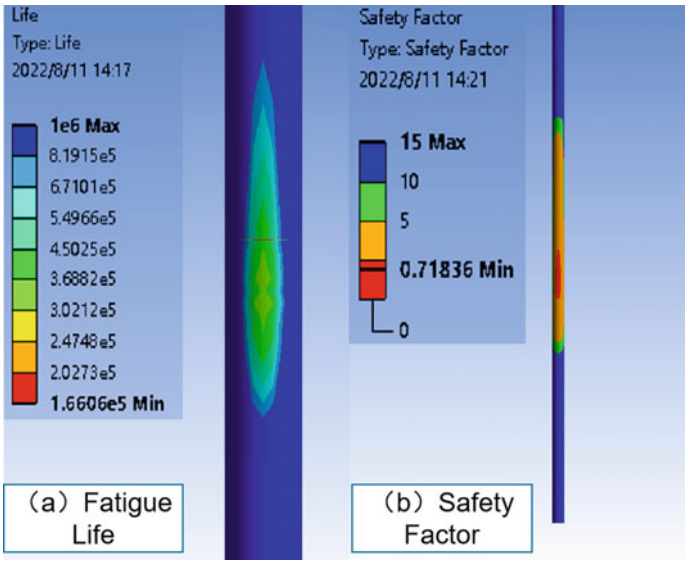

Fig. 5 Considering the fatigue analysis diagram of the weld during typhoon period

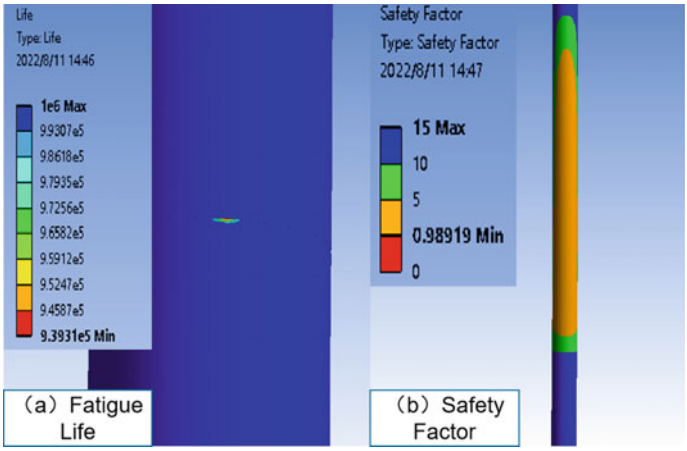

Fig. 6 Fatigue analysis diagram for typhoon period considering weld seam and adding 5m riprap

6 Conclusions

By establishing a load-pile-soil tridimensional fatigue analysis model and analyzing the effects of sea conditions, pile foundation welds and soil layer parameters on the fatigue damage of steel pipe piles, the following conclusions can be drawn:

(1) Regardless of whether the factor of weld is considered, the wave load of the wave height below 3.5 m during the monsoon period will not cause fatigue damage of steel pipe piles with pile diameter of 1.2 m and wall thickness of 20 mm.
(2) Considering the weld during typhoon will cause the fatigue life of steel pipe piles to decrease rapidly, the range of fatigue damage will increase, and the starting position of fatigue damage will shift to the weld.
(3) The fatigue life of steel pipe pile can be increased after the riprap stabilization pile treatment, the fatigue damage range is larger, and the fatigue resistance of steel pipe pile is improved as a whole.

References

1. Xiaoping H, Moan T, Weicheng C (2008) An engineering model of fatigue growth under variable amplitude loading[J]. Int J Fatigue 30(8):2–10
2. Madhavan Pillai TM, Prasad AM (2000) Fatigue reliability analysis in time domain for inspection strategy of fixed offshore structures[J]. Ocean Eng 27(2):167–186
3. Naess A, Pisano AA (1997) Frequency domain analysis of dynamic response of drag dominated offshore structures[J]. Appl Oeean Res19(5–6):251–262
4. Onoufriou T (1999) Reliability based inspection planning of offshore structures[J]. Mar Struct 12(7–8):521–539
5. Xu JH (2014) Dynamic response and fatigue analysis of jack up platform pile legs [D]. South China University of Technology. https://kns.cnki.net/KCMS/detail/detail.aspx?dbname=CMFD201501&filename=1014063792.nh
6. Zhao MC (2014) Fatigue analysis of offshore wind turbine pile foundation under multi load coupling [D]. Chongqing Jiaotong University. https://kns.cnki.net/KCMS/detail/detail.aspx?dbname=CMFD201501&filename=1014367400.nh
7. Liu HT (2007) Fatigue life prediction analysis of offshore jacket platforms under random wave loads [D]. Tianjin University. https://kns.cnki.net/KCMS/detail/detail.aspx?dbname=CMFD2009&filename=2008184493.nh
8. GB 50017–2003 Code for Design of Steel Structures [S]
9. DNV-RP-C203 (2004) Fatigue design of offshore steel structures[S]
10. ABS (2003) Guide for the fatigue assessment of offshore structures[S]
11. Zhang B (2021) Calculation of pile (column) wave force based on stokes fifth-order wave theory and specifications. In: The 4th International conference on information technologies and electrical engineering. Sanya, pp 466–478

Analysis of Expansion Stress Evolution of Concrete Erosion Products for Ocean Engineering

Haihan Huang, Shengdong Zhu, Xianhui You, and Qiming Song

Abstract With the deployment of China's "Maritime Power" strategy and the continuous development of ocean engineering, the safety and sustainability of concrete materials in ocean engineering need to be resolved urgently. In this paper, aiming at the concrete erosion caused by sulfate in marine environment, the evolution analysis of the expansion stress of the erosion products is carried out based on the principles of thermodynamics and crystallography. The results show that there is a liquid film between the ettringite and the pore wall during sulfate erosion in marine environment. The interfacial energy between reactants of different phases should not be neglected, and the liquid film thickness is negatively correlated with the expansion stress. The radial stress on concrete microstructure is composed of expansion stress, seawater pressure and interfacial energy between the concrete pore wall and the seawater. The trends of radial stresses in micro-voids and micro-cracks are basically similarly, both of which are negatively correlated with pore size and positively correlated with erosion time. In addition, the radial stresses in micro-cracks are generally greater than those in micro-voids. During the erosion process, the radial stress is positively correlated with the expansion extend of ettringite.

Keywords Marine environment · Concrete sulfate attack · Ettringite · Expansion stress

H. Huang · X. You · Q. Song
Power Generation Business Department, Fujian Yongfu Power Engineering Co., Ltd., Fuzhou, Fujian, China
e-mail: youxianhui@fjyongfu.com

Q. Song
e-mail: songqiming@fjyongfu.com

S. Zhu (✉)
Knowledge Management Department, Fujian Yongfu Power Engineering Co., Ltd., Fuzhou, Fujian, China
e-mail: zhushengdong@fjyongfu.com

School of Civil Engineering, Southeast University, Nanjing, China

G. Mei et al. (eds.), *Advanced Construction Technology and Research of Deep-Sea Tunnels*, Lecture Notes in Civil Engineering 490,
https://doi.org/10.1007/978-981-97-2417-8_10

1 Introduction

Recently, with the rapid development of the ocean engineering, the safety and sustainability of concrete materials in marine environment attract more and more attention. In a complex and harsh marine environment, concrete materials will be corroded by various harmful ions such as sulfate ions, chloride ions and magnesium ions [1, 2]. Sulfate attack will generate harmful products (e.g., ettringite), which would result in serious deterioration of the concrete due to the expansion and cracking [3, 4]. Subsequently, it would have a significant negative impact on safety and economy of structures and materials in ocean engineering. Unfortunately, the current state-of-the-art research on expansion stress of sulfate erosion products in marine environment is far from adequate.

The problem of sulfate attack in concrete material involves complex reactions between sulfate ions and cement hydration products. Considering the different sources of sulfate ions, sulfate attack can be divided into external sulfate attack (ESA) and internal sulfate attack (ISA) [5]. The sulphate attack of concrete in marine environment mentioned in this paper is an ESA problem. The expansion caused by the sulfate attack is mainly attributed to the formation of ettringite, but the mechanism causing the expansion is still controversial [6]. Regarding the expansion of ettringite, there are two mainstream theories [7]: the crystal growth theory and the water swelling theory. Richards and Helmuth [8] suggested that with the start of the erosion, the surface of expanded particles C4A3S and C3A would be covered by ettringite. When the thickness of ettringite exceeds a certain range, it will push other particles away and cause expansion. Kalousek [9] suggested that the expansion of ettringite is due to the positive relative ratio of hydrate volume to anhydrous volume, which means that the increase in anhydrous volume will generate expansion stress acting on the pore walls. Mehta [10] proposed a mechanism hypothesis for the expansion caused by ettringite. There are two types of ettringite, one is a strip crystal with a size of 10 ~ 100 μm, which is formed when the hydroxide concentration is low and usually does not expand. The other is small rod-shaped crystals with a size of 1 ~ 2 μm, which is formed when the hydroxide concentration is higher, and the damage is often caused by this kind of ettringite [11]. Power [8] showed that the adsorbed water on the surface of ettringite may trigger surface tension, making the surface stretched while the rest is in a compressed state. Therefore, the reason for the expansion of ettringite can be attributed to the reduction of van der Waals force, and the shrinkage caused by the surface tension of ettringite is compensated by the volume expand.

This paper focused on the evolution of radial stresses in concrete during sulfate erosion. A microstructural model of concrete has been developed to consider the interfacial energy between the liquid film and the different phase reactants during the expansion of ettringite. Moreover, the time-varying equations between ettringite content and expansion stress in the microstructure of concrete were established based on thermodynamic and crystallographic principles.

2 Expansion Stress of Erosion Products in Marine Environment

2.1 Theoretical Model of Sulfate Attack

Seawater contains a large amount of sulfate ions, which will continuously be able to corrode the concrete materials. The sulfate attack of the concrete materials can be regarded as the effect of a mixed system with multi-phase coexistence in marine environment. Interfacial energy exists between different phases of reactants and needs to be considered during erosion, whether it is between the ettringite and the seawater or between the seawater and the pore walls. The sulfate erosion reaction is characterized by the following three features: Firstly, although the ettringite and the pore wall are not in direct contact (the gaps between the two are fully filled with seawater, i.e., the liquid film), the pore wall will still be subjected to the expansion stress from the ettringite. Secondly, the pressures on different reactants are not the same (no longer a standard atmosphere). Thirdly, the pore wall is subject to a combination of ettringite expansion stress, seawater pressure and interfacial energy (not just expansion stress).

In marine environment, the liquid film always exists between the ettringite and pore wall during the erosion process. It is assumed that the liquid film is elastic, and the thickness becomes smaller and smaller as the ettringite grows. Figure 1 shows the diagram of liquid film.

The interfacial energy between the ettringite and the liquid film, between the liquid film and pore wall, and between the ettringite and pore wall are defined as γ_{CL}, γ_{WL} and γ_{CW}, respectively. Correns suggested that the interface energies can satisfy the following relation when the ettringite exerts expansion stress on the pore wall [13]:

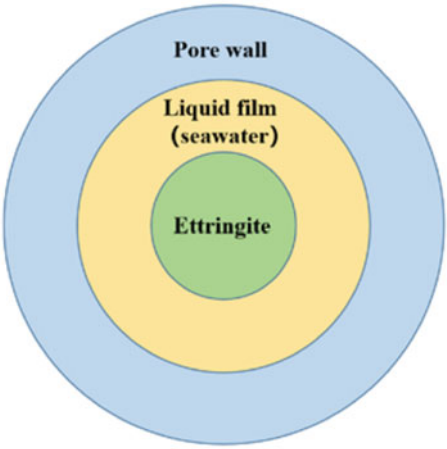

Fig. 1 The diagram of liquid film

$$\Delta\gamma = \gamma_{\mathrm{CW}} - \gamma_{\mathrm{CL}} - \gamma_{\mathrm{WL}} > 0 \tag{1}$$

When $\Delta\gamma > 0$, ettringite will exert expansion stress on the pore wall. Conversely, when $\Delta\gamma < 0$, ettringite could reduce the system energy by contacting the pore wall, meaning there is no crystallization pressure generated during the ettringite growth process.

The stress applied on the pore wall during the ettringite growth process is P_{d}, thickness of liquid film is δ, the relationship between P_{d} and δ is [14]:

$$P_{\mathrm{d}} = \mathrm{P}_0 \cdot e^{-\frac{\delta}{\lambda}} \tag{2}$$

where P_0 and λ are constants, P_0 represents the maximum expansion stress of ettringite, λ is the proportional coefficient. There is a negative correlation between the expansion stress and the liquid film thickness. The smaller the thickness of the liquid film is, the greater the expansion stress will be. Therefore, the liquid film between ettringite and pore wall should not be neglected.

2.2 *The Relation Between Interfacial Energy and Surface Curvature of Ettringite*

The relation between multi-component chemical potential, the system entropy, volume, temperature, and the pressure can be obtained by Gibbs–Duhem equation [15]:

$$\sum_{i=1}^{N} x_i \mathrm{d}\mu_i = V_{\mathrm{s}}\mathrm{d}P_{\mathrm{S}} - S_{\mathrm{S}}\mathrm{d}T \tag{3}$$

where μ_i is the chemical potential of component i, x_i is the mass fraction of component i. The reaction system for sulfate attack of concrete in the ocean consists of ettringite in the solid phase and seawater in the liquid phase. The mass concentration of ettringite is c_{e}, according to Gibbs–Duhem equation [16]:

$$(1 - c_{\mathrm{e}}) \cdot \mathrm{d}\mu_{\mathrm{L}} + c_{\mathrm{e}} \cdot \mathrm{d}\mu_{\mathrm{C}} = V_{\mathrm{S}}\mathrm{d}P_{\mathrm{S}} - S_{\mathrm{S}}\mathrm{d}T \tag{4}$$

where μ_L and μ_C are the chemical potentials of seawater and ettringite, respectively, and P_{S} is the pressure of seawater. The chemical potential is a function of temperature and pressure, so the chemical potential of ettringite can be expressed as, $\mu_{\mathrm{C}} = \mu_{\mathrm{C}}(T, P_{\mathrm{C}})$ and P_{C} is the pressure on the ettringite. According to the definition of Gibbs free energy and chemical potential, the differential of chemical potential of ettringite is expressed as:

$$\mathrm{d}\mu_{\mathrm{C}} = V_{\mathrm{C}} \cdot \mathrm{d}P_{\mathrm{C}} - S_{\mathrm{C}} \cdot \mathrm{d}T \tag{5}$$

since the seawater can be taken as a dilute solution, then the ions in seawater would obey Henry's law. The chemical potential of seawater is expressed as:

$$\mu_{\mathrm{L}} = \mu_{\mathrm{L}}^{\vartheta}(T, P_{\mathrm{S}}) + R_{\mathrm{g}}T\ln(1 - c_{\mathrm{e}}) \tag{6}$$

where $\mu_{\mathrm{L}}^{\vartheta}(T, P_{\mathrm{S}})$ represents the standard chemical potential of seawater under pressure P_{S}. Substituting the differential of the chemical potential of the ettringite and the seawater into Eq. (4), and assuming the reaction happens at a constant temperature, i.e., $\mathrm{d}T = 0$.

$$(1 - c_{\mathrm{e}})\left(V_{\mathrm{L}} \cdot \mathrm{d}P_{\mathrm{S}} - R_{\mathrm{g}}T \cdot \frac{1}{1 - c_{\mathrm{e}}}\mathrm{d}c_{\mathrm{e}}\right) + c_{\mathrm{e}} \cdot V_{\mathrm{C}} \cdot \mathrm{d}P_{\mathrm{C}} = V_{\mathrm{S}} \cdot \mathrm{d}P_{\mathrm{S}} \tag{7}$$

where P_{C} and P_{S} are the pressures of ettringite and seawater, respectively. According to the Laplace equation [17]:

$$P_{\mathrm{C}} = P_{\mathrm{S}} + \gamma_{\mathrm{CL}} \cdot \kappa_{\mathrm{CL}} \tag{8}$$

where γ_{CL} is the interfacial energy between the ettringite and liquid film, and κ_{CL} is the surface curvature of ettringite. The relation between the molar volume of seawater and the partial molar volume of the components can be expressed as [14]:

$$V_{\mathrm{S}} = (1 - c_{\mathrm{e}})\overline{V}_{\mathrm{L}} + c_{\mathrm{e}} \cdot \overline{V}_{\mathrm{C}} \tag{9}$$

substituting Eqs. (8) and (9) into Eq. (7), and that $\overline{V}_{\mathrm{L}} = V_{\mathrm{L}}$:

$$R_{\mathrm{g}}T \cdot \frac{1}{c_{\mathrm{e}}}\mathrm{d}c_{\mathrm{e}} = -\left(\overline{V}_{\mathrm{C}} - V_{\mathrm{C}}\right)\mathrm{d}P_{\mathrm{S}} + V_{\mathrm{C}} \cdot \mathrm{d}(\gamma_{\mathrm{CL}} \cdot \kappa_{\mathrm{CL}}) \tag{10}$$

The reaction is carried out under the condition of pressure change in this paper, i.e., PS ≠ P0. Integrating Eq. (10) and expressing the seawater pressure through Laplace equation, the relation between the surface curvature of ettringite and the interfacial energy can be obtained:

$$\gamma_{\mathrm{CL}} \cdot \kappa_{\mathrm{CL}} = \frac{R_{\mathrm{g}}T}{V_{\mathrm{C}}} \cdot \ln\left(\frac{c_{\mathrm{e}}}{c_{\mathrm{e0}}}\right) + \left(\frac{\overline{V}_{\mathrm{C}} - V_{\mathrm{C}}}{V_{\mathrm{C}}}\right) \cdot \gamma_{\mathrm{LV}} \cdot \kappa_{\mathrm{LV}} \tag{11}$$

2.3 Time-Varying Equation of Liquid Film Thickness

The seawater filled between the gap of the ettringite and the pore wall is defined as the liquid film. Assuming that the micro-voids is a shell with a certain thickness,

and the ettringite is a solid sphere in the micro-voids. The micro-voids and ettringite are concentric spheres (as shown in Fig. 1). The ettringite expands only in the radial direction while it always maintains a spherical shape during the expansion, so the center of the sphere does not move. The time-varying equation of liquid film thickness can be expressed as:

$$\delta(t) = r_{\mathrm{p}} - r_{\mathrm{ett}}(t) \tag{12}$$

where r_{p} and r_{ett}(t) are the radius of the micro-voids and the ettringite. The radius of ettringite is related to the volume, which is related to the content of ettringite. Therefore, the relation between liquid film thickness and ettringite content can be established:

$$\frac{4}{3}\pi r_{\mathrm{ett}}^{3}(t) = \frac{\Delta c_{\mathrm{e}}(t) \cdot V_{\mathrm{P}} \cdot M_{\mathrm{ett}}}{\rho_{\mathrm{ett}}} \tag{13}$$

where Δc_{e} is the variation of ettringite content within a certain time interval, V_{P} is the volume of micro-voids, M_{ett} and ρ_{ett} represent the molar mass and density of ettringite, respectively. Substituting the ettringite radius obtained from Eq. (13) into Eq. (12), the time-varying equation of liquid film thickness can be obtained as:

$$\delta(t) = r_{\mathrm{p}} - 0.0899 r_{\mathrm{p}} \cdot \sqrt[3]{\Delta c_{\mathrm{e}}(t)} \tag{14}$$

2.4 Expansion Stress of Corrosion Products

3 Microstructure Model of Concrete.

Based on the evolution process of concrete micro-voids [18], a concrete microstructure model was established. The microstructure model consists of micro-voids and micro-cracks. Assuming that the micro-voids and the micro-cracks are spheres and cylinders, respectively. Besides, the size of micro-cracks is much smaller than micro-voids. The micro-voids and micro-cracks model are shown in Fig. 2.

With the diffusion of seawater, ettringite would be formed in both micro-voids and micro-cracks. It is assumed that the pieces of ettringite formed in micro-voids and micro-cracks are spheres and cylinders, respectively.

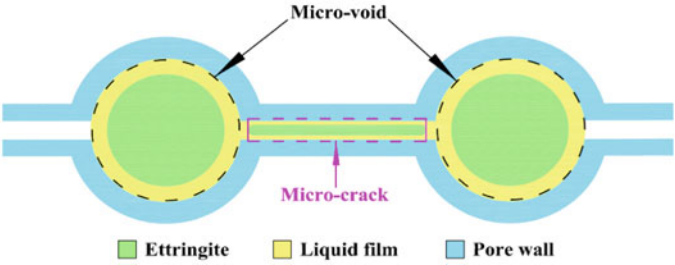

Fig. 2 The diagram of micro-voids and micro-cracks model

4 Expansion Stress Equation of Micro-Voids

By introducing the time variable, the time-varying equation of expansion stress and ettringite content is established. Figure 3 shows the diagram of micro-voids (r_p and r_e represent the radii of micro-voids and micro-cracks, respectively).

Take the point E_1 at the entrance of the micro-voids and any point S_1 inside micro-voids for example (as shown in Fig. 3). The curvature at the two points can be expressed as [14]:

$$\kappa_{CL}^{S_1}(t) = \frac{2}{r_p - \delta(t)} \tag{15}$$

$$\kappa_{CL}^{E_1}(t) = \frac{2}{r_e - \delta(t)} \tag{16}$$

Since the size of micro-voids is much smaller than that of micro-cracks, the curvature at point S_1 is approximately to zero. The pressures at E_1 and S_1 are as follows:

$$P_C(t) = P_S + \gamma_{CL} \cdot \kappa_{CL}^{E_1}(t) \tag{17}$$

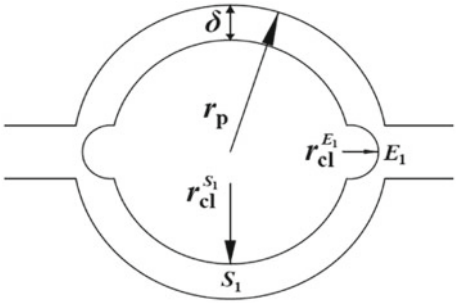

Fig. 3 The diagram of micro-voids [14]

$$P_{\mathrm{C}}(t) = P_{\mathrm{S}} + \gamma_{\mathrm{CL}} \cdot \kappa_{\mathrm{CL}}^{S_1}(t) + P_{\mathrm{d}}(t) \approx P_{\mathrm{S}} + P_{\mathrm{d}}(t) \tag{18}$$

where P_{d} is the expansion stress produced by ettringite, and PS is the pressure of the solution. From Eqs. (17) and (18), it can be seen that the surface of ettringite inside micro-voids (S_1) is affected by seawater pressure, interfacial energy of ettringite and liquid film, and the expansion stress of ettringite. At the entrance of micro-voids (E_1), ettringite grows freely without any expansion stress along the direction of the micro-cracks. According to the crystallographic theory, if the crystal is stable, the pressure on the surface of the crystal must be equal everywhere, otherwise the crystal will dissolve [14]. Therefore, the pressures at point S_1 and point E_1 are equal:

$$P_{\mathrm{d}}(t) = \gamma_{\mathrm{CL}} \cdot \kappa_{\mathrm{CL}}^{E_1}(t) \tag{19}$$

Equation (19) shows that the expansion stress generated by ettringite in the micro-voids has the same effect of the interfacial energy at the entrance of the micro-voids. According to the relationship between the surface curvature and interfacial energy of ettringite are as follows:

$$P_{\mathrm{d}}(t) = \frac{R_{\mathrm{g}}T}{V_{\mathrm{C}}} \cdot \ln\left[\frac{c_{\mathrm{e}}(t)}{c_{\mathrm{e0}}}\right] + \left(\frac{\overline{V}_{\mathrm{C}} - V_{\mathrm{C}}}{V_{\mathrm{C}}}\right) \cdot \gamma_{\mathrm{LV}} \cdot \kappa_{\mathrm{LV}} \tag{20}$$

Equation (20) is the time-varying equation between the expansion stress and the content of ettringite in the micro-voids.

5 Expansion Stress Equation of Micro-Cracks.

The diagram of micro-cracks in concrete is shown in Fig. 4.

Similarly, point E_2 at the entrance of the micro-cracks and any point S_2 in the micro-cracks are taken for analysis. In micro-cracks, the curvatures of these two points are expressed as follows [14]:

$$\kappa_{\mathrm{CL}}^{E_2}(t) = \frac{2}{r_{\mathrm{e}} - \delta(t)} \tag{21}$$

$$\kappa_{\mathrm{CL}}^{S_2}(t) = \frac{1}{r_{\mathrm{e}} - \delta(t)} \tag{22}$$

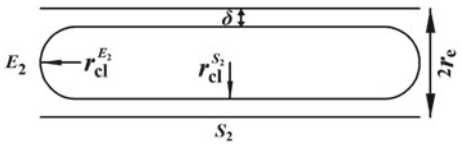

Fig. 4 The diagram of micro-cracks [14]

The pressures at S_2 and E_2 are shown in Eqs. (23)-(24):

$$P_{\mathrm{C}}(t) = P_{\mathrm{S}} + \gamma_{\mathrm{CL}} \cdot \kappa_{\mathrm{CL}}^{E_2}(t) \tag{23}$$

$$P_{\mathrm{C}}(t) = P_{\mathrm{S}} + \gamma_{\mathrm{CL}} \cdot \kappa_{\mathrm{CL}}^{S_2}(t) + P_{\mathrm{d}}(t) \tag{24}$$

According to the equal pressure at the S2 and E2, the relation between the surface curvature of ettringite and the interfacial energy is expressed as:

$$P_{\mathrm{d}}(t) = \frac{1}{2} \cdot \frac{R_{\mathrm{g}} T}{V_{\mathrm{C}}} \ln\left[\frac{c_{\mathrm{e}}(t)}{c_{\mathrm{e0}}}\right] + \left(\frac{\overline{V}_{\mathrm{C}} - V_{\mathrm{C}}}{V_{\mathrm{C}}}\right) \cdot \gamma_{\mathrm{LV}} \cdot \kappa_{\mathrm{LV}} \tag{25}$$

Equation (25) is the time-varying equation between the expansion stress and the content of ettringite in the micro-cracks.

6 Microstructural Stress of Concrete in Marine Environment

Considering the effect of the liquid film, the pore wall is affected by the expansion stress of the ettringite, seawater pressure and the interfacial energy between liquid film and pore wall. The radial stress on the pore wall is [14, 19]:

$$\sigma_r(t) = -P_{\mathrm{S}} - P_{\mathrm{d}}(t) + \gamma_{\mathrm{wL}} \cdot \kappa_{\mathrm{WL}} \tag{26}$$

where P_{S} is seawater pressure, P_{d}(t) is the expansion stress caused by ettringite, γ_{WL} is the interfacial energy between liquid film and pore wall, κ_{WL} represents the curvature of pore wall. $\kappa_{\mathrm{WL}} = 2/r_{\mathrm{p}}$ for micro-voids, and $\kappa_{\mathrm{WL}} = 1/r_{\mathrm{e}}$ for micro-cracks. In addition to radial stress, the pore wall is also subjected to tangential stress, which can be expressed as follows [19]:

$$\sigma_\theta(t) = \gamma_{\mathrm{LV}} \cdot \kappa_{\mathrm{LV}} + \gamma_{\mathrm{CL}}\left[\kappa_{\mathrm{CL}}^{E}(t) - \kappa_{\mathrm{CL}}^{S}(t)\right] - \gamma_{\mathrm{WL}} \cdot \kappa_{\mathrm{WL}} \tag{27}$$

When the porosity of concrete is not high, it can be approximated that $\sigma_\theta \approx -\sigma_{\mathrm{r}}$. For most concrete materials with good performance, whose porosities are generally not high, so the radial stress and the tangential stress are equal, and only the radial stresses are analyzed.

6.1 Stress Analysis of Pore Wall in Micro-Voids

Substitute the time-varying equation of ettringite expansion stress and the Laplace equation of seawater pressure into Eq. (26):

$$\sigma_r(t) = \frac{0.042}{r_p} - 10^5 - 3419060.828 \cdot \ln\frac{c_c(t)}{6.06} - \frac{0.1038}{r_p - 0.0899 r_p \cdot \sqrt[3]{\Delta c_e(t)}} \quad (28)$$

Equation (28) is the time-varying equation between the radial stress and the content of ettringite in micro-voids, and the unit is Pa. The radial stress of the pore wall in the micro-voids depends on the aperture of the micro-voids and the content of ettringite. Figure 5 shows the variation surface of the radial stress as a function of aperture and erosion time.

In Fig. 5, for the same erosion time, the radial stress decreases with the increase of the aperture. While the erosion time lasts, the radial stress will increase accordingly.

In Fig. 6a, the radial stress varies with aperture for different erosion times cases in a relatively consistent trend, which shows that the radial stress decreases with the increase of aperture. When aperture is larger than 100 nm, the radial stress tends to be stable. For the same aperture, the radial stresses with shorter erosion time are larger. After 20 weeks of erosion, the expansion stress tends to be stable, which probably due to the less ettringite content. For smaller apertures, the radial stresses are larger, with the increasement of the aperture, the radial stress increasing velocity changes mildly.

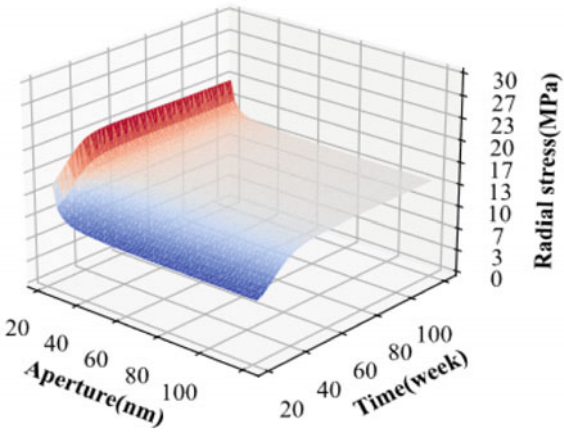

Fig. 5 Variation surface of radial stress with aperture and erosion time for micro-voids

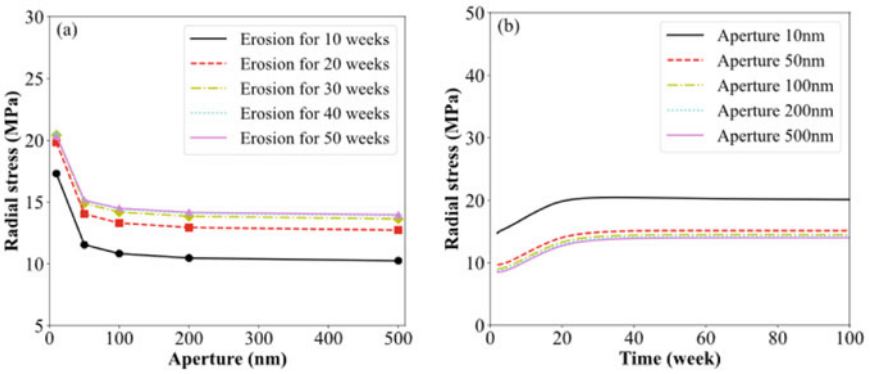

Fig. 6 The curve of radial stress with aperture and erosion time in micro-voids

6.2 *Stress Analysis of Pore Wall in Micro-Cracks*

Substituting the time-varying equation of expansion stress in micro-cracks into Eq. (26):

$$\sigma_r(t) = \frac{0.021}{r_e} - 10^5 - 1709530.414 \cdot \ln \frac{c_e(t)}{6.06} - \frac{0.0819}{r_e - 0.0899 r_e \cdot \sqrt[3]{\Delta c_e(t)}} \quad (29)$$

Equation (29) is the time-varying equation of the radial stress of micro-cracks and the content of ettringite. The radial stresses of the micro-cracks are affected by the content of ettringite and the aperture of micro-cracks. The variation of radial stresses in micro-cracks with the aperture and the content of ettringite is shown in Fig. 7.

It can be seen from Fig. 7 that the trends of the radial stress of micro-cracks and micro-voids are very similar. At the same moment, as the aperture increases, the radial stress on the pore wall also decreases. For smaller cracks, radial stresses tend

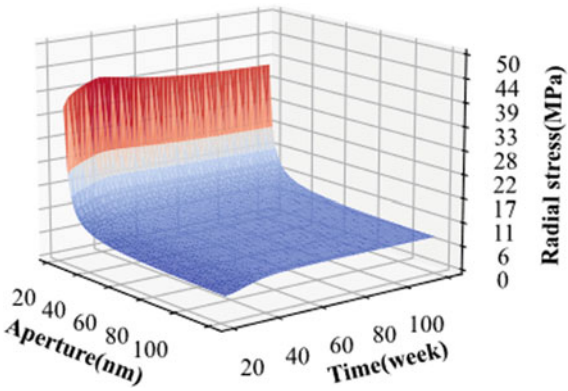

Fig. 7 Variation surface of radial stress with aperture and erosion time for micro-cracks

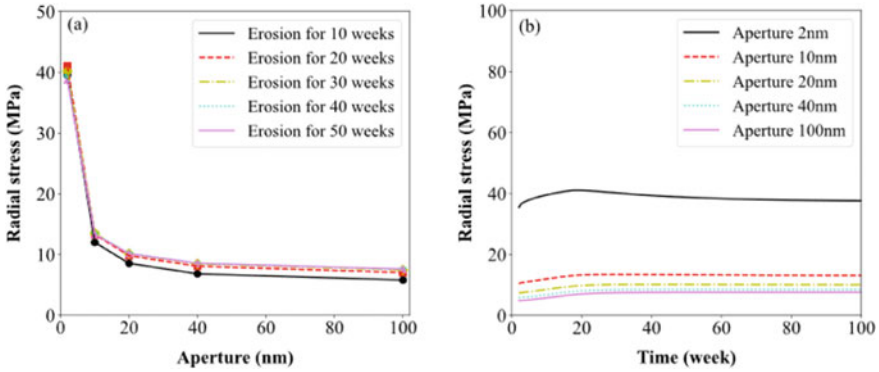

Fig. 8 The curve of radial stress with aperture and erosion time in micro-cracks

to be higher. As erosion time increases, the radial stress on pore wall will increases. Overall, the trends of radial stresses in micro-voids and micro-cracks are similar, but the radial stress in micro-cracks are greater than those in micro-voids.

In Fig. 8a, for the same micro-cracks, the increase of erosion time will cause a mild increasement of the radial stress. For the same erosion time, the radial stress on small cracks is much greater, and the radial stress tends to be stable while the aperture is greater than 20 nm. The radial stress is less sensitive to the extension of erosion time. Compared with the micro-void cases, radial stress in micro-cracks shows a more moderate trend. The maximum radial stresses in micro-cracks are almost twice those of micro-voids.

7 Conclusions

This paper carried out an analysis of the influences of ettringite content on expansion stress in concrete materials in ocean engineering based on thermodynamics and crystallographic theory. By establishing the concrete microstructure model, the time-varying equations of the expansion stress related to the content of ettringite in the micro-voids and micro-cracks were obtained analytically. The evolution analysis of the radial stress of the concrete microstructure was conducted, and the key conclusions are summarized as follows:

1 The sulfate attack process in concrete involves complicated interactions of heterogeneous reactants. There are interface energies between reactants of different phases, and the interaction between different phases in the erosion process cannot be ignored. From the generation phase of the ettringite to the destruction phase of the concrete microstructure, there is always a layer of liquid film between ettringite and pore wall. With the growth of ettringite, the thickness of the liquid film becomes smaller and the expansion stress increases.

2 The concrete microstructure model is composed of micro-voids and micro-cracks. With the diffusion of sulfate ions in micro-voids and micro-cracks, it will directly lead to the formation of ettringite. Moreover, it develops along the micro-cracks on the micro-voids.
3 The trends of radial stress in micro-voids and micro-cracks are similar. It is negatively correlated with aperture and positively correlated with erosion time, respectively. In addition, the radial stress in micro-cracks is greater than that in micro-voids. The radial stress is positively correlated with the expansion extend of ettringite.

Some preliminary research results in this paper provide reference for the subsequent determination of chemical damage variables and the establishment of concrete force-chemical coupling damage model. To understand the concrete erosion products thoroughly and improve of durability and reliability of the concrete materials in marine environment, further quantitative analyses are warranted.

Acknowledgements Support for this paper is provided by Fujian Yongfu Power Engineering Co., Ltd. The authors declare that there is no conflict of interest, and all authors made substantial contributions to the execution of the work.

References

1. Sun D, Cao Z, Huang C et al (2022) Degradation of concrete in marine environment under coupled chloride and sulfate attack: a numerical and experimental study. Case Stud Constr Mater 17:e01218
2. de Rincón OT, Sánchez M, Millano V et al (2007) Effect of the marine environment on reinforced concrete durability in Iberoamerican countries: DURACON project/CYTED. Corros Sci 49:2832–2843
3. Rajasekaran G (2000) Sulphate attack and ettringite formation in the lime and cement stabilized marine clays. Ocean Eng 32:1133–1159
4. Mehta PK (1983) Mechanism of sulfate attack on portland cement concrete—another look. Cem Concr Res 13:401–406
5. Cefis N, Comi C (2017) Chemo-mechanical modelling of the external sulfate attack in concrete. Cem Concr Res 93:57–70
6. Santhanam M, Cohen MD, Olek J (2002) Mechanism of sulfate attack: a fresh look: Part 1: summary of experimental results. Cem Concr Res 32:915–921
7. Cohen M, Theories of expansion in sulfoaluminate-type expansive cements: schools of thought. Cem Concr Res 13:809–818, 198
8. Richards CW, Helmuth RA (1975) Expansive cement concrete-micromechanical models for free and restrained expansion. In TRID, p 42
9. Kalousek G, Benton EJ (1970) Mechanism of seawater attack on cement pastes. Am Concrete Inst J Proc 67:187–192
10. Mehta PK (1973) Mechanism of expansion associated with ettringite formation. Cem Concr Res 3:1–6
11. Marchan J, Odler I, Skalny JP (2001) Sulfate attack on concrete. CRC Press, Florida
12. Powers TC (1965) The mechanism of frost action in concrete, In TRID, p 35
13. Correns CW (1949) Growth and dissolution of crystals under linear pressure. Discuss Faraday Soc 5:267–271

14. Scherer GW (2000) Stress from crystallization of salt in pores. In Proceedings of the 9th International Congress on Deterioration and Conservation of Stone, pp 187–194
15. Miller DG (1963) Duhem and the Gibbs-Duhem equation. J Chem Educ 40:648
16. Lyklema J (1991) Fundamentals of interface and colloid science. Volume I: Fundamentals. London: Academic Press
17. Defay R, Prigogine I, Bellemans A (1966) Surface tension and adsorption. Wiley, New Jersey
18. Li T, Wang SS (2019) Modeling diffusion coefficient of sulfate ion in concrete using probabilistic approach. Constr Build Mater 215:435–446
19. Scherer GW (1999) Crystallization in pores. Cem Concr Res 29:1347–1358

Tunnel Construction Inspection and Safety Assessment Method

Deep Migration Learning-Based Detection of Structural Diseases in Railway Tunnel Lining Structures

Zheng Wei, Jianqiang Zhou, Kexin Wang, and Xiaowen Hu

Abstract It is difficult to quickly and accurately detect defects such as voids, voids, and non compactness in the lining structure of formed railway tunnels. We have conducted in-depth research on the propagation law of ground penetrating radar electromagnetic waves in tunnel lining structures and intelligent detection methods based on deep learning. The finite difference method was applied to numerically simulate the propagation process of electromagnetic waves in tunnel lining structures with different diseases. B-scan radar images were obtained, and the characteristics of voids, voids, and non dense images were summarized. On this basis, a sample library composed of numerical simulation and real radar images was established, and a deep migration method for detecting railway tunnel lining structural defects was proposed. Automatically learning complex disease features and updating network model parameters overcomes the limitations of limited real disease sample sets for tunnel lining structures. The experimental results show that the network after transfer learning can accurately detect defect bodies in actual tunnel lining structures, verifying the effectiveness and feasibility of the proposed method.

Keywords Deep migration · Railway tunnel lining · Structure · Disease detection · Ground penetrating radar

Z. Wei · J. Zhou
Railway Engineering Quality Department, Transportation Engineering Management Center of Zhejiang Province, Hangzhou 310000, China

K. Wang
China Railway 12th Bureau Group 2nd Engineering Co. Ltd., Taiyuan Shanxi 030032, China

X. Hu (✉)
Jiangsu Dongyin Intelligent Engineering Technology Research Institute Co., Ltd, Nanjing 211100, China
e-mail: 489325694@qq.com

G. Mei et al. (eds.), *Advanced Construction Technology and Research of Deep-Sea Tunnels*, Lecture Notes in Civil Engineering 490,
https://doi.org/10.1007/978-981-97-2417-8_11

1 Introduction

The twenty-first century is the century of underground engineering development, China's underground engineering construction into the "blowout" development era, a large number of subway, high-speed rail tunnels are under construction or put into operation [1]. With the increasing number of tunnels put into operation in China's water conservancy, transportation, municipal and other fields, the structural damage of tunnel lining is aggravated year by year, which will threaten the safety of high-speed trains during operation [2]. Therefore, it is necessary to detect the quality of tunnel lining structural disease during tunnel construction or operation to guarantee the quality of tunnel construction.

At present, ground-penetrating radar is one of the main methods for detecting diseases in railway tunnel lining structure. Some scholars have carried out in-depth research on disease numerical simulation, disease identification and detection. Jiang [3] scholars summarized the electromagnetic wave propagation laws and image characteristics of different shapes of cavities in tunnel lining structures in different media, and analyzed the reasons why radar disease images are easy to misjudge. Gao [4] scholars numerically simulated a certain number of radar images of cavity and de hollowing damage, and proposed a recognition method integrating residual network and migration learning. The results show that the method can effectively identify the cavity and dehollowing damage of tunnel lining structure. Yang [5] scholars studied the application of convolutional neural network target detection in disease identification. Typical diseases of tunnel lining structure can be detected to a certain extent. Although the convolutional neural network can identify lining structure diseases, the method still has some limitations. Due to the private nature of real radar disease data of tunnel structures, there are not a large number of real radar image samples for deep learning model training. While the numerical simulation of lining structure disease radar images solves the problem of insufficient number of samples for training, the numerical simulation radar images differ from the real complex and diverse radar images, and there is the problem of poor generalisation ability of the training network in the detection of actual lining structure diseases, which leads to the missed identification or incorrect identification [6].

Aiming at the above problems, based on the foundation of previous research, this paper further investigates the deep migration learning technology for structural diseases of railway tunnel lining [7]. A deep migration intelligent detection method based on radar images is proposed. Among them, migration learning is a learning process that takes advantage of the similarity between numerically simulated radar images and real images, and applies the network weights learned from similar domains to real image detection, which improves the adaptability and generalisation ability of neural networks [8]. The research ideas of this paper are as follows: firstly, gprMax software was used to establish a numerical model of defective body of various geometries, simulate a variety of typical radar images approximating the actual working conditions, and construct a database consisting of numerical simulation and real radar images [9]. Then, a depth migration method for detecting structural

diseases of railway tunnel lining is proposed, and a self-learning and self-updating intelligent detection network model for depth migration of structural diseases of tunnel lining is established, which automatically learns the complex disease characteristics and updates the parameters of the network model. Finally, the effectiveness of the intelligent detection network model is further verified by building a concrete test bed [10]. The problem of poor generalisation ability of the training network in the detection of diseases such as dehollowing and cavities in actual lining structures is solved.

2 Numerical Modelling of Typical Diseases of Tunnel Lining Structures

2.1 Numerical Simulation of Ground-Penetrating Radar

In this paper, gprMax software is used to solve the system of Maxwell's equations for electromagnetic waves of ground-penetrating radar, as shown in Eq. (1). gprMax is a finite-difference time-domain method for solving the system of Maxwell's equations in 3D, which simulates the propagation process of electromagnetic waves in the tunnel lining structure [10]. The finite difference approach is used to discretize Maxwell's rotational equations in time and space.

$$\begin{aligned} \nabla \times E &= \frac{\partial B}{\partial \mathrm{t}} \\ \nabla \times H &= J + \frac{\partial D}{\partial \mathrm{t}} \\ \nabla \cdot B &= 0 \\ \nabla \cdot D &= \mathrm{p} \end{aligned} \tag{1}$$

where: E is the electric field strength (v/m). b is the magnetic flux density (Wb/m^2). h is the magnetic field strength (A/m). j is the current density (A/m^2). d is the electric flux density (c/m^2); ρ is the charge density (c/m^3).

In order to solve the differential Maxwell's system of equations stably, the spatial grid size and time step size need to satisfy the numerical stability condition, which satisfies Eq. (2). At the same time, in order to ensure the accuracy of the calculation results, the time step and spatial grid size also need to take into account the dispersion effect in the electromagnetic wave propagation process, satisfying Eq. (3). Therefore, in this paper, a perfectly matched layer with a finite thickness is used so that the radar incident wave passes through the interfaces without reflection and enters the PML layer.

$$\Delta t \leq \frac{1}{c\sqrt{\frac{1}{(\Delta x)^2}+\frac{1}{(\Delta y)^2}+\frac{1}{(\Delta z)^2}}} \tag{2}$$

$$\Delta x \leq \frac{\lambda}{12}, \Delta y \leq \frac{\lambda}{12}\Delta z \leq \frac{\lambda}{12}\Delta t \leq \frac{T}{12} \tag{3}$$

where: λ is the radar wavelength, which is related to the frequency and relative permittivity of the electromagnetic wave, as shown in Eq. (4).

$$\lambda = \frac{C}{f\sqrt{\varepsilon_r}} \tag{4}$$

where C is the speed of light, f is the excitation frequency, and ε_r is the relative permittivity.

2.2 Numerical Simulation and Discussion of Results

In this paper, for the common cavity, dehollowing and incompactness lesions in tunnel lining structure, the basic knowledge of ground-penetrating radar numerical simulation in the previous section is utilized to determine the parameters such as excitation type, excitation frequency, spatial and temporal step, and the number of layers of the PML unit required for the simulation calculation. And the numerical models of defective bodies with various geometries were established, and the corresponding ground-penetrating radar images were acquired. To this end, this paper formulates the numerical simulation steps for tunnel lining structural diseases, and the specific simulation parameters are shown in Table 1and Fig. 1.

Table 1 Simulation parameters

Parameter name	Numerical value	Parameter name	Numerical value
Air layer thickness/m	0.02	Mesh size/m	0.002
Antenna spacing/m	0.160/0.130/0.06	Pulse waveform	Gaussian
Center frequency/MHz	400/900/1500	Concrete dielectric constant	$\varepsilon_r = 6.4, \sigma = 0.01$
Time window/s	2.64×10^{-8}	Water dielectric constant	$\varepsilon_r = 81$
Air dielectric constant	$\varepsilon_r = 1, \sigma = 0$	Number of PML absorption layers	10

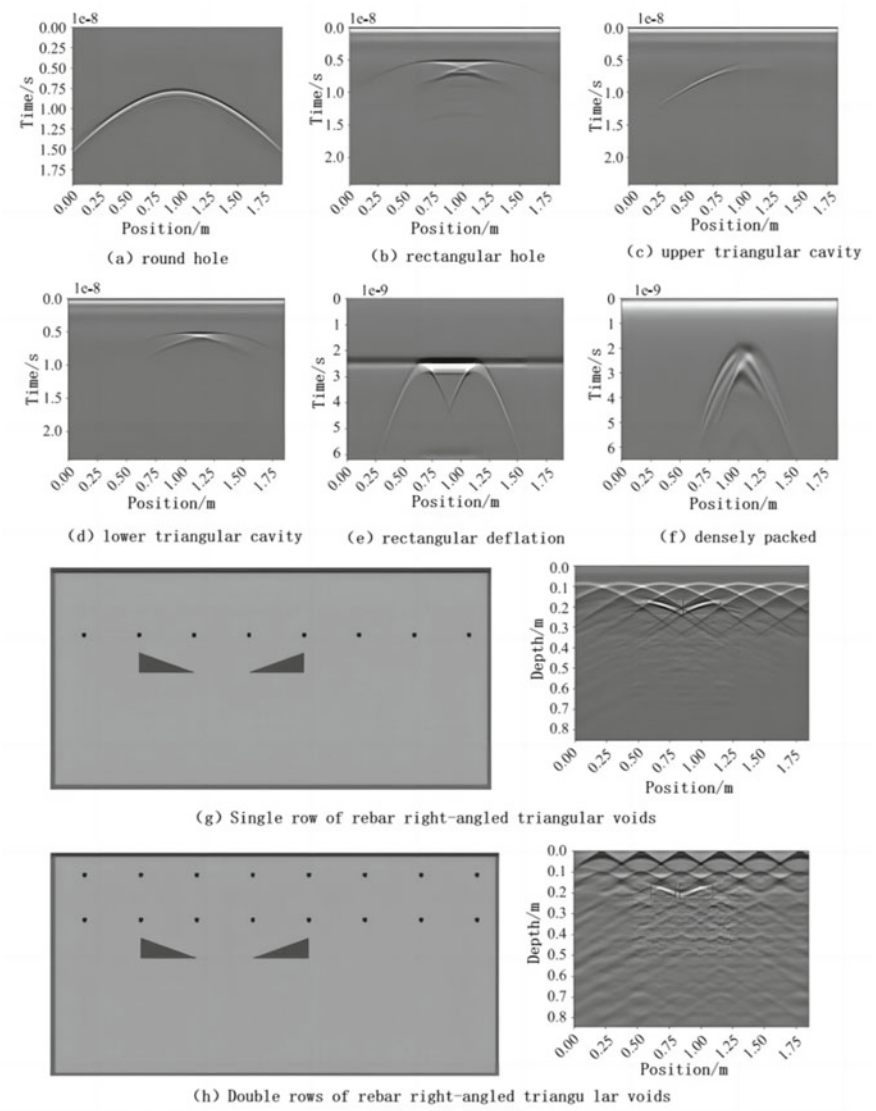

Fig. 1 Typical disease images

3 Intelligent Detection Network for Tunnel Lining Structural Diseases

3.1 Sample Bank

The essence of neural network detection of disease is to construct a neural network classification and logistic regressor, and train the network using a large number of tunnel lining structure disease samples so that its network can accurately detect the disease. Therefore, this paper establishes a sample library based on numerical simulation and real radar images. The finite difference method is applied to simulate the radar images of lining structure without disease and with disease, respectively. Among them, the radar images of hollow, incompact, and dehollowing diseases under different conditions, totaling 1500. At the same time, a number of radar images of tunnel lining structures provided by Zhengwan High Speed Railway, Zhangjihuai, and Qingdao Electric Wave Institute, totaling 149 images, were collated.

3.2 Deep Learning Based Target Detection Network

Currently, deep learning networks for target detection mainly include FasterR-CNN, MaskR-CNN, SSD, YOLOV3, etc. The main drawbacks of FasterR-CNN, MaskR-CNN, SSD are long training time, slow inference speed, and difficulty in detecting small targets. FasterR-CNN, MaskR-CNN, SSD, etc. The main disadvantages of FasterR-CNN, MaskR-CNN, and SSD are long training time, slow inference speed, and difficulty in detecting small targets. YOLOV3 uses a new network architecture, DarkNet53, for feature extraction, and fuses three different sizes of feature maps to predict the bounding box of the target, which realizes the fusion of features at different scales, and enhances the performance of detecting multi-scale small targets. Net53 feature extraction network, the different scaling feature fusion network, and the output composed of convolution. The loss function designed in the model consists of the center coordinate and width-height coordinate error of the target bounding box, the confidence error of the presence or absence of the target in the bounding box, and the classification error.

Aiming at the difficulty of obtaining deep neural networks with generalization due to the small number of real diseases. In this paper, a YOLOV3 network detection idea based on migration learning is proposed to migrate the shared parameters learned from numerical simulation data to the real dataset to further improve the accuracy of disease detection. The YOLOV3 network with migration learning is applied to detect abnormal radar images and identify the corresponding locations. The main ideas for the construction of the detection network structure are: first, the width and height dimensions of the image are scaled to 416, i.e., the shape of the input image to the target detection network is $416 \times 416 \times 3$. Second, the input image is augmented with data enhancement methods such as scaling, translation transformation, flipping,

and color transformation. Also the image target frame is changed accordingly. Then, the numerical simulation images are randomly divided into training and testing sets to train the YOLOV3 network according to the ratio of 7:3 to obtain the weights of the simulation network model. Finally, based on the model parameter sharing and knowledge migration method, the target detection network is trained several times based on real radar image data.

In this study, Adam is chosen as the model optimization strategy, which is a more advanced version of stochastic gradient descent. In this experiment, the starting learning rate of the model is 10–4 and 10–6, respectively, and the dynamic reduction strategy is applied to adjust the learning rate of the training process. That is, after 10 iterations of the model, when the loss curve of the validation set does not decrease, the value of the learning rate will be reduced to the original learning rate of 0.1 after the training. At the same time, this paper adopts the early stopping method to prevent the model generalization performance from deteriorating during the training process and avoid overfitting of the deep learning network. In addition, this paper sets the confidence threshold to 0.5, the intersection ratio of the target bounding box to 0.5, and the number of images for batch training to 8.

In this paper, direct, different migration learning strategies (as shown in Table 2) were used to train YOLOV3 network in real radar image data, and the model convergence speed curve was obtained, as shown in Fig. 2. Figure 2 shows that: the number of iterations required to train YOLOV3 network directly, the loss value is greater than the three kinds of migration learning strategy, thus proving the effectiveness of migration learning strategy in intelligent detection. At the same time, the comprehensive consideration of the number of iterations and loss curve of the kind of migration strategy, this paper adopts the network model of the migration learning strategy two for the disease detection of tunnel lining structure.

Table 2 Transfer learning strategy

Categories	Step 1	Step 2	Step 3
Strategy 1	Train the network output layer and freeze the rest of the layers	Continue training the network feature fusion layer with the output layer and freeze the remaining layers	/
Strategy 2	Train the network feature fusion layer with the output layer and freeze the rest of the layers	Train the entire network layer	/
Strategy 3	Train the network output layer and freeze the rest of the layers	Continue training the network feature fusion layer with the output layer and freeze the rest of the network	Train the whole network

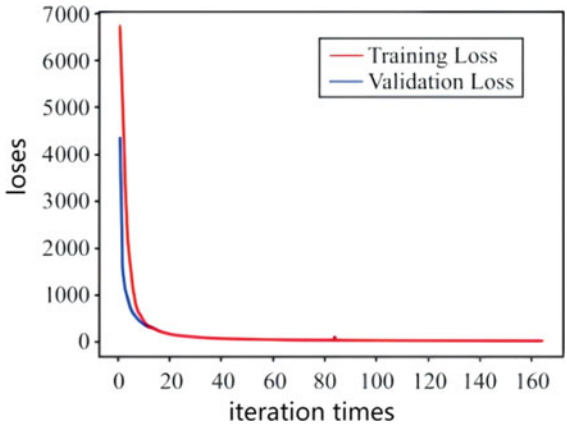

Fig. 2 Convergence curve

3.3 Analysis of the Test Results of the Test Set

Figure 3 shows the P-R curve of the migration network model in the test set by applying the recall and accuracy assessment. Where, AP is the area of the P-R curve, which indicates the accuracy of detection. The accuracy of the network is 91.15%, which indicates that the network model successfully migrates from the source domain to the target domain, and the migration effect is obvious without negative migration.

Figure 4 shows the detection results of the numerical simulation radar image, which can detect circular voids, rectangular voids, upper triangular voids, lower triangular voids, rectangular dehollowing, and incompactness, with a confidence level of 0.99, 0.87, 0.88, 0.79, 0.87, and 0.93. Figure 4 shows the detection results of the real radar image, which can detect rectangular voids, triangular voids, rectangular dehollowing, and incompactness, with a confidence level of 0.99, 0.87, 0.88, 0.79, 0.87,

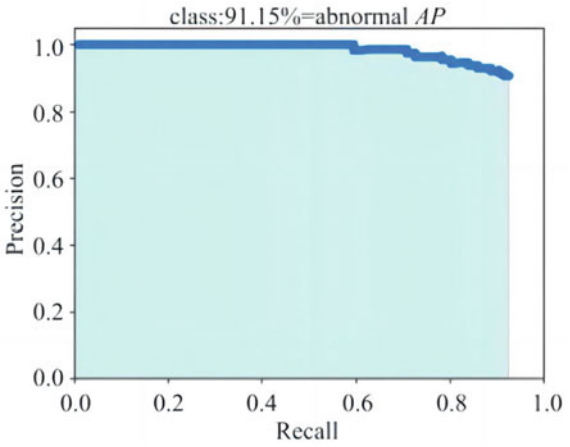

Fig. 3 Test set precision versus recall curves

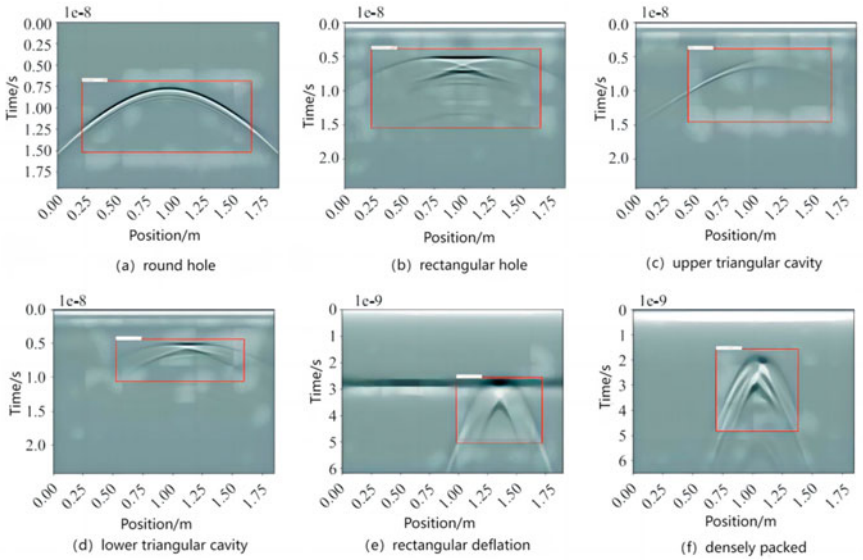

Fig. 4 Numerical radar image detection results

and 0.93 respectively. Their confidence levels are 0.87, 0.62, 0.98, 0.97,0.90, 0.53. The results show that the combination of YOLOV3 network and transfer learning can effectively detect various diseases in different shapes of tunnel lining structures.

4 Lining Structure Test Bed Validation

In order to further test the effect of the intelligent detection network in this paper, the establishment of a defect-containing tunnel concrete test bed, length, width and height of 5 × 1.4 × 1 m, the construction of the process parameters and the actual tunnel to maintain consistency. The test bench installation location for the casting benchmark, in turn, 4 layers of casting.

After 2 months of maintenance of the test bed, using Qingdao Institute of radio waves 900 MHz ground-penetrating radar antenna testing test bed, the collection of measuring lines for 5. Using the range wheel mode, sampling time window of 20 ns, the number of sampling points is 512, the acquisition speed is 128, the data acquisition process is filtered. Data processing using radar data processing software, processing steps include correction of zero bias, amplitude compensation, adjust the zero point, digital filtering, sliding average, signal gain. Analyzing the ground-penetrating radar images of 5 lines, we can see that the 900 MHz ground-penetrating radar antenna can only detect the defective body at a depth of 0.25–0.3 m (radar image shown in Fig. 5), and fail to detect the defective body at 0.425, 0.78 m, which is mainly due to the fact that there is a small amount of water in the internal environment of the test

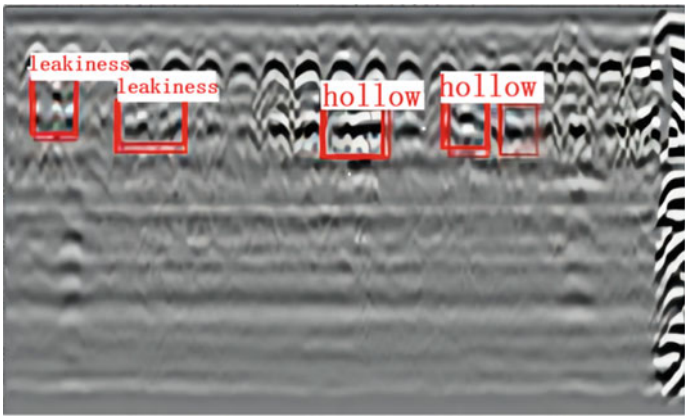

Fig. 5 Image detection results

bench, which greatly attenuates the energy of the electromagnetic wave. In order to verify the effect of this paper's intelligent detection network, the application of the test bench four line of ground-penetrating radar images to verify the detection results in Fig. 5. From Fig. 5, it can be seen that the application of this paper's intelligent detection network detected five defects in the test bench four line of the test bench, and the test bench of the actual location of the defects, the number of coincides with the detection of the five lesions of the confidence level of 0.58, 0.53, 0.76, 0.41, 0.5, 0.5, 0.5 and 0.5, respectively. 5.

5 Conclusions

(1) This paper numerically simulates the propagation law of electromagnetic wave in tunnel lining structure under a variety of working conditions, and summarizes the characteristics of the radar image of hollow, dehollowing, incompact and other diseases. The simulated ground-penetrating radar image database is established, which lays the foundation for the application of ground-penetrating radar in actual lining detection.

(2) At present, this paper in the ground-penetrating radar image anomaly detection to do some research work, to a certain extent to identify the tunnel lining structure whether there is a disease and the location, but cannot distinguish between specific types of disease (cavity, dehollowing, not compact). For this reason, we continue to collect data at the tunnel site to further enrich the radar data of the lining structure with cavity, dehollowing and incompactness. At the same time, on the basis of this model, in-depth study of more refined multi-classification intelligent detection model, to solve the problem of target detection of small sample industrial data.

References

1. Xin L, Shudong W, Yuancun M (2020) Exploration of comprehensive detection methods for disaster caused diseases in railway tunnel lining [J]. High Speed Railway Technol 11(06):74–79
2. Xiyun W (2019) Research on disease investigation and treatment technology of heavy haul railway tunnels [J]. Build Struct 49(S2):988–994
3. Yongqiang J, Jing G, He Y et al (2023) Design and application research on the apparent detection system of tunnel intelligent detection vehicle [J]. Tunnel Constr (Chinese and English) 43(S1):576–590
4. Siren T, Dahlström M, Cronvall T (2023) High-speed train induced vibration measurements in fresh tunnel shotcrete layer[J]. IOP Conf Ser Earth Environ Sci 1124(1):256–268
5. Jianwei Y (2022) Safety calculation method and remediation technical plan for tunnel lining with block falling defects [J]. Railway Const 62(06):116–119
6. Liu Y, Chai X, Lin L, et al (2021) Research and application of railroad tunnel lining disease vectorization based on DXF file[J]. Railway Const 61(12):138–142
7. Martino MR,Giulia M, Salvatore A, et al (2023) Convolutional networks and transformers for intelligent road tunnel investigations[J]. Comp Struct 275
8. Yajun J, Shigui L, Rui Z et al (2022) Research on the causes and classification of diseases in the lining drainage system of operating traffic tunnels [J]. Railway Stand Des 66(03):124–129
9. Meng Q, He C, Li D, et al (2020) Safety analysis of new tunnels with small clearances for three-dimensional intersections based on health inspection of existing tunnels[J]. Value Eng 39(19):165–171
10. Cardellino E, Silva DD, Bilotta A, et al (2023) Fire modelling and structural assessment of concrete linings of underground structures[J]. ce/papers 6(5):205–212

Discrete Element Simulation Study of Multi-Layered Reinforced Geotextile Treatment of Karst Collapse

Di Wu, Jian Wu, Lingyan Deng, and Jianjian Wu

Abstract The use of multi-layered reinforced geotextile to treat karst collapse can reduce the buried range of geotextiles, so as to achieve the purpose of saving project costs. In order to investigate the impact of varying layers of geotextile on the mitigation of collapses in karst regions, this study establishes a Discrete Element Particle Flow Code 2D (PFC2D) model for geotextile treatment with different layer configurations. The analysis in this research encompasses several critical aspects, including the top vertical settlement of soil, variations in tensile forces experienced by the first layer (bottom layer) of geotextile with changes in the position of the settlement plate, and the distribution of tensile forces across different horizontal positions within each layer of geotextile. The findings indicate the following trends: as the number of reinforced geotextile layers increases, there is an overall reduction in the vertical settlement of the soil. When employing multiple layers of geotextile, the first layer (bottom layer) experiences the highest tensile forces. Furthermore, as the number of reinforced geotextile layers increases, there is a general decrease in the tensile forces acting on the first layer (bottom layer).

Keywords Karst collapse · Multi-layered reinforced geotextile · PFC2D

1 Introduction

In karst regions, road surface collapses frequently occur during engineering construction, often characterized by their hidden nature and sudden occurrence, posing significant risks to both human life and property safety [1, 2]. To address this issue, Huckert et al. [3] conducted full-scale model tests on the deformation behavior of

D. Wu · J. Wu · J. Wu
School of Architecture and Transportation Engineering, Guilin University of Electronic Technology, Guilin, China

L. Deng (✉)
Jiangxi Provincial Highway Scientific Research and Design Institute Co, LTD, Nanchang, China
e-mail: 63532418@qq.com

G. Mei et al. (eds.), *Advanced Construction Technology and Research of Deep-Sea Tunnels*, Lecture Notes in Civil Engineering 490,
https://doi.org/10.1007/978-981-97-2417-8_12

reinforced materials and subgrade surfaces under circular collapse. Wittekoek et al. [4] conducted a two-dimensional numerical study, identifying the length and quantity of geogrid anchor rods as critical factors in determining load-bearing capacity. From the analysis, When single-layer geotextile reinforcement treatment of karst collapse. If the buried width of the reinforcement material is too wide, it will cause the excavation surface of the soil to become larger, thereby increasing the engineering cost, and if the buried width is insufficient, anchoring length of the tendon will be insufficient, the stability of the project will be affected. In order to save the project cost, improve the management effect of tendons, and when the highway grade is low, multi-layer reinforced bedding technology can be used to deal with [5]. He et al. [6] examined the loads and deformation experienced by single-layer and multi-layer geogrid-reinforced cushion layers during collapse processes through large-scale indoor model testing. They further analyzed the distribution patterns of subgrade loads across various reinforcement layers and the deformation characteristics of cushion layers. In this study, three numerical models were employed to investigate the impact of different numbers of reinforced geotextile layers on top vertical settlement of the soil, and geotextile tensile force.

2 Methods and Materials

2.1 Discrete Element Model

To investigate the influence of different numbers of reinforced geotextile layers on the management of collapses in karst areas, the subsidence treatment project of the Xihuan Road embankment in Hechi City, Guangxi, China, was taken as a case study. A discrete element numerical model was established for this purpose. Figure 1 illustrates the numerical model of the discrete element, measuring 15 m in length and 10 m in height. The subsidence area includes an active baseplate with a width (B) of 3 m, flanked by stable areas on both sides, each with a width of 6 m. The center of the subsidence area's bottom plate is designated as the coordinate origin (0,0). The model boundary employs wall elements integrated within the Particle Flow Code (PFC) software to simulate the underlying bedrock.

2.2 Discrete Element Simulation Material

In this study, the simulated soil is composed of sandy material, and therefore, a linear contact model is employed for particle interactions. To ensure computational efficiency, the particle radii are appropriately scaled up, and the soil samples are generated using a stepwise expansion method. The model encompasses approximately 24,000 soil particles with particle sizes ranging from 3 to 5 cm. Microscopic

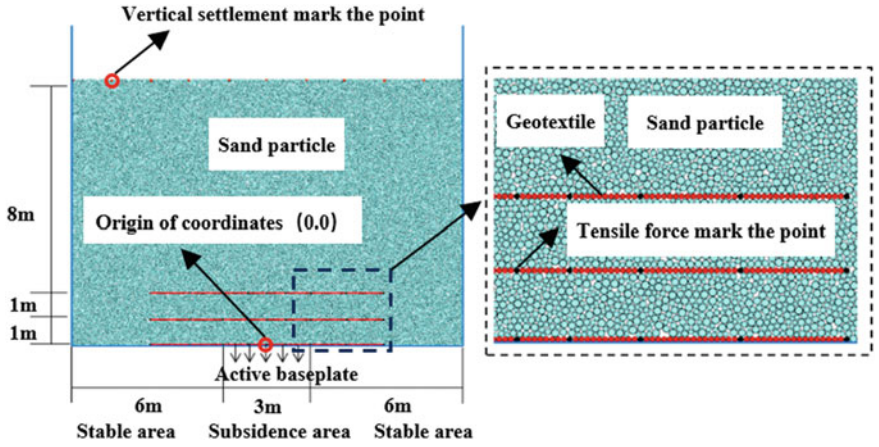

Fig. 1 Numerical model

parameters for discrete elements corresponding to different particle types are detailed in Table 1.

To confirm the correspondence of the microscopic parameters of the soil used in this study to the macroscopic parameters, flexible biaxial tests were conducted under three different confining pressures: 50, 150, and 300 kPa. When the model's friction coefficient was set to 0.2, our calculations yielded an internal friction angle of 14.48° and cohesion of 0 kPa. Figure 2 illustrates the deviational stress–strain curves and schematic representations of the flexible biaxial tests conducted under these three confining pressures, with an interparticle friction coefficient of 0.2.

In this study, the simulation experiments were conducted using a geotextile material that is relatively soft but capable of withstanding a certain shear strength and tensile strength. The selected geotextile particles were modeled using a linear contact bonding model. To ensure computational accuracy and the precise calculation of inter-particle forces within the geotextile, the dimensions of the geotextile particles were appropriately scaled up. A particle generation method based on specific rules was employed to create the specimens, with a total of 188 geotextile particles per layer and a particle diameter of 3 cm.

To confirm the correspondence of the microscopic parameters of the geotextile material used in this study with real-world macroscopic parameters, a tensile test on the geotextile material in ambient conditions was conducted. During the simulation,

Table 1 Particle–particle and particle–wall microscopic parameters

Model type	Normal stiffness, Kn($N{\cdot}m^{-1}$)	Shear stiffness, Ks($N{\cdot}m^{-1}$)	Porosity	Friction
Particle–particle	1e7	1e7	0.18	0.2
Particle–wall	1e7	1e7	–	0.4

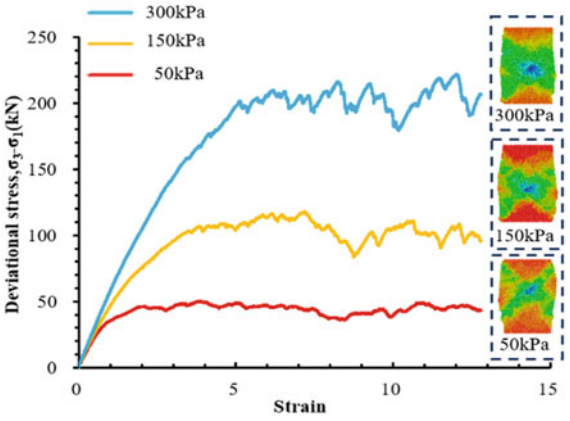

Fig. 2 Deviational stress–strain curve and schematic diagram of flexible biaxia

the left end's first particle was fixed, and a constant velocity of 0.004 m/s was applied to the right end's first particle. The relationship between geotextile tensile force and elongation was recorded. When the elongation reached 32.85%, the tensile force was 200 kN. The microscopic parameters utilized for simulating the geotextile material in this study are presented in Table 2, and schematic diagrams of the tensile test as well as the tensile force–elongation relationship are depicted in Fig. 3.

Table 2 Microscopic parameters of geotextile

Friction	Effective modulus, ($N \cdot m^{-2}$)	Shear strength (N)	Tensile strength (N)
0.68	5e7	1e8	1e7

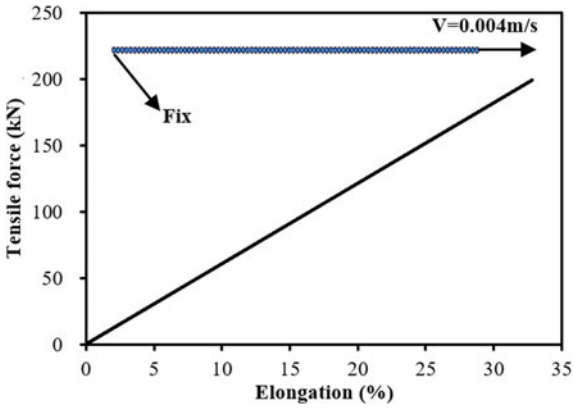

Fig. 3 Tensile force–elongation curve and drawing diagram of tensile test of geotextile

Table 3 Experiment plan

Numerical model	Number of layer(s)	Anchorage length of geotextile, L(m)	Subsidence width, B(m)	Anchorage ratio, L/B
T1	1	3	3	1
T2	2	3	3	1
T3	3	3	3	1

2.3 Discrete Element Simulation Scheme

This study comprised a total of three simulation groups, and the test schemes are detailed in Table 3. In Group T1, the geotextile was buried at a height of H1 = 0 m. In Group T2, the first layer (bottom layer) of geotextile was buried at a height of H1 = 0 m, while the second layer was buried at a height of H2 = 1 m. Group T3 involved the burial of the first layer of geotextile at H1 = 0 m, the second layer at H2 = 1 m, and the third layer at H3 = 2 m.

2.4 Discrete Element Simulation Method

The active baseplate was controlled using the FISH language to move in the negative y-direction at a velocity of $v_y = 0.01$ m/s. The movement was stopped when the active baseplate had a displacement of 0.9 m. The center of the subsidence area of the baseplate was taken as the origin of coordinates(0,0), and the location of the tensile force test points of geotextile are indicated in Fig. 4 and Table 4. In order to get the top vertical settlement of the soil,150 soil particles were marked at the top of the soil, the model was recorded the change of the soil particles in position at the beginning and end, thereby providing data on the settlement of the soil surface.

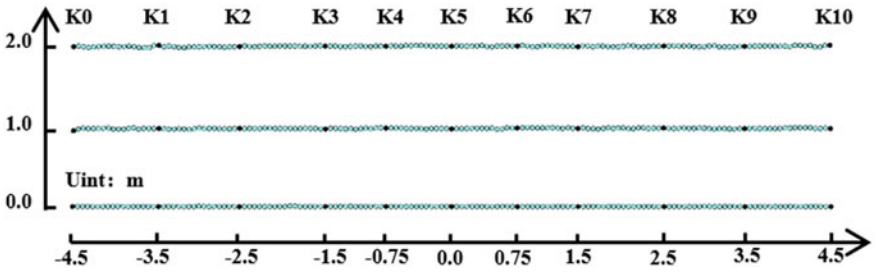

Fig. 4 Schematic diagram of the location of the tensile force test points of geotextile

Table 4 The tensile force test points for each layer of geotextile

Type	Test points	Layer N geotextile		
		N = 1	N = 2	N = 3
Stable area	K0	(−4.5,0.0)	(−4.5,1.0)	(−4.5,2.0)
	K1	(−3.5,0.0)	(−3.5,1.0)	(−3.5,2.0)
	K2	(−2.5,0.0)	(−2.5,1.0)	(−2.5,2.0)
Edge	K3	(−1.5,0.0)	(−1.5,1.0)	(−1.5,2.0)
Subsidence area	K4	(−0.75,0.0)	(−0.75,1.0)	(−0.75,2.0)
	K5	(0.0,0.0)	(0.0,1.0)	(0.0,2.0)
	K6	(0.75,0.0)	(0.75,1.0)	(0.75,2.0)
Edge	K7	(1.5,0.0)	(1.5,1.0)	(1.5,2.0)
Stable area	K8	(2.5,0.0)	(2.5,1.0)	(2.5,2.0)
	K9	(3.5,0.0)	(3.5,1.0)	(3.5,2.0)
	K10	(4.5,0.0)	(4.5,1.0)	(4.5,2.0)

3 Results and Discussion

3.1 Top Vertical Settlement of the Soil

Figure 5 displays the subsidence trends of the top layer in the T1-T3 soil profiles. Notably, all the curves exhibit their peaks within the subsidence area, and as one moves away from this region, an overall reduction in subsidence is observed. With an increase in the number of reinforced geotextile layers, there is a noticeable decrease in the overall subsidence of the top layer. This observation indicates that the augmentation of reinforced geotextile layers effectively mitigates the soil's propensity for subsidence.

3.2 Tensile Force of Geotextile

Figure 6 depicts the trend of geotextile tensile force at test points K0 to K5 in Group T1 as a function of the displacement of the subsidence plate. Notably, within the subsidence area, test points K4 and K5, as well as test point K3 at the boundary between the subsidence and stable regions, exhibit a pattern of initial rapid increase followed by stabilization throughout the subsidence phase. K3, in particular, shows the highest tensile force values, possibly due to stress concentration resulting from the contact between the geotextile and the underlying bedrock. At K2, tensile forces remain relatively constant during the initial 0.2 m of subsidence plate displacement, after which they exhibit a trend of initial rapid increase followed by stabilization after 0.2 m. This behavior is attributed to the incomplete manifestation of the membrane

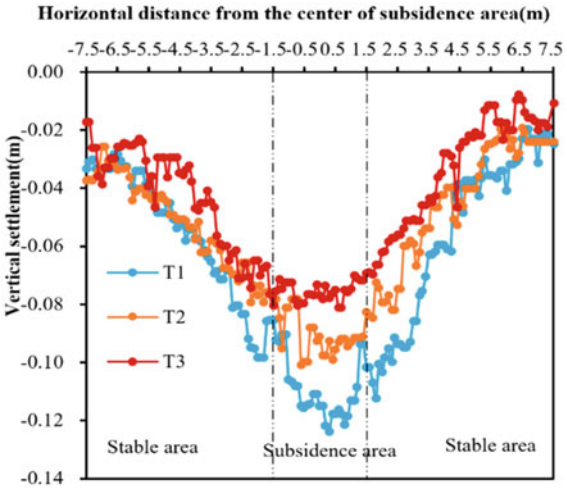

Fig. 5 The trend diagram of top verticle settlement of group T1-T3 soil

tensile force effect in the early stage and its full manifestation in the later stage. For test point K1, tensile forces are nearly negligible during the first 0.35 m of subsidence plate displacement, gradually increasing to 8.11 kN after 0.35 m, and then stabilizing. Tensile forces at test point K0 consistently remain close to 0 kN. The trends in tensile force variation at various test points in the bottom layer of Groups T2-T3 are similar and, therefore, are not further elaborated.

The final tensile force values at all test points for each layer in Groups T1-T3 were sequentially connected from K0 to K10, resulting in the tensile force distribution diagrams at different horizontal positions for the reinforced geotextile layers in T1-T3. Figure 7 illustrates the tensile force distribution at different horizontal positions for the reinforced geotextile layers in T1-T3. From the graph, it can be observed

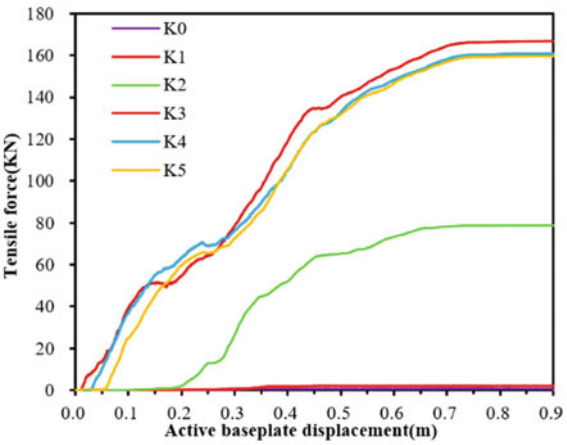

Fig. 6 The trend diagram of test points K0-K5 tensile force with the displacement of the active plate in group T1

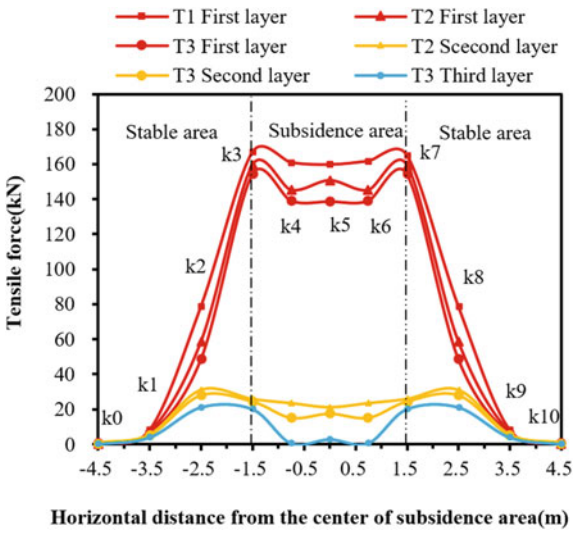

Fig. 7 The tensile force distribution of all geotextiles in groups T1-T3 at different horizontal positions

that with an increase in the number of geotextile layers, the tensile force in the first layer (bottom layer) of geotextile decreases overall. The tensile force in the first layer (bottom layer) of geotextile generally increases from the stable region to the subsidence area, with the maximum tensile force occurring at the edges of the stable and subsidence areas. The maximum tensile force in the non-bottom layer geotextile appears on both sides of the subsidence area in the stable region, and it extends into the stable region. This could be due to the formation of a soil arch in the soil as the height increases, similar to an expansion of the subsidence area, causing test points at the edges of the stable and subsidence areas to move towards the stable region. When multiple layers of geotextile are arranged, the first layer (bottom layer) experiences the highest tensile force.

4 Conclusions

The use of multi-layer reinforced geotextile to treat karst collapse can save the project cost, improve the effect of reinforcing material to treat karst collapse, and the optimal number of layers of reinforced geotextile can be explored in depth in the future. Discrete element numerical simulations were conducted for varying reinforced numbers of geotextile layers, analyzing top verticle settlement of the soil, and geotextile tensile force. The objective was to investigate the influence of different numbers of reinforced geotextile layers on the collapse of karst subgrades. The primary conclusions are as follows:

(1) As the number of reinforced geotextile layers increases, there is a general reduction in the overall settlement of the soil. This indicates that the addition of more reinforced geotextile layers can effectively diminish the tendency for soil collapse.
(2) With an increasing number of reinforced geotextile layers, the tensile force within the bottom layer of the geotextile consistently decreases. Conversely, from the stable area to the collapse area, the tensile force exhibits a general trend of increase. The bottom layer experiences the highest tensile force, followed by the second layer, while the third layer experiences the least tensile force. As the number of reinforced geotextile layers increases, the overall tensile force within the first layer (bottom layer) decreases, while the non-bottom layers of the geotextile share a portion of the tensile force.

Acknowledgements Financial support for this work is gratefully acknowledged by the National Natural Science Foundation of China Grant (No. 42067044), Guangxi Science and Technology Major Program Grant (No.AB23026028), and Science and Technology Project of Jiangxi Provincial Department of Transportation(No.2022H0030).

References

1. Billi A, De Filippis L, Poncia PP, Sella P, Faccenna C (2016) Hidden sinkholes and karst cavities in the travertine plateau of a highly-populated geothermal seismic territory (Tivoli, central Italy). J Geomorphol 255:63–80
2. Gutiérrez F, Benito-Calvo A, Carbonel D, Desir G, Sevil J, Guerrero J, Fabregat I (2019) Review on sinkhole monitoring and performance of remediation measures by high-precision leveling and terrestrial laser scanner in the salt karst of the Ebro Valley, Spain. J Eng Geol 248:283–308
3. Huckert A, Briançon L, Villard P, Garcin P (2015) Load transfer mechanisms in geotextile-reinforced embankments overlying voids: Experimental and analytical approaches. J Geotext Geomembr 3(44):442–456
4. Wittekoek B, van Eekelen SJM, Terwindt J, Korff M, van Duijnen PG, Detert O, Bezuijen A (2022) Geogrid-anchored sheet pile walls; a small-scale experimental and numerical study. J Geosynthet Int
5. Cooper AH, Saunders JM (2016) Road and bridge construction across gypsum karst in England. J Eng Geol 2–3(65):217–223
6. He W, Li K, Wang FH, Ying PB (2016) Experimental study of load distributing behavior of multi-layer geotextile reinforced embankment subjected to the underneath sinkhole in a Karst terrain. J Hydrogeol Eng 1(43):79–84

A Method and Device for Tunnel Defect Detection Based on Image Automatic Collection and 3D Reconstruction

Xufang Deng, Zheng Zhou, Zhenghu Chen, Yi Xu, and Wei Cai

Abstract Long-distance tunnels are essential hydraulic structures that guarantee the safe operation and optimal performance of engineering projects. Monitoring the operational status of tunnels through regular inspections is crucial to promptly detect defects such as seepage, collapses, and damages. This proactive approach prevents structural instability, damages, and blockages, ensuring the safe and stable operation of engineering projects. Water conveyance tunnels are typically long-distance, enclosed spaces with no illumination and no satellite navigation signals. Traditional manual inspection methods suffer from low efficiency, poor accuracy, and high safety risks. The tunnel defect detection method based on image automatic collection and 3D reconstruction addresses these challenges. It enables rapid inspections during flood periods and comprehensive examinations during dry seasons, adapting to the tunnel's water conditions. This method facilitates unmanned intelligent inspections of long-distance tunnels, three-dimensional visualization, and multi-period comparative analysis of defects, offering vast prospects for widespread application. Finally, the proposed method and device were experimentally applied in a practical engineering drainage tunnel to demonstrate their effectiveness and reliability.

Keywords Tunnel · Image automatic collection · 3D reconstruction · Defect detection

X. Deng · Z. Chen · W. Cai
China Yangtze Power Co., Ltd, Wuhan 430014, Hubei, China

Z. Zhou (✉) · Y. Xu
Changjiang Institute of Survey, Planning, Design and Research Co.,Ltd, Wuhan 430010, Hubei, China
e-mail: zhouzheng@cjwsjy.com.cn

National Dam Safety Research Center, Wuhan 430010, Hubei, China

G. Mei et al. (eds.), *Advanced Construction Technology and Research of Deep-Sea Tunnels*, Lecture Notes in Civil Engineering 490,
https://doi.org/10.1007/978-981-97-2417-8_13

1 Introduction

In recent years, China has undertaken the construction of numerous long-distance water conveyance and drainage tunnels, including significant projects such as the South-to-North Water Diversion Project, the Yunnan Central Diversion Project, the Sichuan Yalong River Jinping II Hydropower Station, and various diversion and drainage tunnels for high dams and reservoirs. The operational condition of these tunnels directly influences the safe and stable operation of crucial engineering projects, impacting areas such as people's livelihoods, water supply, flood control, and electricity generation. Consequently, conducting regular inspections is vital to understanding their actual operational status, promptly detecting potential issues such as collapses, damages, blockages, cracks, and seepages, and preventing structural instability, damages, and blockages that could arise from undetected or worsening defects. Ensuring the safety of engineering projects is paramount [1, 2].

Traditional methods of tunnel defect detection primarily rely on manual inspection, combining human efforts with various instruments to inspect defects such as cracks, falling blocks, and seepage. Long-distance water conveyance and drainage tunnels, being enclosed spaces, lack satellite navigation signals, illumination, and have poor conditions for human entry and inspection. This results in low efficiency during manual inspections, inaccurate positioning of defects like cracks, collapses, and damages, and difficulties in timely identification of significant hidden defects [3, 4]. Additionally, the tunnel floor may have sedimentation, pits, steel bars, tree branches, and other obstacles. Inadequate lighting, unclear inspection conditions, and the possibility of falling rocks and blocks pose safety risks during manual inspections.

During manual inspections, various equipment can be employed, such as ultrasonic testing, acoustic emission testing, radar detection, and fiber optic sensing, in addition to visual observation, to detect tunnel defects [5, 6]. Acoustic emission testing utilizes the phenomenon of material acoustic emissions to detect defects in tunnel lining concrete such as cracks. Radar detection determines the existence of cracks on the tunnel lining surface by analyzing the difference in reflection wave strength when radar waves pass through different mediums. Fiber optic sensing detects cracks in tunnel lining concrete by identifying changes in optical waveguides. However, these crack detection methods mentioned above face challenges such as low detection efficiency, poor detection results, difficulties in accurately and efficiently locating crack positions and their orientations within a limited time frame, and the complexity of simultaneously detecting various defects like seepage and damages [7, 8].

In addition to traditional methods, new equipment and technologies have been introduced for tunnel lining concrete crack detection, such as laser scanning detection technology and digital image processing technology. Laser scanning technology primarily utilizes laser scanners to obtain point cloud data of the tunnel lining, determining the presence of cracks based on this point cloud. Alternatively, it constructs images of the tunnel lining based on the reflectivity data of scanned points, further extracting crack information [9, 10]. While laser scanning technology can achieve the

goal of crack detection, its precision is low when detecting small cracks. Additionally, the operational procedures of laser scanners are complex, and their detection efficiency is low, making it challenging to rapidly detect cracks in tunnel lining concrete within a limited time frame. Digital image processing technology utilizes cameras to capture images of the tunnel lining and then employs deep learning algorithms such as neural networks to identify cracks [11–13]. Digital image processing technology replaces human visual recognition with machine vision, allowing for more accurate crack identification and extraction of crack characteristics compared to other methods [14]. However, tunnels are enclosed spaces with long distances and no illumination, and the satellite navigation signals inside the tunnels are weak. As a result, there is a lack of mature and reliable image acquisition equipment that meets the requirements of regular tunnel inspections. Moreover, existing algorithms for identifying and classifying various tunnel defects lack universality, and their accuracy is still insufficient to meet practical inspection requirements. Therefore, this paper proposes a tunnel defect detection method and device based on image automatic collection and 3D reconstruction. This method aims to enhance detection efficiency and accuracy, enabling unmanned intelligent inspections of long-distance underwater tunnels. Experimental applications have been conducted in practical engineering projects to validate its effectiveness and reliability.

2 Technology and Equipment

For water conveyance, diversion, and drainage tunnels, during flood periods, when water flow is swift due to rapid fluctuations in water levels, manual inspection becomes impractical. At this time, there is a need for quick inspections to identify potential issues such as collapses, damages, and blockages within the tunnels. During the dry season, when water depth is shallow and water flow is minimal, more detailed inspections are possible. Based on this approach, image acquisition equipment has been developed. This equipment can be mounted on a mobile platform (e.g., unmanned vehicles, inspection boats, or vehicles) and automatically moves along with the platform, autonomously capturing tunnel wall images and detecting defects. The hardware system of the image acquisition equipment (Fig. 1) consists of four main components: the acquisition system framework, a high-definition single-lens reflex camera for detailed inspections, a fast inspection 360-degree panoramic camera, and an RGB visible light camera combined with an infrared thermal imaging camera.

Fig. 1 Overall layout of the image acquisition hardware system

2.1 Rapid Inspection During Flood Periods

To achieve quick tunnel inspections, an Insta360 Pro 2 panoramic camera is used for rapid image capture. This panoramic camera is equipped with six ultra-wide-angle fisheye lenses, each with a field of view of nearly 180 degrees, enabling 360-degree panoramic photography. It provides a maximum image size of 7680 × 3840 pixels with 8 K resolution. The camera can be mounted on a power-supplied E-port quick-release interface and, depending on the collection requirements and on-site conditions, can be quickly exchanged with a high-precision single-lens reflex camera acquisition device. The extensive coverage of the panoramic camera, coupled with the rapid movement of the platform along the tunnel, enables automatic image capture of the tunnel wall during flood periods. It allows for the rapid identification of significant defects such as extensive cracks, large-scale disintegration, water leakage, and accumulation.

2.2 Comprehensive Inspection During the Dry Season

During the dry season, when water depth is shallow and water flow is minimal, conditions are conducive to slow movement and detailed inspection. For this purpose, a full-frame single-lens reflex camera is used for image capture, with a maximum image size of 7952 × 5304 pixels (8 K) and a resolution of 42 million pixels. Equipped with a 35 mm fixed-focus lens, after sub-pixel processing, it achieves an accuracy of 0.1 mm at a distance of 5 m from the shooting surface. The film resolution is approximately 0.1–0.2 mm per pixel, meeting the accuracy requirements for crack identification of 0.1 mm. It can also identify local small-scale disintegration, leakage, detachment, and other defects, meeting the precision requirements for concrete surface defect detection.

The full-frame single-lens reflex camera is installed on a self-developed 3DOF brushless stabilizing gimbal for physical stabilization to prevent blurring caused by movement platform vibrations during travel. Moreover, the stabilizing gimbal features automatic camera rotation and shooting through program control, as well as real-time communication with the mobile platform.

2.3 Supplementary Inspection with Infrared Thermal Imaging

Water infiltration areas in concrete structures tend to have lower temperatures compared to adjacent areas. Infrared thermal imaging technology is employed to supplement inspections for water leakage points. A thermal imaging camera with a resolution of 40 × 480 is used to identify defects in the tunnel wall due to water infiltration. This is combined with the RGB visible light camera to quickly pinpoint water leakage locations.

2.4 Image Acquisition Process

The displacement statistical regression model utilizes environmental factors as independent variables.

The image overlap rate includes the forward overlap (R_1, along the tunnel axis) and the lateral overlap (R_2, the rotation angle of the camera within the cross-section). Based on the overlap rate, the lateral photo shooting angles and the forward distances of the mobile platform during different-sized tunnel image acquisition can be calculated. If the camera's focal length is f, the sensor length is l = the longest side pixel × pixel size, the sensor width is w = the shortest side pixel × pixel size, and the camera distance from the surface to be measured is D.

During detailed image acquisition, the mobile platform moves along the tunnel axis and stops to allow the image acquisition system to control the camera for 360° circular shooting. The intervals for stopping and the camera's rotation angles for each shot are controlled based on an 80% image overlap requirement. The process of image acquisition along the tunnel axis and the cross-sectional direction is illustrated in Figs. 2 and 3.

As shown in Fig. 4, the axial photo interval N is calculated as follows:

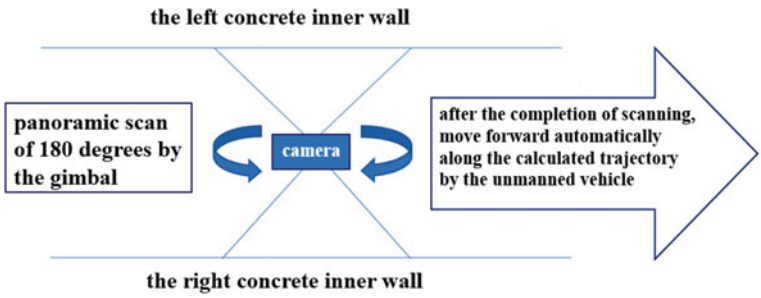

Fig. 2 Process of image acquisition along the tunnel axis

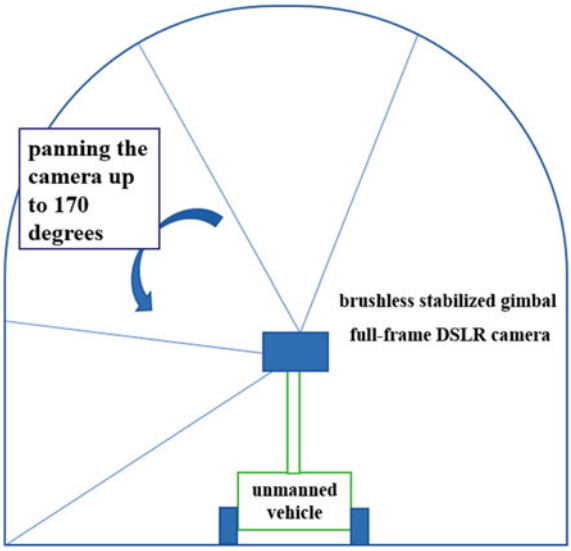

Fig. 3 Illustration of camera rotation for cross-sectional image acquisition

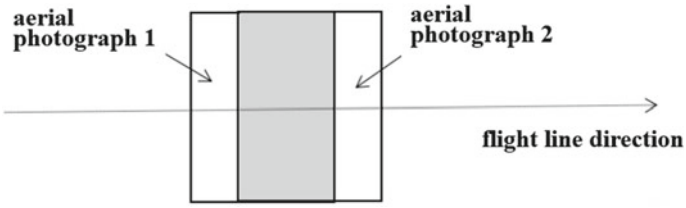

Fig. 4 Axial overlap rate

$$N = W - R_1 \times W = w \times D \times (1 - R_1)/f \tag{1}$$

As shown in Fig. 5, the circumferential photo interval M is calculated as follows:

$$M = L - R_2 \times L = l \times D \times (1 - R_2)/f \tag{2}$$

Using the above formulas, the axial interval is calculated as 1.2 m, which means the platform stops and performs 360° circular image acquisition every 1.2 m of forward movement. When the camera captures images at each stop, the lateral pitch angle of the single-lens reflex camera is 19°, meaning the camera triggers the shutter every 19° of rotation.

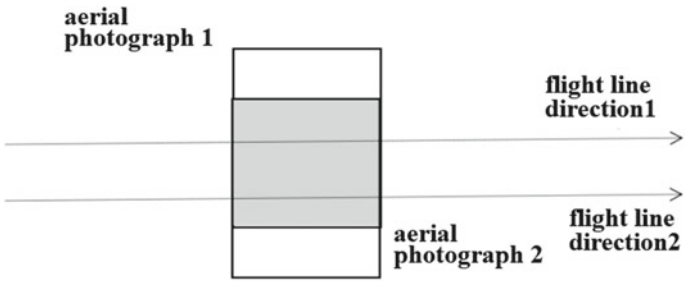

Fig. 5 Circumferential overlap rate

2.5 Three-Dimensional Reconstruction and Localization of Tunnel Defects

The vast amount of image data obtained after image acquisition needs to be stitched together for subsequent defect localization. Image stitching can be based on two reference indicators: coordinate information and photo texture. When satellite navigation signals are strong, the captured images contain three-dimensional coordinate point information, and image stitching can be performed based on these coordinate points to locate the point cloud information. When satellite navigation signals are weak, the captured images themselves do not contain three-dimensional coordinate information and cannot be positioned using point clouds. In this case, stitching can be done based on the texture characteristics of the images. Ultimately, a complete three-dimensional realistic model of the tunnel wall is obtained, serving as the background dataset for defect localization.

Using the fully covered tunnel wall image acquisition data, the stitched images are used to construct the original three-dimensional realistic model of the tunnel, which contains point cloud information with actual coordinates. This model serves as the base map for three-dimensional defect display and enables image feature extraction and defect localization. The defect images automatically detected are associated with the base map of the tunnel's three-dimensional model using image retrieval methods. For defect images detected automatically, the position of the defect can be rapidly calculated based on the position of the mobile platform, camera height, and angle. With the mapping relationship between defect images and the three-dimensional realistic model, along with camera parameters and the distance between the camera and the defect area, the actual size of the defect area can be estimated. Consequently, information such as the actual position of the defect within the tunnel, the type of defect, and the defect size can be obtained. This information is annotated and displayed on the three-dimensional realistic model as the result.

3 Case Study

The image acquisition method and equipment proposed in this paper were applied in an experimental inspection of a drainage tunnel using an automatic mobile platform to validate the effectiveness and feasibility of the developed equipment. The tunnel covered a total distance of 3 km. During on-site testing, the image transmission system was placed on the mobile platform. Data transmission information was received at both the entrance and exit of the tunnel while capturing images along the tunnel axis. This resolved the problem of no satellite navigation signals inside the tunnel, indicating that the image acquisition system is capable of capturing high-definition images and implementing transmission functions within long-distance enclosed tunnel spaces.

The hardware system of the image acquisition equipment was installed on the top of the mobile platform for automatic capture of high-definition images of the tunnel walls. Image stitching and three-dimensional modeling of the tunnel were performed. Point cloud data from the captured portions of the tunnel are shown in Fig. 6, and the three-dimensional realistic model obtained by coupling and stitching based on the coordinate positions of the point cloud is illustrated in Fig. 7.

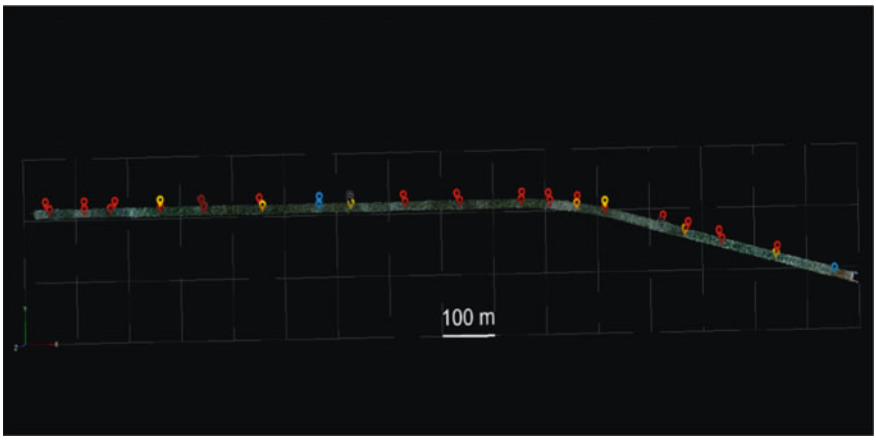

Fig. 6 Point cloud data from captured sections of the tunnel

a. Large-scale Three-dimensional Modeling

b. Three-dimensional Realistic Model of the Tunnel

c. Detailed Structure of the Three-dimensional Model

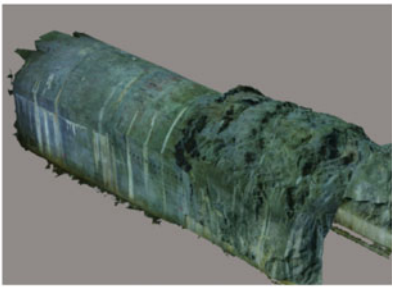

d. Three-dimensional Realistic Model of the Tunnel

e. Detailed Image of Water Seepage inside the Tunnel

f. Detailed Image of Cracks inside the Tunnel

g. Detailed Image of Damaged Tunnel Walls

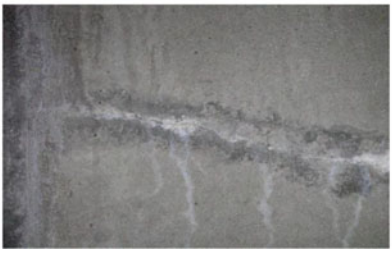

h. Detailed Image of Calcium Analysis of Wall Cracks

Fig. 7 Achievements of the three-dimensional tunnel model

4 Conclusion

In this paper, a tunnel defect detection method and equipment based on automatic image acquisition and three-dimensional reconstruction were proposed. Considering the tunnel water conditions, a combined inspection approach of rapid checks during flood seasons and comprehensive inspections during dry periods was introduced. The proposed method was experimentally applied in the inspection of a drainage tunnel, enabling quick identification of anomalies such as collapses, damages, and blockages within the tunnel. It enhanced the intelligence level of tunnel inspections, significantly improving inspection efficiency and safety.

- The hardware system of the tunnel inspection image acquisition equipment was constructed, consisting of the acquisition system framework, detailed full-frame high-definition camera, general survey 360 panoramic camera, and RGB visible light combined with infrared thermal imaging camera. This system enables rapid checks during flood seasons, detailed inspections during dry periods, and supplementary inspections for water seepage points using thermal imaging. It replaced traditional manual inspection methods, greatly enhancing the efficiency, accuracy, and safety of inspections.
- The tunnel inspection method and equipment proposed in this paper were applied in practical engineering, achieving unmanned automatic inspection of large-scale, long-distance, unilluminated, satellite navigation signal-absent, enclosed drainage tunnels. The system can create three-dimensional models of tunnels, present them in three dimensions, and compare defects over multiple periods. It possesses features of automation, intelligence, and efficiency. The application prospects of this method in the future for large-scale, deeply buried, long-distance unmanned intelligent tunnel inspections are highly promising.

Acknowledgements This study was supported by the China Yangtze Power Co., Ltd. Research Project (Z212102007).

References

1. Zhu Y, Xie M, Zhang K et al (2010) A dam deformation residual correction method for high arch dams using phase space reconstruction and an optimized long short-term memory network. Mathematics 2023:11
2. Xu M, Pang R, Zhou Y, et al (2023) Seepage safety evaluation of high earth-rockfill dams considering spatial variability of hydraulic parameters via subset simulation. J Hydrol 626(A):130261
3. Zhu Y, Zhang Z, Gu C, et al (2023) A coupled model for dam foundation seepage behavior monitoring and forecasting based on variational mode decomposition and improved temporal convolutional network. Struct Control Health Monitor 3879096

4. Koch C, Georgieva K, Kasireddy V et al (2015) A review on computer vision based defect detection and condition assessment of concrete and asphalt civil Infrastructure. Adv Eng Inform 29(2):196–210
5. Yang G, Chen T, Li P et al (2020) Application of ultrasonic and radar methods in tunnel lining crack detection. Hunan Traf Sci Technol 46(1):45–46
6. Wang Y (2012) Research on identification of concrete structural cracks using acoustic emission method. Construction Technology S2:127–129
7. Badrinarayanan V, Kendall A, Cipolla R (2017) SegNet: a deep convolutional encoder-decoder architecture for image segmentation. IEEE Trans Pattern Anal Mach Intell 39(12):2481–2495
8. Rowshandel H, Nicholson GL, Shen JL et al (2018) Characterisation of clustered cracks using an ACFM sensor and application of an artificial neural Network. NDT and E Int 98:80–88
9. Shi B, Xu X, Wang D et al (2005) Research on distributed optical fiber strain monitoring technology for tunnel health diagnosis based on BOTDR. Chin J Rock Mech Eng 24(15):2622–2628
10. Zhou Q (2017) Research on surface state detection technology of vehicle-mounted tunnel repair[D]. China Academy of Railway Sciences, Beijing
11. Xie X, Lu X, Tian H et al (2013) Measurement method of tunnel full section deformation based on ground 3D laser scanning technology. Chin J Rock Mech Eng 32(011):2214–2224
12. Huang S, Bao T, Li Y et al (2023) Semantic segmentation method for hydraulic concrete crack based on improved deeplab V3+ network. Adv Sci Technol Water Resourc 43(1):81–86
13. Huang Y, Liu X, Yuan Y et al (2012) Automatic detection technology for shield tunnel leakage. J Tongji Univ (Natural Science) 46(01):73–78
14. Zhu Y, Tang H (2023) Automatic damage detection and diagnosis for hydraulic structures using drones and artificial intelligence techniques. Remote Sens 15:615

Surface Settlement Induced by Excavation of Double-Line Shield Tunnel

Mingzhe Zhao, Haifeng Wang, Jiaxin Zhang, Xiaoyi Ji, Jiahao Zhang, Yao Liu, Yaxiu Li, and Bowen Xing

Abstract In the construction of the Harbin Metro Line 3 twin-bore tunnel project, the ABAQUS numerical simulation method was employed to investigate the impact of various grouting thicknesses, burial depth ratios, tunnel spacing, and excavation pressures on the geological conditions of the project. Corresponding construction control measures were proposed. The study revealed: (1) Grouting thickness is inversely proportional to ground settlement, with an optimal thickness of 0.3 m; (2) Lateral ground settlement increases with an increasing depth ratio, showing an initial increase followed by a decrease, closely related to soil arching effects; (3) As the distance (L) between two parallel tunnels increases, the peak ground settlement of the left and right tunnels decreases. Smaller tunnel spacing leads to stronger mutual interactions, resulting in a "V"-shaped settlement deformation within the overlapping disturbance zone. When the tunnel spacing is sufficiently large, the mutual interference between the two tunnels diminishes, and the ground settlement deformation is considered the superimposition of two independent tunnel settlements, forming a "W"-shaped settlement trench; (4) Excavation pressure exceeds the static soil pressure, causing soil disturbance, leading to an uplift of the soil in front of the tunnel face and an expansion of the plastic zone in the surrounding soil, ultimately resulting in increased subsequent surface settlement.

Keywords Shield tunneling · Surface settlement · Numerical simulation · Grouting layer thickness · Burial depth ratio · Distance between parallel tunnels · Excavation pressure

M. Zhao · H. Wang · Y. Li
China Communications Infrastructure Maintenance Group Co., LTD, Beijing, China

J. Zhang (✉) · X. Ji · J. Zhang · Y. Liu · B. Xing
University of Science and Technology Beijing, Beijing, China
e-mail: 1123307087@qq.com

G. Mei et al. (eds.), *Advanced Construction Technology and Research of Deep-Sea Tunnels*, Lecture Notes in Civil Engineering 490,
https://doi.org/10.1007/978-981-97-2417-8_14

1 Introduction

The underground railway engineering is a highly anticipated project characterized by its massive construction scale, lengthy duration, substantial investment, and significant societal benefits. Therefore, it is essential to conduct specialized research on safety and geological issues that may arise during subway construction. In the construction of urban rail transit in major cities, it has gained increasing popularity due to its fast construction pace, high level of automation, safety, and environmental features. However, irrespective of the measures taken, they can result in disturbances to the surrounding soil and have an impact on the ecological environment. For instance, this can lead to issues such as tilting of nearby buildings, damage to underground pipelines, and ground subsidence, among others [1].

With the development of tunnel boring technology, the issue of ground subsidence caused by tunnel excavation has increasingly captured people's attention. Scholars from both domestic and international backgrounds have conducted extensive research on the surface settlement induced by shield tunnel construction [2–5]. Xin et al. [6], based on two tunnels within the Hangzhou Rail Transit Line 3 project, the Industrial University Station to Liuhe Station section, utilized a 3D numerical simulation method to analyze the deformation and the effects of tunnel excavation on adjacent bridge pier foundations. Ngoc et al. [7] employed numerical simulation methods to analyze the impact of subway construction at different distances on subway construction and the surrounding ground subsidence in operational subway projects. Alessandra et al. [8], using two deep-buried tunnels located in fine-grained sandy soil layers as an example, improved the model's predictive accuracy by adjusting geological parameters with observation data, and conducted numerical simulations and calculations. In the Beijing Metro Line 12 project, Wang et al. [9] adopted FLAC three-dimensional numerical simulation method to obtain the deformation characteristics of the strata and the surface when the shield traverses the existing railway. Zhang et al. [10] used the finite element method to analyze the influence of various factors on the surrounding environment in the shield construction process, and analyzed the influence of various factors on the surrounding environment, providing a theoretical basis for engineering construction. Based on the sandy soil foundation of a section of Nanchang subway, Zhao et al. [11] made a theoretical analysis and research on the ground subsidence before and after tunnel excavation by combining the method of mathematical regression analysis and numerical simulation, and obtained the changes of ground subsidence caused by tunnel excavation. Zhifu [12] analyzed the cause of surface subsidence during tunnel excavation and proposed the treatment method based on the measured data of the first phase of the first phase of Zhengzhou Metro Line 5.Based on the measured data of a rail transit tunnel construction site in Hangzhou, Gao [13] took surface settlement, tunnel settlement and tunnel settlement as the main research content, and used mathematical statistics to study the common rules of silt layer settlement and deformation under the condition of high water head. Jiahui et al. [14] conducted construction technology and engineering survey of EPB shield in Liancheng Town of Huaian East Railway

Station shield working well in the Yellow River flood area, and obtained deformation characteristics of soil after the high-speed rail underpass through the wall. Dezhi et al. [15] took the existing buildings in urban areas through the subway shield as an example, and studied the effect of subway shield construction on existing buildings on the ground by combining measured data and numerical simulation. On this basis, the settlement control standards for existing buildings were proposed. Aiming at the ground subsidence caused by subway shield construction, Liu et al. [16] studied the change and interaction mechanism of ground subsidence under its influence by constructing a three-dimensional finite element simulation model combined with engineering observation data. Jun et al. [17] studied the problem of adjacent ground subsidence caused by shield construction. By constructing a finite element simulation model and combining with engineering monitoring data, Xiu et al. [18] revealed its action mechanism in the formation.

In summary, previous studies have predominantly focused on investigating the patterns of surface settlement caused by shield tunnel construction, with an emphasis on varying construction methods for different geological strata. However, there has been limited research on the surface settlement patterns resulting from shield tunneling through fine-grained sandy layers. In this study, the authors conducted three-dimensional numerical simulations using ABAQUS software during the construction of the double-track tunnels of the Harbin Rail Transit Line 3. They investigated the impact of grouting layer thickness (r), excavation pressure (p), tunnel depth ratio (H/D), and the distance between the double tunnels (L) on surface settlement. The study provides relevant recommendations for construction control in this context.

2 Engineering Background and Model Construction

This article is based on the civil engineering project of the second phase of Harbin Rail Transit Line 3. The project spans from the Dingxiang Park Station to the Sports Park Station, forming an overall inverted V-shaped slope longitudinally. Both the left and right line segments have a length of 819.789 m, resulting in a total length of 1639.578 m. The tunnel passes through fine sand layers and medium-coarse sand layers. Construction is carried out using a shield machine, with a designed tunnel outer diameter (including lining thickness) of 6 m, an inner diameter of 5.4 m, and a lining segment thickness of 0.3 m. Each segment is 1.2 m wide and assembled with staggered joints. The tunnel center is approximately 13 m below the ground. The geological cross-section and geological structure of this section are depicted in Fig. 1.

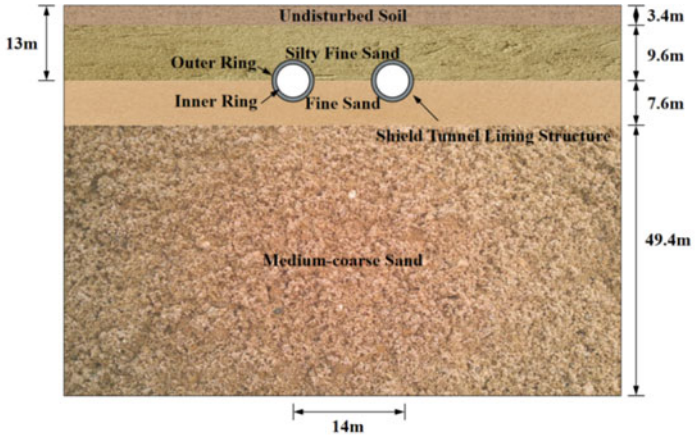

(a) Histogram of geological structure

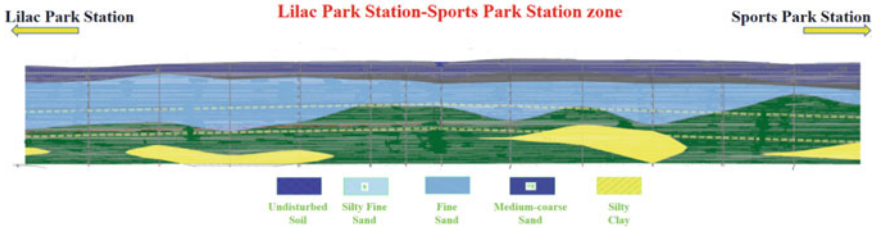

(b) Geological Cross-Section of the Section

Fig. 1 Geological cross-section and geological structure map of the section

3 Calculation Model

In this study, the mechanical simulation model for shield tunnel construction is implemented using the ABAQUS finite element program. ABAQUS is known for its high accuracy in numerical simulations of shield tunnel excavation, making it one of the preferred programs for this purpose.

3.1 Basic Model Assumptions

In order to maintain consistency with actual construction, several computational assumptions need to be made before the study:

(1) Neglect small variations in the terrain and all soil layers along the tunnel alignment, simplifying them as uniform horizontal layers;
(2) Assume the rock mass as an ideal elastic–plastic medium;

(3) Disregard time effects of rock deformation and the influence of groundwater seepage;
(4) Ignore the in-situ stress within the soil layers and stress concentration near the geological boundaries;
(5) Consider the rock mass as an isotropic and homogeneous material;
(6) Set the initial stress field as the initial stress field of the surrounding rock;
(7) Model the excavation-induced disturbance by reducing the modulus of the disturbed rock mass in the disturbance zone.

3.2 Parameter Selection

When conducting numerical simulation studies, it is necessary to select representative sections for modeling. Based on previous research, the lateral range boundary that affects soil deformation is roughly about 4 times the tunnel diameter away from the tunnel's side, while the vertical range boundary is approximately 3 times the tunnel diameter away from the tunnel bottom. Beyond these boundaries, the impact is nearly zero. Combining these findings with design parameters such as tunnel depth, the final dimensions of the ABAQUS model were determined to be 100 m in the lateral (x) direction, 100 m in the advancing (y) direction for the rock tunnel, and 70 m in the vertical (z) direction. Six cross-sections of the model required the setup of essential boundary conditions, with the top surface set as a free surface, and the other surfaces receiving corresponding displacement constraints. The ABAQUS model constructed for the research project is depicted in Fig. 2.

The soil layers in ABAQUS were simulated using the Mohr–Coulomb constitutive model. The lining segments and the shield machine's outer shell were simulated using shell structure elements and set as elastic materials. The overall finite element analysis used linear hexahedral elements, with a total model divided into 196,802 nodes and 210,764 elements of type C3D8R. The soil properties in the layers at the tunnel depth were determined based on geological reports and material properties

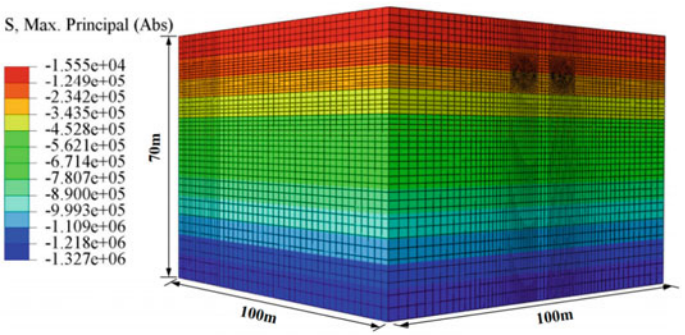

Fig. 2 ABAQUS model

Table 1 Physical and mechanical parameters of each soil layer

Soil types	Elevation of soil layers/m	Unit weight γ (kN/m^3)	Young's modulus/ MPa	Poisson's ratio μ	Cohesion/ kPa	Friction Angle/°
Undisturbed soil	3.4	18.3	5	0.35	8	18
Silty fine sand	9.6	19.2	17	0.3	0	31
Fine sand	7.6	19.3	21	0.3	0	34
Medium-coarse sand	49.4	19.5	24	0.3	0	37

to meet the requirements for accurately reflecting the construction conditions. The mechanical parameters for each soil layer are presented in Table 1.

3.3 Simulating the Shield Tunnel Construction Process

Following the working principles of the shield tunneling machine, the simulated construction steps are as follows:

(1) Establish material models for the soil layers, the shield tunneling machine, the waiting layer, and lining segments. Categorize these materials and assign the corresponding material parameters. Assemble these material models on the assembly board. For the initial stress zone, consider only self-weight effects and apply deformation corrections.
(2) Based on the "live" and "dead" element method, create the analysis steps. During excavation of each layer of soil, activate the waiting layer, lining segments, and grouting layer. Simulate the support provided by the cutterhead to the rear soil using the positive-pressure method during excavation, thereby achieving support for the rear soil. Determine the numerical value of the static pressure that the construction process bears.
(3) After each week of the tunnel boring machine's operation, remove the support from the previous week, generate new support, and adjust the stiffness and other parameters of the shield tunnel support material. Utilize synchronous grouting to implement grouting around the tunnel's surrounding rock using the grouting method. Apply grouting pressure to the surrounding rock and set corresponding operational procedures. Meanwhile, while maintaining a constant grouting pressure, layer the grouting material and conduct numerical simulations.
(4) According to the numerical model, set the overall excavation into 80 excavation steps. During the 80 excavation steps, the shield shell supports the surrounding rock. After the construction is completed, the tunnel is fully penetrated.

3.4 Numerical Simulation Validation

Currently, there are several methods for predicting settlement in subway engineering, including statistical methods using measurement data (such as the Peck formula) and numerical methods using finite elements and boundary elements. This article employs a comparative analysis between measured data and numerical simulation data to validate the results.

This article uses the actual measured ground settlement data during the construction of the double tunnels of Harbin Metro Line 3 as reference, and conducts a comparative analysis with the numerical solution results, as shown in Fig. 3, the surface settlement along the tunnel excavation direction exhibits a good fit between measured and simulated data. The maximum fitting error between numerical simulation and actual settlement on the left tunnel side is 12.61%, while on the right tunnel side, it is 10.56%. These results validate the accuracy of the numerical simulation in this article, indicating that using ABAQUS finite element software for simulating shield tunnel construction can provide valuable guidance for practical engineering projects.

As depicted in Fig. 4, it shows settlement cross-sections of the tunnel at different excavation steps. During the shield tunneling process, the excavation of soil disturbs the surrounding soil, resulting in settlement of the surface soil. As the advancement continues, the unexcavated soil experiences compression, leading to a certain degree of uplift in the unexcavated area. In the region where excavation support has been completed, the peak surface settlement occurs directly above the tunnel. Through

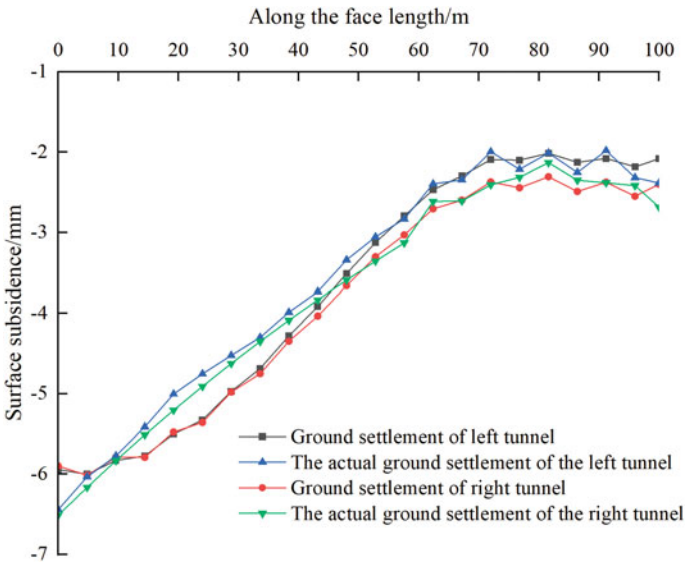

Fig. 3 Comparison between actual settlement curve and numerical simulation settlement curve

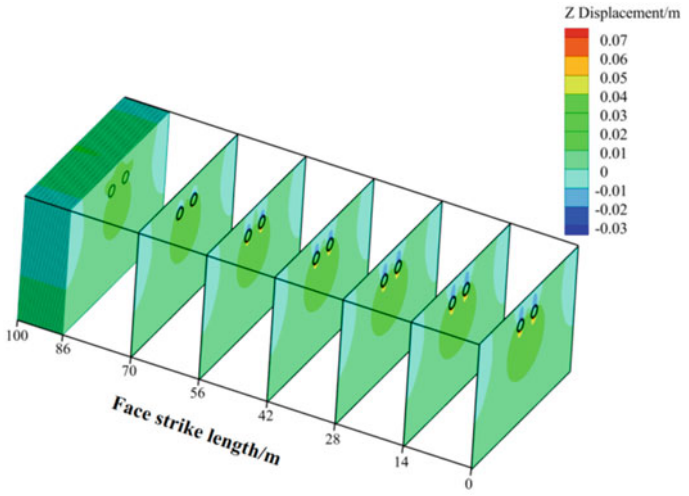

Fig. 4 Multi-analysis step slice displacement nephogram

support and reinforcement measures, the excavated area forms a stable settlement region.

4 Analysis of the Impact of Shield Tunneling Construction Parameters on Surface Settlement

4.1 Scheme Design

Three factors were selected for the study: grouting thickness (r), depth-to-diameter ratio (H/D, where H represents the vertical distance from the tunnel top to the ground surface, and D represents the tunnel excavation diameter), thrust pressure (P), and the distance between twin tunnels (L). The study focused on observing lateral surface settlement and, in turn, delving into the impact of each parameter on surface settlement during shield tunnel construction. The specific scheme settings are detailed in Table 2.

4.2 Influence of Different Grouting Thickness on Surface Settlement During Shield Tunnel Excavation

In order to study the influence of different grouting thicknesses on surface settlement during tunnel construction, we set various tunnel grouting thicknesses (r), including

Table 2 Tunnel boring machine construction parameter configuration plan

Scheme	Grouting thickness *r*/m	Distance between two tunnels *L*/m	Burial depth ratio *H/D*	Excavation pressure *p*/kPa
Scheme 1	0, 0.1, 0.2, 0.3	8	1.67	142
Scheme 2	0.31	4, 8, 12, 16	1.67	142
Scheme 3	0.31	8	2, 3, 4, 5	142
Scheme 4	0.31	8	1.67	100, 142, 200, 300

0, 0.1, 0.2 and 0.3 m. The distance between the two tunnels (*L*) was set at 8 m, and the depth from the tunnel crown to the ground surface (*H/D*) was 10 m, which corresponds to a depth-to-diameter ratio of 1.67. We observed that as the grouting thickness increased, surface settlement decreased, with the maximum displacement settlement occurring directly above the tunnel crown. After the tunnel was fully penetrated, we generated lateral surface settlement values for each grouting thickness and obtained corresponding lateral surface settlement curves for different grouting thicknesses, as shown in Fig. 5.

Based on the research results from Fig. 5, we observed that the peak of surface settlement typically occurs directly above the tunnel. With other construction parameters held constant, increasing the grouting layer thickness effectively reduces the deformation of the surface soil, and the peak surface settlement decreases as the grouting layer thickness increases. Specifically, when there is no grouting, the numerical simulation indicates a peak surface settlement of 13.32 mm, directly above the tunnel. When the grouting layer thickness is 0.1 m, the lateral surface settlement

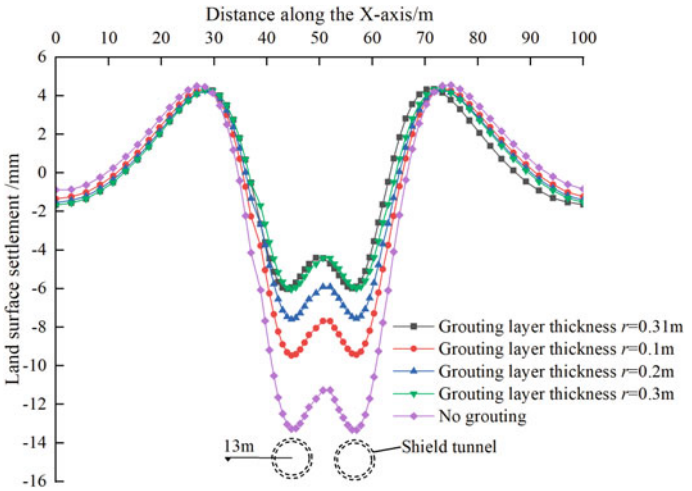

Fig. 5 Lateral surface settlement curves corresponding to tunnel boring machine excavation with different grouting thicknesses

peak is 9.47 mm; at 0.2 m grouting layer thickness, the lateral surface settlement peak is 7.59 mm; at 0.3 m grouting layer thickness, the lateral surface settlement peak is 6.04 mm.

The results indicate that within a certain range, increasing the grouting layer thickness effectively fills the gap between the shield tail and reduces ground settlement during shield tunnel excavation. However, based on practical engineering experience, an excessively thick grouting layer may have an impact on the surrounding soil mechanics, leading to soil disturbance and being detrimental to controlling surface settlement. Therefore, it is important to carefully select the grouting layer thickness in real-world engineering. The process from no grouting to injecting a 0.3 m thick grouting layer results in a significant reduction in peak surface settlement. Taking various factors into consideration, a grouting layer thickness of 0.31 m is found to meet the practical requirements in the project.

4.3 The Impact of Twin Tunnel Spacing on Surface Settlement

This subsection aims to investigate the influence of different twin tunnel spacing on surface settlement. Various tunnel distances (L) were selected, including 4, 8, 12, and 16 m, for numerical simulation and analysis. In the numerical simulation parameters for shield tunnel construction, a grouting layer thickness of 0.31 m, a tunnel excavation step length of 1.2 m, and a depth-to-diameter ratio (H/D) of 1.67 (corresponding to a crown depth of 10 m) were chosen.In the numerical models, after the completion of tunneling, lateral surface settlement curves for different spacing were generated, as illustrated in Fig. 6.

Based on the observations from Fig. 6, it is evident that as the distance (L) between the two parallel tunnels increases, the surface settlement for both the left and right tunnels gradually decreases. With the increasing distance (L) between the two parallel tunnels, the surface settlement curves expand outward, and the settlement area also becomes larger. The original "V"-shaped settlement trough gradually evolves into a broader "W" shape, becoming shallower and wider. When the distance (L) between the twin tunnels increases from 4 to 8 m, the change in the settlement distribution curve transforms from the initial "V" shape to a "W" shape.

This change can be primarily attributed to the fact that when the distance between the tunnels is small, the mutual interference between them gradually intensifies. This leads to an increased deformation of the surface settlement in the common disturbance area, thus forming a "V"-shaped settlement trough. Conversely, when the distance between the tunnels is larger, the mutual interference caused by construction weakens. In this case, the surface settlement is considered as the superposition of the independent settlement and deformation effects of the two separate tunnels, resulting in the "W"-shaped settlement trough.

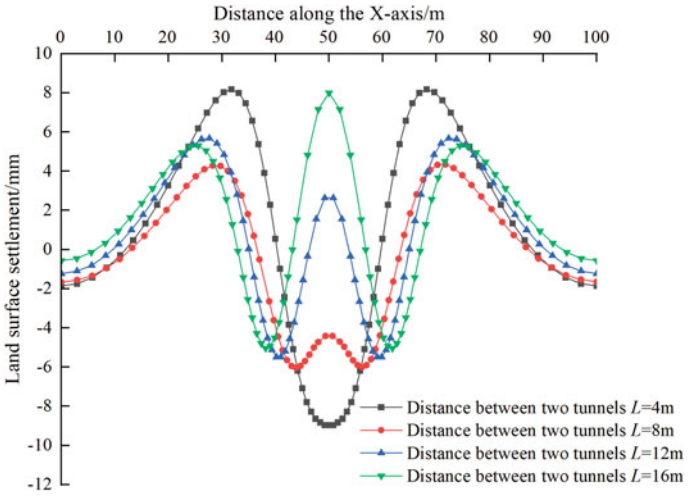

Fig. 6 Lateral surface settlement curves corresponding to tunnel boring machine excavation with different spacings

4.4 Impact of Different Depth-To-Diameter Ratios on Surface Settlement

This section aims to investigate the influence of different depth-to-diameter ratios (*H/D*) on surface settlement during tunnel construction. We considered various *H/D* ratios, specifically 2, 3, 4, and 5, which correspond to crown depths of 12, 18, 24, and 30 m, respectively. Numerical simulations were conducted with a 0.31m grouting layer thickness and a tunnel excavation step of 1.2 m. Once the tunneling was complete, we generated lateral surface settlement curves for each *H/D* ratio, as depicted in Fig. 7.

Based on the observations from Fig. 7, we can conclude that the maximum surface settlement of shield tunnels exhibits an increasing trend initially and then decreases as the depth-to-diameter ratio (*H/D*) increases. When *H/D* increases from 1.67 to 2, the maximum surface settlement rises from 6.03 to 9.47 mm. When *H/D* increases from 2 to 3, the maximum surface settlement decreases from 9.47 to 5.63 mm. As *H/D* increases from 3 to 4, the maximum surface settlement further decreases to 5.17 mm. Finally, as *H/D* increases from 4 to 5, the maximum surface settlement decreases to 4.22 mm.

The numerical simulation results for deeply buried tunnels show that the maximum surface settlement exhibits a trend of increasing and then decreasing. This phenomenon occurs because tunnels with relatively small depth-to-diameter ratios ($H/D = 1.67$) have less disturbance to the surrounding soil during excavation, and during the excavation process, the soil naturally forms an arch, which reduces surface settlement. As the depth-to-diameter ratio increases (from $H/D = 1.67$ to 2), the influence zone of the soil arch above the tunnel is limited. With the increase in

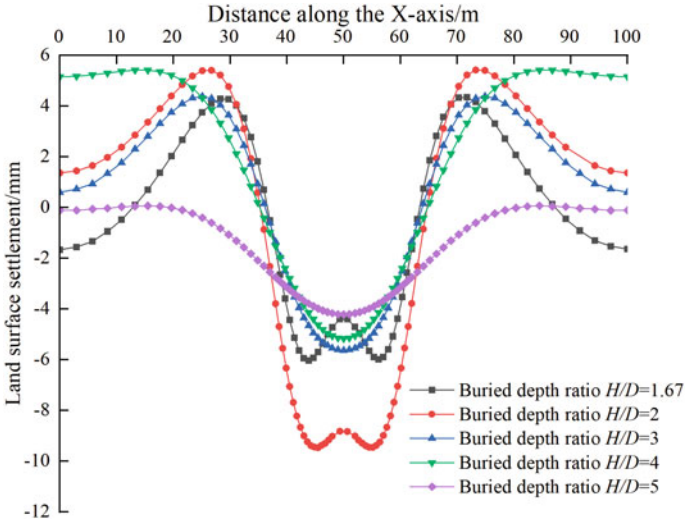

Fig. 7 Lateral surface settlement curves corresponding to tunnel boring machine excavation with different depth-to-diameter ratios

depth, the soil exerts greater pressure on the tunnel. However, at this point, the soil arch above the tunnel cannot provide sufficient support, leading to increased surface settlement. When the depth-to-diameter ratio continues to increase (from 2 to 5), the soil arch gradually forms, and the self-supporting capacity of the surrounding rock is greater than the self-weight stress of the soil. Consequently, the deformation of the soil layer decreases.

4.5 Effects of Different Excavation Pressures on Surface Settlement

In this study, the grouting layer thickness of the tunnel is 0.31m, the burial depth is 10m (the burial depth ratio $H/D = 1.67$), and the excavation step of the tunnel is 1.2m. We considered four different excavation pressures: 100, 142, 200, and 300kPa. After the tunnel is completely excavated, we generated lateral surface settlement curves for various excavation pressures, and these curves are shown in Fig. 8, revealing the lateral surface settlement patterns associated with different excavation pressures.

According to the data from Fig. 8, it is evident that, with all other construction parameters held constant, increasing the excavation pressure leads to an increase in the peak of the lateral surface settlement curve. Specifically, when the excavation pressures are 100, 142, 200, and 300 kPa, the corresponding numerical simulation results indicate that the peak of the lateral surface settlement is 4.27, 6.03, 8.46, and 12.64 mm.

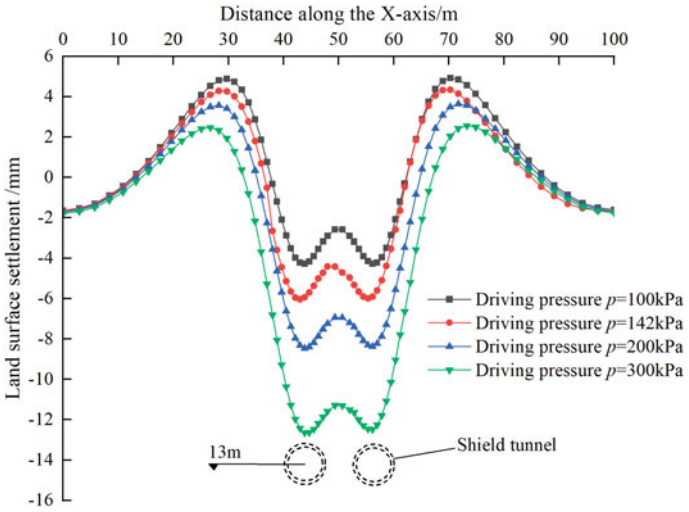

Fig. 8 Shows the lateral surface settlement curves corresponding to different excavation pressures during shield tunneling

When the excavation pressure increases from 100 to 300kPa, the excavation pressure exceeds the static earth pressure of the face, resulting in increased soil disturbance and, in turn, causing an uplift of the soil ahead of the face. This leads to a larger plastic zone in the surrounding soil, resulting in later-stage settlement deformation and an increase in surface settlement.

According to theoretical analysis and engineering experience, the excavation pressure should be slightly less than the stress relief value of the face soil. The differences in disturbances caused by different excavation pressures are relatively small. Therefore, considering both lateral deformation and economic benefits, an excavation pressure of 142 kPa was chosen for the project, which meets the practical requirements.

5 Optimization Analysis of Surface Settlement Deformation

The accuracy of the ABAQUS numerical simulation model was verified based on actual surface settlement data. By varying the selected parameters, we examined the impact of different grouting thicknesses, burial depth ratios, and the distance between the two tunnels on surface settlement. This allowed us to perform an optimization analysis of surface settlement deformation.

(1) Within a certain range, a thicker grouting layer results in better filling of the annular gap at the shield tail, leading to reduced ground settlement during shield excavation. However, based on practical engineering experience, the

grouting layer should not be excessively thick, as it can impact the stress on the surrounding soil and hinder the control of surface settlement. Numerical simulations show that the peak settlement values for grouting radii of 0.3 and 0.31 m are very close, measuring 6.03 and 6.04 mm, respectively. Taking all factors into account, an optimal grouting layer thickness of 0.3 m is recommended. Nevertheless, an actual construction choice of 0.31 m meets construction requirements but results in some material loss.

(2) When the distance between tunnels is small, the mutual interference between them gradually intensifies, leading to increased settlement and deformation in their common disturbance area. In contrast, when the distance between tunnels is larger, the mutual interference effects caused by construction diminish. In this case, ground settlement is considered as the superposition of the independent settlement and deformation effects of the two tunnels. In actual engineering, with a distance of 8m between the two tunnels, the ground settlement is minimal and meets practical requirements.

(3) The maximum settlement due to shield tunnel excavation occurs at the crown of the tunnel. Construction activities disturb the geological layers, and the displacement and deformation of the surface soil decrease with increasing depth. In the actual construction with a depth-to-diameter ratio (*H/D*) of 1.67, the impact on surface settlement is relatively small. If the depth is increased, it is recommended to have a depth-to-diameter ratio of 5 or higher. With greater depth, it is advantageous for the formation of a soil arch, which leads to minimal impact on surface settlement.

(4) Excavation pressure plays a significant role in shield tunnel excavation. The excavation pressure of the shield machine should be lower than the static earth pressure of the face soil. As the excavation pressure increases, it causes less disturbance to the soil, resulting in smaller soil settlement. When the excavation pressure exceeds the static earth pressure of the face soil, it leads to increased soil disturbance and, in turn, causes the uplift of the soil in front of the face, enlarges the plastic zone of the surrounding soil, and results in later-stage settlement and deformation, increasing surface settlement. In this study, an excavation pressure of 142 kPa meets the requirements of the working conditions.

6 Conclusion

This study utilized the ABAQUS finite element software to establish a finite element calculation model for the construction of double-line tunnels for Harbin Metro Line 3. Through the analysis, it was found that the longitudinal surface settlement curves in the numerical simulation data were similar to the actual observed results, with maximum errors in longitudinal surface settlement of 12.61 and 10.56% for the left and right tunnels, respectively. It has been verified that the numerical simulation in this study is reliable. In the context of practical engineering, this study explored the influence of grouting layer thickness, depth-to-diameter ratio, spacing between

the two tunnels, and excavation pressure on surface settlement, and the following conclusions were drawn:

(1) During shield tunnel excavation, ground subsidence is inevitable. Through the analysis of grouting layer thickness, excavation pressure, depth-to-diameter ratio, and the spacing between the two tunnels, the calculated surface settlement curves closely matched the actual settlement curves observed in the field. The maximum vertical settlement was consistently located directly above the tunnel crown. To avoid excessive settlement, during the actual construction process, underground reinforcement techniques such as grouting or soil freezing can be employed to enhance the mechanical properties of the soil, thereby reducing the extent of settlement.
(2) Increasing the grouting layer thickness appropriately can reduce the impact on the ground during shield tunnel construction, resulting in a greater reduction in surface settlement. However, it should be noted that a thicker grouting layer is not necessarily better, as an excessively thick grouting layer can affect the strength of the soil and may lead to resource wastage.
(3) The morphology of ground settlement distribution curves during shield construction of parallel twin tunnels is significantly influenced by the proximity and distance, exhibiting a transition from a "V" shape to a "W" shape. Therefore, in shield tunneling practice, it is recommended to pay special attention to the impact of the relative spacing between twin tunnels on subsurface deformations in order to reduce the impact of shield construction on nearby buildings and the surrounding environment. In the actual construction process, it is recommended to moderately increase the spacing between the two tunnels to reduce the impact on nearby tunnels and surface settlement.
(4) The maximum settlement caused by shield tunnel excavation occurs at the crown position of the tunnel. Construction with a shield machine extends soil disturbance to the surface, and the displacement and deformation of the soil above the tunnel decrease with decreasing soil depth. With an increase in depth, when the soil above the tunnel is thick enough to form a stable soil arch, the peak surface settlement reduces.
(5) During shield tunnel excavation, the excavation pressure significantly exceeds the static earth pressure of the soil, causing soil disturbance and resulting in the uplift of the soil in front of the tunnel face and the expansion of the plastic zone in the surrounding soil. This ultimately leads to increased subsequent surface settlement. Therefore, during the construction process, it is necessary to ensure that the tunneling pressure matches the static soil pressure at the face to minimize surface settlement.

This study solely focuses on factors such as grouting layer thickness, excavation pressure, burial depth ratio, and tunnel spacing, without considering various factors like different soil layers, permeability, excavation speed, among others. Furthermore, due to the complexity of subsurface structures and the non-uniformity of material properties, there is a certain degree of deviation between theoretical results and actual results. Future research will incorporate a comprehensive analysis of various

potential influencing factors and conduct in-depth investigations into the impact of these parameters on both TBM and shaft sinking methods.

Funding: This research was financially supported by the Bingtuan Science and Technology Program (Grant No.2023AB016-02), which are all gratefully acknowledged.

References

1. Mingming Q (2013) Study on prediction of ground deformation induced by shield tunneling in urban metro tunnel [D]. Nanchang Hangkong University
2. Jun H, Zhang D, Guizhen X (2007) Analysis of overlying strata deformation patterns in stacked tunnels [J]. Rock Soil Mech 28(12):5. https://doi.org/10.3969/j.issn.1000-7598.2007.12.029
3. Xiaowu T, Ji Z, Wei L et al (2010) Study on soil deformation during shield tunneling construction [J]. Chin J Rock Mech Eng 2:6
4. Koyama Y (2003) Present status and technology of shield tunneling method in Japan[J]. Tunnel Underground Space Technol Incorp Trenchless Technol Res 18(2/3):145–159. https://doi.org/10.1016/S0886-7798(03)00040-3
5. Park KH (2005) Analytical solution for tunnelling-induced ground movement in clays[J]. Tunnel Underground Space Technol Incorp Trenchless Technol Res 20(3):249–261. https://doi.org/10.1016/j.tust.2004.08.009
6. Xin Z, Jianhui Y, Tao L (2022) Analysis of the impact of shield tunnel construction on the pile foundation of short range side crossing bridges [J]. J Underground Space Eng 002:018
7. Do N-A, Daniel D, Oreste P (2015) 3D numerical investigation on the interaction between mechanized twin tunnels in soft ground[J]. Environ Earth Sci 73(5):2101–2113. https://doi.org/10.1007/s12665-014-3561-6
8. Paternesi A , Schweiger HF, Scarpelli G (2017) Parameter calibration and numerical analysis of twin shallow tunnels[J]. Rock Mech Rock Eng 50(5):1–20. https://doi.org/10.1007/s00603-016-1152-4
9. Wang J, Lu C, Mengyu H (2022) Three-dimensional Numerical simulation analysis and construction suggestions for shield tunneling [J]. Guangdong Civil Arch 29(1):4
10. Zhang Y, Dayong W, Zhuangzhuang Z et al (2022) Numerical simulation analysis of subway shield tunnel construction in Tianjin Binhai Soft Soil Field [J]. Constr Technol (Chinese & English) 51(21):6
11. Zhao G, Wang T, Liu J (2021) Study on surface settlement characteristics of shield tunnel in Nanchang sand stratum [J]. Shanghai Constr Sci Technol
12. Zhi-fu L (2021) Problems and treatment measures of ground settlement in shield construction of subway tunnel [J]. Smart Cities 007(002):149–150
13. Gao M (2020) Research on monitoring and control index of shield construction in high water level silt formation [J]. Eng Res
14. Jiahui Z, Juncai L, Zhengguo Z, Huang F (2021) District shield under wear high-speed sedimentation analysis and construction parameters control [J]. J Nanjing Univ Technol Nat Sci https://doi.org/10.3969/j.iSSN.1671-7627.2021.01.018
15. Dezhi W, Fangyi N, Rui W et al (2023) Analysis of impact of shield tunnel under surface buildings [J]. Eng Qual 41(5):66–69 (in Chinese)
16. Liu J, Lu J, Dongdong X (2019) Double shield tunnel excavation surface settlement deformation law research [J]. J Urban Surv (5):6
17. Jun D, Qiang J (2019) Near the earth's surface caused by shield tunnel construction building subsidence study [J]. J Shandong Const Univ 34(5):7
18. Xiu Y, Linlin W (2019) Subway shield interval through sand layer and the impact analysis in both buildings [J]. Railway Surv 45(2):6

The Close Proximity Impact of a Newly Constructed Large Cross-Section Twin-Arch Tunnel Crossing an Existing Tunnel

Dapeng Hai, Liangwen Wei, Guoqi Su, Jie Zheng, Dan Wang, Wei Tian, Yu Tang, and Zejian Hua

Abstract With the Xinsen Avenue Tunnel Project in Chongqing Gaoxin District as the research context, this study investigates the degree of impact on an existing tunnel resulting from the construction of a new twin-arch tunnel that crosses over it. Utilizing finite element analysis methods, the study explores the displacement and stress variation patterns in the existing tunnel following the construction of the new tunnel, considering different clearances, crossing angles, and rock mass grade factors. Additionally, based on a composite discernment criterion involving additional stress and additional displacement, this study establishes longitudinal and transverse impact zones for intersecting tunnels. The research findings reveal that in terms of longitudinal impact, the clearance factor exerts a more substantial influence compared to rock mass grade and crossing angle factors. Regarding transverse impact, the area affected by parallel undercrossing is greater than that of parallel overcrossing, and the impact area is minimized when the new and existing tunnels are in a horizontally side-by-side configuration. The study's conclusions provide a theoretical basis and practical reference for the control of construction in similar large cross-section tunnel intersections.

Keywords Twin-arch tunnel · Existing tunnel · Numerical simulation · Impact zones

D. Hai · G. Su · J. Zheng · D. Wang · W. Tian
China Construction Seventh Engineering Division Corp. LTD, Zhengzhou 45004, China
e-mail: 19401427@qq.com

L. Wei (✉) · Y. Tang · Z. Hua
Scholl of Civil Engineering, Chongqing Jiaotong University, Chongqing 400074, China
e-mail: weiliangwen@163.com

G. Mei et al. (eds.), *Advanced Construction Technology and Research of Deep-Sea Tunnels*, Lecture Notes in Civil Engineering 490,
https://doi.org/10.1007/978-981-97-2417-8_15

1 Introduction

To alleviate the increasingly congested urban surface traffic conditions, the development and utilization of urban underground space have become a current trend, giving rise to underground interchange tunnel projects [1, 2]. This inevitably raises the issue of constructing new tunnels in close proximity to existing ones. The original stress and deformation fields around the existing tunnels will undergo significant changes due to the excavation of the neighboring new tunnels [3]. The research aims to assess the extent of the impact on existing tunnels during the construction of new tunnels, and based on the impact zones, formulate relevant control measures.

Currently, there have been some achievements in the research on impact zoning for tunnel proximity construction. Internationally, the Japan Railway Technical Research Institute [4] has systematically elaborated on tunnel proximity projects and proposed criteria for tunnel proximity levels. In China, Wenge Qiu [5] has further delved into proximity and introduced proximity zone guidelines. Wenhao Fan [6] conducted a study on the impact zones when a new double-line shield tunnel passes beneath an existing tunnel, using displacement criteria. Xianguo Wu [7] conducted a proximity study based on the increment of stress in existing tunnels, considering different tunnel spacing ratios and burial depth ratios under various conditions. Charle [8] through a series of three-dimensional centrifugal tests, the response of an existing tunnel in sandy soil to the excavation of a new tunnel perpendicular to it is studied. Kim et al. [9] carried out a series of tunnel–tunnel interaction tests using a 1g model in clay. They found that the section of the existing tunnel directly above the new tunnel was vertically compressed due to the large jacking force induced by the installation of the liner of the new tunnel.

In the aforementioned studies, tunnel impact zones are typically divided using a single discernment criterion. In this paper, based on the Xinsen Avenue Tunnel Project in Chongqing Gaoxin District, we propose a composite discernment criterion involving additional displacement and additional stress in the existing tunnel. This criterion is employed to study the impact zones when a new twin-arch tunnel passes over an existing tunnel.

2 The Mechanical Principles of Tunnel Proximity Construction

Tunnel excavation leads to stress redistribution within a certain range, and in cases of underground projects involving proximity construction, multiple stress alterations occur, making structural loading more intricate.

2.1 Initial Stress State

Before tunnel excavation, the rock mass is in a balanced and stable state of stress. In the numerical simulations in this paper, the initial stress state only takes into account the self-weight stress field. The expressions for the vertical stress at a depth of h are as follows:

$$\sigma_z = \lambda_1 h_1 + \gamma_2 h_2 + \cdots + \gamma_n h_n = \sum_{i=1}^{n} \lambda_i h_i \tag{1}$$

In the equation, λ represents the bulk density of the rock or soil, and h stands for the thickness of the overlying rock or soil.

2.2 The Secondary Stress State After Tunnel Excavation

In the excavation of a circular tunnel with a radius of a, the elastic secondary stress state around the tunnel can be expressed as follows:

Radial Stress:

$$\sigma_r = \frac{\sigma_y}{2}[(1-\alpha^2)(1+\lambda) + (1-4\alpha^2+3\alpha^4) \times (1-\lambda)\cos 2\phi] \tag{2}$$

Tangential Stress:

$$\sigma_t = \frac{\sigma_y}{2}[(1+\alpha^2)(1+\lambda) - (1+3\alpha^4) \times (1-\lambda)\cos 2\phi] \tag{3}$$

In the equations: $\alpha = a/r$, a represents the tunnel radius, and r represents the radial distance to the tunnel center; $\lambda = \sigma_X/\sigma_y$, σ_y represents the initial stress, and ϕ denotes the friction angle within the surrounding rock.

3 Leveraging Project Overview

Based on the Xinsen Avenue Tunnel Project in Chongqing Gaoxin District. The new twin-arch tunnel passes over the existing Gaoteng Avenue Tunnel in an area where the geological formations consist mainly of moderately weathered mudstone with interbedded sandstone, and the surrounding rock grade is ranging from IV to V. The overburden thickness ranges from 16.6 to 25.6 m, the tunnel height is 12.2 m, the width is 16.5 m, and the tunnel excavation cross-sectional area is approximately 400 square meters. The hidden excavation section of the Xinsen Avenue Tunnel starts at station K1 + 100 and extends to K1 + 255, with a length of 155 m. The clear distance

Fig. 1 A practical view of the Xinsen avenue tunnel entrance construction

between the crowns of the Xinsen Avenue Tunnel and the Gaoteng Avenue Tunnel is only 6 m. Taking into account various factors, the decision was made to employ the dual-side-wall pilot tunnel method for the construction of the new twin-arch tunnel. The site construction drawing is shown in Fig. 1.

4 Establishing the Numerical Model

4.1 Basic Assumptions

In this study, numerical simulations are conducted using Midas GTS NX, based on the following basic assumptions: (1) The geological materials are homogeneous and isotropic, and the ground surface is horizontal. (2) The existing tunnel is treated as a homogeneous solid, with initial structural loading considered only for the self-weight of the soil. (3) Since the tunnel deformation mainly occurs during the initial support construction phase, and the secondary lining is primarily for safety reserves, it is not simulated.

4.2 Model Dimensions and Parameter Settings

A three-dimensional elasto-plastic constitutive model is established, using the Mohr–Coulomb criterion as the plastic failure criterion. The soil is simulated using 3D

solid elements, while the initial shotcrete is simulated using 2D plate elements. To eliminate boundary effects, the dimensions of the foundational model in this paper are set as 180 m*160 m*100 m, as depicted in Fig. 2. Material parameters and model calculation conditions are shown in Tables 1 and 2.

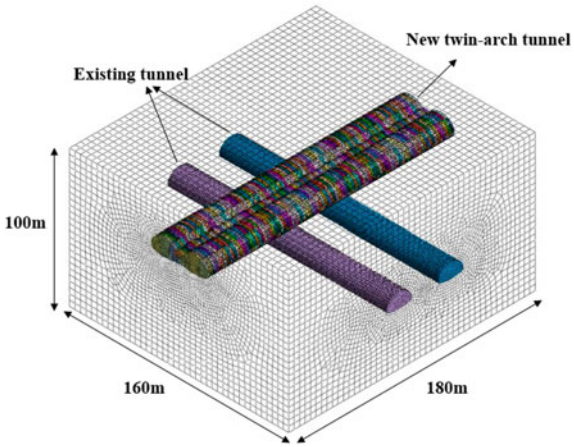

Fig. 2 Numerical calculation model

Table 1 Model parameters

Name	Elastic modulus E/ GPa	Poisson's ratio μ	Internal friction angle Φ/°	Cohesive strength c/ MPa	Bulk density λ/ (kN/m^3)
Initial support	15	0.2	/	/	24
Partition Wal	42	0.2	/	/	26
Temporary support	25.2	0.25	/	/	24
Grade III surrounding rock	20	0.25	50	1.5	25
Grade IV surrounding rock	7	0.3	39	0.7	23
Grade V surrounding rock	2	0.35	27	0.2	20

Table 2 Calculation conditions of the model

Operating condition	Basis of division	Spacing	Included angle	Surrounding rock grade
1	Vertical clear distance	H = 0.5D	α = 90°	V
2		H = 1D	α = 90°	V
3		H = 2D	α = 90°	V
4		H = 4D	α = 90°	V
5	Surrounding rock grade	H = 1D	α = 90°	III
6		H = 1D	α = 90°	IV
7		H = 1D	α = 90	V

4.3 Criteria for Impact Zoning.

This paper chooses a composite criterion based on additional stress and displacement as the basis for determining the impact zones when the new double-line shield tunnel passes beneath the existing tunnel. Currently, there is no unified standard in China for defining impact zones in the case of a new tunnel being in proximity to an existing tunnel. Therefore, on the basis of references [10, 11], a composite criterion considering the rate of additional stress change and additional displacement in the existing tunnel is used as the basis for determining the impact zones. The maximum range of influence for both criteria is considered, and the areas affected by the construction of the new tunnel are divided into zones. It is defined here that an additional stress change rate of 15% and 5% in the existing tunnel caused by the construction of the new tunnel is used as thresholds for strong, weak, and no impact zones. The rate of additional stress change can be expressed as:

$$\omega = \left| \frac{\sigma_1 - \sigma_2}{\sigma_1} \right| \times 100\% \tag{4}$$

In the equation, σ_1 represents the initial stress value of the existing tunnel structure before the excavation of the new tunnel, and σ_2 is the maximum stress value in the existing tunnel structure after the excavation of the new tunnel.

5 Longitudinal Impact Zoning of New Tunnel Overcrossing Construction on the Existing Tunnel

5.1 Longitudinal Impact Zoning of New Tunnel Construction on the Existing Tunnel Under Different Vertical Clear Distances

Four different calculation scenarios (0.5D, 1D, 2D, 4D) were defined based on the ratio of the clear distance between the two tunnels to the diameter of the existing tunnel (H/D). The study examined the relationship between the deformation of the existing tunnel and the vertical clear distance between the two tunnels during the construction of the new tunnel. Maximum additional displacement values and the maximum rate of additional stress change were extracted for various locations in the existing tunnel, including the crown, left and right sidewalls, and the bottom, as shown in Figs. 3 and 4.

From Fig. 3, it can be observed that when the new double-arch tunnel is constructed above the existing tunnel, the existing tunnel exhibits an overall uplift deformation. The maximum vertical displacement occurs at the overlap section between the new and existing tunnels. Additionally, the additional displacement at various locations decreases as the vertical net distance between the new and existing tunnels increases.

Figure 4 shows that as the spacing increases, the maximum stress change rate of the existing tunnel gradually changes from an "M" shape to an inverted "V" shape, eventually becoming almost a horizontal straight line. The variation pattern of the maximum stress change rate of the existing tunnel is roughly similar to the pattern of additional displacement change in the existing tunnel.

Based on the above zoning criteria, the longitudinal impact partition diagram of the existing tunnel under different vertical net distances can be obtained, as shown in Fig. 5.

From Fig. 5, it is evident that the impact zone of the existing tunnel, due to the construction of the new tunnel crossing over it, changes significantly with variations in the net distance between the two tunnels. When the net distance between the new and existing tunnels is 0.5D, the longitudinal impact zone of the existing tunnel (strong impact zone + weak impact zone) is the largest. However, when the distance between the two tunnels increases to 4D, the existing tunnel is entirely within the no-impact zone.

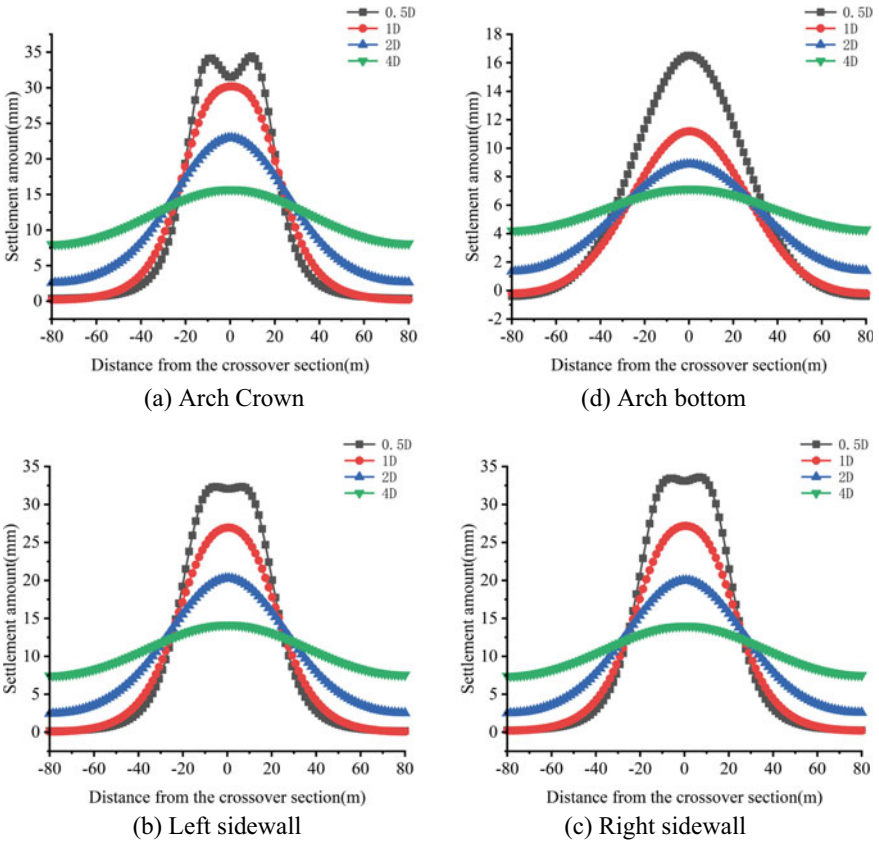

Fig. 3 Additional vertical displacement of existing tunnels with different clearances

Fig. 4 Maximum rate of change of stress in existing tunnels with different clearances

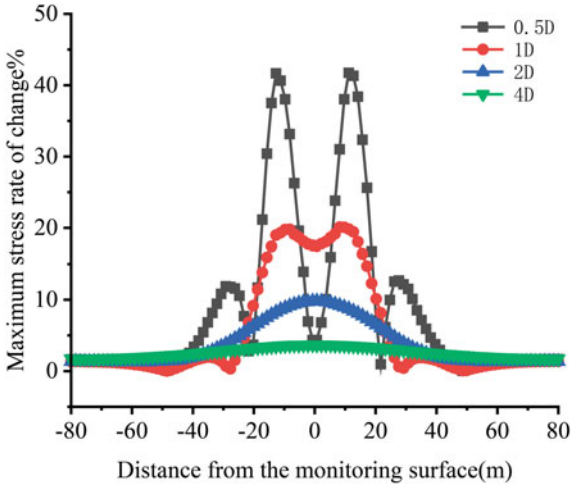

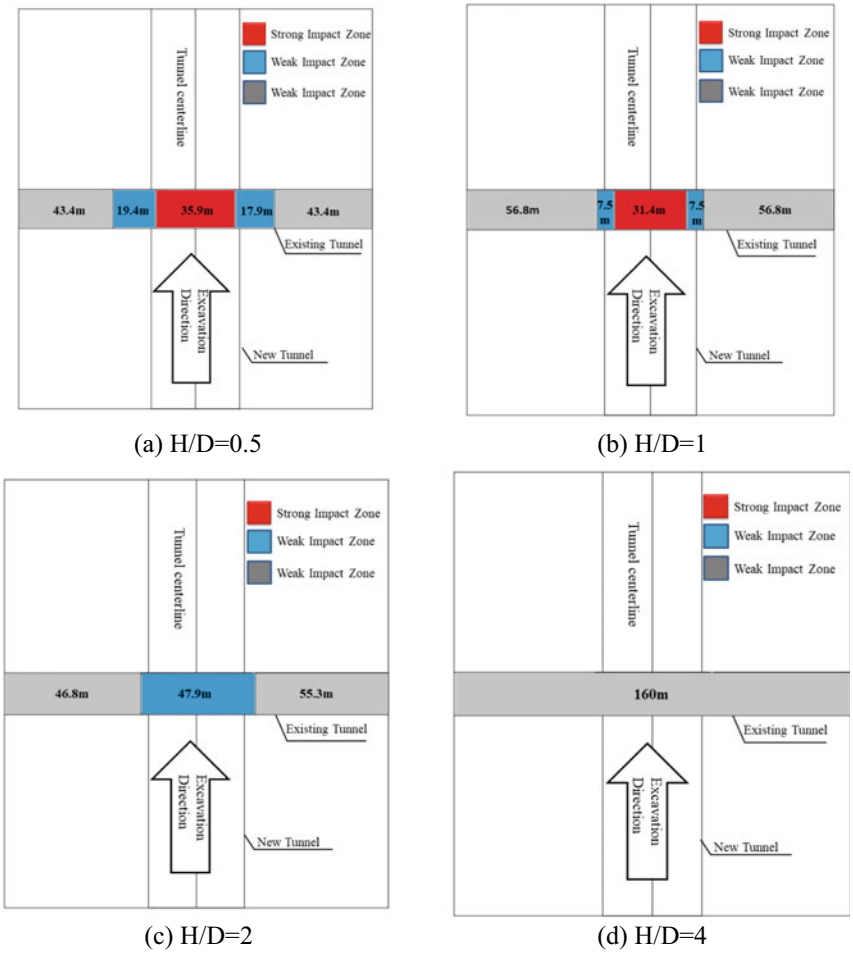

Fig. 5 Vertical impact zoning of existing tunnels with different vertical clear distances

5.2 Different Surrounding Rock Grade's Impact on the Longitudinal Impact Zones of the Existing Tunnel During New Tunnel Construction

Using the finite element software Midas GTS, maintaining a constant vertical overlap angle and net distance between upper and lower crossing tunnels at 90° and 1D, respectively, the rock mass levels are sequentially changed to III, IV, and V. This analysis investigates the impact of new double-arch tunnel construction on the mechanical properties of the surrounding rock and support structures of the existing tunnel for different rock mass levels. The results are presented in Figs. 6 and 7.

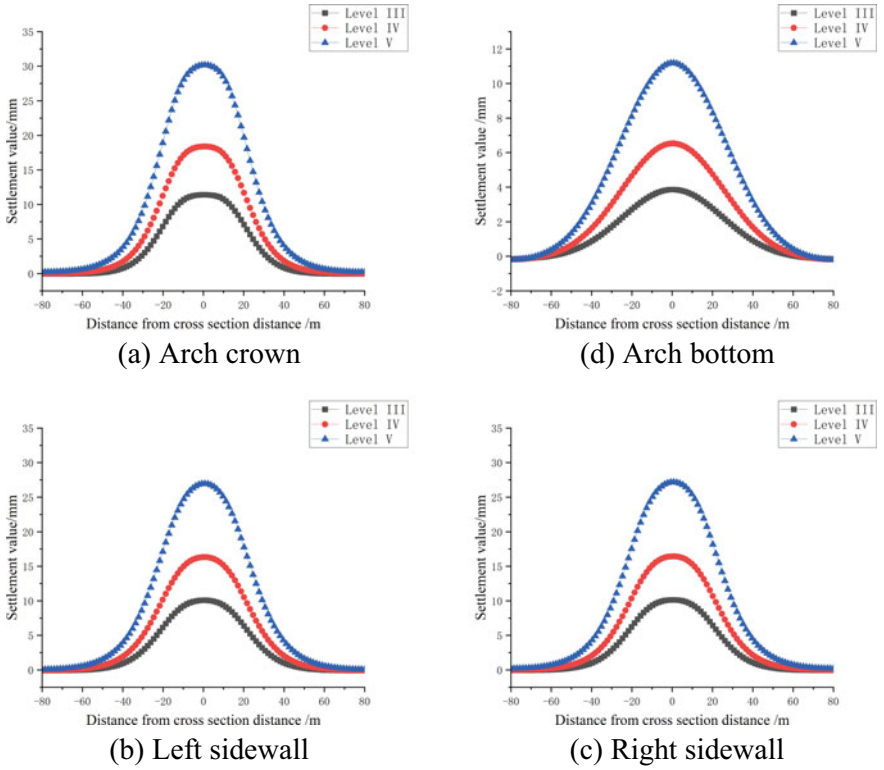

Fig. 6 Additional vertical displacement of existing tunnels under different surrounding rock grades

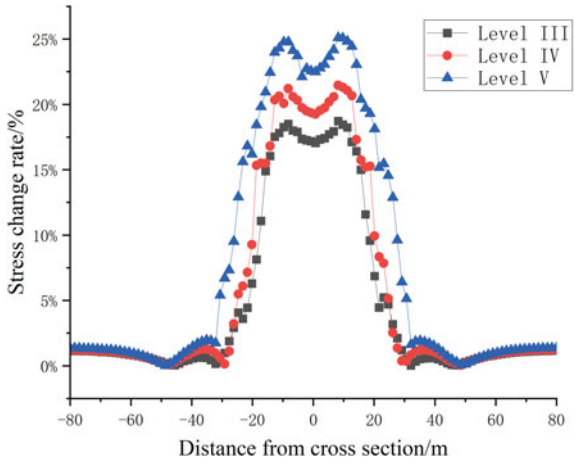

Fig. 7 Maximum rate of change of stress in existing tunnels under different surrounding rock grades

From Figs. 6 and 7, it can be observed that with a decrease in the surrounding rock grade, the vertical additional displacement increments and additional stress change rate generated in the lining of the existing tunnel due to the construction of the new tunnel gradually increase. For different surrounding rock grades, the maximum vertical displacement increments and additional stress change rate at each monitoring location occur in the overlapping sections of the upper and lower tunnels. The vertical displacement increments and additional stress change rate in the surrounding rock of the existing tunnel gradually decrease as you move away from the intersection point.

Based on the above zoning principles, different longitudinal impact zones of the existing tunnel under different surrounding rock grades can be determined, as shown in Fig. 8.

From Fig. 8, it can be observed that with the same net distance and crossing angle between the new and existing tunnels, as the surrounding rock grade increases, the longitudinal impact range of the new double-arch tunnel construction on the existing tunnel gradually decreases. Under Grade III surrounding rock conditions, the range of the unaffected zone in the existing tunnel is 119.6 m, the range of the weakly affected zone is 12 m, and the range of the strongly affected zone is 28.4 m. Under Grade IV surrounding rock conditions, the range of the unaffected zone in the existing tunnel is 110.6 m, the range of the weakly affected zone is 12 m, and the range of the strongly affected zone is 37.4 m. Under Grade VI surrounding rock conditions, the range of the unaffected zone in the existing tunnel is 98.6 m, the range of the weakly affected zone is 15 m, and the range of the strongly affected zone is 46.4 m.

6 Transverse Impact Zoning of New Tunnel Crossing Construction on Existing Tunnel

By changing the orientation angle between the new and existing tunnels, a two-dimensional model is established to simulate the impact of new tunnel overcrossing and undercrossing construction on the existing tunnel. Simultaneously, the relative spacing between the new and existing tunnels is altered. Five groups of relative net distances are selected from close to far (0.5D, 1D, 2D, 3D, 4D), and nine sets of relative angles are chosen (0°, -30°, -45°, -60°, -90°, 30°, 45°, 60°, 90°). The model dimensions are 240 m in the horizontal direction and 200 m in the vertical direction. Material parameters are consistent with those mentioned earlier. The layout for the parallel adjacent condition of the two tunnels is shown in Fig. 9.

Based on the above scenarios, numerical simulations were conducted using the finite element software Midas GTS. The maximum vertical displacement and stress change values of the existing tunnel were extracted and obtained, with results shown in Figs. 10 and 11.

Based on the simulation results shown in Figs. 10 and 11, the influence boundary values based on the additional displacement criteria and the additional stress criteria were obtained using linear interpolation. The maximum value between the two was

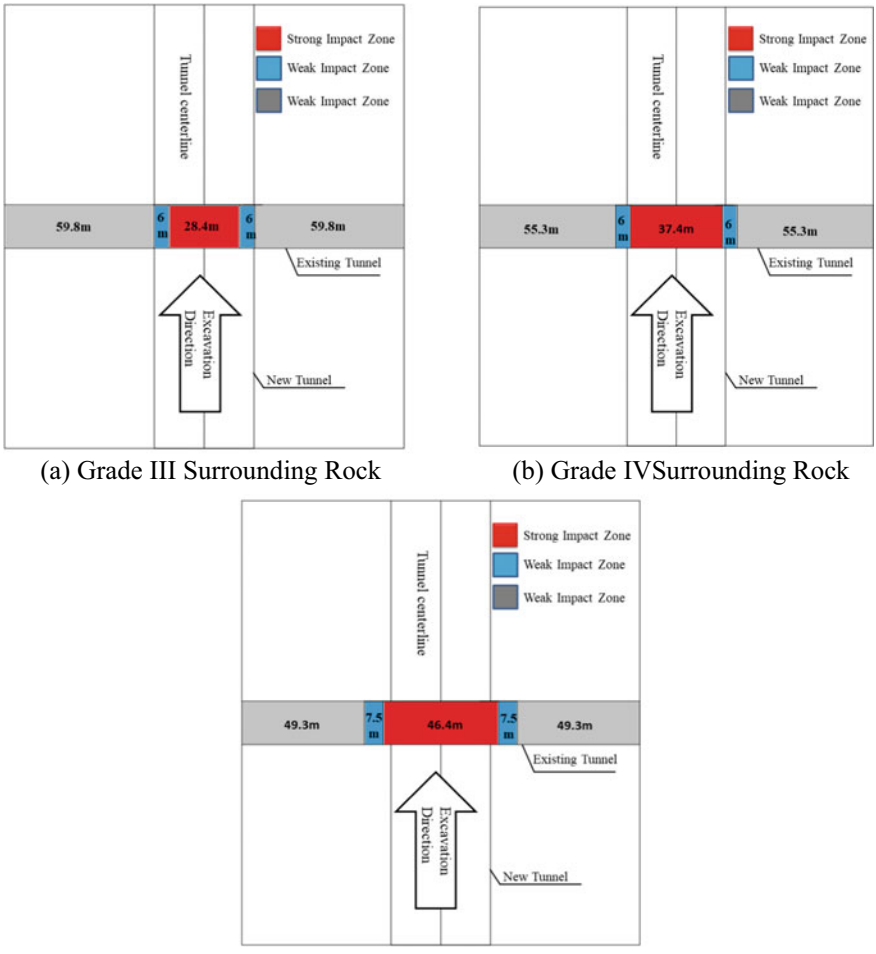

Fig. 8 Vertical impact zoning of existing tunnels with different rock grades

used as the standard for dividing the influence zones for the composite criteria. The final result is the impact zone map for the new tunnel adjacent to the existing tunnel, as shown in Fig. 12.

From the lateral impact zone map in Fig. 12, it is clear that the impact range of the new tunnel's upward construction is generally smaller than the impact range of the new tunnel's downward construction.

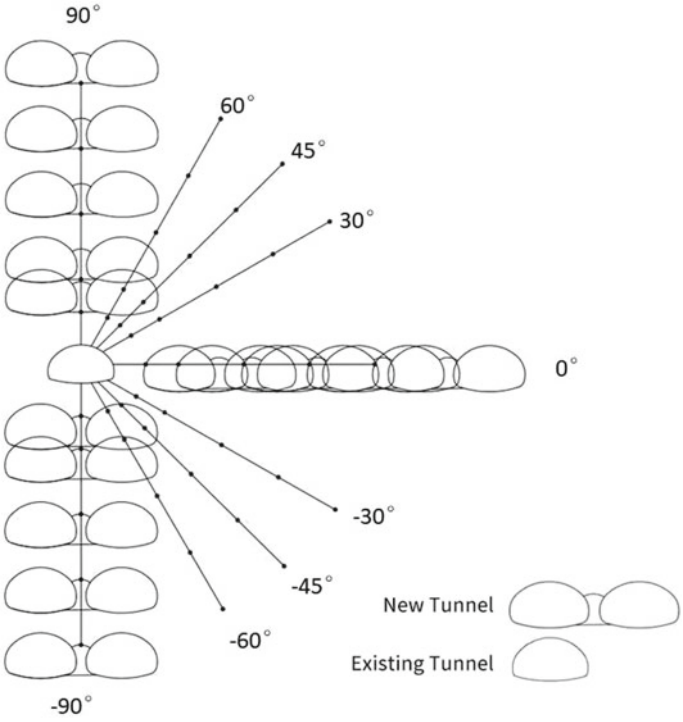

Fig. 9 Two tunnels parallel close working condition

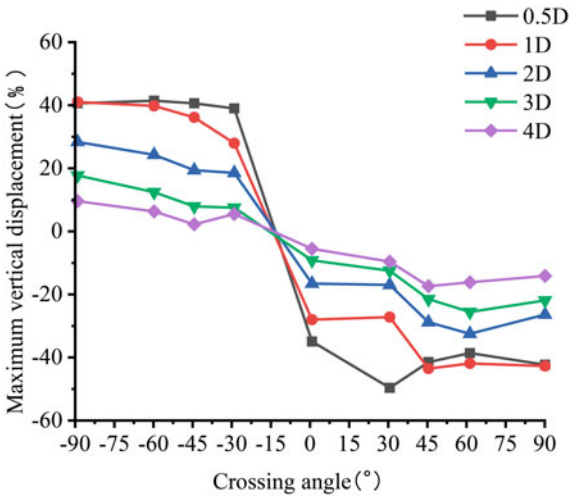

Fig. 10 Maximum vertical displacement of the existing tunnel

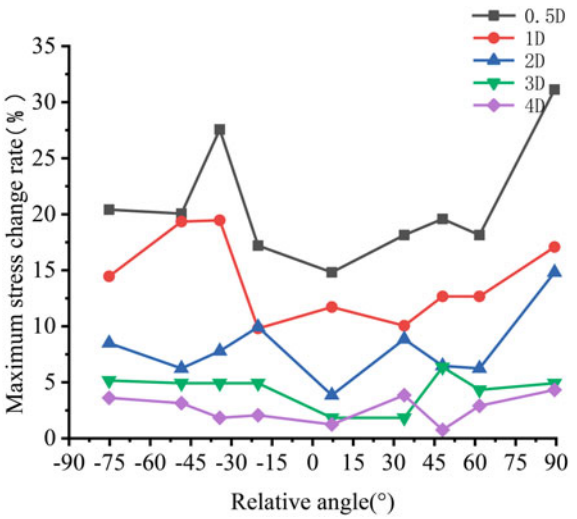

Fig. 11 Maximum rate of change of stress in existing tunnels with different clearances

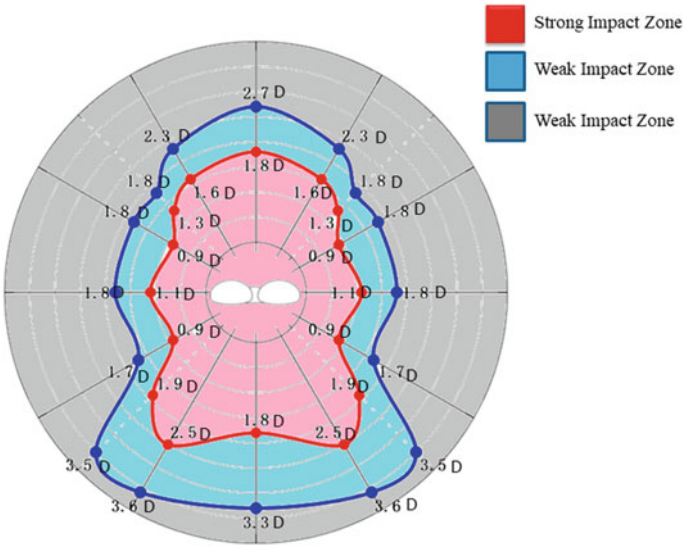

Fig. 12 Lateral impact zone map of the new tunnel adjacent to the existing tunnel

7 Conclusion

(1) When the vertical clearance of the interchange tunnel is less than 2D, the overlapping section of the existing tunnel is in the strong impact zone of the new tunnel construction. When the vertical clearance increases from 2 to 4D, the original weak impact zone of the existing tunnel becomes an unaffected zone.

Changing the rock grade can lead to the presence of strong, weak, or unaffected zones within the existing tunnel. As a result, the influence of the vertical clearance factor is more pronounced than that of the rock grade factor.

(2) Regarding the lateral influence of new tunnel construction on existing tunnels: the maximum impact range for parallel upward crossing is 2.7D, and for parallel downward crossing, it is 3.6D, while horizontal parallel construction has the smallest impact range of only 1.8D. This shows that the impact range for parallel downward crossing is greater than that for parallel upward crossing. When the new and existing tunnels are in a horizontally parallel relationship, their impact range is the smallest.

(3) This study considered the impact of factors such as vertical clearance, crossing angle, and rock grade, but did not encompass factors such as tunnel support parameters and excavation methods. Further research is needed in the future.

Funding This research was jointly supported by the National Natural Science Foundation of China (Project No. 52204087) and the Science and Technology Project of the Chongqing Municipal Education Commission (Project No. KJQN202200746).

References

1. Cao L, Fang Q, Zhang D et al (2018) Subway station construction using combined shield and shallow tunnelling method: Case study of Gaojiayuan station in Beijing [J]. Tunn Undergr Space Technol 82:627–635
2. Yuan W, Fu HL, Zhang JB et al (2018) Analytical prediction for tunneling-induced ground movements with modified deformation pattern[J]. Int J Geomech 18(6):04018039
3. Fu J, Zhao N, Qu Y et al (2022) Effects of twin tunnel undercrossing excavation on the operational high speed railway tunnel with ballastless track[J]. Tunn Undergr Space Technol 124:104470
4. Brox D (2017) Practical guide to rock tunneling[M]. CRC Press
5. Qiu W (2003) Research on mechanics principle and countermeasures of underground engineering proximity construction [D]. Guan Baosu. Southwest Jiaotong University, Tutor
6. We F, Xie S, Zhou F et al (2023) Case study on proximity impact zoning and control measures of new double-track shield tunnel under existing tunnel [J]. Modern Tunnel Technol 60(04):43–57
7. Wu X, Yang S, Tian J et al. (2021) Analysis of the influence of shield tunneling construction on the proximity of existing tunnels and research on proximity zoning[J]. J Civil Eng Manag 38(04):96–109+114
8. Ng CWW, Boonyarak T, Mašín D (2013) Three-dimensional centrifuge and numerical modeling of the interaction between perpendicularly crossing tunnels. Can Geotech J 50(9):935–946. https://doi.org/10.1139/cgj-2012-0445
9. Kim SH, Burd HJ, Milligan GWE (1998) Model testing of closely spaced tunnels in clay. Géotechnique 48(3):375–388. https://doi.org/10.1680/geot.1998.48.3.375
10. He J (2018) Study on the mechanical behavior of asymmetric closely adjacent tunnels construction process[D]. Beijing Jiaotong University, Beijing
11. Wang J (2020) Study on the construction mechanical effect and stability of new overpass tunnel undercrossing existing tunnel at a short distance[D]. Chongqing University, Chongqing

Influence of Seepage Pressure Loading History on the Progressive Fracture Process of Concrete

Xiaofeng Xu

Abstract The historical data of seepage pressure and flow rate can be used to speculate to some extent the development process of concrete micro crack structures. Based on the dynamic propagation of cracks in concrete measured in triaxial seepage tests, an equation reflecting the relationship between the dynamic size of cracks and the seepage rate was established, and a practical method for predicting the propagation process of micro cracks in concrete was obtained by measuring the seepage water flow rate through experiments.

Keywords Seepage pressure · Water flow · Micro cracks · Concrete

1 Introduction

With the series of measures taken by Beijing to tap new sources of groundwater and to conserve existing groundwater, as well as the commissioning of the Middle Route of the South-to-North Water Diversion Project in 2014, the groundwater level in Beijing has inevitably rebounded, forming a new urban groundwater environment [1]. Regardless of the structural form of the subway tunnel, the main building material is concrete, and the safety of the subway tunnel depends largely on the mechanical properties of the lining concrete material. The deformation and failure behavior of concrete materials are essentially the result of the evolution of internal micro cracks (micro pores), and understanding the micro structure of micro cracks helps to understand macroscopic behavior. In addition to utilizing micro mechanical methods such as CT scanning and ultrasonic testing to understand the micro structure of micro cracks, historical data on seepage water pressure and flow rate can also be used to speculate to some extent on the development process of micro cracks.

X. Xu (✉)
School of Architectural and Survey & Mapping Engineering, Beijing Polytechnic College, Beijing 10042, China
e-mail: 344514996@qq.com

G. Mei et al. (eds.), *Advanced Construction Technology and Research of Deep-Sea Tunnels*, Lecture Notes in Civil Engineering 490,
https://doi.org/10.1007/978-981-97-2417-8_16

The subway section is built in underground rock and soil mass, and some structures are under the action of water pressure for a long time. When the groundwater level rises, it may lead to cracking, water seepage, floating and structural corrosion of some section structures [2]. However, the subway lining generally bears the load of traffic during the operation stage, and the complex stress state and structural design only consider the mechanical properties of concrete under unidirectional stress state, which varies greatly [3]. Due to insufficient understanding of the influence of pressure water on the performance of subway concrete materials [4–7], the current subway structural design specifications do not take pressure water into consideration, and only rely on artificially increasing the design strength of the lining. This not only lacks scientific basis, but also is not conducive to reducing construction costs. At present, the mechanical property tests and theoretical research of concrete under water pressure stress need to be further explored, and it is urgent to strengthen research to further reveal the influence of seepage water pressure on the fracture process of concrete.

The deformation and failure of concrete materials are essentially the result of internal micro cracks (micro-pores) under external load. Research on micro crack structures is helpful for studying the failure behavior of concrete. Currently, there are many studies on micro crack structures using CT scanning, ultrasonic detection, and other methods [8–13]. This article reveals the development process of concrete micro cracks through the study of the process of seepage pressure loading and the flow rate in cracks.

2 Experimental Design

2.1 Experimental Method and Sample Preparation

The triaxial-seepage coupling experiments are completed on the TAW-3000 electro-hydraulic servo rock triaxial testing machine. The parameters of the testing machine are shown in the literature 1 [14], the experiment was conducted with axial loading at a strain rate of 10^{-4}/s.

The sampling size on the standard concrete test block is ϕ 49 $\times$ 98 mm, and the time for the 4Mpa permeating water pressure to act on the concrete test piece is 48 h. After the pressure is applied, the test piece is soaked in non-pressure water for more than 6 h, and after the internal pressure gradient dissipates, the coupling test is performed (Fig. 1).

Fig. 1 TAW-3000 electro-7hydraulic servo rock triaxial testing machine

2.2 Results of the Experiment

The test results are shown in the Table 1. The failure state of the concrete specimen after the test is shown in Fig. 2.

Table 1 Experimental results under triaxial-seepage coupling conditions

Confining pressure (MPa)	Permeating water pressure (MPa)	$\sigma_{1p(MPa)}$		ε_{1p} (×10–3)		ε_{2p} (×10–3)		$E_{c.}$(Gpa)	
		Test value	Average value	Test value	Average value	Test value	Average value	Test value	Average value
5	4	131.33	129.96	3.69	3.83	-1.31	-1.23	4.78	-4.33
		127.89		3.62		-1.16		4.22	
		130.65		4.18		-1.21		3.99	

Fig. 2 Failure model of concrete samples subjected to triaxial-seepage coupling conditions

3 Analysis Method and Principle of Historical Data of Seepage Water Pressure and Flow

The impermeability of concrete is very strong, and external water can only move through the cracks that have formed inside the specimen under the action of water pressure. Assuming that the water transport process in concrete follows the law of fracture seepage, the following relationship exists between flow rate, water pressure, and crack parameters:

$$\dot{q} \propto \frac{Nd^m}{L}(\sigma_w\prime - \sigma_w) \tag{1}$$

q、$\dot{q}$-total water injection quantity, volume flow;

σw、$\sigma_w\prime$-Pore water pressure (water pressure inside the test piece), seepage water pressure (pump pressure at the end of the test piece);

L.d and *N* -the effective length, width, and number of dynamic hydraulic cracks;

m- Experience index (generally > 1).

The 'effective' crack size refers to the portion of the crack that can be in contact with water and allow water to flow through it. For example, if the width of a water-containing crack is too small for water to flow through it, then the crack width $d = 0$ and does not contribute to the total number of cracks *N*.

As crack growth inevitably increases with crack length, width, and number, it will inevitably be reflected in changes in flow rate and water pressure according to the above formula. Conversely, the crack growth can also be inferred by the flow rate and water pressure.

It should be noted that the axial equal strain rate loading method was used in this experiment, and the derivative of the cumulative water injection rate *q* with respect to axial strain measured in the experiment is equivalent to the flow rate in the formula. In addition, during the crack propagation process, the length *L*, width *d*, and even the number *N* of cracks will increase, but the rates of increase are different. The length L usually increases much faster than the width *d*, while the rate of increase of the number *N* of cracks varies at different stages of crack propagation.

4 Analysis Results of Historical Data of Seepage Water Pressure and Flow

Taking the typical test of concrete under the conditions of confining pressure of 5 Mpa and seepage pressure of 4 Mpa as an example, the change curves of relevant physical quantities are plotted in Fig. 3. As the external load increases, the length, width, and number of cracks in the concrete increase, and the amount of water pumped in also increases with the increase in the number of cracks and the expansion of

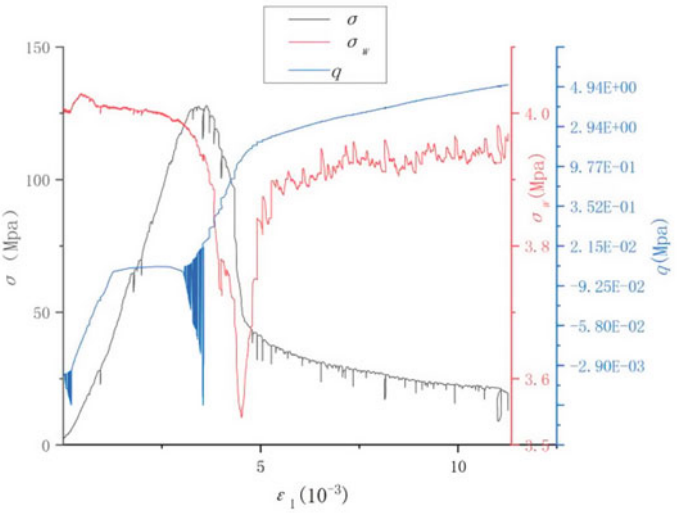

Fig. 3 History curves of water volume and pressure (confining pressure equals to 5 MPa, Axial loading rate equals to 10^{-4}/s)

cracks. However, the growth of each physical quantity exhibits the following stage characteristics as the cracks expand:

① Stage 1: As shown in the q-ε curve in Fig. 3, the slope (volume flow $\dot{q}$) of the curve in this stage is negative, and according to formula (1), the pore pressure σ_w > pump pressure $\sigma_w\prime$. . This indicates that the axial load level at the beginning of loading is not high (the axial pressure is set to 1 kN at the beginning of the test), the Poisson effect is not obvious, and the constraint of confining pressure (5 MPa) leads to the compaction of internal pores. The pore water generates high pressure ($\sigma_w > \sigma_w\prime$) due to compression, and finally flows $\sigma_w\prime$ out under the action of pressure difference. At the beginning of the pump pressure adjustment process, the water squeezed into the interior of the test piece was gradually compressed and discharged back, resulting in pump body backflow.

Further analysis of the shape of the q-ε curve during this stage reveals that the concave shape indicates a rapid $\dot{q}$ decrease in flow velocity, while the water pressure $\sigma_w\prime$ gradually decreases during this stage. According to the formula, the pore pressure σ_w must decrease at a faster rate. The most likely cause of the rapid decrease in σ_w is the increase in pore volume, indicating that the pores (microcracks) have begun to expand during this stage.

The end point of this stage is the lowest point of water injection on the q-ε curve (the point corresponding to $\dot{q} = 0$), which is also the critical point of hydraulic crack propagation. Before this point, the crack hardly propagates (mainly due to dilatancy), and after this point, the crack enters the propagation stage. Therefore, this critical

point of crack propagation is close to the damage point on the stress–strain curve (the q-ε curve shown in Fig. 3).

② Stage 3: This phase $\dot{q}$ rapidly rises as the deformation increases, and simultaneously $\sigma_w{}'$ rapidly decreases (Fig. 1). According to the above formula, Nd^m/L is bound to increase rapidly. Further analysis reveals that due to the fact that cracks have just initiated in this phase, the crack propagation rate should not be very high, meaning that the increase rates of L and d are not significant. As a result, the sharp increase in water injection in this phase is mainly due to the rapid increase in the number of cracks N. In other words, this phase is mainly a stage of rapid initiation of hydraulic cracks.

③ Stage 3: The starting point of this stage is the turning point of the water pressure curve from a decreasing trend to an increasing trend, which basically corresponds to the inflection point of the water injection curve. From Fig. 1, it can be seen that the q-ε curve in this stage is convex upward, with the slope gradually decreasing and tending to a stable value. At the same time, the water pressure increases rapidly, and eventually also tends to a stable value. According to the formula, $\dot{q}$ rapid decrease and $\sigma_w{}'$ rapid increase inevitably lead to a decrease in Nd^m/L at a faster rate. However, in this stage, N has basically increased to its maximum value, and d will only increase and cannot decrease, so the crack length L will inevitably extend at an unprecedented speed until the test piece is completely penetrated to form a macroscopic fracture crack. When the penetrated macroscopic crack appears, L, d, and N all stop growing (in fact, the stability of d also requires a certain residual strength as a guarantee), the crack stops expanding, and the flow rate $\dot{q}$ is also stable under constant pump $\sigma_w{}'$ pressure, maintaining a stable seepage state.

5 Conclusions

In summary, through the analysis of the flow and water pressure history curves in the concrete triaxial-seepage coupling test, some information about crack propagation can be obtained qualitatively or even quantitatively (with the help of appropriate fluid–solid coupling models). If combined with stress–strain curve collaborative analysis, more information can be obtained. However, it should be noted that the crack belongs to hydraulic crack (crack in which water can seep), so the obtained results can only reflect the microcrack structure changes in the area where the flowing water touches.

Acknowledgements This article is one of the phased achievements of the R&D Program of Beijing Municipal Education Commission's "Mechanism Research on the Cracking Process of Metro Concrete under hydro-mechanical coupling" (KM201810853005)

References

1. Luo F, Liu C, Han X (2011) Numerical analysis on the influence of the rising groundwater level on the metro tunnel structure. China Railway Sci 32(1):81–85
2. Brassington FC (1990) Rising groundwater levels in the United Kingdom. Proc Inst Civ Eng 88(6):1037–1057
3. Jiang J, Tang G (1988) Concrete in state of triaxial stress. China Railway Press, Beijing
4. Wang J, Xu S (2011) Test study of concrete fracture under water pressure. Constr Technol 40(342):43–47
5. Li Q, Wang H (2006) Influence of ambient water on properties of concrete. Sci Online 1(2):83–94
6. Xu S, Wang J (2009) Crack propagation in a concrete dam under water pressure and determination of the double-K fracture parameters. Chin Civil Eng J 42(2):119–125
7. Li DuS, Zi A (2012) Review of the research on the effect of pore water pressure on concrete damage. Pearl River 33(03):13–18
8. Morgan IL, Ellinger H, Klinksiek R et al (1980) Examination of concrete by computerized tomography. ACI J 77(1):23–27
9. Büyüköztürk O (1998) Imaging of concrete structures. NDT E Int 31(4):233–243
10. Lawler JS, Keane DT, Shah SP (2001) Measuring three-dimensional damage in concrete under compression. ACI Mater J 98(6):465–475
11. Chen H, Ding W, Pu Y, Dang F (2006) Real-time observation of the mesoscopic fracture process of concrete under uniaxial compression condition CT. J Hydraul Eng 09:1044–1050
12. Guo D, Zuo J, Zhang H, Xu H (2009) CT observation of crack propagation law of high-strength concrete. J Chin Ceram Soc 37(10):1607–1612
13. Wang L, Cheng W (2008) Progress in numerical simulation of concrete based on micromechanics (I). Re Appl Buil Mater 08:1–3
14. Niu X, Zhang Q, Yue Z (2013) Current situation and development trend of the rock triaxial testing machine. Rock Soil Mechan 34(02):600–607

Numerical Study of the Long-Term Settlement of Deep Drainage Tunnels in Soft Stratum

Qixuan Zhu, Zhijie Cao, Zhen Xu, Tao Sui, and Xilin Lü

Abstract The deep tunnel drainage system has been used to solve urban flooding issues recently. However, inadequate research was conducted on the long-term settlement of deep drainage tunnels in soft soils. In this paper, a quasi-static finite element simulation was conducted based on a pipeline model in submerged soft soils. The pipeline suffered from long-term water filling-discharge cycles, which led to the settlement of the underlying soils below the pipeline. Settlements induced by cumulative plastic strain and pore pressure dissipation are isolated. The results reveal that the dissipation-induced settlement is negligible, and a recently proposed cumulative deformation formulation can reasonably predict the settlement. During the whole cycle stages, soil settlements mainly occurred within a certain depth below the pipeline. These findings can provide useful references for designing and safely operating deep tunnel drainage systems in soft soil areas.

Keywords Deep drainage tunnels · Long-term settlement · Cyclic loading · Empirical model

1 Introduction

Deep tunnel drainage systems, as a form of grey sponge technology, have been applied in practice for many years [1–3]. The underground tunnels are typically buried within 30–60 m to provide a large storage capacity and drainage capability. The system does

Q. Zhu · X. Lü (✉)
Department of Geotechnical Engineering, Tongji University, Shanghai 200092, China
e-mail: xilinlu@tongji.edu.cn

Key Laboratory of Geotechnical and Underground Engineering of Ministry of Education, Tongji University, Shanghai 200092, China

Z. Cao · Z. Xu · T. Sui
Shanghai Municipal Engineering Design and Research Institute (Group) Co. Ltd., Shanghai 200092, China

G. Mei et al. (eds.), *Advanced Construction Technology and Research of Deep-Sea Tunnels*, Lecture Notes in Civil Engineering 490,
https://doi.org/10.1007/978-981-97-2417-8_17

not conflict with other underground structures in the shallow layer and provides an effective way to utilize urban land resources.

Generally, storage facility operations have continuous loading and unloading processes, e.g., long-term filling and discharging of water loads, which can be simplified as long load cycles with large fluctuations. Previous research reports that the long-term cyclic loading [4–6] could induce a softening effect in soils surrounding the tunnels due to high compressibility and large porosity of deposits. As a result, the storage tunnel structures have high risks of deforming and even cracking, undermining the normal supply, drainage functions, and water environmental management within the city. To ensure the safety and maintenance of the deep tunnel, a proper estimation of the settlement of surrounding soil during the operational period, which also represents the settlement of the tunnels, is beneficial and worth discussing.

Research on deep tunnel drainage systems is still in its early stages. Since relevant studies mainly concentrate on case analyses, structural construction, and planning, there is a lack of research concerning the long-term operation and maintenance aspects. Presently, empirical methods have been successfully applied to predict long-term settlement in subway tunnels and soft soil roadbeds [7–9]. However, these methods have not yet been applied to predict the long-term operational settlement of deep drainage tunnels in soft soil areas. In this paper, a combined approach of quasi-static finite element analysis and layered summation method were testified based on a deep drainage system in soft soils. Considering water filling-discharge cycles and the cycle-induced loads, the long-term settlement of deep tunnels was predicted and analyzed.

2 Cumulative Deformation of Saturated Soft Clay Under Cyclic Loading

The long-term settlement of soil under undrained cyclic loading can be divided into two parts: cumulative plastic deformation and end-of-shake consolidation settlement resulting from pore pressure dissipation. Empirical prediction formulas generally require the calculation of the first-cycle plastic strain and pore pressure, and then extensively and uniquely determine the relationship among the number of loading cycles, cumulative strain, and pore pressure. Factors like loading intensity and stress history are simply considered. The earliest wide-used model was an exponential model proposed by Monishmith [10] $\varepsilon_p = AN^b$, which directly established the relationship between cumulative plastic strain ε_p and the number of cycles N. . Here, parameter A represents the first-cycle strain ($N = 1$), and parameter b is a fitted parameter. Based on Monishmith's exponential model, optimized empirical fitting calculation models and formulas were further proposed, and were combined with the layered summation method to calculate the long-term settlement of soft soil foundation [11–14]. Combining previous research results, the calculation formulas have been widely recognized and applied, as shown in:

$$Q = a(\frac{q_d}{q_{ult}})^n(\frac{p_0}{p_a})^c N^b \tag{1}$$

where Q is cumulative plastic strain or pore pressure; q_d is the dynamic deviator stress generated in the foundation after the first loading; q_{ult} is the undrained shear strength, p_0 is the consolidation mean stress; N is the number of load cycles; parameters a, n, c, b are obtained by experimental fitting, in which a and n reflect the influence of dynamic deviator stress on cumulative settlement, and c and b respectively reflect the effects of confining pressure and number of repetitions on settlement during operation. In default, $p_a = 101.3kPa$.

3 Prediction of the Long-Term Settlement of Deep Drainage Pipelines

The total length of the deep drainage system project in Shanghai is approximately 15 km, with a tunnel diameter of 10 m and a burial depth of about 50 m. A typical cross-section of the tunnel and shaft is shown in Fig. 1, where the tunnel is called a 'pipeline' since its length is much greater than its dimension.

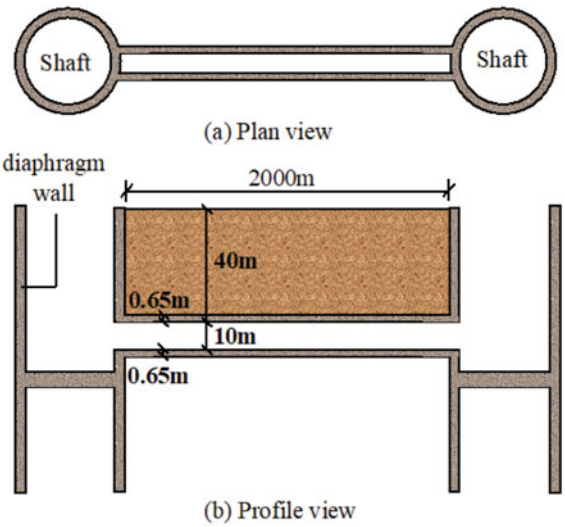

Fig. 1 Schematic diagram of deep drainage pipeline and shafts

3.1 Stress Distribution in the Foundation Under Water Filling and Discharging Conditions

The settlement prediction method based on empirical fitting formulas only requires the calculation of plastic strain and pore pressure generated in the first cycle, enabling the establishment of a relationship between the number of cycles and cumulative strain as well as pore pressure. The finite element method or elastic theory solution is a proper tools to analyze the static and dynamic shear stresses in the foundation after the first cycle loading as described in Eq. (1). In this case, the finite element method was used for calculation due to its superior capability to simulate engineering environments and its higher computational accuracy. Since the effects of water flow in deep pipelines were approximately neglected, it was transformed into an analysis of statically distributed forces repeated multiple times.

The finite model was built on plane strain condition as shown in Fig. 2, due to the significantly larger axial length in comparison with the radial dimension of the tunnel. The width of the model is 110 m, determined by a circle range that has 5 times the diameter of the tunnel. The height of the models is also 110 m to adequately account for settlement within a substantial range beneath the tunnel. The depth of the tunnel bottom is 50 m and the tunnel diameter is 10 m. Consequently, settlement of the foundation soil within a 60 m range below the tunnel can be considered. The boundary conditions on lateral sides are horizontally constrained, and horizontally and vertically fixed at the bottom. The whole model is saturated and submerged; the soil is evaluated using specific gravity. Figure 3 illustrates the representative cross-sectional distribution of soil layers and the position of the deep drainage tunnel. The specific values of various physical parameters for each soil layer were obtained from the engineering geological survey report as listed in Table 1.

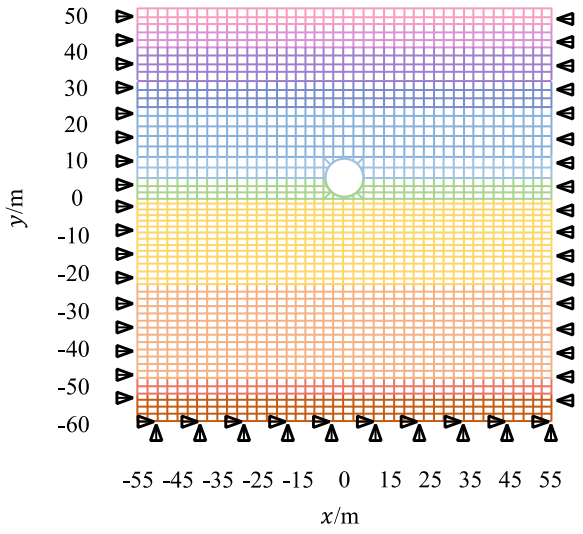

Fig. 2 FE model for stress distribution analysis

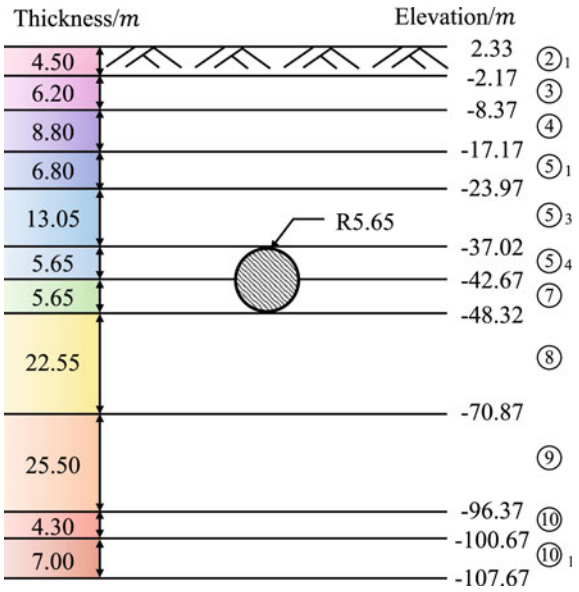

Fig. 3 The distribution of soil in a typical section

The dynamic-load-induced stress change in underlaying soil was evaluated in this way: (1) extracting the initial static deviation stress q_s based on stress distribution at different depths along the central axis below the pipeline; (2) then, applying water load on the underlaying soil below the pipeline, by assuming a full flow inside the pipeline and simplifying the load as a uniform distribution with a resultant water pressure of 76.969 kPa; (3) recording the magnitude of the deviatoric stress at different depths along the central axis below the tunnel after applying the water load, where the increment value represents the dynamic-load-induced deviatoric stress q_d during water filling and draining in the flood season.

The accuracy of the evaluation of stress change is crucial for predicting foundation deformation under cyclic loading. In the determination of the mean effective stress p_0 of the soil after consolidation, it was assumed that the soil layer is under a consolidated state in a lateral earth pressure coefficient K_0. The vertical stress was determined by the self-weight stress of stratified soil, and the horizontal stress was decided upon the lateral earth pressure coefficient K_0. The specific calculation method is shown as follows.

$$p_0 = \frac{(1+2K_0)}{3}\sum_{i=1}^{k}\gamma_i' h_i \tag{2}$$

where k is the number of upper soil layers at the stress calculation point; γ_i' is the effective unit weight of the i-th upper layer of soil; h_i is the thickness of the i-th upper layer of soil.

Table 1 Physical parameters of soil layers

Serial number	Soil type	Thickness/m	Density/ $(10^3 kg/m^3)$	Compressibility modulus/MPa	Poisson's ratio	Permeability coefficient/ (m/s)	Lateral pressure coefficient	Porosity e	Effective internal friction angle $\varphi'/\circ$
②$_1$	Silty clay	4.50	1.85	5.03	0.38	2E-8	0.48	0.926	28.5
③	Muddy silty clay	6.20	1.75	3.34	0.41	1E-7	0.50	1.175	29.6
④	Muddy clay	8.80	1.70	2.68	0.41	1E-8	0.53	1.335	27.9
⑤$_1$	Clay	6.80	1.76	3.82	0.41	2E-8	0.51	1.127	30.5
⑤$_3$	Silty clay with silty sand	13.05	1.79	5.20	0.38	3E-7	0.47	1.001	31.6
⑤$_4$	Silty clay	5.65	1.95	6.36	0.38	1E-8	0.45	0.699	32.4
⑦	Silty sand with silty clay	5.65	1.94	11.55	0.33	5E-6	0.37	0.694	-
⑧	Silty clay	22.55	1.84	5.76	0.35	3E-7	0.47	0.900	32.8
⑨	Silty sand with silty clay	25.50	2.01	15.56	0.35	5E-4	0.38	0.570	33.0
⑩	Clay	4.30	2.00	10.97	0.38	2E-7	0.51	0.641	31.6
⑩$_1$	Silty clay with silty sand	7.00	1.95	8.67	0.38	5E-5	0.51	0.710	32.0

The undrained shear strength q_{ult} of saturated soft clay consolidation can be calculated using the undrained shear strength formula under the K_0 consolidation state.

$$q_{ult} = Mp_c[\frac{M+\alpha}{2M}]^{\frac{\lambda-\kappa}{\lambda}} \tag{3}$$

$$\alpha = 3(1-K_0)/(1+2K_0) \tag{4}$$

$$M = 6\sin\varphi\prime/(3-\sin\varphi\prime) \tag{5}$$

where λ and κ represent the slopes of the normal consolidation line and rebound line in the $e-lnp$ space, respectively. Referring to previous test results [15], λ was taken as 0.182 and κ as 0.0347, while for the subsequent layers,λ and κ were both taken as 0.0991 and 0.0129, respectively.

In the selected project, Suzhou River section of Shanghai, the tunnel is buried more than 40 m below the ground surface, and the underlying stratum is composed of silty clay. The soil samples taken in reference [13] are consistent with those used in this study. The parameters obtained through dynamic hollow cylinder torsional shear tests in reference [13] can be employed for analysis. Here, a, n, c, b represent parameters of the cumulative plastic strain calculation model, while a_u, n_u, c, b_u denote parameters of the cumulative pore pressure calculation model. The values of $a, n, c, b, a_u, n_u, c, b_u$ were set to 0.076, 1.408, 0.5, 0.408, 0.0385, 1.37, 0.5, and 0.32, respectively.

3.2 *Calculation of Long-Term Settlement in the Foundation of Deep Tunnels*

The settlement of the foundation induced by the cumulative deformation of undrained soft clay can be calculated by Eq. (6).

$$s_s = \sum\nolimits_{i=1}^{n} \varepsilon_i^p h_i \tag{6}$$

where ε_i^p is the cumulative plastic strain of the i-th layer, and n is the total number of compressible layers.

By conducting finite element simulations to obtain stress components and using Eq. (1), it is possible to calculate the undrained cumulative deformation of each soil layer, which can then be superimposed to obtain the settlement of the foundation soil. As the model calculates the settlement of the foundation within a depth range of 60 m below the storage pipeline, the soil layers were divided into more than fifty layers with unequal thicknesses based on the finite element mesh size. Each layer

has an approximate thickness of 1 m. The total settlement was calculated using the layered summation method for these fifty-plus layers of soil.

The settlement induced by cumulative pore pressure dissipation can be calculated by Eq. (7).

$$s_v = \sum_{i=1}^{n} m_{vi} h_i u_i U_i \tag{7}$$

where s_v is the consolidation settlement caused by the dissipation of cumulative pore pressure, u_i is the undrained cyclic cumulative pore pressure of the i-th layer, m_{vi} is the volume compression coefficient of the i-th layer, U_i is the degree of consolidation of the i-th layer, h_i is the thickness of the i-th layer, and n is the number of sub-layers. From a long-term perspective, it can be assumed that the cumulative pore pressure is completely dissipated, indicating a consolidation degree of 100%.

Finally, the settlement S_s obtained from plastic cumulative deformation was superimposed with the settlement S_v obtained from cumulative pore pressure dissipation to obtain the total settlement S.

3.3 Analysis of Long-Term Settlement

For the deep tunnel, considering 50 cycles of water filling and draining each year, the settlements induced by cumulative plastic strain after 1 year, 2 years, 6 years, and 12 years are estimated as 0.084, 0.111, 0.175, and 0.232 m respectively. The consolidation settlements caused by pore pressure dissipation after 1 year, 2 years, 6 years, and 12 years are 0.0006, 0.0008, 0.0011, and 0.0014 m respectively. The total settlements after 1 year, 2 years, 6 years, and 12 years are 0.085, 0.112, 0.176, and 0.234 m. The variation of settlements over time is shown in Fig. 4.

It is obvious from the graph that the total settlement increases exponentially with operational time. The settlement induced by cyclic cumulative pore pressure dissipation is much smaller than the settlement caused by cyclic cumulative plastic strain, which the former is negligible. The depth distribution of settlements referring

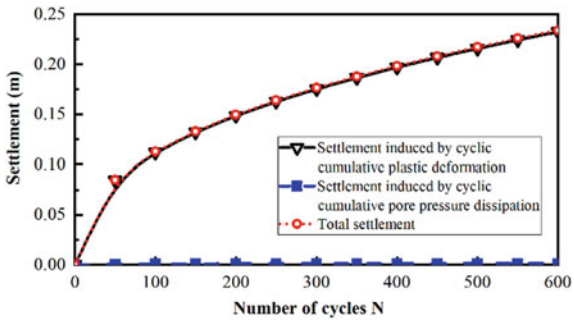

Fig. 4 Relationship between settlement of foundation and cyclic number

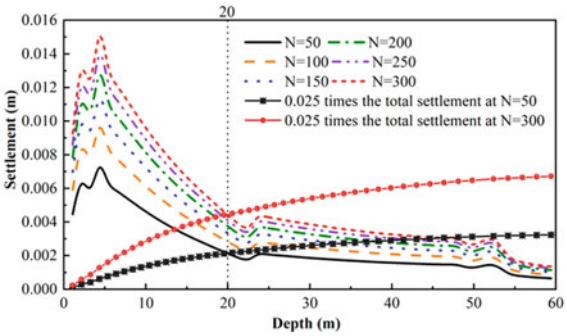

Fig. 5 Settlement of each compression subjected to different loading cycles

to the tunnel bottom is shown in Fig. 5, where N is the number of cycles and depth is the relative depth to the tunnel bottom. According to the requirements for calculating depth in the layered summation method, when the compression of a certain layer of soil is less than 0.025 times the current total compression, the compression of that layer and all layers below it is considered neglected. The curves of 0.025 times the total settlement of the soil under N = 50 cycles (1 year) of cyclic loading intersect with the curves of compressibility of each soil layer under N = 50 cycles at a depth of 20 m, indicating that the compressibility of a single soil layer at 20 m depth is already 0.025 times the total settlement. Two curves also intersect at 20 m depth when subjected to N = 300 cycles (6 years), suggesting that the settlement below 20 m can be considered negligible compared to the total settlement. Hence, compression below 20 m is no longer considered.

4 Conclusion

By combining the formulas for cumulative plastic strain and cumulative pore pressure with the layering summation method, a simplified calculation method for the long-term settlement of saturated soft clay under cyclic loading conditions was established. The long-term settlement of urban deep storage tunnels in soft soil areas was studied. The conclusions obtained are as follows:

Considering the low-frequency heavy load characteristics of cyclic water loads, the cumulative deformation calculation model for saturated soft clay under cyclic loading conditions previously proposed was proved to reasonably predict the settlement during the operation period of urban deep storage tunnels. The results show that the consolidation settlement caused by pore pressure dissipation is extremely small compared to the cumulative deformation caused by cyclic loading and it can be almost neglected. Furthermore, cumulative deformation mainly occurred within a certain depth below the deep storage pipeline due to its large diameter and the high water level. In summary, the cyclic water filling and discharging loads tend to cause

significant settlement during the operation of the deep tunnel pipelines, so it should be given attention in their planning and construction.

The prediction settlement method combining empirical formulas and layered summation method proven to be a good tool for settlement estimation of deep drainage pipelines in an elastic soil deposited horizontally. However, it cannot directly reflect the nonlinear characteristics of stress and deformation, and further research should be conducted.

Acknowledgements The financial support by the Shanghai Municipal Science and Technology Commission Project (23692106500) is gratefully acknowledged.

References

1. He WW, Wang MH, Wu JJ (2023) Typical case analysis of deep tunnel drainage system at home. Water Purific Technol, 1–8.
2. Nguyen TT, Ngo HH, Guo WS, Wang XC, Ren NQ, Li GB, Ding J, Liang H (2019) Implementation of specific urban water management. Sponge City Sci Total Environ 652:147–162
3. Li Q, Wang F, Yu Y, Huang ZC, Li MT, Guan YT (2019) Comprehensive performance evaluation of LID practices for the sponge city construction: a case study in Guangxi, China. J Environ Manage 231:10–20
4. Japan Road Association (1989) A technical guide to ground treatment in road engineering. CAI Sijie, translator. Beijing: China Communications Press
5. Qian JG, Du ZB, Lu XL, Huang MS (2019) Effects of principal stress rotation on stress-strain behaviors of saturated clay under traffic-load-induced stress path. Soils Found 59(1):41–55
6. Yang Q, Tang YQ, Yuan B, Zhou J (2019) Cyclic stress–strain behaviour of soft clay under traffic loading through hollow cylinder apparatus: effect of loading frequency. Road Mater Pavement 20:1026–1058
7. Cai Y, Chen Y, Cao Z et al (2018) A combined method to predict the long-term settlements of roads on soft soil under cyclic traffic loadings. Acta Geotech 13:1215–1226
8. Chai JC, Miura N (2002) Traffic-load-induced permanent deformation of road on soft subsoil. J Geotech Geoenviron Eng 128(11):907–916
9. Ni J, Indraratna B, Geng X, Carter JP, Chen Y (2015) Model of soft soils under cyclic loading. Int J Geomech 15(4):04014067
10. Monismith CL, Ogawa N, Freeme CR (1975) Permanent deformation characteristics of subgrade soils due to repeated loading. Transp Res Rec 537:1–17
11. Li D, Selig ET (1996) Cumulative plastic deformation for fine-grained subgrade soils. J Geotech Eng 122(12):1006–1013
12. Chai JC, Miura N (2002) Traffic-load-induced permanent deformation of road on soft subsoil. J Geotech Geoenviron Eng 28(11):907–916
13. Huang M, Yao Z (2016) Effect of the principal stress direction on cyclic cumulative deformation and pore pressure of soft clay. Procedia Eng 143:811–819
14. Yao ZM, Zhang MH, Chen JH (2012) Cyclic accumulative pore pressure explicit model of saturated soft clay and long-term settlement calculation of subway tunnel roadbed. J China Railw Soc 34(09):87–92
15. Mao P (2022) Study on earth pressure distribution pattern of ultra-deep circular shaft and its influential factors. Chin J Undergr Space Eng 18(01):257–267

Fatigue Response Analysis of Wind Power Pile Foundation Under Full Cycle Action of Typhoon

Bo Zhang, Shiding Su, Jiaqi Wu, and Shuhui Lv

Abstract As an important component of offshore wind turbine foundation, steel pipe piles are subject to cyclic loads in the marine environment for a long time, especially the waves caused by typhoon, which are easy to cause fatigue damage of steel pipe piles. Based on a project example, a load pile soil ternary fatigue analysis model is proposed by combining relevant specifications, structural mechanics and finite element method, and the important factors that affect the fatigue damage of pile foundation structures in the whole cycle of typhoon are pointed out. The method of fatigue response analysis of wind power pile foundation structure in this paper has certain guiding significance for practical engineering application.

Keywords Steel pipe pile · Wave load · Typhoon · Fatigue response

1 Introduction

Fatigue analysis is a key link of steel structure foundation. In the fatigue assessment of offshore engineering structures, the fatigue cumulative damage analysis method based on S–N curve and Miner linear cumulative damage theory is commonly used

B. Zhang (✉) · S. Su · J. Wu · S. Lv (✉)
CCCC Fourth Harbor Engineering Institute Co, Ltd, Guangzhou 510230, Guangdong, China
e-mail: zbo7@cccc4.com

S. Lv
e-mail: lshuhui@cccc4.com

Key Laboratory of Environment and Safety Technology of Transportation Infrastructure Engineering, CCCC, Ltd, Guangzhou 510230, Guangdong, China

B. Zhang
State Key Laboratory of Tropical Oceanography, South China Sea Institute of Oceanology, Chinese Academy of Sciences, Guangzhou 510301, Guangdong, China

University of Chinese Academy of Sciences, Beijing 100049, China

G. Mei et al. (eds.), *Advanced Construction Technology and Research of Deep-Sea Tunnels*, Lecture Notes in Civil Engineering 490,
https://doi.org/10.1007/978-981-97-2417-8_18

[1]. Currently, most of the fatigue assessment methods adopted by various classification societies are based on S–N curve to check the fatigue of offshore pile foundations [2].

As an important component of offshore wind turbine foundation, steel pipe piles are subject to random wind, wave, current and working load for a long time. The wind, wave, current load is a kind of variable load. Under the action of alternating load, the stress in the structural material will change with time, resulting in fatigue damage of the steel pipe pile [3]. In particular, the waves caused by typhoon are characterized by stages, large energy and long period. Therefore, it is very valuable to establish a load-pile-soil ternary fatigue analysis model in combination with the field engineering application of finite element method to analyze the fatigue response of pile foundation structures during the whole typhoon period.

2 Project Overview and Natural Conditions

An offshore wind power project is located in unshielded offshore deep-water area, which is characterized by frequent typhoons and strong monsoon wind. When the typhoon comes, the pile foundation that has been constructed will easily lead to the fracture of the steel pipe pile under the reciprocating action of wind, wave and current. The elevation of pile head above the water surface is small, and the wind load is much smaller than the wave load. Therefore, only wave action is considered.

The wave load changes continuously in a typhoon cycle. In order to study the fatigue damage of steel pipe piles in a typhoon cycle, it is necessary to analyze it in stages. For offshore wind farms, a typhoon cycle can be divided into three periods: approaching period, landing period and far away period. Take typhoon “Lianhua” as an example. In the afternoon of July 8, “Lianhua” opened close to the east coast of Guangdong and became a typhoon at 20:00. The maximum wind force near the center was 12. At 12:15 on July 9, “Lianhua” landed in the coastal area of Jiadong Town, Lufeng City, Guangdong Province. At the time of landing, the maximum wind force near the center was 12, and then quickly weakened to a tropical depression. According to the typhoon period, the wave information with a wave height of more than 4 m was statistically analyzed, as shown in Fig. 1 and Table 1.

3 Calculation of Pile Foundation Load and Establishment of Finite Element Model

As the ratio of wave height to water depth is large, the wave load has strong nonlinearity, so the wave load on pile foundation calculated by Stokes fifth order wave theory and Morison equation [4] is shown in Table 2.

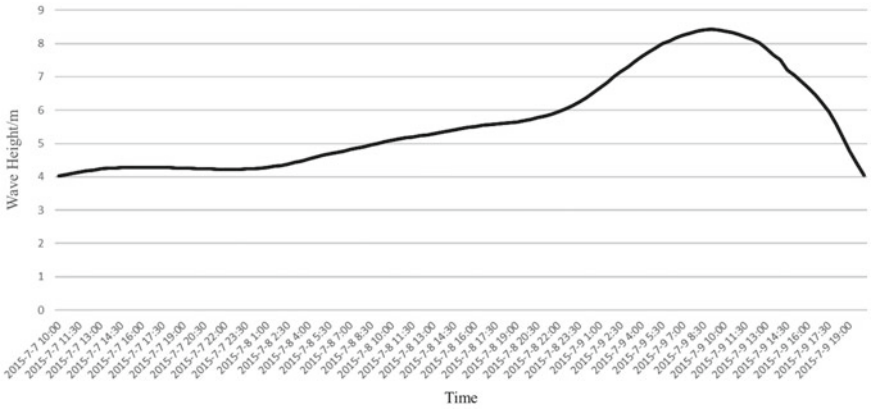

Fig. 1 Wave Height of Typhoon "Lianhua"

Table 1 Wave Information of Typhoon "Lianhua"

Typhoon period	Start time	End time	Wave height (m)	Wave period (s)	Wave direction (°)	Cycles
Approaching period	2015–7-7 10:00	2015–7-8 22:30	4.7	11	130	11,940
Landing period	2015–7-8 22:30	2015–7-9 17:30	7.6	10	145	6840
Far away period	2015–7-9 17:30	2015–7-9 20:00	4.9	9	145	1000

Table 2 Wave load on pile foundation

Typhoon period	Maximum total wave force Pmax (kN)	Maximum total bending force Mmax (kN · m)	The distance from the action point to the mud surface (m)
Approaching period	57.0	901.4	15.8
Landing period	155.5	2896.4	18.6
Far away period	64.1	1105.4	17.3

The finite element model is used to model the pile and foundation. The solid element is used for the pile foundation and soil. The contact treatment is used for the internal and external sides of the pile foundation and the soil. As shown in Fig. 2, See Tables 3 and 4 for the material parameters of the pile foundation and soil respectively.

The contact property is defined by the pile soil surface to simulate the shear transfer and relative displacement between the pile and soil. The master–slave contact algorithm is used to select the pile with high stiffness as the main control surface, the soil surface as the subordinate surface, the pile soil contact is in the form of Mohr Coulomb friction penalty function, and the sliding friction coefficient of the interface

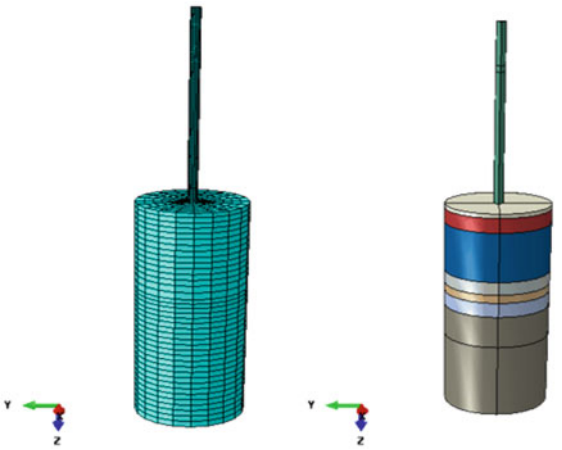

Fig. 2 Pile soil finite element model diagram

Table 3 Pile foundation material parameters

Model	Density ρ (kg/m3)	Modulus of elasticity E (GPa)	Poisson's ratio μ	Yield strength fs (MPa)
Q345	7850	206	0.3	345

Table 4 Soil layer material parameters

Soil layer No	Soil layer	Thickness t (m)	Density ρ (g/cm3)	Compression modulus Es (MPa)	Internal friction angle Φ (°)	Cohesive force c (kPa)
①1	Silt	0.73	0.51	3.953	1.6	2.5
①2	Sludge mixed with sand	2.6	0.6	4.866	17.3	3.5
③3	Mucky soil	8.8	0.74	3.580	2.1	16.2
⑥2	Silty fine sand	2.3	0.25	12.0	24	18.8
⑥3	Silty soil mixed with sand	1.5	1.86	12.0	24	27.0
⑧	Completely weathered granite	2.6	0.88	11.045	28.5	21.7
⑨	Strongly weathered granite	–	0.87	9.393	26.7	31.8

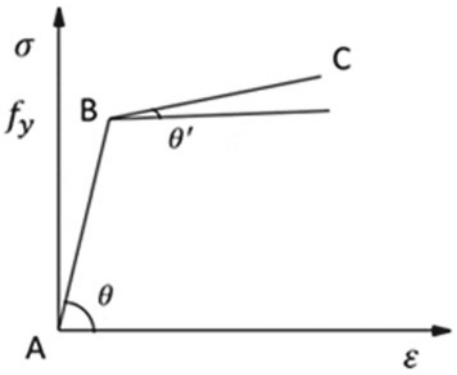

Fig. 3 Double diagonal model

is selected. The finite element model of steel pipe pile and soil is established by using 6-faceted 8-node linear reduced integral solid element. Through trial calculation, the soil diameter of the vertical pile is 10 times of the pile diameter, which can basically eliminate the influence of the boundary on the results. The soil bottom is fully restrained, and the lateral displacement is restrained.

The steel pipe pile is made of Q345B, which belongs to low alloy steel. Refer to the Standard for Design of Steel Structures (GB50017-2017) [5]. When the material is Q345B and the wall thickness is 16 mm $\ll$ 40 mm, the design value of the yield stress of the steel pipe pile at the mud surface is 335 MPa, and the minimum ultimate tensile strength is 470 MPa. As the steel is low alloy steel, the double diagonal model (as shown in Fig. 3) is used for numerical modeling in this paper, where the secondary strengthening stiffness of the model is about one percent of the initial stiffness.

When fatigue analysis of steel pipe pile is carried out through finite element software, the historical data after interpolation is used for loading, and Soderberg theory is used to correct the stress life of steel pipe pile materials with only a single S–N curve.

4 Fatigue Analysis Results

According to the accumulation of fatigue damage of steel pipe piles in different periods in a typhoon cycle, it is found that after 17.6 equal load histories, steel pipe piles will experience fatigue damage within the range of 1.3 m below the sand and mud surface to 2.8 m above the mud surface, resulting in pile foundation failure. The minimum safety factor of pile foundation is 1.84, which means that after the wave load in typhoon period is expanded to 1.84 times, The steel pipe pile is subject to fatigue failure after a typhoon cycle of cyclic loading, and the results are shown in Fig. 4.

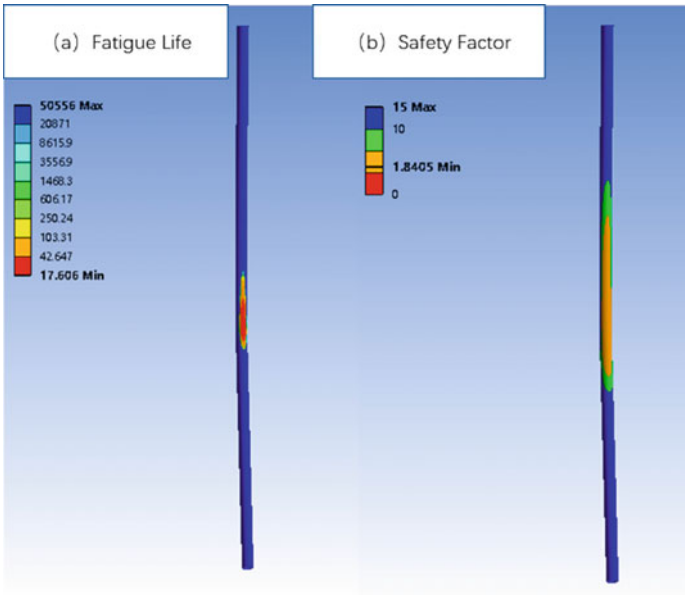

Fig. 4 Cloud Chart of Fatigue Analysis of Steel Pipe Piles in the Period of Typhoon "Lianhua"

If only the wave height during the landing period of typhoon "Lianhua" is increased by 1 m, that is, from 7.6 to 8.6 m, and other parameters remain unchanged, the wave load on pile foundation is shown in Table 5.

After the wave height of typhoon "Lianhua" increased by 1 m during the landing period, the fatigue analysis results are shown in Fig. 5. The service life of the pile foundation decreases rapidly, and the fatigue damage range becomes larger. After 2.8 load histories of the pile foundation, the steel pipe pile will have fatigue failure within the range of 1.6 m below the sand and mud surface to 3.7 m above the mud surface, resulting in the failure of the pile foundation. The minimum safety factor of pile foundation is 1.22, which means that after the wave load in typhoon period is expanded to 1.22 times, the steel pipe pile will undergo fatigue failure under the cyclic load of a typhoon period.

Table 5 Wave load on pile foundation after wave height increases 1 m during landing

Typhoon period	Maximum total wave force Pmax (kN)	Maximum total bending force Mmax (kN · m)	The distance from the action point to the mud surface (m)
Approaching period	57.0	901.4	15.8
Landing period (wave height 8.6 m)	206.6	4000.1	19.4
Far away period	64.1	1105.4	17.3

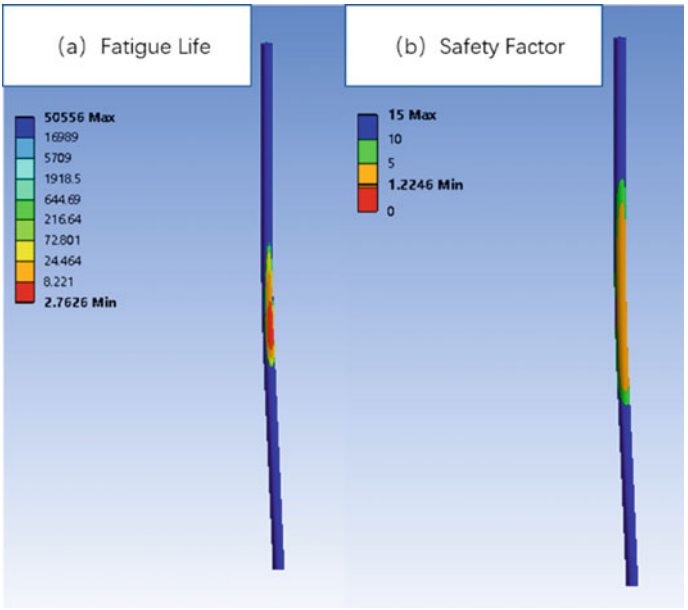

Fig. 5 Cloud chart for fatigue analysis of steel pipe pile after wave height increase of 1 m during landing

5 Conclusion

This paper based on a project example, by combining the relevant specification, structural mechanics, and finite element method, established the pile soil load—ternary fatigue analysis model, and the typhoon period all pile structure fatigue response analysis, pointed out that the law of the pile foundation damage, in the case of other parameters constant, slightly increase the typhoon wave height, will cause the service life of pile foundation, And the range of fatigue damage is larger. The fatigue response analysis of pile foundation structure during the whole cycle of typhoon is of great significance to the optimization of pile stabilization measures and the improvement of the service life of pile foundation.

Acknowledgements Foundation Project: The Estuary, Coast and Island Engineering Innovation Team Construction Project of Guangdong Laboratory of Southern Marine Science and Engineering (Zhuhai), No.311020009.

References

1. Xu JH (2014) Dynamic response and fatigue analysis of jack up platform pile legs [D]. South China University of Technology

2. Zhao MC (2014) Fatigue analysis of offshore wind turbine pile foundation under multi load coupling [D]. Chongqing Jiaotong University
3. Liu HT (2007) Fatigue life prediction analysis of offshore jacket platforms under random wave loads [D]. Tianjin University
4. Zhang B (2021) Calculation of Pile (column) Wave Force Based on Stokes Fifth-order Wave Theory and Specifications[C]//The 4th International Conference on Information Technologies and Electrical Engineering, pp 1–6
5. GB 50017–2003 Code for Design of Steel Structures [S]

Electrochemical Corrosion Study of 20MnTiB High Strength Bolt Under the Simulation of Humid Climate in Chongqing

Juan Wen, Xianping Gao, Yuehua Deng, and Fanglin Zhang

Abstract High strength bolts for steel structure bridges have been used in humid environment for a long time, and are prone to corrosion and failure under the combined action of corrosion environment and load. The electrochemical corrosion performance of 20MnTiB high strength bolt was studied by simulating the humid climate in Chongqing. The results were shown that under the same condition, the corrosion resistance was increased both with the increase of pH and the increase of corrosion time. According to the EDS and XRD results, after immersion at different pH values for 168 h, the main corrosion products are Fe_2O_3, Fe_3O_4 and FeOOH. All the results demonstrated that after immersion at different pH values for 168 h, the sample corrosion resistance was improved, and was significantly increased with the increase of pH value, which is closely related to the corrosion product film on the sample surface.

Keywords 20MnTiB · High strength bolt · Electrochemical corrosion · pH · Corrosion time

1 Introduction

In the field of bridge construction, high strength bolts, as the key connecting fasteners of bridge trusses, play a significant role in the safety connection between steel structure trusses. Thus, the safety property of the bolt will determine the life of the whole

J. Wen · Y. Deng
Department of Quality Testing and Inspection, Yibin University, Yibin 644000, P.R. China

X. Gao (✉)
Chongqing Solid Waste Management Service Center Co. Ltd, Chongqing 401120, P.R. China
e-mail: gaoxianping841005@163.com

F. Zhang
Department of Mechanical and Electrical, Guang'an Vocational & Technical College, Guang'an 638550, P.R. China

G. Mei et al. (eds.), *Advanced Construction Technology and Research of Deep-Sea Tunnels*, Lecture Notes in Civil Engineering 490,
https://doi.org/10.1007/978-981-97-2417-8_19

steel structure. With the continuous development of society, the construction of more and more bridge structures are towards the direction of high strength and large span, which will require better properties of high strength fasteners.

Corrosion will change the mechanical properties of steel structure, which is an important disease of steel structure bridge. According to the data of Japanese statistics, the strength of the steel structure under stress will be decreased by 10 ~ 15% when 1% of the steel is corroded; and the structure will be scrapped when 5% of each side for the steel is corroded [1]. For the steel bridges, the failure of connecting nodes is one of the dominant breaking modes. For one steel bridge along one railway in China, the annual rupture rate of high strength bolt because of corrosion is about 0.2% [2]. And the breakage rate of high strength bolts in the steel structure of Chongqing Chaotianmen Yangtze river bridge is about 0.0025% [3]. At present, many large bridges are built at home and abroad, which are all steel bridges, in the coastal cities or along the river, in the environment of high humidity, high salt or serious air pollution. For the Nanpanjiang Bridge constructed in 1998, it was detected in 2008 that the joints on the main truss were corroded, with 80% moderate corrosion (rust pit depth 0.6–1.2 mm) [4]. The precipitation and adsorption of harmful materials onto the bridge is one predominant reason for the corrosion. Besides, the exposure time, relative humidity, temperature, wind speed, corrosive medium and other factors can also influence the corrosion behavior of steel [5–8]. These investigations illustrate that the high strength bolts at the steel joints are prone to corrosion by the industrial and Marine atmosphere and undergo rupture, which will endanger the safety of the whole steel bridge.

Therefore, in this paper, based on previous research and through the investigation on atmospheric environments of Chongqing City in recent years, corrosion solution was designed to simulate the humid climate of Chongqing, and the electrochemical corrosion experiments of high strength bolts were carried out under simulated conditions of humid climate in Chongqing as functions of corrosion time and pH. The results will provide scientific fundamentals and research guidance for the maintenance and protection of the bridges.

2 Experimental Methods

2.1 Design and Formulation of Simulated Corrosion Solution

According to the Ecological Environmental Bulletins from 2010 to 2018 released by Chongqing Ecology and Environment Bureau (Chongqing Ecology and Environment Monitoring Center), the atmospheric pollution in Chongqing has transformed from coal-burning pollution to complex pollution by vehicle engine exhaust and soot. Although acid rain is effectively controlled, the pollution from nitrogen oxides, ozone and dust particles is on the rise. The pH value of precipitation has risen from about 4.5 in the past to about 5.5 in recent years.

Table 1 Corrosion solution compositions simulating the annual precipitation in Chongqing (mg/L)

	SO_4^{2-}	NO_3^-	NH_4^+	Ca_2^+	Mg_2^+	Cl^-	K^+	Na^+	F^-
Corrosion solution	10.24	6.57	3.77	3.82	0.19	0.59	0.5	0.21	0.11

Based on the precipitation components in Chongqing from the above Chongqing's Bulletins, and the reports [9–13] by Liu and Zhang, et al., the indoor accelerated corrosion solution compositions were designed by improving the content of sulfate radical in 2017 annual precipitation in Chongqing to simulate the humid climate in Chongqing as shown in Table 1.

According to the method of ion concentration equilibrium, the corrosion solution was prepared by analytical reagent and distilled water, and the pH value of the corrosion solution was adjusted by using precise pH meter, nitric acid solution and sodium hydroxide solution.

2.2 Preparation of Electrochemical Corrosion Samples

Electrochemical corrosion samples of high strength bolts with corrosion area of 10 × 10 mm were prepared. Then the samples were encapsulated with epoxy resin. One side was considered as the working surface for electrochemical testing and microscopic analysis, the gap of which was embedded with resin, while the other side was connected with electrode wires. The working surface was polished with 800#, 1200# and 2000# metallographic sandpaper, respectively, and then polished with 2.5 μm diamond spray until the surface was finished. The polished surface was washed with acetone to remove the oil, then washed with deionized water, cooled with cold air, and placed in a dryer for later use. According to relevant reports and standards [14, 15], two factors, corrosion time and the pH of the corrosion solution, were mainly considered in the electrochemical corrosion experiments.

2.3 Analysis and Test Methods

According to the design of electrochemical corrosion experiment, the samples were immersed in 200 times concentration of corrosion simulation solution with different pH values. After reaching the target corrosion time, the samples were taken out, and the electrochemical study, surface morphology and corrosion products of the corrosion surface were analyzed.

The polarization curves and electrochemical impedance spectra (EIS) of high strength bolts were analyzed by using the UTOLAB comprehensive electrochemical test system. The chemical composition and microstructure morphology of the

corrosion products were analyzed by scanning electron microscope (SEM), energy dispersive spectrum (EDS) and X-ray diffraction (XRD).

3 Electrochemical Performance Analysis of 20MnTiB High Strength Bolt

3.1 Polarization Curve

Figure 1 shows the electrochemical polarization curves of the samples after immersion in the 200 times concentration of corrosion simulation solution for 0 h, 8 h, 36 h, 96 h and 168 h at different pH values.

In order to further quantitatively analyze the corrosion mechanism, the polarization curves were fitted by Tafel method. The results are shown in Table 2, and the fitting parameters included the anode Tafel slope (ba), cathode Tafel slope (bc), self-corrosion potential (E), corrosion current (I), corrosion rate (V_c) and polarization resistance (R_p).

Figure 1 demonstrates that the polarization curves of the samples varied little over time when immersed in the corrosion simulation solutions with different pH values for 0–96 h, and the polarization curves at pH of 3.5 and 5.5 were similar. While after immersion for 168 h in the corrosion solution, the polarization curve was significantly changed, as Fig. 1e reveals. The corrosion potential was increased obviously with the increase of pH values. At pH 5.5 and 7.5, the anodic polarization curve showed obvious inflection point, and at the same polarization potential, the polarization curve shifted to the left with the increase of pH, indicating that anodic passivation of electrochemical corrosion is increased significantly and the anodic reaction is inhibited, thus enhancing the corrosion resistance of the materials. Simultaneously, at pH of 3.5, the anodic polarization curve of the sample still did not show an obvious inflection point. This may be mainly because the presence of a large amount of hydrogen ions and chloride ions in the strong acid corrosion simulation solution, which will result in the failure of the formation of stable corrosion products and lead to a remarkable corrosion tendency of the sample.

Table 2 demonstrates that under the same corrosion time, the corrosion current of the samples was decreased with the increase of pH. And under the same pH of 3.5 and 5.5 in the acid environment, the corrosion current was decreased with the increase of the corrosion time. When the pH was 3.5 without immersion, the corrosion current reached the peak and the corrosion rate reached 0.73839 mm/a, the corrosion resistance was the worst. While under the neutral and slightly alkaline pH 7.5, the corrosion current reached the maximum at 8 h corrosion time (only slightly higher than that at 96 h corrosion time in the acid environment), and then was decreased with the increase of corrosion time. This can be explained that when the sample is immersed for a short time (within 8 h), complete corrosion products are not formed on the sample surface, and the surface metal directly contacts with the corrosion

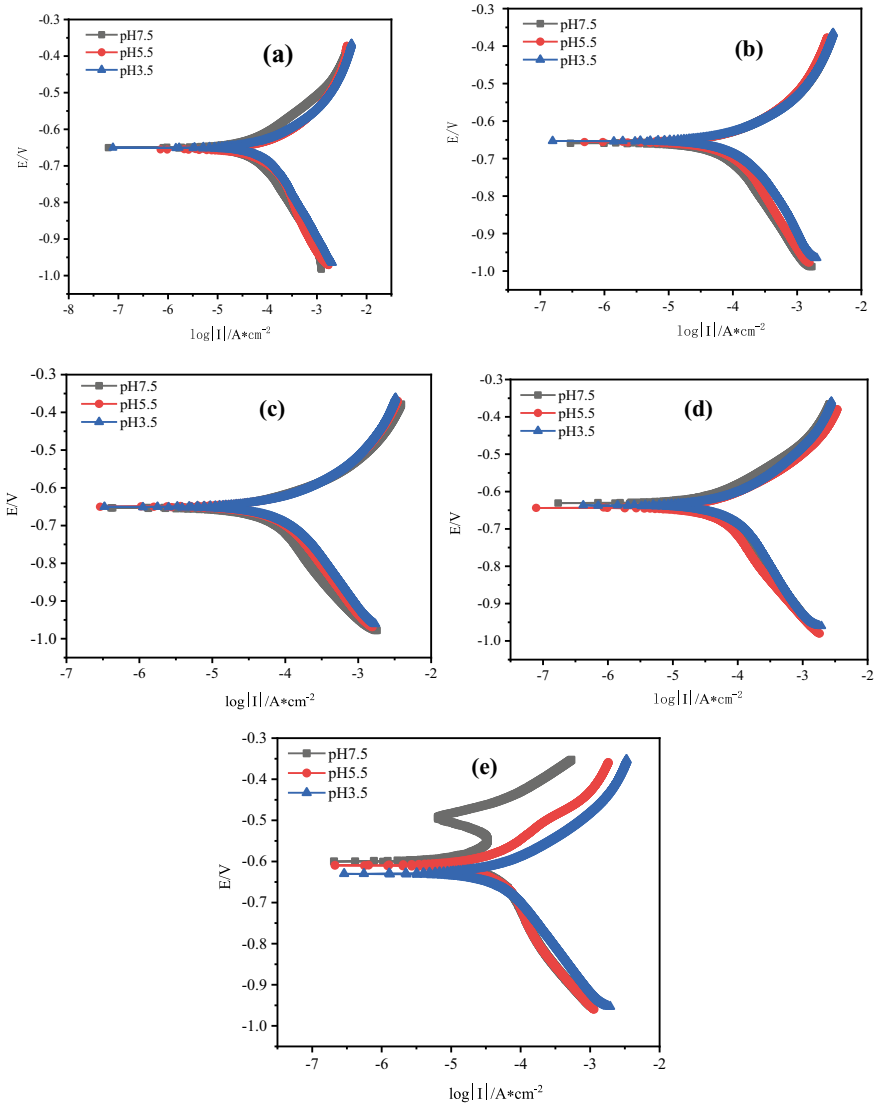

Fig. 1 The electrochemical polarization curves of the samples after immersion at different pH values for different time **a** 0 h **b** 8 h **c** 36 h **d** 96 h **e** 168 h

simulation solution, which will result in a direct reaction between the sample and the erosion ions in the corrosion simulation solution. Thus, the corrosion tendency of the samples will be relatively high.

In summary, after immersion at pH of 7.5 for 168 h, the corrosion current density reached the minimum value of 1.7624 × 10–5 A/cm, while the corrosion potential

Table 2 Fitting results of the electrochemical polarization curves

Time (h)	pH	ba (V/dec)	bc (V/dec)	E (V)	I(A/cm^2)	Vc(mm/a)	R_P (Ω)
0	3.5	0.14344	0.35899	-0.65101	6.294×10^{-5}	0.73839	285.98
	5.5	0.15471	0.52189	-0.65651	$6.092 \times 10–^{5}$	0.71467	295.47
	7.5	0.12101	0.23021	-0.65021	3.285×10^{-5}	0.38537	547.95
8	3.5	0.16605	0.31066	-0.65405	6.1477×10^{-5}	0.7212	292.79
	5.5	0.17099	0.44892	-0.65689	5.2565×10^{-5}	0.61665	342.44
	7.5	0.14391	0.38343	-0.66015	4.4473×10^{-5}	0.52173	404.74
36	3.5	0.16671	0.35538	-0.65122	5.1355×10^{-5}	0.60246	350.5
	5.5	0.15357	0.41291	-0.65073	4.7363×10^{-5}	0.55563	380.04
	7.5	0.12908	0.38505	-0.65409	3.5445×10^{-5}	0.41581	507.83
96	3.5	0.16831	0.34387	-0.63807	4.1965×10^{-5}	0.4923	428.93
	5.5	0.13119	0.35011	-0.6444	3.3826×10^{-5}	0.39682	532.14
	7.5	0.13694	0.26628	-0.63043	2.9608×10^{-5}	0.34734	607.95
168	3.5	0.13245	0.27822	-0.63058	3.3436×10^{-5}	0.39225	538.34
	5.5	0.15081	0.37101	-0.60969	2.3974×10^{-5}	0.28124	750.82
	7.5	0.45589	0.16747	-0.59895	1.7624×10^{-5}	0.20675	1021.4

and polarization resistance reached the maximum, and the corrosion resistance was the best.

3.2 Eis

According to the literature [16, 17] and the actual EIS of the samples in the corrosion simulation solution, Fig. 2a was selected as the equivalent circuit after immersion for 0 h and 8 h, and Fig. 2b was considered as that after immersion for 36 h, 96 h and 168 h.

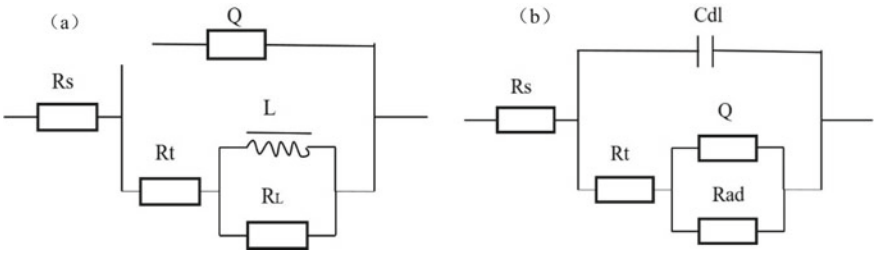

Fig. 2 The equivalent circuit models **a** R(Q(R(RL)), **b** R(C(R(QR))

In Fig. 2, Rs is the solution resistance; Rt is the charge transfer resistance; Q represents the non-ideal capacitance of the corrosion product film. Due to the uneven corrosion product film, constant phase angle element Q is used to replace the ideal capacitor C. L is inductive reactance; RL is the inductive resistance; Rad is the adsorption resistance of the electrode surface. Cdl is the double-layer capacitance on the interface; Rp represents the polarization resistance, and the corresponding value reflects the corrosion degree of the metal [16], which is defined as Rp = Rt when at the initial stage of immersion (0 h, 8 h), otherwise Rp = Rt + Rad.

Figure 3 shows the EIS of the samples at different pH values for 0 h, 8 h, 36 h, 96 h and 168 h, respectively, and EIS were fitted by Zsimdemo software according to the equivalent circuit models of R(Q(R(RL)) and R(C(R(QR)) in Fig. 2. The results are listed in Table 3.

Figure 3a and b show that EIS was mainly composed of capacitive arc at high frequency region and inductive arc of contraction at low frequency region when the samples were immersed at different pH for 0 h and 8 h. And the contraction of the real part at low frequency region indicated the adsorption phenomenon on the surface of electrode corrosion product film [18, 19]. Figure 3c to e show that the EIS exhibited characteristics of mono-capacitive arc resistance, and no induced arc resistance with obvious shrinkage low-frequency area, when the sample is immersed in different pH corrosion simulation solution for 36 h, 96 h and 168 h, respectively. This may be because the redox reaction between metal Fe and hydroxide ions in the solution in the early stage of corrosion will initially form γ-FeOOH with a greater activity. γ-FeOOH can be considered as a cathode to absorb electrons and react with water to form Fe·OH·OH as an intermediate, which is the main reason for the inductive reactance in the EIS [17, 18]. However, this intermediate is prone to react with oxygen to obtain FeOOH and Fe3O4, which will lead to the gradual disappearance of the inductive reactance arc in the low-frequency region with the increase of immersion time [19].

Within the immersion time of 168 h, the capacitive reactance arc radius of the impedance spectrum gradually increased with the increase of pH value. Table 3 shows that Rp value was also increased with the increase of pH value. Above results indicated that the corrosion resistance of the sample in the neutral environment is significantly greater than that in the acid environment.

Table 3 also shows that at the same pH, with the increase of corrosion time, the polarization resistance of the sample first illustrated a decrease and then overall increase trend. This may be because, in the corrosion process, the corrosion product film is gradually formed on the sample surface and will completely cover the sample surface to play a protective effect on the substrate. Therefore, with the increase of immersion time, the corrosion resistance for the initial immersion 36 h in the acid corrosion simulation solution was relatively small, while that was gradually increased after 36 h. However, in the neutral environment, the corrosion rate of the sample is relatively low, and until 96 h for immersion, the formed corrosion products start to act a protective role on the sample, and the corrosion resistance will be increased accordingly. And in the conditions of immersion for 168 h and pH of 7.5,

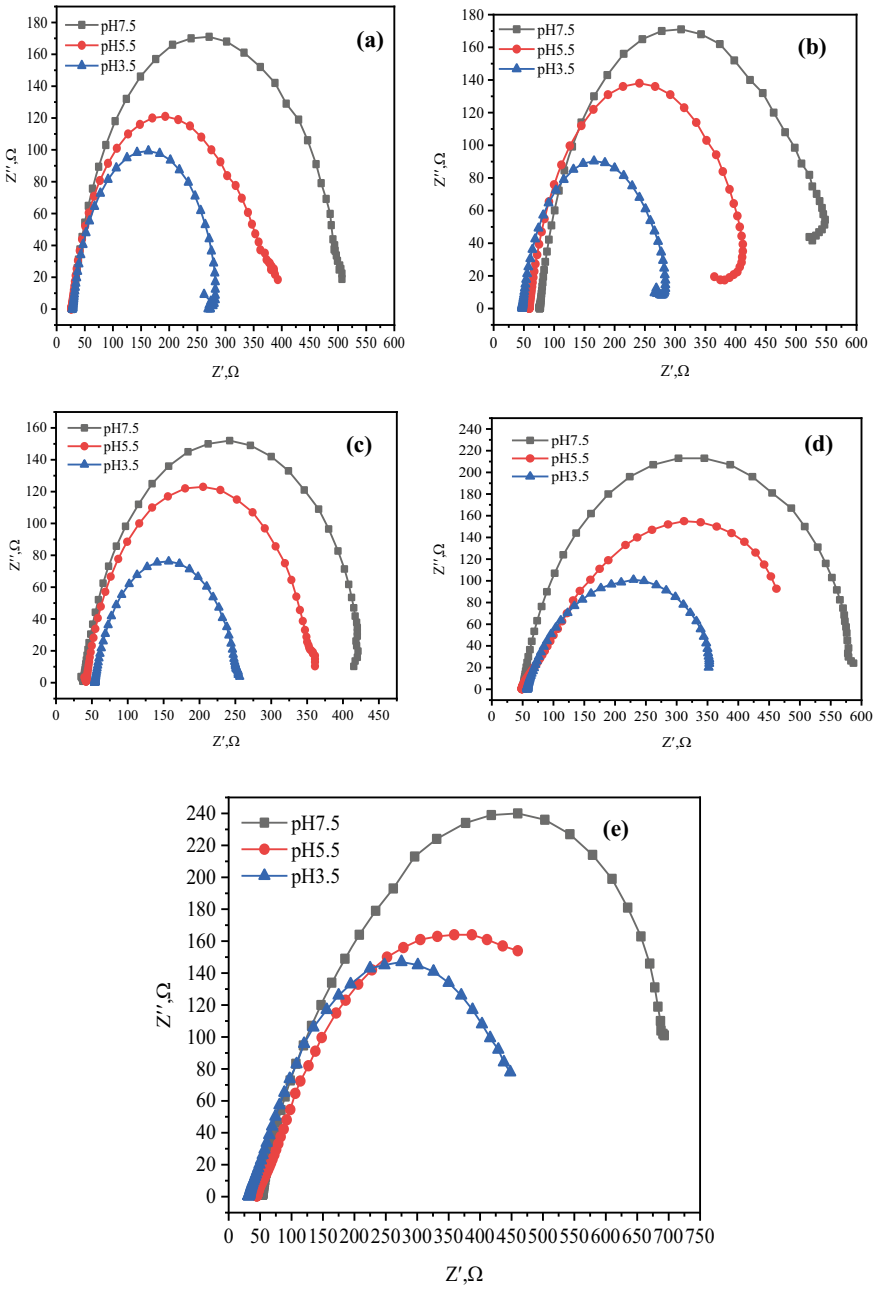

Fig. 3 The EIS of the samples after immersion at different pH values for different time **a** 0 h **b** 8 h **c** 36 h **d** 96 h **e** 168 h

Table 3 The fitting results of the EIS

Time/h	pH	Rs/Ω·cm^2	Rt/Ω·cm^2	R_L/Ω·cm^2	Rad/Ω·cm^2	Rp/Ω·cm^2
0	3.5	28.27	244.2	19.53	0	244.2
0	5.5	26.04	361.5	22.5	0	361.5
0	7.5	27.97	483.6	24.3	0	483.6
8	3.5	47.2	233.1	7.995	0	233.1
8	5.5	58.92	347.9	11.68	0	347.9
8	7.5	75.95	483.8	19.7	0	483.8
36	3.5	54.08	8.167	0	190.8	198.967
36	5.5	35.14	6.822	0	318.8	325.622
36	7.5	30.44	7.515	0	391.2	398.715
96	3.5	57.61	16.73	0	301.6	318.33
96	5.5	49.41	18.5	0	516.9	535.4
96	7.5	50.28	6.173	0	542.2	548.373
168	3.5	32.38	12.04	0	471.7	483.74
168	5.5	45.14	11.72	0	617.3	629.02
168	7.5	36.08	16.72	0	725.9	742.62

the polarization resistance reached the maximum of 742.62 Ω, which is consistent with the above polarization test results

In summary, with the increase of immersion time, the corrosion resistance of the sample was increased to some extent, which is associated with the formation of corrosion product film on the sample surface. However, with the decrease of pH, the corrosion resistance was decreased significantly, which is mainly because that in the acid conditions, the presence of large amounts of hydrogen ions and erosive chloride ions will result in stability decline of the corrosion product film. Thus, the protection of base material performance is limited.

3.3 Microstructure of Electrochemical Corrosion Specimen

The electrochemical corrosion sample was immersed in the corrosion simulation solution at different pH values (200 times the concentration of the original corrosion simulation solution) for 168 h, and the microscopic morphology was observed by SEM as shown in Fig. 4.

Figure 4a shows that after immersion for 168 h at pH of 7.5, the sample surface was covered with a dense passivation film, which has a certain protective effect on the substrate material. There were some corrosion products on the surface of passivation film, which were distributed in clusters or flocculent state, as an indicator of α-FeOOH [20]. Related studies [21] have shown that stable α-FeOOH can effectively prevent water, oxygen and other corrosive substances from reaching the matrix-rust

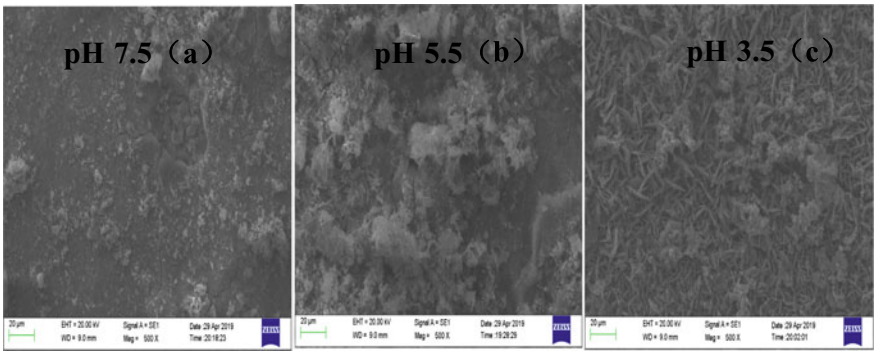

Fig. 4 The SEM of the samples after immersion at different pH values for 168 h

interface, thus reducing the corrosion rate of the matrix material. Figure 4b shows that there were white flocculent and minor needle-like materials distributed on the sample surface after immersion in the corrosion solution with pH value of 5.5 for 168 h, as an indicator [20, 22] of major α-FeOOH and minor γ-FeOOH. Compared with Fig. 4a, the corrosion products formed on the sample surface were more than that at pH of 7.5 after immersion for 168 h, which indicated that in the acid environment, the corrosion reaction between the sample and the corrosion simulation solution was more severe.

Figure 4c reveals that the corrosion products were in the main form of needle-like states and minor form of flocculent state for the samples immersed in the corrosion simulation solution at pH of 3.5 for 168 h. It suggested that the corrosion products are mainly γ-FeOOH and minor α-FeOOH with cross distribution [20, 22, 23], and there was tiny crack on the passive film.

3.4 XRD and EDS Analyses of Corrosion Products

The the surface corrosion products were analyzed by XRD and EDS, and the results are shown in Fig. 5 and Table 4.

Figure 5 shows that, after immersion at different pH values for 168 h, the main corrosion products on the sample surface were Fe2O3, Fe3O4 and FeOOH, with tiny Fe peaks. And with the change of pH value, the phase of the corrosion products did not change significantly. The presence of Fe peaks in the rust layer may be because of the thin rust layer, which will enable X-rays to penetrate the rust layer and reach the inner matrix. Combined with the microscopic morphology of corrosion products in Fig. 4, it was speculated that there are mainly two kinds of corrosion products, namely, γ-FeOOH and α-FeOOH.

Table 4 demonstrates that the corrosion products were mainly Fe and O elements, with minor S elements, which is consistent with the XRD result of iron oxides and

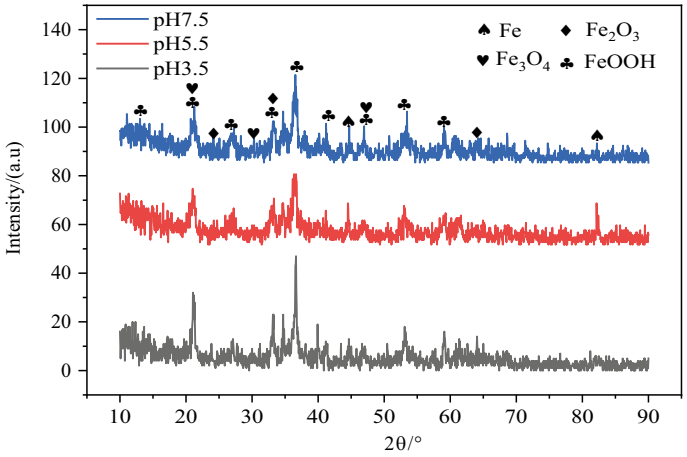

Fig. 5 The XRD of the corrosion products of samples after immersion at different pH values for 168 h

Table 4 The EDS results of the corrosion products of samples after immersion at different pH values for 168 h(Wt%)

pH	Position	C	O	S	Mn	Cr	Ca	Fe	Total
7.5	18	1.77	16.26	1.72	–	–	–	80.25	100
	19	1.74	20.70	3.96	1.06	–	–	72.53	100
	20	2.23	21.74	4.90	–	–	–	71.14	100
	21	2.20	19.02	4.43	–	0.80	–	73.55	100
5.5	6	2.82	26.69	3.52	–	–	–	66.98	100
	7	0.67	10.73	3.61	0.95	0.58	–	83.45	100
	10	1.65	18.84	3.32	–	–	0.38	75.81	100
	11	1.77	20.79	3.66	–	0.61	–	73.16	100
3.5	13	1.61	18.27	0.15	0.49		0.59	78.87	100
	14	1.68	14.50	0.09	–	–	0.47	83.27	100
	15	1.94	14.63	0.27	–	–	0.63	82.53	100
	16	–	0.97	–	–	0.61	–	98.41	100

iron hydroxide in Fig. 5. With the decrease of the pH, the O element content in the corrosion products gradually declined. This may be because the sample had a relatively faster corrosion rate in acid environment than that in neutral environment. Therefore, the faster formation of a layer of corrosion product film on the sample surface will help isolated from the corrosion solution, thus to prevent oxygen to enter.

4 Conclusion

The electrochemical corrosion performance of 20MnTiB high strength bolt was studied by simulating the humid climate in Chongqing. The results were shown that:

Under the same corrosion time, the corrosion current was decreased with the increase of pH, the arc radius of EIS capacitive reactance showed gradually increasing trend, and the polarization resistance value Rp was also increased with the increase of pH value.

At the same pH, the corrosion current was decreased with the increase of corrosion time, and polarization resistance presented first decrease and then the trend of overall increase.

The main corrosion products are mainly consist of elements of Fe and O, followed by C and S, and other elements that existing in the corrosion simulation solution. The phase of the corrosion products did not change significantly with the change of pH value, while with the increase of the corrosion time, the corrosion products transformed from the original FeOOH to the more stable Fe2O3 and Fe3O4.

All the results demonstrated that after immersion at different pH values for 168 h, the sample corrosion resistance was improved, and was significantly increased with the increase of pH value, which is closely related to the corrosion product film on the sample surface.

References

1. Xu Xuesong. Analysis of the impact of steel structure corrosion on the safety production of heat engine plants and countermeasures [C]. 2017 4th marine materials and corrosion protection conference
2. Jiang Zhongliang, Wang Tianzai (1982) Fracture mechanics analysis of stress corrosion cracking of high strength bolts[J]. Ind Constr 7:42–48
3. Wen Juan, Li Zheng, Hu Tao, Liu Lan. Simple analysis on failure of high strength bolts in Chongqing Chaotianmen Bridge[C]. AEMCME2018, Materials science and engineering
4. Mu Yuchong, Zhong Yuan, Gong Chengbing. Comparison of bridge and culvert technical specifications between China and the United States from the perspective of inspection and evaluation of Nanpanjiang bridge [C]. Proceedings of 2013 national bridge academic conference, China
5. Cui Zhemin (2015) Hydrogen embrittlement testing evaluation method research of high strength fasteners[D]. Zhejiang University of Technology
6. Xianming Z (2004) Research and development trend of high strength bolt steel [J]. Heat Treatm Technol Equipm 25(1):33–36
7. Lin Q, Yang X (2009) Fracture analysis of a high strength bolt[J]. Hot Working Technol 38(2):128–130
8. Enhui W (1982) Investigation on corrosion of high strength bolts [J]. Railway Constr 11:40–41
9. Liu Qiang (2007) Study on the corrosion behavior of steel wires in the cable of Long Span cable stayed bridge [D]. Chongqing University
10. Yongjiang Z, Mao D, Li, Yingying (2018) The geochemical character of precipitation of Qianjiang District in Chongqing [J]. Environ Monit China 34(2):47–57

11. Zhao Liang, Lu qunmin, Li Li, Luo Yunzhu, Yang Qingling, Chen Gang (2013) Chemical characteristics of atmospheric precipitation at Wanzhou District of Chongqing [J]. Environ Ecol Three Gorges 35(02):9–15
12. Weihua S, Li, Qingfang, Li, Yingying, Jing Y (2017) Wang Wenfang tendency and correlations of chemical composition in precipitation in Qianjiang district[J]. Environm Sci Manag 42(06):144–148
13. Zhang Can, Meng Xiaoxing, Zhang Guanli (2018) Acid rain pollution in Chongqing [J]. J Green Sci Technol (16):11–14
14. Xiang Bin, Hu Tingting, Liao Shiguo, Huang Wen, Zhang Shengtao (2009) Corrosion behavior of AM60B magnesium alloy in acid rain with different pH value [J]. Material Protect 42(5):65–67
15. Xiang Bin, Zuo Xiuli, Li Xing (2010) Corrosion behavior of 35 steel in simulated acid rain solution [J]. Mater Protect 43(1):54–56
16. Xie Fei (2013) Research on corrosion behavior of X80 pipeline steel and its weld joint in simulated Ku'erle soil solution[D]. China University of Petroleum (EastChina)
17. Shi Yanyan (2008) The electrochemical studies of atmospheric corrosion of typical metals[D]. Zhejiang University
18. Stratman M, Bohnenkamp K, Engell H-J (1983) An electrochemical study of phase-transitions in rust layers. Corros Sci 23(9):969–985
19. Kamimure T, Hara S, Miyuki H, Yamashita M, Uchida H (2006) Composition and protective ability of rust layer formed on weathering steel exposed to various. Corros Sci 48(9):2799–2812
20. Wu Zhifeng, Song Yiquan, Feng Yufei, An Yue (2017) Study on corrosion behavior of low alloy high strength weathering steel in simulated industrial atmosphere under wet and dry alternating condition[J]. Hot Work Technol 46(12):104–106
21. Asami K, Kikuchi M (2003) In-depth distribution of rust on a plain carbon steel and weathering steels exposed to coastal-industrial atmosphere for 17 years [J]. Corr Sci 45(11):2671–2688
22. Wu Hon Yan, Zhao Yanmin, AI Zhengrong, Du Linxiu, Wang Guodong (2013) Corrosion behavior of high strength weathering steels in simulated industrial atmosphere environment[J]. Trans Mater Heat Treatm 34(11):150–155
23. Shiyan Z, Dan L, Xu, Yang Ying, Zeqi WL, Xiaokui Y (2017) Corrosion behaviours of 30CrMnSiA high-strength steel in industrial and marine atmosphere environments[J]. Equip Environm Eng 14(5):25–30

Numerical Simulation of the Influence of Piling on the Surrounding Soil

Dongyue Ci and Chuanyao Gu

Abstract In pile driving construction, the soil around the pile will produce vibration and compaction effects to destroy the safety and stability of the surrounding pipelines and buildings. To study the deformation of surrounding soil during piling, this paper adopts ABAQUS finite element analysis software to drive piles at the penetration rates of 7.5, 5, 2, 1 and 0.2 cm/s, respectively, to study the variation law of soil stress and displacement. The results show that the stress distribution below the pile tip is hemispherical, with a range of 6 times the pile diameter, and there is stress concentration at the pile tip. The soil deformation first produces downward compression deformation, then oblique extrusion, and finally vertical unloading under the action of pile side friction resistance. With the increase of the distance from the pile axis, the vertical displacement of the ground surface on the pile side gradually decreases and tends to be gentle at twice the pile diameter. With the increase in penetration rate, the vertical stress at the pile tip increases to a certain extent, but the change is not obvious. The conclusion above can provide some reference value for practical piling construction.

Keywords Injection pile · Numerical simulation · Rate of penetration

1 Introduction

With the further expansion of the modern city, the engineering geological conditions are becoming more and more complex, and the search for a safe and stable foundation has become the primary goal of the project builders. Among many foundations, pile foundation can be widely used due to its advantages of safety and strong adaptability. In the construction of pile foundation, there are three main modes: hammer method,

D. Ci (✉) · C. Gu
School of Civil Engineering and Architecture, University of Jinan, Jinan, Shandong, China
e-mail: 1360540291@qq.com

C. Gu
e-mail: cea_gucy@163.com

G. Mei et al. (eds.), *Advanced Construction Technology and Research of Deep-Sea Tunnels*, Lecture Notes in Civil Engineering 490,
https://doi.org/10.1007/978-981-97-2417-8_20

static pressure method and vibration method [1]. Among them, the hammer method has the advantages of fast construction speed, small power needed, small space required for operation, good mobility and so on, and has become the most commonly used pile driving method.

At the same time, the hammer method also has many adverse effects. In the process of pile driving, it will cause the soil vibration around the pile. A project in Jiangan District, Wuhan city, Hubei Province, caused the vibration caused by the construction of pile foundation, which caused dispute cases and brought economic losses to the project. Secondly, in the process of piling, the continuous penetration of the pile makes the soil around the pile open around, thus producing the soil squeezing effect [2], Bring adverse effects to the project. Due to the crowding effect of a project in Zhaotong City, Yunnan Province, the vertical displacement of the soil is serious, which causes problems such as surface uplift. At the same time, the process of piling will also have a certain impact on the surrounding environment, resulting in noise, dust and other environmental pollution problems.

In order to ensure the safety and stability of pile foundation, many scholars at home and abroad have done a lot of research on the penetration process of pile body. The new method was applied to the calculation of the stress and strain at the pile end during the deep foundation construction [3]. Somebody proposed the problem of large prediction error of bearing capacity and optimized the pile driving process [4]. The severity of the vibration influence caused by the construction site is analyzed [5]. Two different piling methods, hammer and static pressure, were used to compare their ability to penetrate coarse soil layers of different thickness [6]. Somebody compared the penetration resistance and bearing capacity of model piles by pushing, impact and vibration piling in dry sand foundation and saturated sand foundation [7]. Somebody studied the penetration mechanism of sand pipe pile in the model test, and the results showed that at a certain depth, with the continuous increase of h/D [8].

Among the many research methods of penetration mechanism, numerical analysis method is a method of using simulation software to simulate the piling process, which has the advantages of high efficiency, short period and small cost, and has been widely used. Somebody used ANSYS/LS-DYNA software to simulate the penetration process of the pile body, and analyzed the displacement and stress changes of the soil during the penetration process [9]. Somebody used the finite element software to establish the model and study the vibration attenuation law caused by the piling process [10]. Somebody used ABAQUS to establish a three-dimensional finite element model to study the vibration influence of hammer strike pile driving [11]. By comparison with the measured data in the engineering, the vibration attenuation law of the soil in the process of hammer driving is summarized. Somebody used ANSYS/LS-DYNA to analyze the penetration mechanism of the pile body and the stress change process inside the pile body by using the hammer driving method [12]. Somebody compared the model test and numerical simulation of vibration pile installation in saturated sand to verify the existing simulation techniques [13]. Somebody used ABAQUS finite element software to establish a model of the vibration penetration process of steel pipe pile, and analyzed the impact of the vibration penetration rate, penetration resistance and the ratio of static load and dynamic load force [14].

Table 1 Type styles

Solum	Medium sand	Medium-coarse sand	Round gravel
Depth (m)	109.9	68.5	21.6
Density (kPa)	1810	1910	2060
Modulus of elasticity (kPa)	18,000	24,100	26,400
Poisson ratio	0.3	0.3	0.3
Internal friction angle (°)	37.5	37.8	37.9
Cohesive strength (kPa)	0	0	0

In this paper, numerical simulation is used to simulate the piling process with ABAQUS finite element software, and to study the deformation behavior of soil, which provides some reference value for practical engineering.

2 Materials and Methods

2.1 Model Parameter

Since the elastic modulus of the pile and the difference of the soil, the deformation of the pile can be ignored, and the pile can be regarded as a rigid body part. In order to simplify the model, the pile is 20 m long, the diameter is 2 m, the pile end is 60° cone Angle, and the penetration depth is 15 m (7.5 times the pile diameter). Since the pile adopts analytically rigid body simulation, it is not necessary to set the material parameters of the pile.

The soil is modeled with an axially symmetric shell, 150 m (7.5 times pile length) wide and 200 m deep (10 times pile length), so as to reduce the influence of boundary conditions on the simulation results. Mohr–Coulomb model is used for the properties of soil, which is simple and practical, has few parameters and can well reflect the actual situation. It is widely used in the field of geotechnical technology. Model parameters of soil are shown in Table 1.

2.2 Finite Element Model

Theoretically speaking, the static pressure pile will deform the surrounding soil in the process of penetration, and will bring the generation and dissipation of excess pore pressure. However, the law of soil stress distribution and the formation and dissipation of excess pore pressure is very complex, which is difficult to solve well by general theoretical methods. Therefore, because this paper studies the influence of penetration rate on piling, so the pore water pressure can be ignored.

Fig. 1 Soil mesh division

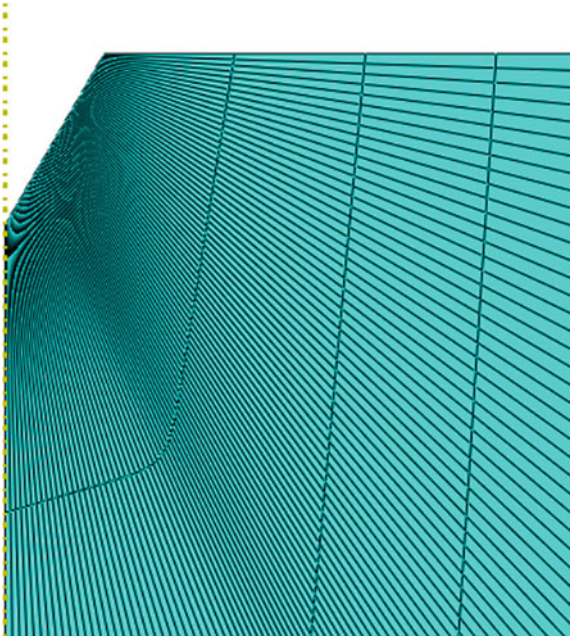

The interaction between piles and soil during simulated pile penetration is a highly nonlinear deformation behavior, so defining the primary and secondary contact surface is adopted during simulated contact. Using the meshing technique of pile penetration with large deformation, Fig. 1. Different penetration rates were set at 7.5, 5, 2, 1, 0.2 cm/s to study the effect on pile end stress.

3 Results and Discussion

3.1 Stress Distribution Law in the Soil During Pile Penetration

Figure 2a shows the horizontal stress of the soil on the pile side (S11); Fig. 2b shows the stress in the vertical direction of the soil (S22).

According to the figure, the radial stress is the largest at the pile end and gradually decreases along the horizontal direction, the stress distribution is hemispherical, the range is 6 times the pile diameter, the radial stress below the pile end decreases rapidly; the maximum vertical stress is within 2 times the pile diameter range below the pile end. Compared with the law of radial stress distribution, the stress bubble of the vertical stress is small horizontal but large in the vertical.

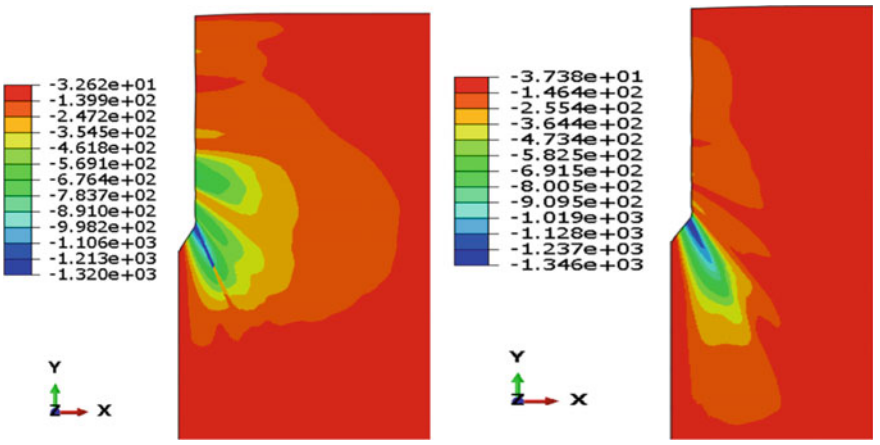

Fig. 2 Cloud diagram of stress distribution in soil side of pile when passing into 15 m

3.2 The Crowding Effect of Pile Penetration

Figure 3 shows the cloud displacement of soil on the pile side when the pile body passes into 15 m.

During piling, the soil structure around the pile is disturbed, which changes the stress state of the soil and produces the squeezing effect. If not handled properly, it will cause damage to the surrounding road surface and buildings, so that the surrounding excavation pit will collapse or increase.

It can be seen from the figure, during the process of piling, the soil below the pile end is under pressure first, which causes the soil to move below. As the pile continues

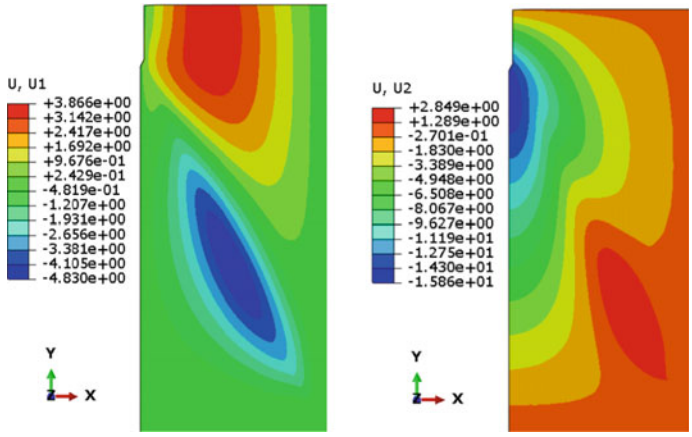

Fig. 3 Horizontal and vertical displacement of the soil on the pile side when passing into 15 m

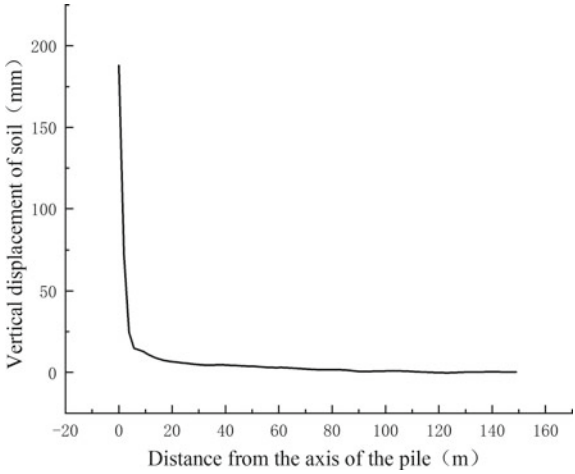

Fig. 4 Vertical displacement of ground surface near pile side

to penetrate, the soil began to move oblique, at the same time, the contact between the pile and the soil will produce the pile side of the resistance, making a certain vertical displacement, when the soil into a certain depth, the displacement of the soil above the pile end is very small, that is, when the penetration of the pile is not deep, the soil is loaded; when the pile continues to pass downward, the soil is unloaded.

Figure 4 shows the vertical settlement of the surface near the pile side; the vertical displacement of the soil is maximum near the pile wall and then decreases rapidly along the radial direction; at 2 times the pile diameter from the pile axis, indicating that the vertical displacement on the soil surface affects 2 times the pile diameter during the piling. In addition, with the increasing penetration depth of the pile body, the maximum uplift displacement of the surface on the pile side is small.

3.3 The Influence of the Pile Penetration Rate

The cloud map of stress in the horizontal direction at different penetration rates 7.5, 5, 2, 1, 0.2 cm/s is shown in Fig. 5. As can be seen from Fig. 5, with the increase of the penetration rate, the distribution shape of soil resistance in the radial direction is roughly the same, that is, the penetration rate has little influence on the stress field distribution, but the stress conditions in different depths have certain changes, and it changes with the penetration depth as shown in Table 2. The graph of the change of pile end resistance with penetration depth and penetration rate is shown in Fig. 6.

It can be seen from Fig. 6 that as the penetration depth increases, the pile end resistance is also increasing, but the penetration rate is very little affected. For the soil of the same depth, increasing the penetration rate increases the stress weakly.

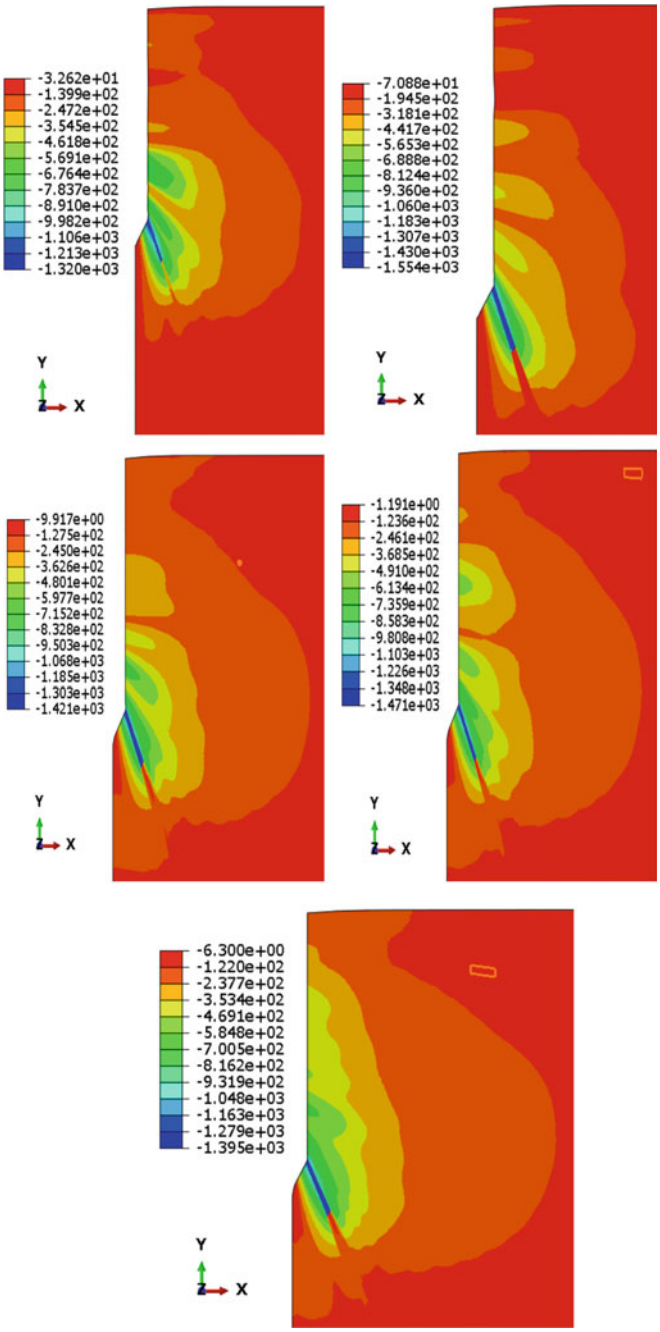

Fig. 5 Radial stress cloud diagram of 15 m at different penetration rates

Table 2 Changes of pile end resistance with penetration rate

Speed (cm/s) Degree of depth (m)	3.00	6.00	9.00	12.00	15.00
7.5	13.85	658.99	909.50	789.27	854.49
5	32.90	666.13	747.91	675.30	669.84
2	52.44	521.78	811.01	781.46	699.89
1	97.08	451.01	750.99	854.78	761.47
0.2	63.07	466.39	734.96	812.75	730.30
7.5	13.85	658.99	909.50	789.27	854.49

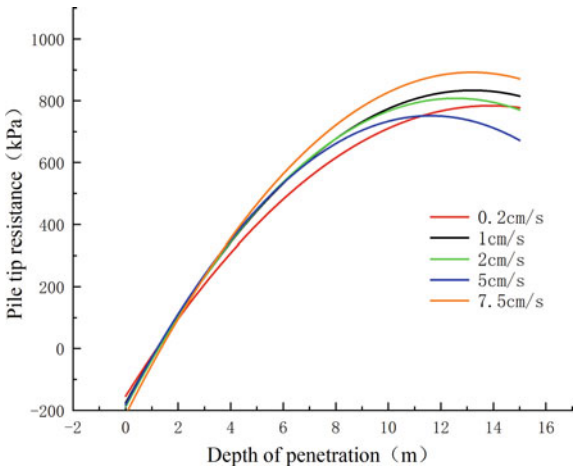

Fig. 6 Change diagram of pile end resistance with penetration depth

4 Conclusion

Through the above sorting and analysis of the integrated simulation results, the main conclusions can be summarized as follows:

The stress distribution below the pile end is hemispherical, the stress field diffuses from the pile end to the surrounding, and there is stress concentration at the pile end.

With the increase of penetration depth, the soil first produces downward compression deformation, then oblique extrusion, and in addition, the uplift displacement decreases with the increase of the distance from the pile axis, and becomes flat at 2 times the pile diameter.

With the increase of the penetration depth, the pile end resistance is also increasing, but its penetration rate is very little affected. For the soil of the same depth, increasing the penetration rate increases the stress weakly.

References

1. Fu T (1993) Pile hammer in piling and its interaction with piles. Geotech Found 7(2):41–47
2. Wei L, Li S, Du M et al (2021) Numerical analysis of soil squeezing effect of static pressure pipe pile based on CEL method. J South China Univ Technol (Nat Sci Ed) 49(04):28–38
3. Baligh MM (1985) Strain path method. J Geotech Eng 111(9):1108–1136
4. Li T, Xu Z, Luo J (2010) Simulation algorithm for precast pile driving process. Highw Eng 35(5):75–81
5. Than Da Vamoorthy TS (2004) Piling in fine and medium sand—a case study of ground and pile vibration. Soil Dyn Earthq Eng 24(4):295–304
6. Wu W (2007) A comparative study on the penetration ability of static pressure and hammer sinking pile. J Fujian Inst Eng 5(3):240–242
7. Moriyasu S, Shinkuma M, Matsumoto T et al (2020) Influence of cyclic pile behaviour caused by surging and vibratory pile driving on the penetration resistance and bearing capacity. In: Geotechnics for sustainable infrastructure development
8. Gavin, Kenneth G, Lehane et al (2003) The shaft capacity of pipe piles in sand. Can Geotech J 40(1):36–45
9. Zhou M, Zhu N, Zhang P (2014) Numerical simulation of the piling process based on ANSYS/LS-DYNA. Comput Knowl Technol 10(09):2152–2154 + 2158
10. Ekanayake SD, Liyanapathirana DS, Leo CJ (2013) Influence zone around a closed-ended pile during vibratory driving. Soil Dyn Earthq Eng 53:26–36
11. Lin Y, Wang Q, Chen S et al (2019) Finite element analysis of the influence of hammer pile driving on the vibration of surrounding buildings. J Fujian Univ Eng 17(4):6
12. Hu B, Zhu Z, Wang Z (2012) Study on the dynamic stress of pile body in the process of hammer hitting and pile driving. Build Sci 28(7):87–89
13. Chrisopoulos S, Vogelsang J, Triantafyllidis T (2017) FE simulation of model tests on vibratory pile driving in saturated sand. Springer International Publishing
14. Xiao Y (2018) Finite element analysis of high frequency vibration penetration rate of large diameter steel tube pile based on ABAQUS. J Chongqing Univ: Nat Sci Ed 41(9):105–112

Key Construction Technology and Engineering Material Research

Experimental Study on the Factors Influencing the Arch Height of Overlying Soil in Karst Area

Di Wu, Aiwen Li, Yongli You, and Jianjian Wu

Abstract On the evolution of collapsed soil caves, it is important to consider the soil arching effect and the factors that influence arch height. This study examines the impact of collapse width and filling height on load distribution and soil displacement to uncover the stability mechanisms of soil cavities. The findings reveal that: (1) Explaining the formation of soil sinkholes in terms of load sharing, it is evident that the soil arching effect enables transfer of pressure exerted above the soil arch to the nearby stable region that results in stress deflection within the stable area. (2) Interpretation of soil cave evolution based on displacement angle, indicating that the process of collapsing the soil cave triggers the soil arch effect due to the uneven force of soil particles, leading to soil settlement. (3) Arch height is the primary factor for measuring the soil cave stability from the perspective of soil displacement. Compared to the factor of filling height, the collapse width has more influence on the arch height. Thus, engineers working in karst areas should prioritize understanding the stability mechanism of soil holes to enhance the safety and reliability of construction projects.

Keywords Overlying karst collapse · Soil arch effect · Soil arch height · Modeling tests

D. Wu · A. Li · J. Wu
School of Architecture and Transportation Engineering, Guilin University of Electronic Technology, Guilin 541200, Guangxi, China
e-mail: wudi@guet.edu.cn

J. Wu
e-mail: guetcoiln_w@163.com

Y. You (✉)
Jiangxi Provincial Highway Scientific Research and Design Institute Co., Ltd., Nanchang 330002, Jiangxi, China
e-mail: 578977662@qq.com

G. Mei et al. (eds.), *Advanced Construction Technology and Research of Deep-Sea Tunnels*, Lecture Notes in Civil Engineering 490,
https://doi.org/10.1007/978-981-97-2417-8_21

1 Introduction

Many soil holes in karst regions threaten people's safety and property [1], particularly during road construction. This situation has drawn the attention of domestic and foreign scholars to the stability of earth holes in karst regions.

In terms of the research factors impacting soil caverns stability, Qin et al. [2] developed an equation to determine the stability coefficient when approaching a critical state of collapse in a karst region. Santo et al. [3] discovered that the stability coefficient of soil holes is tied to the height of the upper layer of overburden soil. Chen et al. [4] and Wei and Sun [5] discovered that the stability coefficient of the soil hole is higher when the overburden layer is thicker and with the higher water level. Xu and Song [6] conducted scaled-down model tests and discovered that the arch height should be between 1.0 times and 1.5 times the width of the collapse. These studies show that the stability of earth cavities is determined by the stability coefficient, which impacted by the collapse width and upper cover layer thickness.

On the research of deformation mechanisms in the development of soil cavities, Parise and Lollino [7] conducted a study using numerical simulation to analyse the stress of soil cavities to reveal the damage mechanism of the soil cavity. Shen et al. [8] found soil cavity development involves generating and eliminating the soil arch effect of the cover soil body. On the other hand, Juan et al. [9] suggested a suspension chain line soil arch model to explain how the earth arch effect works during the collapse of earth holes. It is clear that the stability of soil holes are connected to the earth arch effect, and this effect is significant for keeping the holes stable in the evolution.

In summary, in the stability study of the soil caverns, there mainly used the methods of numerical simulations and formula derivation, and less often used test methods presently. It hinder the further disclosure of the stability mechanism of soil caves. Additionally, during the soil cave evolution, the height of the soil arch is the stable support condition of the cave, but also the key to play the soil arch effect, which should be paid attention to in the research process. Thus, this paper conducted a scaled-down model test on the collapse of soil caves, which research how the height of the arch affects cave stability when subjected to arching effect, aiming to reveal the stability mechanism of soil holes.

2 Model Test

2.1 Experiment Device and Implementation Schemes

The experimental design references the case of collapse of a long pothole (about 1.5 m long and 1 m wide) at Laiwu City, Shandong Province. Depending on the site's structure and experiment conditions, the design similarity ratio is defined as 10. According to the similarity ratio, and consider the convenience of the test operation, the experiment box used in the test was 1.5 × 0.6 × 1.5 m (length × width ×

Table 1 Experiment scheme

Research contents	Test group	Cohesion c (kPa)	Depth of filling H (m)	Collapsed width B (m)
Collapse width	Z1	1	1	0.3
	Z2	1	1	0.2
	Z3	1	1	0.1
Depth of fill	Z4	1	0.6	0.3
	Z5	1	0.2	0.3

Table 2 Basic performance index of Li-jiang sand

Material	Air drying moisture content (%)	The biggest dry density ($kg \cdot m^{-3}$)	Cohesion (kPa)	Internal friction angle (°)
Li-jiang sand	1.05	1.68	0.2	32

height), which has a glass perspective surface and movable floor settlement system. Additionally, in order to carry out the load-sharing test between collapse area and stable area under different collapse widths, setting 0.3 m wide collapse area and 0.6 m stabilization zone on both sides as the standard group. The specific test scheme is shown in Table 1. In terms of packing, test materials using Lijiang sand, filtered through a 2 mm sieve prior to testing. Based on geotechnical tests, the test sand found to be poorly graded silt. The material properties can be found in Table 2.

2.2 Arrange of Test Monitoring Points

To study the effects of settlement width and fill height on the load distribution and soil displacement in the collapse zone, displacement measuring points were placed every 10 cm along the center line and monitored with displacement meters. Additionally, according to the symmetry principle of the soil arching, the soil pressure in the stable area on both sides of the collapse area is assumed to be equal, hence, only the soil pressure box is placed in the right stability area to monitor the soil pressure. The data of tests are collected by the static strain meter. The arrangements of test's measuring point are depicted in the Fig. 1. In addition, using the particle image speed measuring equipment (PIV) to monitor the vertical displacement of the soil particles. The test site picture is shown in Fig. 2.

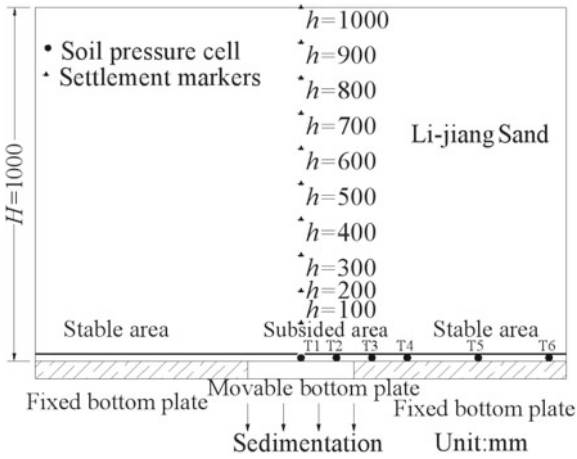

Fig. 1 Measurement point layout diagram

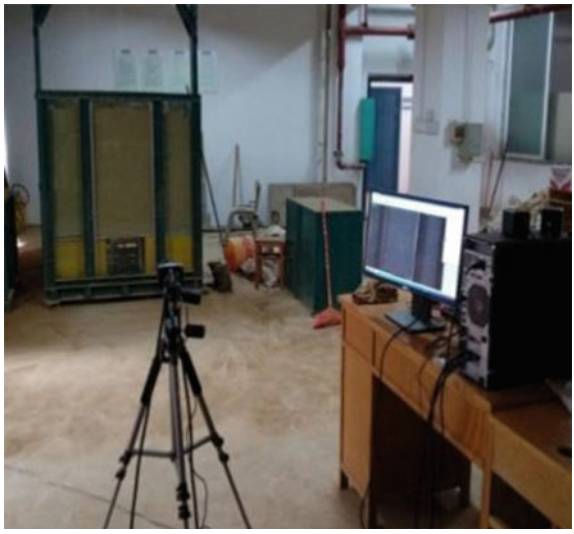

Fig. 2 Field drawing of the retaining wall model

3 Results and Discussion

3.1 Effect of Different Collapse Widths on Soil Cave Stability

Analysis of the soil vertical displacement results. Figure 3 displays the map of soil displacement cloud of groups Z1, Z2 and Z3 under PIV observation. Apparently, vertical displacement increasing as the soil approaches the collapsing zone, and the distribution of soil particles during collapse is in an arch. The allowable settlement value resulting from urban underground works is 0.03 m [10]. Thus, it is considered

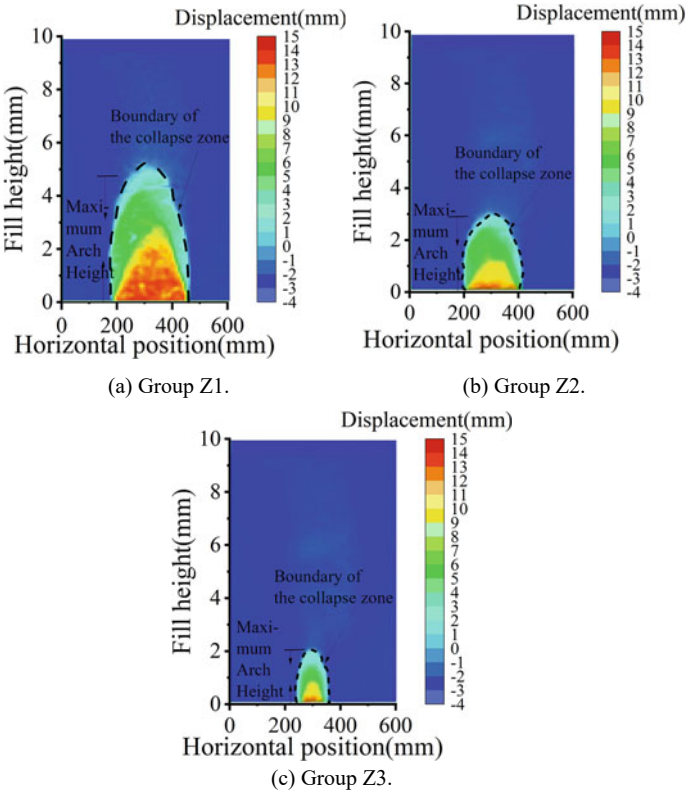

Fig. 3 Displacement cloud map at different collapse widths

as instability, if the range of uneven ground settlement exceeds 0.03 m in the test. It revealed the range of unstable soil depths in groups Z1, Z2, and Z3. This confirms that the soil above the arch height is stable, while the soil below the arch is unstable.

Simultaneously, Fig. 4 shows cloud map of vertical displacement variations at soil locations Z1, Z2, and Z3. Overall, the filling's displacement gradually reduced as the filling height increased. Groups Z1, Z2 and Z3 had a displacement value of zero at 0.92 m, 0.32 m and 0.19 m respectively, indicating that the soil arch had reached its maximum height. This indicates that with the collapse width decreases, the maximum arch height decreases. Thus, from the displacement perspective, the height of the arch is the crucial factor for evaluating the stability of a soil caves, which should be emphasis in engineering.

Effects on load-sharing. Figure 5 depicts the soil pressure curve in the collapse area at T1, T2, T3, and T4, alongside the relative settlement of the activity floor under various collapse widths. First, based on the analysis of the measuring points in the collapse area, it is evident that the change trend of T2 is similar to that of T1. Dividing this curve into two stages: a steep drop followed by a slow change.

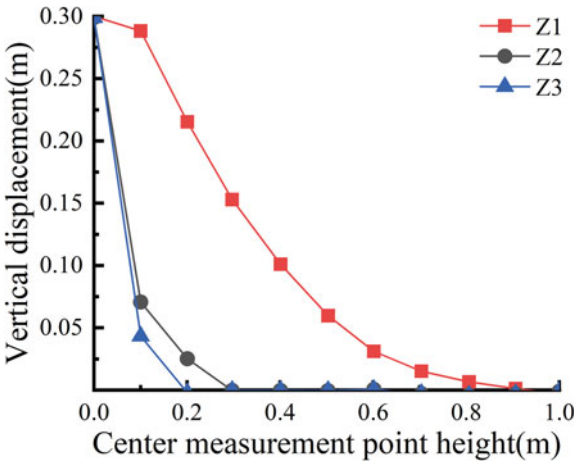

Fig. 4 Vertical displacement change diagram of the collapse center line measuring points under different collapse widths

Additionally, the difference in soil pressure between the beginning and end of each soil group is not substantial. Filling of the boundary of the collapse zone is not only generate a displacement due to contact with the boundary, but also subject to principal stress deflection due to boundary constraints. Consequently, soil pressure decreased more near the boundary of the collapse zone than in its center. Secondly, analyzing the T3 sites located near the edge of collapse in test. Clearly, the soil pressure distribution curves at the T3 point in three groups, all with 0.02 m as the boundary are sequentially divided into two phases of sharp increase and slow decrease. In the stage of subsidence, the maximum soil pressure of Z2 and Z3 is greater than 50%. It is due to the earth arch is formed between the stable area and the subsidence area, which means the transfer of loads. Moreover, analyzing the T4 measurement points shows that the soil pressure at the T4 points of Z1, Z2 and Z3 test groups gradually stabilized from 0.005 m after different increases, but the overall rise rate decline in order. Implying that the collapse width is large while the soil pressure value is high. In addition, T3 and T4 points could raise the soil pressure in the stable area. This indicates that the existence of soil arching effects could transfer the overburden load to the stable region, causing an increase in soil pressure. The wider the collapse width, the greater the soil pressure of the stable area. Besides, due to the T5 and T6 measuring points are further from the collapse area than the T4 measuring points, the variation in soil pressure with respect to bottom plate settlement is less than T4, which is not being discussed.

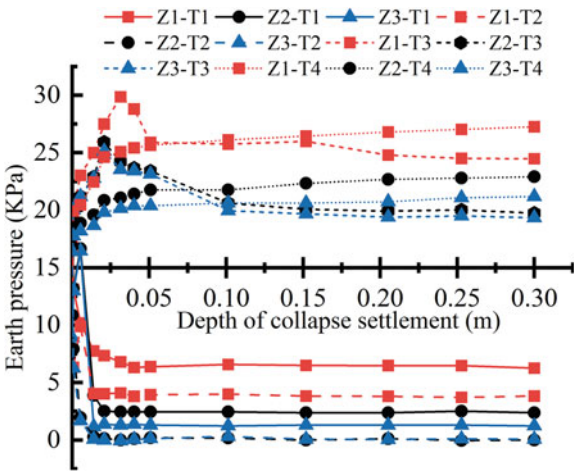

Fig. 5 Change curve of soil pressure at each measuring point under different collapse widths

3.2 *Influence of Different Filling Height on the Stability of Soil Cave*

Effects on load-sharing. Figure 6 illustrates the trend in soil pressure for T4 points in Z4 and Z5 groups. As shown in the figure, the change trend of soil pressure in T4 measuring points in Z4 and Z5 groups is similar to that of the Z1 group, indicating that filling height has minimal impact on the load-sharing component. Meanwhile due to T4 is a representative load sharing point near the foot of the arch, the rest of the points would not be analyzed further. Because comparing to T4, T3 measuring point is susceptible by near the collapse area, while T5 points and T6 points exhibit less load sharing at the arch foot owing to their distance from the collapse zone.

Analysis of the soil vertical displacement results. Figure 7 displays the vertical displacement curve of the centerline collapse area for Z4 and Z5 groups once the movable plate settles at 0.3 m. The analysis focuses solely on measuring points under 0.2 m in height. As seen in the figure, the curves of the three setting conditions nearly overlap. Upon settlement completion, the vertical displacement of Z4 and Z5 was 0.025 m, however, the Z4 and Z5 test groups had a vertical displacement of 0.021 m and 0.02 m, respectively, at the $h = 0.2$ m marker points. Demonstrating at a specific collapse width, a critical stability value exists in the soil arch height. Additionally, when the fill thickness reaches an adequate level, the increase in height of the overlying soil layer has minimal impact on the soil arch height.

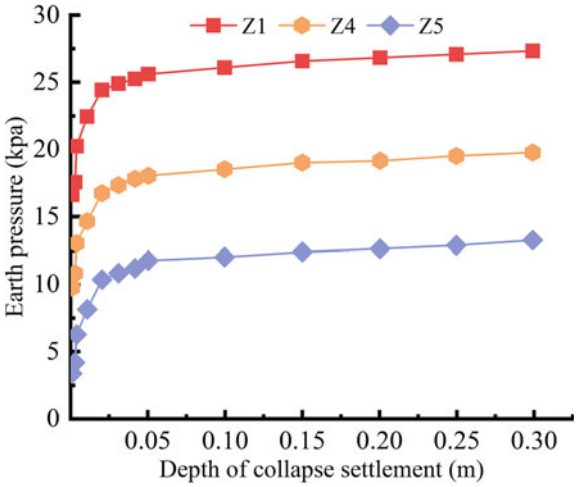

Fig. 6 Variation curve of soil pressure at T4 measurement point at different filling heights

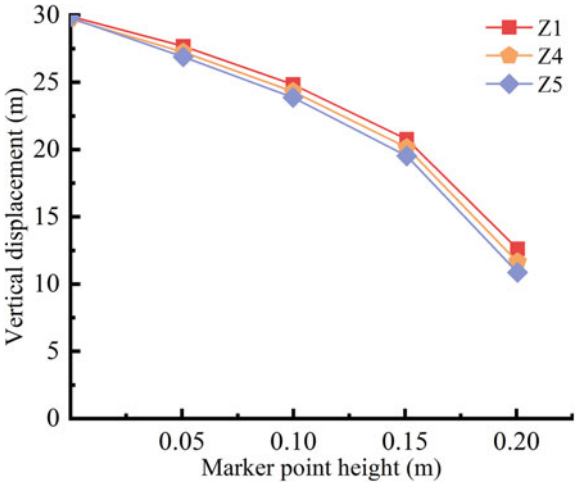

Fig. 7 Vertical displacement curves for settlement up to 0.3 m at different fill heights

4 Conclusion

The study analyzed the effect of changes in slump width and filling height on the maximum soil arch height and load distribution in the slump region. The main research conclusions are the following.

- During collapse, load in the stable area increasing. This indicates that the soil arching effect transfer the load from the overlying soil to the stable area to maintain stability of the earthen cave.

- In the process of collapse, the soil particles settle unevenly. However, soil particles with the same displacement create a maximum arch interface finally which stabilizes the settlement. This effect is referred to as the soil arching effect.
- The narrower the collapse width, the stronger the stability of the soil cave and the lower the maximum arch height. However, the filling height does not significantly affect the stability and arch height of the soil cave.

Acknowledgements Financial support for this work is gratefully acknowledged by the National Natural Science Foundation of China Grant (No. 42067044), Guangxi Science and Technology Major Program Grant (No. AB23026028), and Science and Technology Project of Jiangxi Provincial Department of Transportation (No. 2022H0030).

References

1. Sheinin VI, Anikeev AV, Kochev AD, Korol OA (2023) Analysis of causes and geomechanical schematization of catastrophic karst subsidence development. KSCE J Civ Eng 60:348–355
2. Qin JW, Song GX, Pan GM (2021) Cause and law of karst collapse in the urban complex environment: an example of Beihuanxincun, Guigang City. Carsol Sin 40:230–237
3. Santo A, Budetta P, Forte G, Marino E, Pignalosa A (2017) Karst collapse susceptibility assessment: a case study on the Amalfi Coast (Southern Italy). Geomorphol Amst 285:247–259
4. Chen HB, Guo RJ, Chen XJ (2022) Collapse model and influence factor analysis of covered karst soil cave induced by vacuum erosion. J Eng Geol 30:1284–1291
5. Wei YY, Sun SL (2018) Comprehensive critical mechanical model of covered karst collapse under the effects of positive and negative pressure. Bull Eng Geol Environ 77:177–190
6. Xu C, Song ST (2015) Scaled model tests of soil arching effect in geosynthetic reinforced and pile supported embankments. Chin J Rock Mech Eng 34:4343–4350
7. Parise M, Lollino P (2011) A preliminary analysis of failure mechanisms in karst and man-made underground caves in Southern Italy. Geomorphology 134:132–143
8. Shen J, Jian WB, Su TJ, Hong RB, Zhang SB (2020) Research on the evolution process of earth cave collapse in karst area—earth cave collapse in Zhangkeng nature village, Longyan City as an example. J Water Resour Arch Eng 18:1–8+64
9. Juan A, Marina M, Laura A, Gema DLM, Jorge PG, Vicente N (2020) A catenary model for the analysis of arching effect in soils and its application to predicting sinkhole collapse. Geotechnique 72:11–46
10. Zhu YG, Zhou XJ, Deng B (2008) Criteria for control of surface settlement of underground structures during subway construction. Sichuan Constr 28:86–87

Experimental Study on Frost Heave Characteristics of Silty Clay Beneath Operating Stations in Twin Tunnel Freezing

Lei Wang

Abstract Artificial ground freezing method construction is widely applied in the subway construction in Shanghai. In the project of the twin tunnel freezing method crossing the operating Line 10 station at No.18 Guoquan Road in Shanghai, the tunnel is located in the silty clay with a water content of 38.5%. The frost heave pressure of the silty clay will cause uplift and even cracking of the already operating station. Taking the Shanghai silty clay as the research object, this study investigates the influence of the cold end temperature and conductive temperature on the frost heave pressure of the soil through laboratory frost heave experiments and similar simulation experiments. The results show that under closed freezing conditions, there is a good linear relationship between the frost heave pressure of the silty clay and the cold end temperature, while under open freezing conditions, the frost heave pressure of the soil has a quadratic relationship with the temperature difference of the soil under the structure's base plate. The research findings will provide valuable references for projects such as the freezing method for crossing operating stations and existing lines in Shanghai subway construction.

Keywords Artificial ground freezing · Frost heave · Freezing scheme · Similarity simulation experiment · Freezing underpassing project

1 Introduction

The freezing method has been widely applied in the construction of Shanghai subway, and it is commonly used in projects such as auxiliary tunnels, underground pump rooms, and station entrances [1, 2]. It has shown good performance in water-rich

L. Wang (✉)
Beijing China Coal Mine Engineering Co., Ltd., Beijing 100013, China
e-mail: tumuwanglei@yeah.net

China Coal Research Institute, Beijing 100013, China

College of Civil and Transportation Engineering, Shenzhen University, Shenzhen 518060, China

G. Mei et al. (eds.), *Advanced Construction Technology and Research of Deep-Sea Tunnels*, Lecture Notes in Civil Engineering 490,
https://doi.org/10.1007/978-981-97-2417-8_22

soil layers, but has also caused safety accidents [3]. With the large-scale construction of subway lines in Shanghai, the issue of intersections and transfers between different lines has emerged, leading to the construction of multiple station crossings, surface buildings, and inter-station tunnels. This poses new challenges for the design and construction of subway systems when crossing through water-rich soil layers. Ensuring the safety of the structures above in such engineering projects becomes a key and difficult task.

In the project of the twin tunnel freezing method crossing the operating Line 10 station at No.18 Guoquan Road, Shanghai, the tunnel is designed to underpass through the soft soil layer using the freezing method. The proposed internal diameter of the up and down tunnels is 5.9 m, with assembled segment thickness of 0.35 m. To ensure smooth excavation by shield tunneling and provide a clearance diameter of 7 m, the distance between the top of the tunnel segments and the station floor is 2.209 m, and the designed distance between the freezing pipes and the station floor is 0.76 m, as seen in Fig. 1.

According to the design, the station platform is located below the 0 °C line. The station is greatly affected by low temperatures, and frost heave has a significant impact on the upper operating station. Therefore, it is necessary to study the frost heave characteristics of the grayish powdery clay at the ⑤11 layer.

Currently, a large number of studies are conducted in laboratories, following the "MT/T 593.2-2011 Physical Mechanical Properties Test of Artificial Frozen Soil Part II: Soil Frost Heave Test Method" for frost heave pressure testing. The frost heave pressure in a closed frost heave test refers to the average axial thrust per unit area generated after a unidirectional freezing process under conditions without lateral deformation and with restrictions on the upper and lower surfaces (no deformation). However, the frost heave pressure in engineering occurs under conditions with lateral deformation, so there is a difference between the frost heave pressures induced under closed and non-closed conditions. The objective of this study is to investigate the frost heave pressure characteristics under closed and non-closed conditions for this specific engineering scenario.

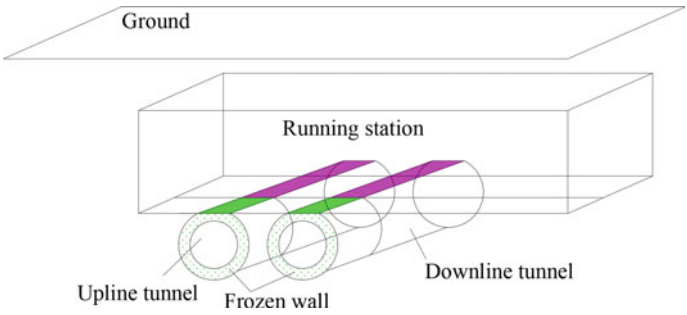

Fig. 1 The map of the proposed tunnel and frozen wall and station

Lou and Chen [4] analyzed the technical risks of using the freezing method for the Shanghai Sports Center Station of Shanghai Metro Line 4, which crosses Line 1 at zero distance, and demonstrated the reliability of the freezing method for constructing soft soil subway stations with zero-distance crossings. Lin et al. [5] conducted theoretical calculations on the freezing design for the Shanghai Sports Arena crossing the original Shanghai Metro Line 1 at Shanghai Sports Station in the second phase of the Shanghai Metro Mingzhu Line project and concluded that the design freezing method is reliable. Tang et al. [6] conducted experimental research on the frost heave characteristics of silty clay under freezing conditions and obtained the frost heave characteristics of silty clay under closed test conditions. Cheng [7] concluded that sandy soil has a small frost heave pressure, while saturated soft clay has a large frost heave pressure. Cai et al. [8] established a time-dependent prediction model for surface frost heave displacement caused by tunnel horizontal freezing construction based on the theory of random media. Alzoubi et al. [9] proposed a two-dimensional intermittent freezing model based on mass, momentum, and energy conservation, indicating that adopting the intermittent freezing method can reduce engineering power consumption by 40%. Cai [10] conducted experimental research on the temperature field and frost heave settlement variation in double-line tunnel formations, obtaining that adopting a sequential freezing method for double-line tunnels can to some extent reduce ground frost heave displacement.

2 Project Overview

Please follow these instructions as carefully as possible so all articles within a conference have the same style to the title page. This paragraph follows a section title so it should not be indented [2, 3].

The construction method for the Shanghai Metro Line 18, which crosses the operational Line 10 at Guoquan Road Station, involves reinpressurement through freezing followed by excavation using the underground mining method to form the tunnel for Line 18.

The proposed dual-line tunnel intersects with the station vertically. The centerline elevation of the frozen excavated tunnel is −19.011 m, while the ground elevation is +3.2 m. The up and down lines of the tunnel need to sequentially pass through the main structural elements of the newly built Line 18 Guoquan Road Station, including the A-wall, the eastern main structure of Line 10 Guoquan Road Station (B-wall), the western main structure of Line 10 Guoquan Road Station (C-wall), as well as the maintenance structure of Exit 4 of Line 10 Guoquan Road Station (D-wall), see in Fig. 2.

The ⑤11 layer consists of grayish powdery clay with the presence of calcareous nodules, organic matter, etc. The soil is relatively uniform, very moist, in a soft-plastic state, and exhibits high compressibility. The parameters are shown in the Table 1.

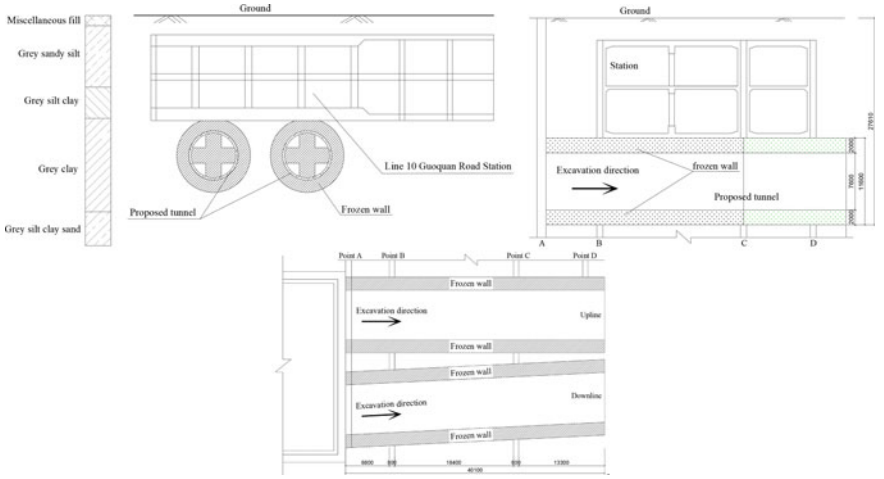

Fig. 2 Location map of the proposed tunnel and Guoquan Road Station

Table 1 Soil parameters

Soil layer no.	Soil name	Water content $W\%$	Saturation $Sr\%$	Porosity e	Liquid limit $W_L\%$	Plastic limit $Wp\%$
⑤11	Grey powdery clay	38.5	97	1.09	40.4	23.3

3 Enclosed Frost Heaving Test

3.1 Test Procedure

(1) Prepare a cylindrical soil sample with a diameter of 50 mm and a height of 100 mm by configuring the moisture content and filling the soil into a sample cylinder. Put the sample into the frost heaving testing machine.
(2) Set the temperature of the top and bottom plates of the frost heaving testing machine. The temperature of the hot plate is set to 20 °C. The temperature of the cold plate is divided into 4 groups, which are set to −20 °C, −15 °C, −10 °C, and −5 °C, respectively. Repeat the tests.

3.2 Results and Analysis of Enclosed Frost Heaving Test

The frost heaving pressure curves at different cold-end temperatures are shown in the Fig. 3.

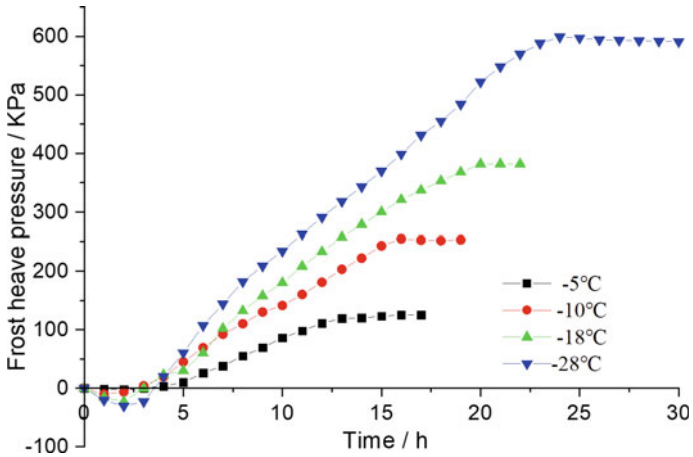

Fig. 3 Frost heave pressure curve at different cold end temperatures

As can be seen from the Fig. 3, with the decrease of the cold-end temperature, the frost heaving pressure of the ⑤11 grayish powdery clay sample gradually increases. From the change pattern of the frost heaving pressure–time curve, the frost heaving process of the ⑤11 grayish powdery clay body can be divided into four stages: the (1) freezing and shrinking stage where the volume of the soil body reduces before cooling to 4 °C; the (2) rapid growth stage of frost heaving pressure where the water begins to freeze and the frost heaving pressure starts to increase rapidly; the (3) slow growth stage of frost heaving where the ice formation is gradually sufficient and the frost heaving grows slowly; and the (4) stable stage where the ice formation reaches good stability. It can be obtained that there is a good linear relationship between the maximum frost heaving pressure of the soil and the experimental cold-end temperature, which can be expressed as $F1 = 0.03|T1|$.

4 Open Freeze–Thaw Experiment

4.1 Similarity Criteria

During the experiment, the physical model must satisfy a series of similarity criteria such as temperature, humidity, stress, displacement, etc. In the construction process of the upper structure under the frozen tunnel, the following criteria are primarily considered:

(1) The temperature field similarity criterion for the absorption of heat from the soil by low-temperature saline water, leading to the freezing of moisture in the soil, is expressed as Eq. (1):

$$F(F_0, K_0, R, \theta) = 0 \tag{1}$$

Here, F_0 represents the Fourier criterion, K_0 denotes the Kosovic criterion, R represents the geometric criterion, and θ refers to the temperature criterion. The experimental soil is taken from the actual construction site, hence the temperature and water content parameters in the model are equivalent to those of the in-situ soil. Thus, the similarity ratio for parameters such as soil temperature, internal friction angle, Poisson's ratio, porosity, etc., during the experiment is 1.

The humidity field criterion for the soil in Eq. (2):

$$\Theta = \frac{w}{w_0} \tag{2}$$

Here, w_d represents the humidity of the soil after freezing, and w_0 is the initial soil humidity. According to the humidity criterion, the heat conduction process and the water migration process are mathematically similar, both of which abide by the Fourier criterion. Therefore, under the conditions of geometric similarity, as long as the temperature field is similar, the humidity field can achieve "self-simulation" and be similar.

(2) The non-dimensional stress-displacement field equation for deformation caused by freezing and excavation of the overlying soil can be expressed as Eq. (3):

$$F\left(\frac{E_d}{\sigma}, \frac{\mu_d}{D_s}, \frac{H}{S_d}, \frac{E_d}{rH}\right) = 0 \tag{3}$$

Here, H is the depth of the tunnel, D is the tunnel diameter, S_d is the thickness of the frozen wall, μ_d represents displacement, σ denotes stress, r is the bulk density, and E_d is the modulus of deformation.

(3) Stiffness criterion: Deformation occurs in the upper structure due to frost heave or thaw settlement. According to linear elastic mechanics, the deflection of a structure under external forces is inversely proportional to its stiffness, i.e., as in Eq. (4)

$$u_\mathrm{s} \infty 1/K \tag{4}$$

Here, u_s represents the displacement caused by frost heave pressure, $K = EI$ is the stiffness of the structure's base plate, and I is the moment of inertia.

Based on the aforementioned criteria, the similarity ratios for temperature, stress, time, length, density, and displacement can be expressed as Eq. (5):

$$\begin{aligned} C_\mathrm{T} &= C_\mathrm{S} = 1 \\ C_\mathrm{t} &= n^2 \\ C_\mathrm{L} &= C_\rho = C_\mathrm{d} = n \end{aligned} \tag{5}$$

Here, n represents the geometric scale ratio, C_T, C_S, C_t, C_L, C_ρ, and C_d are the similarity ratios for temperature, stress, time, length, density, and displacement, respectively.

4.2 Similar Simulation Experiment Design

According to the actual engineering size and reserved reasonable boundary conditions, the length direction of the boundary condition is set to 75 m and the width and depth are set to 36 m. The geometric reduction ratio is n = 1/25 and the net size of the simulated test is 3 × 1.5 × 1.5 m. The actual diameter of the tunnel is 7 m, which is converted to a diameter of 280 mm. The tunnel mainly lies in the grayish powdery clay layer of layer ⑤11. The model soil is taken from the site, and the thickness of the model soil layer is based on the actual thickness and calculated by the geometric similarity ratio. The compactness of the soil is controlled by using the press plate, and after filling each layer, an environmental-consistent sample is taken with a ring cutter to measure its moisture content.

To ensure the reasonable placement of freezing pipes in the model experiment, the principle of equal total heat dissipation must be used to select the position and number of freezing pipes. In the model experiment, the actual arranged freezing pipes need to be simplified. The total heat dissipation capacity of the freezing pipes is $Q = ndhk$, where n is the number of freezing pipes, d is the outer diameter of the freezing pipes, H is the freezing depth, and k is the heat dissipation coefficient of the freezing pipes. Using calcium chloride solution as the refrigerant, the specific gravity is 1.265, and the flow rate reduction ratio is 1/25. The flow rate reduction ratio and the cooling capacity reduction ratio are both 1/15625.

According to Fourier's criterion, the time ratio is $n^2 = 1/625$. That is, 1 min in the model experiment is equivalent to 625 min in reality. The freezing time is set to 45 days, so the experimental time is 104 min. According to the Kosovich criterion, the temperature similarity ratio is 1, which means that the temperature of any point in the model is the same as that of the corresponding point in the prototype. The stress field ratio is 1:1, and the similarity ratio of the specific weight of the soil is 1/25. That is, the specific weight of the model soil should be 25 times that of the site soil. Since the model material is the same as the prototype, a loading method is used to satisfy the similarity ratio of the specific weight of the soil. Based on the weight of the overlying station, the applied pressure is calculated to be 80t. Two 50t jack are set up for the reaction pressure under the overlying station, and each jack applies a pressure of 40t to satisfy the similarity ratio of the specific weight of the soil, as seen in Fig. 4.

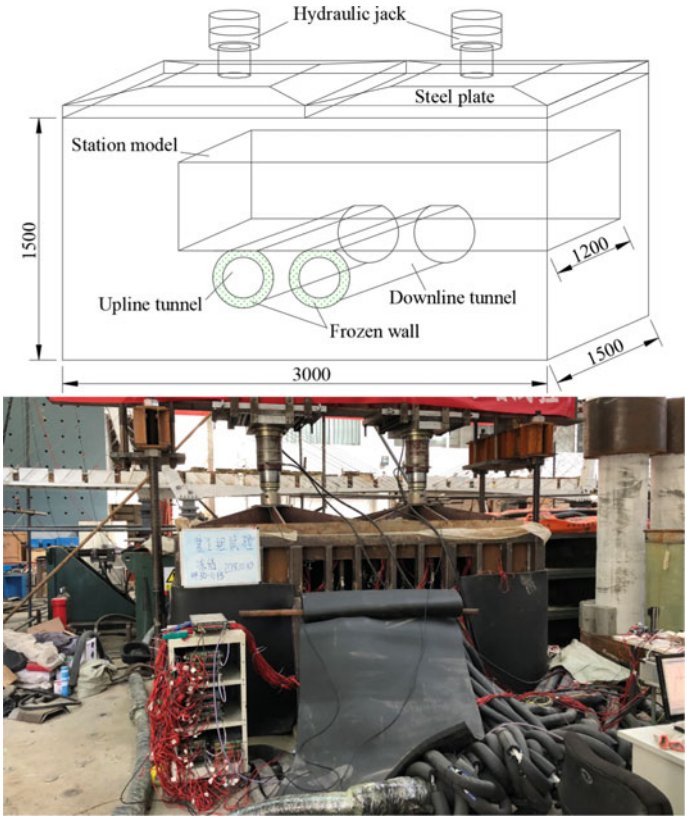

Fig. 4 Experimental principles and field

4.3 Monitoring System

A total of 85 DS18B20 digital temperature sensors are used for temperature monitoring, which are installed on the station floor, tunnel excavation axis horizontal plane, and vertical plane. For the frost heaving pressure of the lower frozen soil mass on the station floor, four LY-350 miniature soil pressure boxes with a size of Φ17 × 8 mm are installed on the bottom surface of the station floor model and directly above the tunnel. The static strain acquisition instrument DH3815N from Donghua Testing is used to collect data in full bridge mode. 6 linear displacement sensors are used to collect data on the frost heaving displacement of the station floor, see in Fig. 5. The probes are supported on the station floor to collect data on frost heaving displacement at different locations.

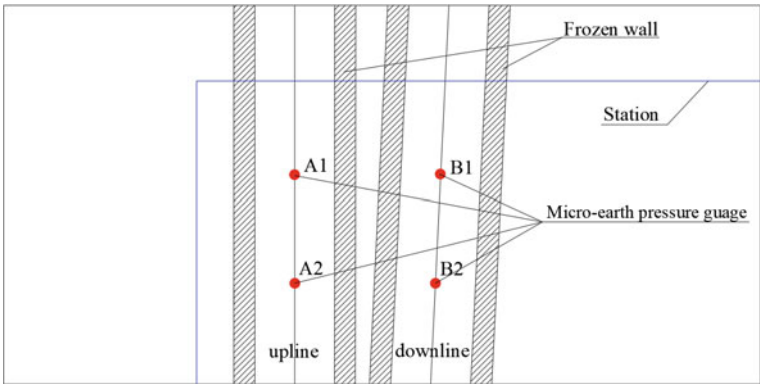

Fig. 5 Location of micro-earth pressure gauges

4.4 Results and Analysis of Open Frost Heaving Tests

The frost heaving pressure rise curve and temperature difference curve are extracted and synthesized in table form using error bars, as shown in Fig. 6.

Figure 6 shows that there is a certain linear relationship between temperature difference and time. The formula can be derived as follows: $T = 0.5481t + 0.2729$ ($t > 5d$), where t is the active freezing time.

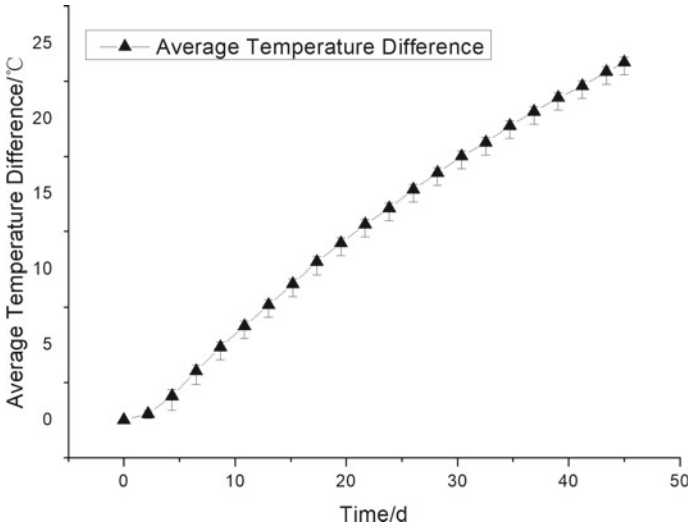

Fig. 6 Temperature difference curve of soil at the bottom of station

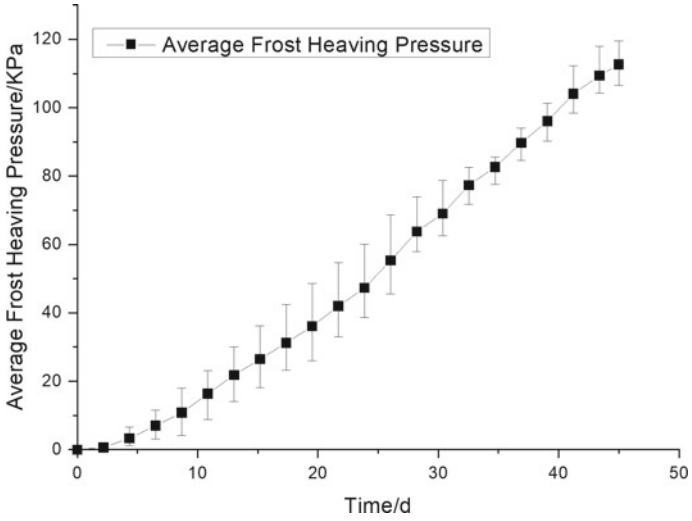

Fig. 7 Frost heave pressure curve at the bottom of the structure

Figure 7 shows that there is a quadratic equation relationship between frost heaving pressure and time. The formula can be derived as follows: $F = 0.0219t^2 + 1.6854\text{t} - 3.6537$ (t > 5d), where t is the active freezing time.

In the different projects, the active freezing time is different, which leads to different freeze effects (temperature differences) on the upper soil mass. Therefore, a more reasonable temperature difference is used as a variable to express frost heaving pressure, as seen in Fig. 8. After combining these two factors and solving them, we obtain $\text{F2} = 0.0729\text{t2} + 3.30351\text{t} - 4.4873$, where T2 is the freezing temperature difference of the structural floor with active freezing time > 5d.

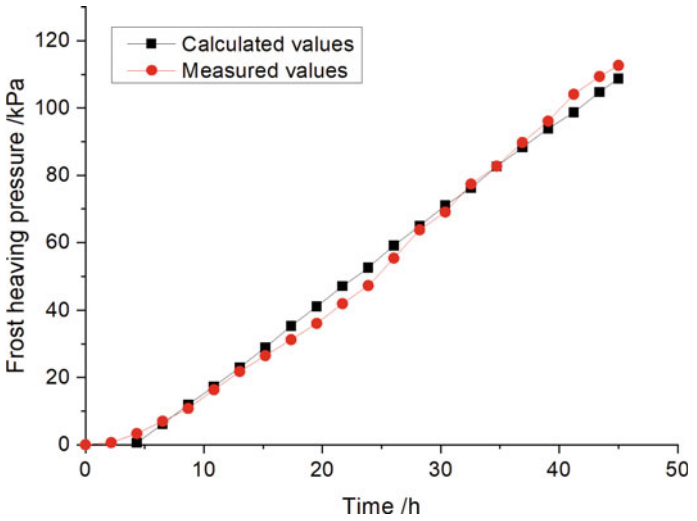

Fig. 8 Compared of measured frost heave pressure and calculated value

5 Conclusion

In closed system tests, there is a good linear relationship between the maximum frost heaving pressure of soil and the experimental cold end temperature, and the calculated formula is $F_1 = 0.03|T_1|$. In open system tests, as the twin freezing tunnel underpass station, the maximum frost heaving pressure on the bottom plate of the station no longer follows the above formula, which is related to the temperature difference between the lower soil mass and the bottom plate in a certain regularity. The frost heaving pressure gradually increases with the increase of the bottom plate temperature difference. The formula is $F_2 = 0.0729t^2 + 3.30351t - 4.4873$, which T_2 is the freezing temperature difference of the structural floor with active freezing time > 5d.

This formula has some reference value for evaluating the frost heaving pressure in underpass frozen tunnel engineering and can calculate the temperature of the constructed floor by expanding speed of the freezing wall indirectly. By evaluating the frost heaving pressure size through the floor temperature, we can estimate the potential damage caused by freezing to the structure.

Acknowledgements The authors would like to thank Ming Li and Qiang Ren for collection of soil samples, and Shurong Xu, Wei Gao, Hang Ding and Shizhuo Dong for preparation of simulation experiments.

Funding This research was supported by the National Natural Science Foundation of China (grant number 52008197).

References

1. Chen X, Xu B (1995) Reinforce the tunnel connecting channel pumping station by freezing method: the freezing project of the large pumping station of Ninghai West Road, Shanghai Metro Line 1. Mine Constr Technol 2:6–8
2. Chen Z, Li F (2007) Analysis on formation of frozen soil wall for connected aisle in metro tunnel. Constr Technol s1:202–204
3. Wang Y, Wang L, Zhang J et al (2020) Indirect coupling method for structural analysis of refuge chamber. J Vibroeng 22:1618–1628
4. Lou G, Chen Z (2007) Shanghai Metro Stadium Station Crossing Line 1 freezing construction risk control. In: Shanghai international tunnel engineering seminar
5. Lin H, Jiang X, Liang G (2004) Application of freezing method construction in crossing section of Shanghai Metro interchange station. In: Selected works of national mining construction conference, vol 1
6. Tang Y, Hong J, Yang P et al (2009) Frost-heaving behaviors of mucky clay by artificial horizontal freezing method. Chin J Geotech Eng 31:772–776
7. Cheng Z (2003) Coupling study on freezing temperature, stress and moisture field of multiple cold sources in shallow tunnel engineering, Central South University
8. Cai H, Peng L, Zheng C (2012) A duration prediction model of surface frost heave induced by tunnelling with horizontal freezing method. Rock Soil Mech 33:1761–1768
9. Alzoubi MA, Sasmito AP, Madiseh A et al (2017) Intermittent freezing concept for energy saving in artificial ground freezing systems. Energy Procedia 142:3920–3925
10. Cai H (2012) Prediction methods and their engineering application of ground frost heave and thawing settlement in subway tunnel horizontal freezing construction. Central South University

Study on the Engineering Characteristics of Deep Soft Soil in South China

Xudong Zhou, Meijuan Chen, and Peiyun Shi

Abstract By testing the physical and mechanical properties of soft soil samples in Liuxi River Basin and analyzing them in comparison with the properties of soft soil in other areas of Guangdong, it is found that they are different from the properties of soft soil in other areas, which can provide a reference and guidance for the construction of soft soil foundation in Liuxi River Basin. It can provide reference and guidance for the construction on soft soil foundation in Liuxi River Basin.

Keywords Liuxi River · Soft soil · Physical and mechanical properties · Engineering characteristics

1 Introduction

Soft soil geology is the most common geological environment in China's civil engineering construction. With the increasing improvement of China's people's livelihood project construction, it is especially important to solve the soft soil geology problem in the project construction. Liuxi River is located in the northwestern part of Conghua District, Guangzhou, which is the mother river of Guangzhou, and the deep soft soil is widely distributed. In recent years, Song et al. [1] quantitatively analyzed the mineral composition and binding water characteristics of marine soft soils in Shenzhen area. Gu et al. [2] determined the HSS model parameters of typical marine soft soil in Yangjiang area, Guangdong. Cai et al. [3] studied the spatial characteristics of soft soil parameters in Nansha area, Guangzhou, China, using mathematical and statistical methods and random field theory. Liu et al. [4] carried out a series of undrained variable circumferential pressure cyclic triaxial tests on saturated soft soils at the mouth of the Pearl River using the GDS dynamic triaxial test system. Liu et al. [5] studied the sub-consolidation characteristics and the change rule of

X. Zhou (✉) · M. Chen · P. Shi
Zhejiang Zhongzheng Geotechnical Technology Company Limited, Jinhua, Zhejiang Province, China
e-mail: 980208918@qq.com

G. Mei et al. (eds.), *Advanced Construction Technology and Research of Deep-Sea Tunnels*, Lecture Notes in Civil Engineering 490,
https://doi.org/10.1007/978-981-97-2417-8_23

sub-consolidation coefficient of soft soil with high water content in the sea phase of Zhuhai. Although the research on soft soil in China has made great progress, Song et al. [6], Kang [7], Li [8], Meng and Zhou [9], Zhou and Li [10], Ahad [11], Tawseef and Bashir [12], Kim et al. [13] so on have studied the soft soil in many places in Guangdong, but they only focus on the soft soil in the Pearl River Basin and other areas, and the research on the nature of the soft soil in the Liuxi River Basin has not been carried out. In this project, the soft soil in Liuxi River Basin was drilled and sampled, and the particle analysis, water content, consistency index, straight shear, consolidation and other tests were carried out on the soil samples to understand the special particle composition, water content and other coefficients, and on the basis of which the problems that are likely to occur in the construction were analyzed, so that it can be used as a reference for the construction on the soft soils in Liuxi River Basin.

2 Overview of the Test

2.1 Sampling Site Selection

In this test, the soft soil in different locations and depths of the experimental teaching building of Guangdong Institute of Water Conservancy and Electric Power Vocational and Technical College Conghua Campus in Liuxi River Basin of Guangzhou was selected for drilling and sampling, and the number of boreholes was 15 in total, with a total footage of 450.88 m. The total number of boreholes is 15, and the total footage is 450.88 m.

2.2 Test Program

The test can be divided into sieve analysis method and density meter method according to the particle size. Calculation formula:

$$X = \frac{m_A}{m_B} \times 100\%.$$

Natural Index Test

(1) Moisture content test. Adopt drying method: Select 20 g soil sample into the box, weigh the total mass, put it into the oven to dry until constant weight and then cool it down, weigh the box and dry soil mass. Calculation formula:

$$\omega = \frac{m_\omega}{m_s} \times 100\% = \frac{m_1 - m_2}{m_2 - m_0} \times 100\%$$

(2) Density test. Adopt ring knife method: take soil samples with ring knife, the ratio of mass and volume of soil in the ring knife is the wet density of soil; dry the soil, the ratio of mass and volume of soil in the ring knife after drying is the dry density of soil. The ratio of mass and volume of the soil in the ring knife after drying is the dry density of the soil. Calculation formula:

$$\rho=\frac{m}{V}=\frac{m_1-m_2}{V},\ \rho_d=\frac{\rho}{1+\omega}$$

(3) Specific gravity test. The specific gravity bottle method is used: the volume of the soil particles is calculated according to the difference between the mass of a certain amount of dry soil before and after it is put into a water-filled specific gravity bottle, and the specific gravity of the soil particles is then calculated. Calculation formula:

$$G_S=\frac{m_s}{m_1+m_s-m_2}\times G_{\omega t}$$

Limit Water Content Test

Adopting liquid limit and plastic limit combined determination method: using liquid-plastic limit combined tester, take about 200 g of soil samples through 0.5 mm sieve, and prepare different consistency samples in three portions, read the depth of sinking of the cone and determine the water content of the samples after 5 s; the water content of the soil samples corresponding to the sinking depth of 17 mm is the liquid limit of the soil samples, and the water content of the soil samples corresponding to the sinking depth of 2 mm is the plastic limit of the soil samples.

Consolidation Test

Adopt the ring knife method: use the ring knife to cut the original moving soil sample, and take the residual soil to determine the water content. The specimen is placed in the protective ring of the compression container, and the bottom plate, moist filter paper and permeable stone are put on in turn.

Then put in the pressurized guide ring and pressure plate. Pressurized observation: Load level is 50, 100, 200, 400 kPa. Initial porosity ratio calculation formula; after pressurized porosity ratio calculation formula:

$$e_0=\frac{G_S\rho_\omega(1+\omega_0)}{\rho_0}-1.$$

Calculation formula of initial pore space ratio: calculation formula of pore space ratio after pressurization:

$$e_i=e_0-(1+e_0)\frac{\sum\Delta h_i}{h_0}.$$

Direct Shear Test

A group of four specimens are cut with a ring cutter according to engineering needs and sheared under vertical pressure (50, 100, 150, 200 kPa). Calculation formula: $\tau_f = CR$.

3 Test Results and Analysis

3.1 Particle Composition

The specific surface area of the soil varies with the size of the particles that make up the soil. Therefore, the degree of interaction with the outside world, the type of water content, the nature and the quantity of the particles are different for different sizes of particles. The specific surface of a soil is expressed as the total surface area of all the particles per unit volume. The large variations in specific surface values due to the different sizes of the particles inevitably lead to a large variation in the specific surface area. The sudden change in the properties of the soil is caused by the composition of minerals in natural soils with different sized particles. The different sizes of particles in natural soil are composed of different types of minerals, which will directly affect the engineering properties of the soil. The particle contents of the soil samples are shown in Table 1.

From Table 1, the curvature coefficient Cc of the test soil samples ranges from about 13, and the coefficient of inhomogeneity Cu $\geq$ 5, which is a well-graded soil. In geotechnical engineering, the well-graded soil is easy to get high dry density and good mechanical properties after compaction, which is suitable for filling projects. In addition, well-graded soils are more porous and have better permeability and can be used in drainage structures and filter back layers.

3.2 Natural Indicators (Table 2)

(1) Water content test. Changes in water content will change the physical and mechanical properties of the soil, and this effect is manifested in various aspects, such as the consistency, saturation degree, mechanical properties and structural strength of the soil. From Table 2, after taking the average value of each group of tests, the water content is 31.48, and the water content is low.

(2) Density test (ring knife method). Determination of dry and wet density of soil, understanding of soil sparsity and wet and dry state, used to convert the other physical properties of soil index.

(3) Specific gravity test (specific gravity bottle method). To determine the specific gravity of the soil and to provide the necessary data for calculating other physical

Table 1 Particle composition of test soil samples

Sample No.	Sampling depth (m)	Gravel soil			Sandy soil			Fine-grained soil
		Driftstone (>200%)	Pebbles (20–200%)	Rounded gravel (2–20%)	Coarse (0.5–2%)	Medium (0.25–0.5%)	Fine (0.075–0.25%)	Powdery (<0.075% or 0.005–0.075%)/ sticky grains (<0.005%)
AK11	6.6–6.8	–	–	–	–	–	–	–
AK12	11.4–11.6	–	–	15.50	18.00	8.00	3.00	55.50
AK21	6.6–6.8	–	–	14.00	30.30	17.40	4.30	34.00
AK22	11.4–11.6	–	–	7.00	12.50	7.50	3.00	70.00
AK23	18.6–18.8	–	–	15.50	17.50	8.50	3.00	55.50
AK31	8.6–8.8	–	41.70	27.30	14.00	5.70	2.30	9.00
AK32	11.4–11.6	–	–	14.50	15.00	8.00	2.00	60.50
AK41	6.2–6.4	–	50.80	31.50	9.40	5.30	2.30	0.70
AK51	4.3–4.5	–	–	–	–	–	–	–
AK52	9.1–9.3	–	47.60	20.10	15.00	6.30	2.00	9.00
AK53	11.4–11.6	–	–	13.00	15.50	7.00	2.00	62.50
AK61	3.3–3.5	–	–	–	–	–	–	–
AK62	6.6–6.8	–	–	15.70	29.30	22.00	3.70	29.30
AK63	11.4–11.6	–	–	11.00	13.00	7.50	3.50	65.00
AK64	20.9–21.1	–	–	12.50	15.50	8.00	4.00	60.00

Table 2 Statistical values of the main natural state indexes of the test soil samples

Sample number	Sampling depth (m)	Density (g/cm^3)		Specific gravity of soil particles	Water content ω (%)	Pore ratio (e)	Saturation degree (Sr)	Porosity (n)
		Wet density	Dry density					
AK11	6.6–6.8	1.85	1.41	2.68	30.80	0.895	92.20	47.20
AK12	11.4–11.6	1.83	1.44	2.68	27.00	0.860	84.20	46.20
AK21	6.6–6.8	–	–	–	–	–	–	–
AK22	11.4–11.6	1.78	1.31	2.68	35.70	1.043	91.70	51.10
AK23	18.6–18.8	1.84	1.39	2.68	31.90	0.921	92.80	47.90
AK31	8.6–8.8	–	–	–	–	–	–	–
AK32	11.4–11.6	1.86	1.40	2.68	32.60	0.911	95.90	47.70
AK41	6.2–6.4	–	–	–	–	–	–	–
AK51	4.3–4.5	1.78	1.32	2.65	35.10	1.011	92.00	50.30
AK52	9.1–9.3	–	–	–	–	–	–	–
AK53	11.4–11.6	1.79	1.35	2.68	32.70	0.987	88.80	49.70
AK61	3.3–3.5	1.81	1.39	2.67	29.80	0.915	87.00	47.80
AK62	6.6–6.8	–	–	–	–	–	–	–
AK63	11.4–11.6	1.84	1.41	2.68	30.60	0.902	90.90	47.40
AK64	20.9–21.1	1.83	1.42	2.68	28.60	0.883	86.80	46.90
Mean		1.82	1.39	2.68	31.48	0.93	90.23	48.22

and mechanical properties of the soil. The specific gravity bottle method is used for soils with a grain size of less than 5 mm.

3.3 Indicators of Consistency

The classification of the soil is determined by determining the liquid limit and plastic limit of the soil, which can be determined from the water content of the soil in its natural state (Table 3). The liquid limit of the specimen is given in Table 3.

Plastic limit, the plasticity index $I_p = \omega_L - \omega_p$ and the liquidity index $I_L = \frac{\omega - \omega_p}{\omega_L - \omega_p}$ were calculated. In order to determine the softness and hardness of the remodeled soil, the following criteria were used to determine the softness and hardness of the remodeled soil. The soil sample IL is 0.4%, and the soil sample IL is 0.4%. The IL of this soil sample is 0.4, which is a plastic state.

Table 3 Statistical values of main consistency indexes of test soil samples

Sample No.	Sampling depth (m)	Liquid limit (%)	Plastic limit (%)	Plasticity index	Liquidity index
AK11	6.6–6.8	36.60	22.20	14.40	0.60
AK12	11.4–11.6	38.40	25.00	13.40	0.15
AK21	6.6–6.8	–	–	–	–
AK22	11.4–11.6	42.70	27.30	15.40	0.55
AK23	18.6–18.8	43.30	27.50	15.80	0.28
AK31	8.6–8.8	–	–	–	–
AK32	11.4–11.6	44.60	28.80	15.80	0.24
AK41	6.2–6.4	–	–	–	–
AK51	4.3–4.5	34.20	19.70	14.50	1.06
AK52	9.1–9.3	–	–	–	–
AK53	11.4–11.6	44.50	29.50	15.00	0.21
AK61	3.3–3.5	37.30	23.60	13.70	0.45
AK62	6.6–6.8	–	–	–	–
AK63	11.4–11.6	41.90	27.30	14.60	0.23
AK64	20.9–21.1	39.90	24.50	15.40	0.27
Average		40.34	25.54	14.80	0.40

3.4 Consolidation Index

The relationship between compressive deformation and loading of the specimen under lateral and axial drainage conditions is determined. The test was analyzed by the consolidation test (rapid method) (see Table 4 for test results). The compressibility of the soil directly affects the deformation values of the foundation. As shown in Table 4, this test sample soil is high Compressive soil with large foundation deformation.

3.5 Shear Index

Through the direct shear experiment, the horizontal shear stress was applied under different vertical pressures σ to obtain the shear stress τ at the time of damage, and finally the internal friction angle φ and cohesive force C were determined.

(The test results are shown in Table 5). As can be seen from Table 5, the test sample soil is a soil with low shear strength. When this soil is used as building foundation, it has a weak potential ability to resist shear stress and shear deformation under external load, and it is easy to be in the limit state of shear damage, and the shear stress reaches the limit value.

Table 4 Statistical values of main consolidation indexes of test soil

Sample No.	Sampling depth (m)	Cohesion C (kPa)	Angle of internal friction Φ (°)
AK11	6.6–6.8	17.80	8.40
AK12	11.4–11.6	18.00	16.10
AK21	6.6–6.8	–	–
AK22	11.4–11.6	16.60	17.40
AK23	18.6–18.8	15.40	19.80
AK31	8.6–8.8	–	–
AK32	11.4–11.6	13.90	24.10
AK41	6.2–6.4	–	–
AK51	4.3–4.5	6.80	3.40
AK52	9.1–9.3	–	–
AK53	11.4–11.6	21.90	17.80
AK61	3.3–3.5	21.60	13.50
AK62	6.6–6.8	–	–
AK63	11.4–11.6	14.10	17.30
AK64	20.9–21.1	28.20	15.20
Average		17.43	15.30

Table 5 Statistical values of main shear indexes of test soil samples

Sample No.	Sampling depth (m)	Compression coefficient (MPa^{-1})	Compression modulus (MPa)
AK11	6.6–6.8	0.462	4.10
AK12	11.4–11.6	0.506	3.68
AK21	6.6–6.8	–	–
AK22	11.4–11.6	0.631	3.24
AK23	18.6–18.8	0.558	3.44
AK31	8.6–8.8	–	–
AK32	11.4–11.6	0.589	3.24
AK41	6.2–6.4	–	–
AK51	4.3–4.5	0.592	3.40
AK52	9.1–9.3	–	–
AK53	11.4–11.6	0.487	4.08
AK61	3.3–3.5	0.550	3.48
AK62	6.6–6.8	–	–
AK63	11.4–11.6	0.514	3.70
AK64	20.9–21.1	0.427	4.41
Average		0.53	3.68

4 Conclusion

According to the comparison of specific parameters (Table 6), it can be seen that the soft soil in Liuxi River Basin is sandy clay, while the soft soil in other areas of Guangdong is mostly silt and silty clay. Compared with the soft soils in other areas, the soft soils in Liuxi River Basin are mostly silt and silty clay. The domain soft soil has the following characteristics:

(1) The water content is low, with an average of 28.92%. Due to the thin water-binding film on the surface of the soil particles, the spacing is small, and the inter-granular electric force is mainly gravitational, so the relative displacement resistance of the soil particles is large, and it is difficult to overcome the resistance under the effect of compaction energy. Therefore, the compaction effect is poor, the pore ratio and compressibility are relatively small, and the soil is dense. Compared with silt, the sandy clayey soils in the Liuxi River basin have relatively good engineering properties, are generally less prone to uneven settlement, and are economical and easy to construct.
(2) Compared with other areas, the soft soils in the Liuxi River Basin have higher cohesion and internal friction angles, higher shear strength, and higher bearing capacity. Since most of the damages to building foundations and geotechnical structures are shear damages, the soil can resist shear stress under external loads when used for building foundations. Therefore, when this soil is used for building foundation, its potential ability to resist shear stress and shear deformation under external load is relatively strong, and it is not easy to reach the state of shear damage.
(3) The liquidity index of the soil sample is small at 0.36, and the soil sample is hard and plastic. Compared with silt, clayey soil in this state has the ability to mold various shapes under external force and keep the original shape unchanged after the external force is removed, which is of great significance to ensure the quality of the project.

In summary, the engineering properties of sandy clayey soil in Liuxi River Basin in Guangzhou are better than those of soft soil in other areas of Guangdong.

Table 6 Comparison of specific parameters

Sampling name	Name of soil layer	Physical index				Mechanical index			
		Natural water content ω (%)	Natural density (g/cm^3)	Pore ratio (e)	Liquidity index	Compression coefficient (MPa^{-1})	Cohesion C (kPa)	Angle of internal friction ϕ (°)	Permeability coefficient
Dongguan	Silt-clay	54.50	1.66	1.66	1.54	7.39	1.11	5.00	0.40
Foshan	Silt	87.00	1.52	1.78	1.58	2.56	6.51	2.85	–
Zhuhai	Silt	74.10	1.56	1.90	2.00	2.30	5.90	4.70	–
Middle River	Silt	57.71	1.62	1.62	1.53	1.57	8.89	5.56	–
Shenzhen Baoan	Sludge	78.04	1.57	2.10	–	0.98	–	–	17.00
Jiangmen Xinli	Silt	57.40	1.66	1.52	2.60	1.30	–	–	–
Nansha	Silt-clay	48.86	1.74	1.49	2.02	1.12	10.20	7.40	–
Xinhui	Silt	85.70	–	–	–	3.10	14.20	0.50	–
Guangzhou Panyu	Silt	85.60	1.45	2.38	1.61	1.69	6.20	3.50	–
Guangzhou Conghua	Sandy clayey soil	28.92	1.85	0.87	0.36	0.52	16.90	17.80	–

Acknowledgements Ministry of Housing and Urban Rural Development Science and Technology Plan Project (2020-K-149)

References

1. Song J, Fang J, Gong W, Tang Q (2023) The material composition and binding water characteristics of marine soft soils in Shenzhen. Acta Sci Natur Univ Sunyatseni 62(1):57–63
2. Gu X, Liu W, Chen X, Lin Y, Xiao J, Wu C (2021) Experimental study on HSS model parameters for marine soft soils in Yangjiang, Guangdong Province. Chin J Geotech Eng 43(2):41–44
3. Cai Z, Qiao S, Tan J, Liu Y (2023) Study on characteristics and spatial heterogeneity of deep silt soft soil in Nansha Port Area. Chin J Undergr Space Eng 19(3):897–910
4. Liu S, Gao Z, Hu B, Yu S, Zhao Y, Yan X, Huang J (2023) Experimental study on dynamic characteristics of soft soil in Pearl River Delta under cyclic confining pressure. Acta Sci Natur Univ Sunyatseni 62(4):131–138
5. Liu W, Li T, Xu R, Ge M (2022) Secondary consolidation deformation characteristics and coefficient selection of Zhuhai marine soft soil. J Railw Sci Eng 19(5)
6. Song X, Wang Z, Park W (2019) Research on engineering characteristics of large area deep soft soil in western center of Zhuhai. J Rock Mech Eng 38(07):1434–1451
7. Kang H (2010) Comprehensive research on soft soil foundation treatment in Nansha. Doctoral Dissertation, Central South University, Hunan
8. Li C (2006) Engineering characteristics of soft ground and settlement prediction model in Pearl River Delta Region. In: The 20th anniversary of the establishment of Guangdong Geotechnical Mechanics and Engineering Society and Academic Symposium
9. Meng Y, Zhou S (2016) Discussion on engineering characteristics of soft soil and soft foundation treatment measures in Shenzhen area. Resour Environ Eng 2016(3):450453
10. Zhou H, Li Y (2011) Exploration of micro-mechanisms of soft soil engineering characteristics in Pearl River Delta Region. Ind Build 41(7):8286
11. Ahad O (2023) Coupled creep and nonlinear consolidation of soft soils in disturbed state concept framework. Comput Geotech 166
12. Tawseef RH, Bashir AM (2023) Effect of nano-gypsum on mechanical properties cement admixed marginal silty soil. Constr Build Mater 408
13. Kim P, Kim YG, Ri GH, Kwak S, Ri KS (2023) Nonlinear consolidation analysis of saturated multi-layered soil with continuous drainage boundary. Int J Numer Anal Methods Geomech 47(16):3114–3126

Study on the Rationality of Tunnel Plane Strain Model Based on Stress Release Principle

Haijun Zhao, Heyi Liu, Tiannan Chen, and Jiangrong Pei

Abstract Based on the finite element difference software FLAC3D, a three-dimensional refined simulation model for tunnel excavation and a plane strain model based on the stress release principle were established. By comparing the deformation characteristics of surrounding rock and the stress distribution of support structures, it is concluded that, apart from slight differences in the stress distribution of the steel arch, the results of the plane strain model and the three-dimensional refined model show high consistency in the deformation characteristics of surrounding rock and the stress distribution of anchor bolts. The calculated results for the maximum load on a single anchor bolt differ by 13.25%, and the differences in surrounding rock deformation and the maximum load on the steel arch are both less than 8%. The plane strain model based on the stress release method can well match the three-dimensional refined model, indicating its feasibility for practical engineering analysis.

Keywords Stress release rate · Tunnel excavation · 3D fine model · Plane strain model · FLAC3D

1 Introduction

Tunnel excavation construction is a complex three-dimensional and temporal problem [1]. During the construction process, the front of the construction face is the unexcavated stratum, and the back is the excavated tunnel. Excavation disrupts the equilibrium state of the original stress field in the rock mass, leading to unloading rebound and stress redistribution in the surrounding rock. The excavation continuously generates dynamic disturbances in the surrounding rock. Part of the stress and deformation in the rock mass near the excavation face is gradually released as the

H. Zhao
Shandong Huake Planning and Architectural Design Co., Ltd., Liaocheng 252000, China

H. Liu (✉) · T. Chen · J. Pei
China Institute of Water Resources and Hydropower Research, Beijing 100048, China
e-mail: heyiliu0914@163.com

G. Mei et al. (eds.), *Advanced Construction Technology and Research of Deep-Sea Tunnels*, Lecture Notes in Civil Engineering 490,
https://doi.org/10.1007/978-981-97-2417-8_24

excavation face advances, causing changes in the stress state of the surrounding rock induced by excavation. This ultimately affects the deformation and failure modes of the tunnel surrounding rock [2]. Therefore, the evolving stress process in the surrounding rock throughout the entire tunnel excavation process has always been a key concern in today's tunnel engineering field [3].

With the gradual development of numerical simulation technology, three-dimensional numerical simulation can now accurately simulate the process of tunnel excavation. However, when a large number of numerical calculations are required, true three-dimensional simulation calculations are very complex and time-consuming. Therefore, some scholars have proposed a method using the principle of stress release to simulate the process of tunnel excavation [4]. The stress release rate, i.e., after tunnel excavation, the stress in the rock mass is released due to unloading, resulting in a corresponding reduction in nodal forces on the tunnel face [5]. The ratio of the reduction in nodal forces on the tunnel face compared to the pre-excavation support force is called the stress release rate. This simulation method, by selecting a reasonable stress release rate and applying the corresponding support force, simulates the spatial effects of the excavation process, achieving the goal of using a two-dimensional plane strain model to simulate the three-dimensional tunnel excavation process [6]. This method is commonly used in the simulation of tunnel excavation and support processes, the release of ground pressure, the calculation of support structure forces, and discussions on the timing of tunnel support [7, 8].

While the calculation speed of a two-dimensional plane strain model is faster and more conducive to controlling variables when solving the deformation of surrounding rock or the force characteristics of support structures based on the stress release method [9], whether the two-dimensional model can match the calculation results of the three-dimensional model well and reproduce the spatiotemporal effects of the three-dimensional problem of tunnel excavation is still a topic without a unified viewpoint among scholars [10]. Based on the aforementioned issues, in order to investigate whether the two-dimensional model based on the stress release theory is suitable for addressing the three-dimensional spatiotemporal problem of tunnel excavation, this study utilizes the finite element simulation software FLAC3D. The stress release rates corresponding to excavation and unloading in the three-dimensional model are input into the two-dimensional plane strain model for analysis. A comparative analysis of the calculation results of the two-dimensional and three-dimensional models is conducted from the perspectives of surrounding rock deformation and the forces on support structures. This aims to validate the rationality and practicality of the tunnel excavation simulation method based on the stress release principle in actual engineering applications.

2 Three-Dimensional Refined Model and Plane Model Based on Stress Release Method

2.1 Three-Dimensional Refined Simulation Model

In the context of a tunnel project in Xinjiang, a specific tunnel section was selected for investigation. The selected tunnel section has a burial depth of 240 m, with the predominant rock type being Carboniferous volcanic breccia, classified as Class IIIb surrounding rock, and exhibiting a horseshoe-shaped cross-section. The geological survey data provided the physical–mechanical parameters for the rock mass and material properties for the support structures, as presented in Tables 1 and 2, respectively.

Leveraging the finite element finite difference software FLAC3D, a three-dimensional refined simulation model was established (Fig. 1). The boundaries of the model were set at a range of 30 m (approximately 4 times the tunnel diameter) around all sides, with a longitudinal length of 90 m and an overall size of 60 × 60 × 90 m. Normal constraints were applied to the boundaries and bottom, and vertical uniformly distributed loads were added to the top to simulate the gravity load of the overlying rock mass. To analyze the deformation characteristics of the surrounding rock during tunnel excavation, a monitoring section is established at Y = 39 m along the excavation axis. Due to the relatively large deformation values at the top, sidewalls, and bottom positions of the horseshoe-shaped section during excavation, monitoring points are set at these positions. The average deformation completion rate of each monitoring point is taken as the final deformation completion rate of the tunnel.

Table 1 Physical mechanical parameters of rock mass

The class of surrounding rock masses	Depth (m)	Modulus of elasticity (GPa)	Density ($kg{\cdot}m^{-3}$)	Poisson's ratio	Cohesion (MPa)	Angle of internal friction (°)	Coefficient of horizontal pressure
IIIb	240	6.5	2650	0.275	0.7	35.87	1.35

Table 2 Material parameters of support structures

Support structures	Modulus of elasticity (GPa)	Poisson's ratio	Compressive strength (MPa)	Tensile strength (MPa)
HW125 steel arch	206	0.3	215	215
Φ22 grouted rock bolt	200	0.3	–	360
C30 concrete	30	0.2	30	–

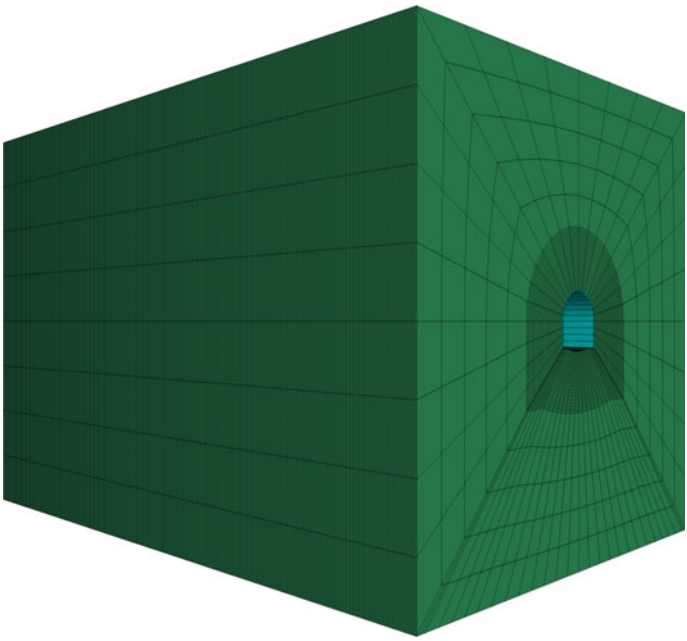

Fig. 1 Three-dimensional refined simulation model

2.2 Stress Release Method and Plane Strain Model

The computation of stress release rates encompasses methodologies such as the reverse stress approach, unbalanced force stress method, and incremental stress technique. Among these, the reverse stress method stands out for its adept control of variables, particularly in simulating the spatial effects on the excavation face during tunneling. The procedural sequence involves: 1. Imposing constrained boundary conditions on the computational model to ascertain the initial stress equilibrium under gravitational influence; 2. Post-tunnel excavation, calculating a single step and determining the unbalanced forces (Fi) at various nodes along the excavation face; 3. Achieving a targeted alteration in the surrounding rock stress release rate (λ) by applying reverse virtual support forces ($Fn = (1 - \lambda)Fi$) to individual nodes; 4. Eliminating virtual support forces, introducing initial support structures, and iteratively computing until reaching a state of equilibrium.

Based on the reverse stress method, the established plane strain model is illustrated in Fig. 2. The model extends along the tunnel axis for a length of 2.7 m, with overall dimensions of 60 $\times$ 60 $\times$ 2.7 m. The midsection along the tunnel axis is selected as the monitoring cross-section. A single excavation of the tunnel is performed, and after excavation, the initial surrounding rock stress is incrementally released into 20 equal parts (i.e., gradually adding corresponding virtual support forces Pi). Starting with the initial release of 5% of the surrounding rock stress, deformation data for

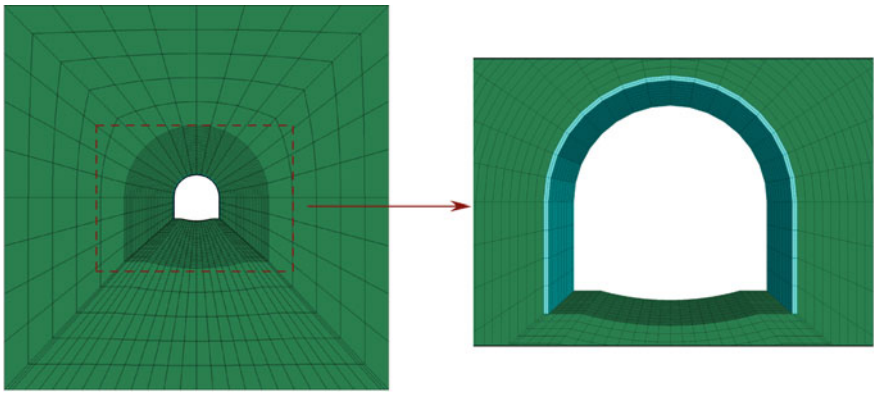

Fig. 2 Plane strain model based on the stress release method

the rock mass are obtained at this stress release rate. Subsequently, the surrounding rock stress release rate is increased in 5% increments, following a gradient, until the surrounding rock stress is fully released.

3 Comparison of Computational Results

The key to simulating the three-dimensional spatiotemporal effects using the stress release method lies in the correspondence between the stress release rate and the control distance of the retaining surface. In this study, the completion rate of surrounding rock deformation is used as a bridge, aligning the three-dimensional refined model's curve of surrounding rock deformation completion rate against the distance to the retaining surface with the curve of surrounding rock deformation completion rate against the stress release rate in the plane strain model. Taking the control distance of the retaining surface as 1 m, as shown in Fig. 3, the corresponding stress release rate is 78.35%. The following compares the characteristics of surrounding rock deformation and the force characteristics of support structures between the three-dimensional refined model and the plane strain model.

3.1 Deformation Characteristics of Surrounding Rock

The deformation characteristics of tunnel surrounding rock in the two models are illustrated in Figs. 4 and 5, respectively.

It can be observed that the calculated results of surrounding rock deformation in both models exhibit similar patterns of variation. Specifically, in the Z-direction (vertical direction) of the tunnel, there is a slight settlement at the top greater than

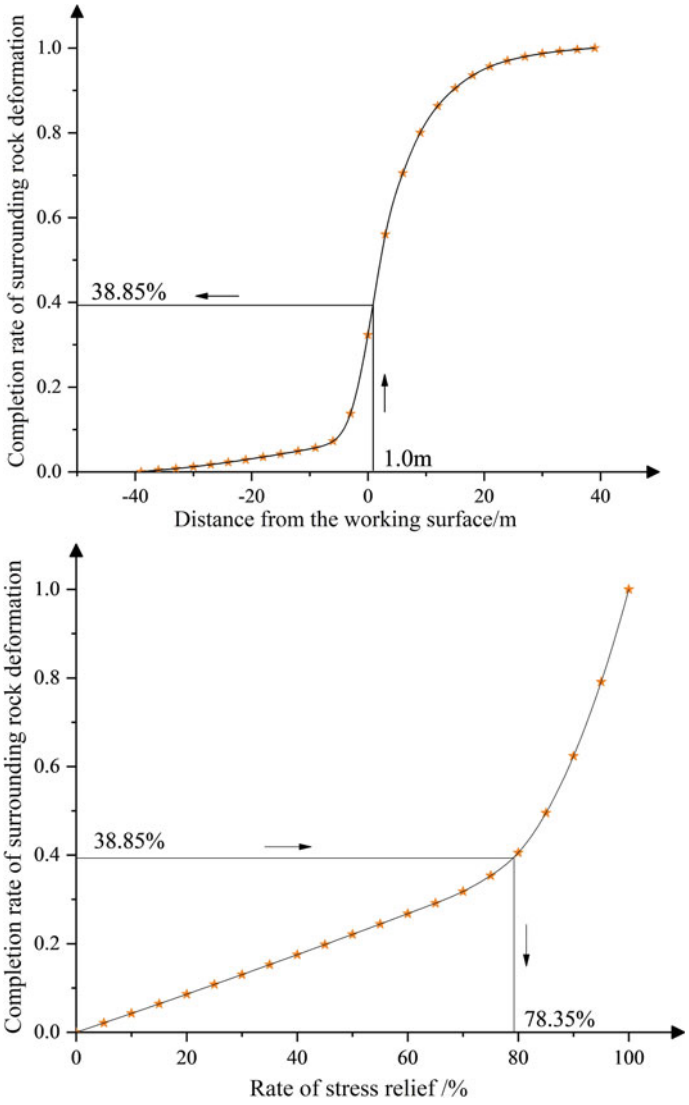

Fig. 3 The correspondence process between the control distance of the retaining surface and the stress release rate

the uplift at the bottom. In the X-direction, the convergence deformation on both sides is essentially consistent. While the numerical values of the surrounding rock deformation show slight deviations, the maximum settlement of the arch crown in the plane strain model is 12.163 mm, compared to 11.32 mm in the three-dimensional model, with a difference of 7.45%. The maximum uplift at the bottom in the plane

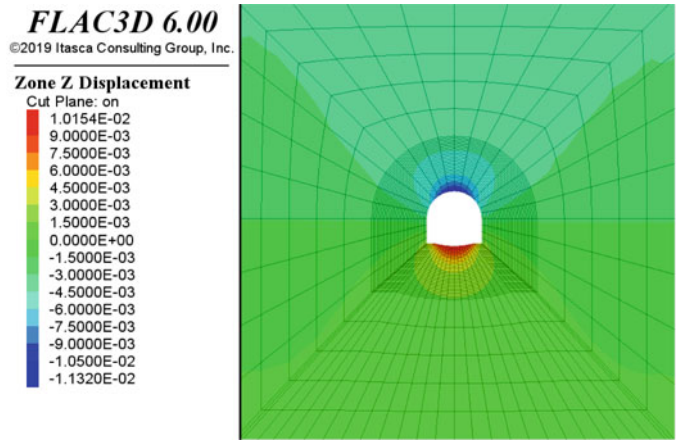

(a) Results of the three-dimensional model

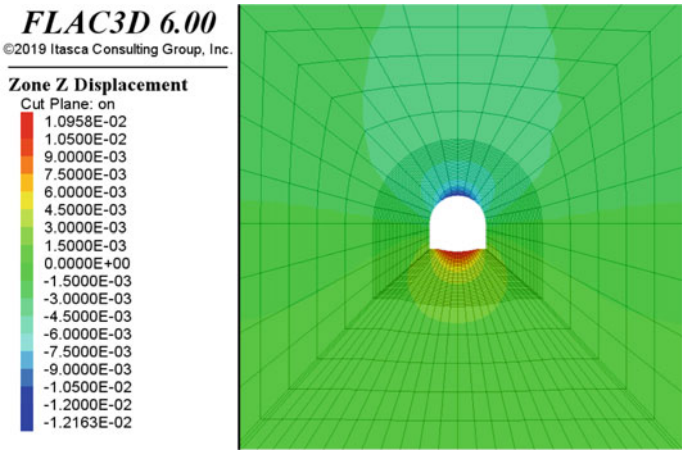

(b) Results of the plane strain model

Fig. 4 Deformation in the Z-direction of surrounding rock

strain model is 10.958 mm, which is 7.92% larger than the 10.154 mm in the three-dimensional model. In the X-direction, the maximum convergence deformations in the two models are 13.192 and 12.917 mm, with a difference of only 2.13%. From the perspective of surrounding rock deformation, although the calculated results of the plane strain model are slightly larger, the error does not exceed 8%, which meets the allowable error for engineering purposes. When considering deformation results from two directions, the difference in deformation in the Z-direction is relatively significant. This difference may be attributed to the fact that the Z-direction represents the maximum principal stress direction in the initial stress field. The disparity in the maximum principal stresses between the two models is greater in the vertical

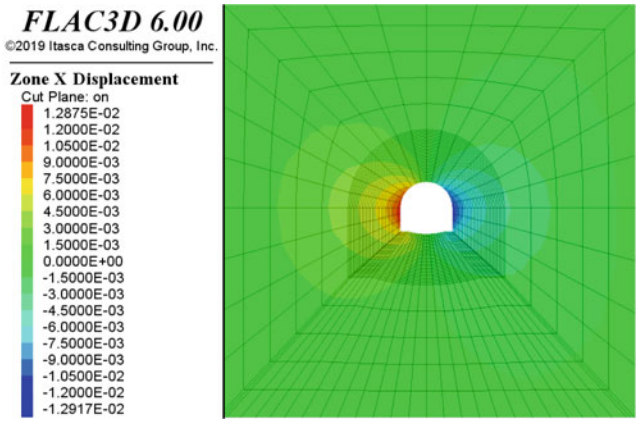

(a) Results of the three-dimensional model

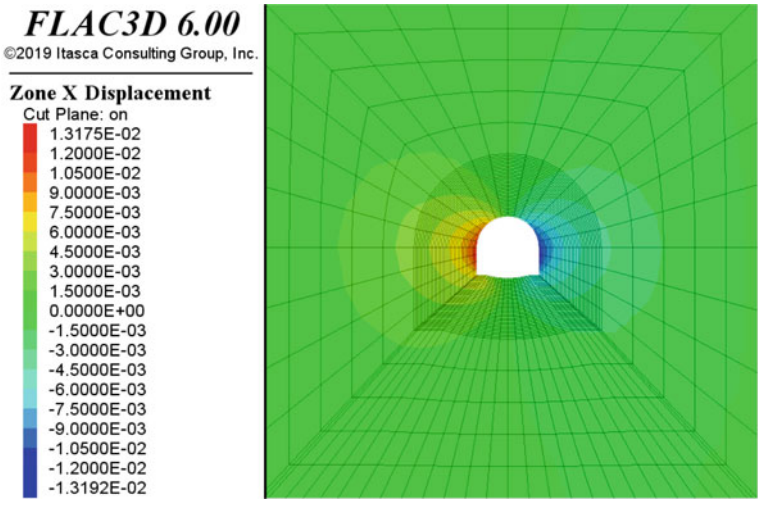

(b) Results of the plane strain model

Fig. 5 Deformation in the X-direction of surrounding rock

stress direction than in the horizontal stress direction. This implies that in practical engineering, special attention should be given to the differences in settlement at vault of the tunnel.

3.2 Mechanical Characteristics of Segment Structure

The stress conditions of the tunnel support structures in the two models are illustrated in Figs. 6 and 7, respectively.

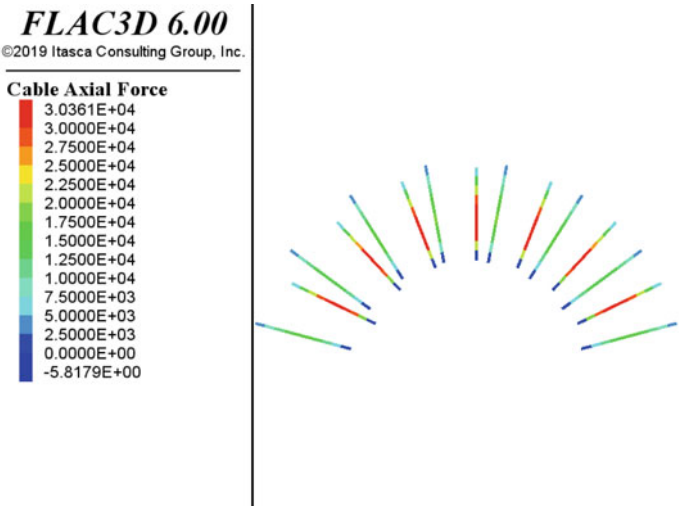

(a) Results of the three-dimensional model

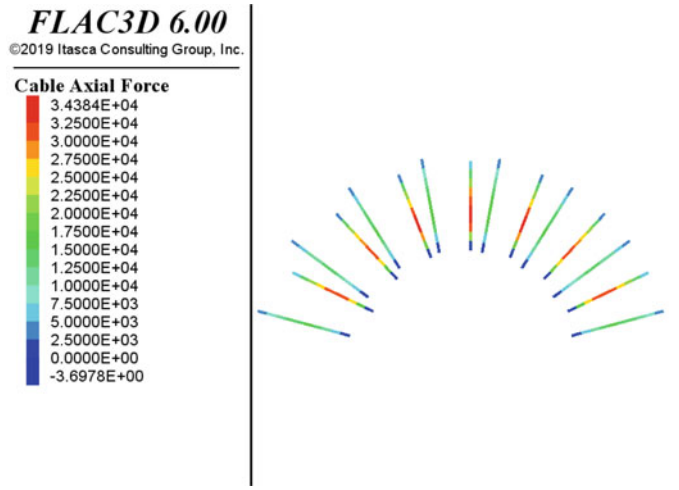

(b) Results of the plane strain model

Fig. 6 Forces on rock bolts

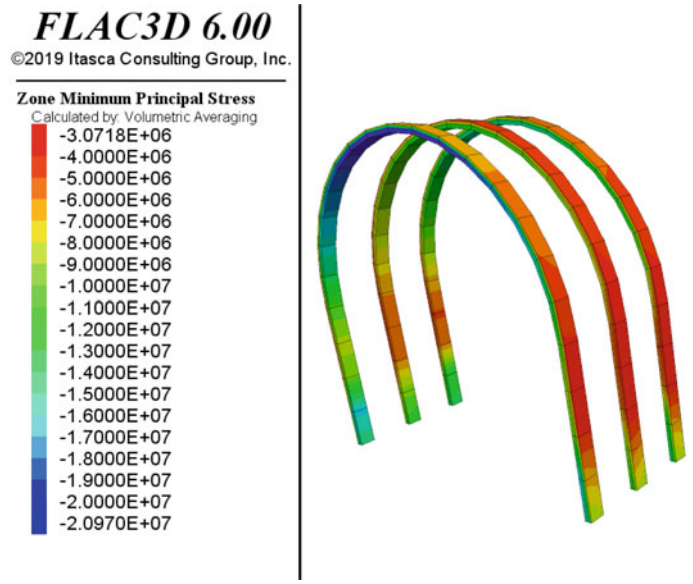

(a) Results from the three-dimensional model

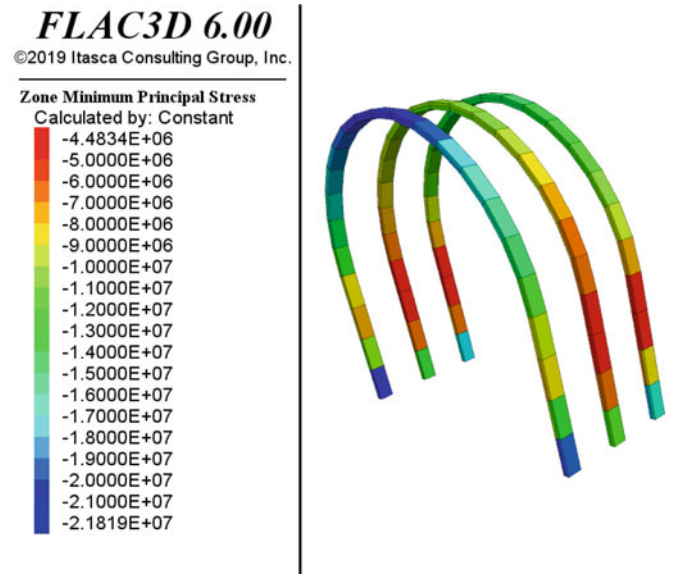

(b) Results from the plane strain model

Fig. 7 Forces on steel arches

It can be observed that in the distribution of forces on rock bolts, the calculation results of the plane strain model and the three-dimensional refined model are essentially the same. Both models show that the maximum tensile stress is experienced in the middle of the top rock bolt on the front side of the tunnel, while the forces on the rock bolts on the rear side are more evenly distributed. In terms of specific values, the maximum tensile stress on a single rock bolt in the plane strain model is 34.348 kN, while the result from the three-dimensional model is 30.361 kN, resulting in a difference of 13.25%. In the distribution of forces on the steel arches, there is a slight difference in the calculation results between the two models. The steel arches are simulated using two layers of calculation elements. In the plane strain model, the forces on the two layers of elements are basically consistent. In the distribution of forces on the steel arches, there is a slight difference in the calculated results between the two models. The steel arches are simulated using two layers of calculation elements. In the plane strain model, the forces on the two layers of elements are basically consistent. In the three-dimensional model, however, the inner elements experience slightly higher compressive stresses than the outer elements. In terms of specific values, the maximum compressive stress on a single steel arch in the plane strain model is 21.819 MPa, while the result from the three-dimensional model is 20.97 MPa, resulting in a difference of only 4.05%. The cause of this difference may be that the calculation elements in the Y-direction are identical in the plane strain model, leading to convergence in the results for the forces on the steel arches. In contrast, the elements in the Y-direction in the three-dimensional model have different sizes, resulting in more pronounced differences between the calculation elements.

In summary, considering the comprehensive comparison results, the calculation results of the plane strain model and the three-dimensional refined model exhibit a high degree of consistency in the deformation characteristics of surrounding rock and the distribution of forces on rock bolts. While the forces on steel arches show slight differences due to the subdivision of calculation elements, the overall agreement is notable. In terms of specific values, the maximum force on a single rock bolt differs by 13.25% between the two models. However, both values are significantly below the design strength for tensile capacity of the rock bolt, minimizing the safety risks associated with model selection. The differences in surrounding rock deformation and the maximum force on the steel arches are both below 8%.

In conclusion, the use of the plane strain model based on the stress release method demonstrates good compatibility with the three-dimensional refined model. In situations where extensive computations are required, the plane strain model can be considered feasible for practical engineering analysis.

4 Conclusion

This paper is set against the engineering context of a tunnel project in Xinjiang. Leveraging the finite element numerical software FLAC3D, we constructed a three-dimensional refined simulation model for tunnel excavation and a plane strain model based on the stress release method. Through an examination of surrounding rock deformation and the forces acting on support structures, we validated the rationale of the plane strain model in simulating the three-dimensional spatiotemporal challenges of tunnel excavation. In conclusion, the following findings were obtained:

(1) The curve of surrounding rock deformation completion rate against the distance to the retaining surface obtained from monitoring points in the three-dimensional refined model aligns with the curve of surrounding rock deformation completion rate against the stress release rate obtained from monitoring points in the plane strain model. This alignment is achieved through the common indicator of surrounding rock deformation completion rate, enabling the plane strain model to simulate the spatiotemporal challenges of three-dimensional excavation.
(2) The calculation results of surrounding rock deformation in the plane strain model and the three-dimensional refined model exhibit a fundamentally similar pattern of variation. While there are slight numerical deviations, with a difference of 7.45% in the maximum settlement at the arch crown, 7.92% in the maximum uplift at the bottom, and only 2.13% in the maximum convergence deformation in the X-direction.
(3) Regarding the maximum tensile stress on a single rock bolt, there is a difference of 13.25% between the calculation results of the plane strain model and the three-dimensional refined model. However, the numerical values are well below the design strength for the tensile capacity of the rock bolt, minimizing the safety risks associated with model selection. In the distribution of forces on the steel arches, although there is a slight difference in the calculation results, the specific numerical values differ by only 4.05%.

In conclusion, considering both the deformation of surrounding rock and the forces on support structures, although there are slight differences in the numerical values between the plane strain model and the three-dimensional model, they fall within the acceptable range of engineering error. Moreover, the trends in the calculation results are consistent between the two models. Therefore, in practical engineering analysis where extensive computations are required and three-dimensional or refined modeling is impractical, using the plane strain model based on the stress release method as a substitute for the three-dimensional refined model to analyze the three-dimensional spatiotemporal problem of tunnel excavation is feasible. It's important to note that during the tunneling process, the stress on the surrounding rock in the unexcavated portion ahead of the working face also undergoes changes, but a two-dimensional model may struggle to simulate the state of the rock mass before excavation. This is an aspect that needs to be carefully considered in future research efforts.

Acknowledgements This work was financially supported by grants from the National Natural Science Foundation of China (Grant Nos. 51879284 and 52179121).

References

1. Habumuremyi P, Xiang YY (2023) A 3-D analytical continuous upper bound limit analysis for face stability of shallow shield tunneling in undrained clays. Comput Geotech 164:105779
2. Martin V, Erich P, Georgios A (2023) Strength, deformability and permeability of kakiritic rocks from the Gotthard base tunnel. J Rock Mech Geotech Eng 15:2224–2237
3. Wang FY, Zhou KG, Fang Y, Xu GY, Wang HW, Zhuo B (2021) Analysis of surrounding-rock disturbance caused by TBM excavation of deep-buried railway tunnel. Tunn Constr 41:240–247
4. Zhou T (2023) Study on the reserved deformation of large cross-section tunnel saturated Q2 loess considering the release of surrounding rock stress. J Anhui Jianzhu Univ 31:16–21
5. Wang SM, Peng XY, Chen B, Wang XM, Ruan L (2022) Surrounding rock stress release rate of shield tunnel in upper-soft and lower-hard strata. Tunn Constr 42:594–601
6. Xu C, Xia CC, Han CL (2022) Elastoplastic solutions for deep tunnel excavation in weak rocks with high geostress considering different stress release measures. Int J Appl Mech 14:2250077
7. Feng JM, Yan CW, Ye L, Ding XQ, Zhang JR, Li ZL (2019) Evaluation of installation timing of initial ground support for large span tunnel in hard rock. Tunn Undergr Space Technol 93:103087
8. Zhang YJ, Su K, Zhu HZ, Qian ZD, Wu HG (2020) Installation time of an initial support for tunnel excavation upon the safety factors of surrounding rock. Appl Sci 10:5653
9. Hou GY, Li JJ (2012) Analysis of complete process of interaction of surrounding rock and support under elastoplastic deformation condition. Rock Soil Mech 33:961–970
10. Zhang CG, Zeng KH (2016) Comparisons of spatial-effect approaches for tunnel excavation using convergence-confinement method. Rock Soil Mech 37:1417–1424

Effect of Iron Tailings Fine Powder as Admixture on the Properties of Cement Mortar and Concrete

Wei Tai, Xiaogen Tong, Kaifeng Zhang, and Zuoqiu Luo

Abstract The paper conducts feasibility tests on iron tailings fine powder as concrete mineral admixture, and compares its performance with traditional admixture fly ash and ground limestone powder to make effective use of stone powder resources. The fluidity and mechanical properties of cement mortar of the three admixtures are respectively tested. And the influence on compressive strength, shrinkage and chloride penetration resistance of C30, C35 and C40 concrete under different curing conditions. The results show that the chemical composition of iron tailings is similar to that of fly ash and belongs to siliceous powder. The 1, 2 and 3 h mobility losses of iron tailings and fly ash are similar, but higher than those of limestone powder. The mortar strength of the first three admixtures at 14d age is close to that of the other two admixtures at 14–60d age, and the activity index and strength change with age are consistent. Under different curing conditions, the compressive strength of the three kinds of admixture concrete is as follows: fly ash concrete > iron tailings powder concrete > limestone powder concrete; The addition of iron tailings is beneficial to improve the shrinkage performance and chloride ion penetration resistance of concrete, and can play a role in filling the micro-pore structure, which has the technical feasibility as an inert admixture.

Keywords Iron tailings fine powder · Cement mortar · Concrete · Activity index · Mechanical strength · Shrinkage property

W. Tai · X. Tong (✉) · K. Zhang · Z. Luo
China West Construction North CO. Ltd. Xi'an, Shanxi 710065, China
e-mail: 793818815@qq.com

W. Tai
e-mail: taiv@163.com

K. Zhang
e-mail: 326360945@qq.com

Z. Luo
e-mail: 793818815@qq.com

G. Mei et al. (eds.), *Advanced Construction Technology and Research of Deep-Sea Tunnels*, Lecture Notes in Civil Engineering 490,
https://doi.org/10.1007/978-981-97-2417-8_25

1 Introduction

With the rapid development of the national economy, all kinds of major infrastructure and livelihood projects have been started, resulting in a rapid increase in the amount of concrete as a major building material [1]. As the commonly used high-quality mineral admixtures in cement concrete, fly ash, mineral powder and other resources have also been consumed in large quantities and are on the point of exhaustion [2], which brings great pressure to the stable and healthy development of the concrete industry. Therefore, it has become an urgent problem to find new admixtures that are easy to obtain, of high quality and low price, and with abundant reserves. China has a large amount of iron tailings industrial solid waste, due to its low comprehensive utilization rate, resulting in a large amount of accumulation, not only occupy land resources, pollute the environment, but also prone to collapse, landslide and debris flow and other potential safety risks [3–6]. Iron tailings micro-powder is the tailings produced after iron concentrate is extracted from iron ore plants, and the particle size of which is less than 0.075 mm after screening and grinding [7–10]. If it can be used as an admixture for concrete production, it can not only expand the selection of admixtures for concrete, but also help to save resources and turn waste into treasure. For this reason, scholars at home and abroad have carried out exploration and research.

Song Shaomin et al. [11] found that when the content of fine powder of iron tailings was 20%, the amount of admixture would not be increased to meet the workability requirements of concrete, and the compressive strength at 28d age would meet the design value requirements. Zhang Hongru et al. [12] showed that the mechanical properties of UHPC can be significantly improved under autoclaved curing and constant temperature water culture by using iron tailings micro-powder instead of quartz powder to prepare UHPC. Huang Zexuan et al. [13] studied the influence of mixed iron tailings fine powder and fly ash on the deformation and durability of concrete. When the content of iron tailings fine powder does not exceed 50%, the drying shrinkage of concrete can be reduced and the frost resistance can be improved. Kexin Huang et al. [14] studied the influence of different amounts of iron tailings fine powder on the mechanical properties and durability of high-strength concrete under high temperature environment. According to Zhou shuang et al. [15], the slump of C40 self-compacting concrete increases slowly, while the compressive strength decreases gradually with the increase of iron tailings micro-powder content. Liu Xuan et al. [16] used skarn type iron tailings micro-powder as raw material to prepare cementing material, and found that the iron tailings had the best mechanical strength when the micro-powder content was 40%. Huang Jingjing et al. [17] found that a large amount of iron tailings micro-powder in the cement system would reduce the hydration gelling property of the material, while autoclaved curing could improve the crystallinity of C-S-H gelling. Mingjing Yang [18] with Cheng et al. [19] found that by increasing the specific surface area of the fine powder of iron tailings by mechanical grinding to improve its hydration reactivity, it can meet the performance requirements of being used as concrete mineral admixtures.

To sum up, iron tailings have been widely used as cementing material components and concrete mineral admixtures. However, due to the different geological conditions and discharge technologies of iron tailings ponds in different regions, the properties of iron tailings are quite different. In this paper, we try to use iron tailings as mineral admixtures, and compare limestone powder with fly ash. Firstly, the physicochemical properties of the three admixtures are compared and analyzed. Then, it replaces the cement of equal quality to study the different influence rules on the fluidity, mechanical strength and activity index of cement mortar, and on this basis, the experimental study on the influence of the types of admixtures on the performance of different grades of C30 ~ C40 concrete is carried out, so as to preliminatively determine the feasibility of iron tailings fine powder as mineral admixtures.

2 Materials and Methods

2.1 Test Raw Materials

(1) Cement: adopt Shaanxi Tongchuan Shengwei P·O 42.5 grade.
(2) admixture: fine powder fineness of iron tailings is 25.9%, mobility ratio is 99%; Fly ash obtained from Tongchuan Huaneng Power Plant Grade II fly ash, fineness of 21.3%, water requirement ratio of 97%; The fineness of limestone powder is 24.8%, and the water requirement ratio is 102%. The mineral powder adopts Delon S95 grade, with a specific surface area of 426 m^2/kg and a density of 2.9 g/cm^3.
(3) Fine aggregate: natural river sand is used, the fineness modulus is 2.5, the apparent density is 2650 kg/m^3, and the loose packing density is 1690 kg/m^3.
(4) Coarse aggregate: continuous graded gravel with a particle size of 5–25 mm is used, the apparent density is 2650 kg/m^3, the loose packing density is 1580 kg/m^3, and the crushing index is 6%.
(5) Water reducing agent: polycarboxylic acid high efficiency water reducing agent produced by China Construction West Construction New Material Technology Co., LTD., with a solid content of 12.6%;
(6) Water: tap water.

2.2 Test Methods

The fluidity of cement mortar is tested according to the "Method for Determination of cement mortar fluidity" (GB/T2419-2005). The compressive and flexural strength of cement mortar is determined by referring to the Test Method for cement mortar Strength (ISO method) (GB/T17671-1999). The activity index of mineral admixtures was tested according to the Technical Specification for Application of Mineral Admixtures (GB/T 51003-2014). According to the Standard of Test Method

for Mechanical Properties of Ordinary Concrete (GB/T 50081–2002), the cube specimens with dimensions of 100 × 100 × 100 mm were formed, and the compressive strength of concrete of different ages was tested. Non-contact method and electric flux method were used to test the self-shrinking and chloride ion penetration resistance of concrete, and the specific test methods were carried out according to the "Standard for Long-term Performance and Durability Test Method of ordinary Concrete" (GB/T 50082-2009).

3 Results and Discussion

3.1 Characteristics Analysis of Different Kinds of Mineral Admixtures

The main chemical compositions of the three admixtures of iron tailings fine powder, fly ash and ground limestone powder are compared in Table 1, and their XRD spectra are shown in Fig. 1. According to the XRD pattern analysis in Fig. 1, quartz accounts for the largest proportion in the mineral composition of iron tailings micro-powder and fly ash, and the main component of quartz is SiO_2, which is also consistent with the highest chemical component content of SiO_2 in Table 3 and Table 4. In addition, the main chemical components of the two are roughly the same, which are mainly Si, Al and Fe (Fig. 2). The Fe content of iron tailings is 26.6%, and the Fe content of fly ash is 7.8%. According to the analysis of Fig. 3 and Table 1, the mineral composition of ground limestone powder is mainly composed of $CaCO_3$ (calcite), which corresponds to the highest CaO content in the chemical composition. According to the above analysis, similar to fly ash, the fine iron tailings powder is mainly siliceous powder, while the ground limestone powder is calcareous powder.

According to the microsilty rock facies analysis of iron tailings in Fig. 2, it can be seen that the tailings are mainly composed of clay minerals, epidotes, quartz, metal minerals, etc., and have the characteristics of flake blastoblastic structure and plate structure. The mineral is mainly composed of fine clay minerals, and the arrangement has a certain orientation. The particle size distribution of clay minerals is about 0.003 × 0.003 mm, colorless and transparent under a single polarizing lens, some of them are transformed into sericite, the flash is obvious, and the interference color

Table 1 Main chemical composition of admixture

Species	Ingredient content/%									
	SiO_2	Al_2O_3	Fe_2O_3	CaO	K_2O	MnO	MgO	TiO_2	SO_3	Other
Iron tail ore powder	45.1	18.6	26.6	0.3	4.1	0.7	1.0	0.7	0.7	2.2
Fly ash	53.9	24.4	7.8	5.1	3.5	0.1	1.1	1.6	0.9	1.6
Limestone powder	1.2	0.8	0.3	97.4	0.1	–	–	0.07	0.02	0.11

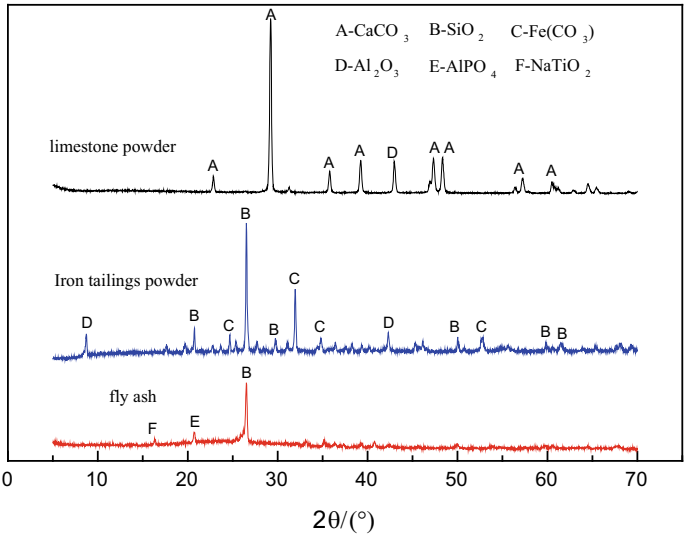

Fig. 1 XRD pattern of limestone powder

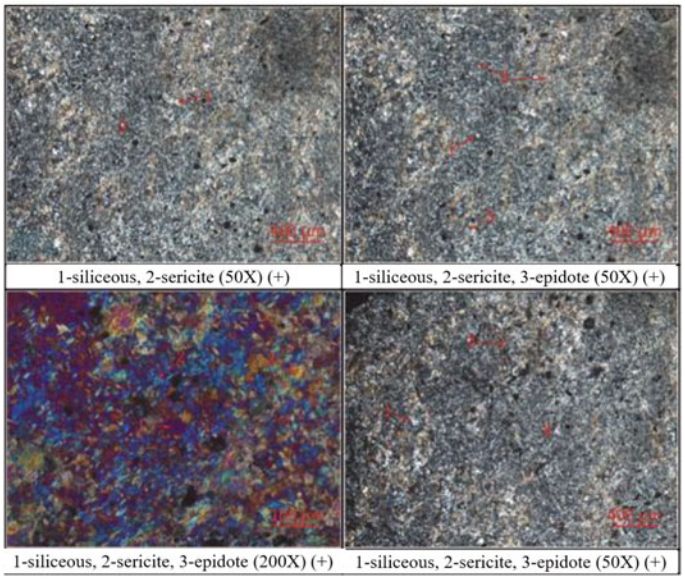

Fig. 2 Microsilty rock facies analysis of iron tailings

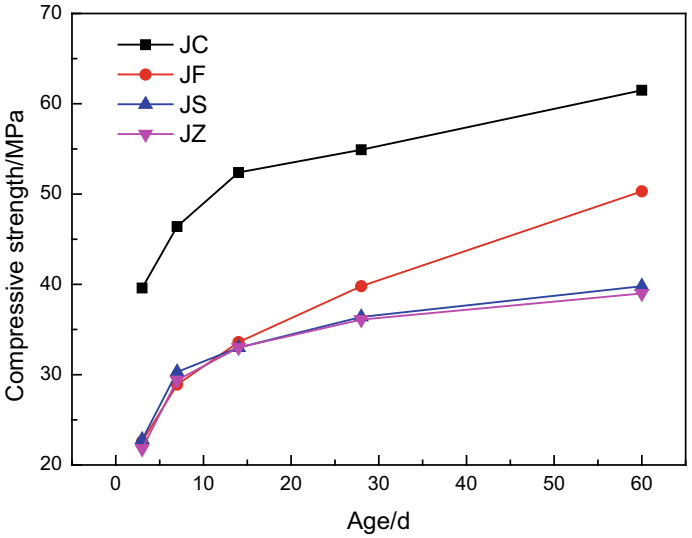

Fig. 3 Compressive strength

becomes secondary blue violet. The particle size distribution of epidote is about 0.05 × 0.05 mm. Under the microscope, the epidote is yellow-green, the interference color is blue-violet, and the height is protrude. The quartz particles are colorless inside, and the particle size distribution is about 0.01 × 0.01 mm, which is unevenly distributed inside the rock. The feldspar filling inside the rock contains microcrystalline quartz with a particle size less than 0.02 × 0.02 mm, which belongs to the mineral with alkali-silica activity.

3.2 Comparison of the Influence of Different Mineral Admixtures on the Properties of Cement Mortar

The total mass of the cementing material is 450 g, and three kinds of admixtures such as fly ash, limestone powder and tussah stone powder are used to replace 30% cement dosage respectively. The mixing ratio used in the test is shown in Table 2.

Influence of the type of admixture on the loss of fluidity of mortar during warp time

In the test, when the admixture content is adjusted to reach the same initial flow of mortar, the admixture content and flow loss during warp time of three different admixtures are compared, and the results are shown in Table 3.

As can be seen from Table 3 above, when the initial fluidity of mortar is the same, the admixture dosage of limestone powder and iron tailings micro-powder is higher than that of fly ash. From the perspective of fluidity, the compatibility of fly ash system and water reducer is the best. The fluidity loss of the three admixtures was

Table 2 Test ratio of cement mortar/g

ID	Cement	Limestone powder	Tussah stone powder	Fly ash	Standard sand	Water
JC	450	–	–	–	1350	225
JF	315	–	–	135	1350	225
JS	315	135	–	–	1350	225
JZ	315	–	135	–	1350	225

JC—refers to pure cement reference group; JF—fly ash doped test group; JS—limestone powder mixed test group; JZ—iron doped tailings micro-powder test group, the same below

Table 3 Fluidity of mortar with different admixtures

ID	Admixture content/%	Initial fluidity/mm	1 h fluidity/mm	2 h fluidity/mm	3 h fluidity/mm
JF	0.6	280	250	225	195
JS	1.5	280	270	260	240
JZ	1.5	280	240	230	205

Table 4 Concrete mix ratio

ID	Strength class	Concrete materials (kg/m^3)								Admixture/%
		Cement	Mineral powder	Fly ash	Limestone powder	Iron tailings fine powder	Sand	Stone	Water	
A1		240	60	60	0	0	1020	827	190	2.3
A2	C30	240	60	0	60	0	1020	827	190	2.3
A3		240	60	0	0	60	1020	827	190	2.5
B1		270	60	60	0	0	965	860	191	2.3
B2	C35	270	60	0	60	0	965	860	191	2.3
B3		270	60	0	0	60	965	860	191	2.4
C1		300	60	60	0	0	910	870	180	2.3
C2	C40	300	60	0	60	0	910	870	180	2.3
C3		300	60	0	0	60	910	870	180	2.4

different at different times. The fluidity loss rates of fly ash and iron tailings were similar at 1 h (10.7%, 14.3%), 2 h (19.6, 17.9%) and 3 h (30.4, 26.8%), respectively. However, the 1 h, 2 h and 3 h flow loss of limestone powder blended mortar is lower than that of the other two types of admixture powders, which are 3.6, 7.1 and 7.1%, respectively. Through comprehensive comparison of fluidity and fluidity loss, it can be seen that the addition of limestone powder has a good effect on improving the fluidity loss of colloidal sand. This is because the fineness of limestone powder is

larger than that of cement, which can make the discontinuous gradation of micro-aggregate more reasonable. The water in the original cement void is replaced by limestone powder, and the free water increases to make up for the loss of fluidity. Because the fly ash contains more glass beads in its structure, it can improve the flow, and the admixture content is lower when the initial flow degree is the same, and the retarded components contained in the admixture are correspondingly reduced, which is the main reason for the large loss of the flow rate during the period. The chemical composition of iron tailings micro-powder contains a high proportion of Fe_2O_3, which has a certain adsorption effect on water reducing agent, so the flow loss rate is larger with the extension of time.

Influence of admixture type on strength and activity index

The mechanical strength and activity index of pulverized iron tailings, fly ash and limestone powder at different curing ages are shown in Figs. 3, 4 and 5.

It can be seen from Figs. 3 and 4 that the compressive strength and folding strength of the mortar mixed with three different admixtures increase with the extension of curing time, and the compressive strength and folding strength of the experimental groups are basically similar at the early age of 14d. With the further development of the age, the compressive strength and folding strength of single fly ash increase the fastest after the age of 14d. Compared with the single limestone powder and iron tailings powder group, the compressive strength and bending strength of 28d colloidal sand are increased by 9.3 and 10.2%, respectively, and 8.0 and 14.1%, respectively. However, the strength of the three admixtures at each age is lower than that of the pure cement reference group. In combination with Fig. 5, it can be seen that the activity index of the three admixtures and the change law of cement strength

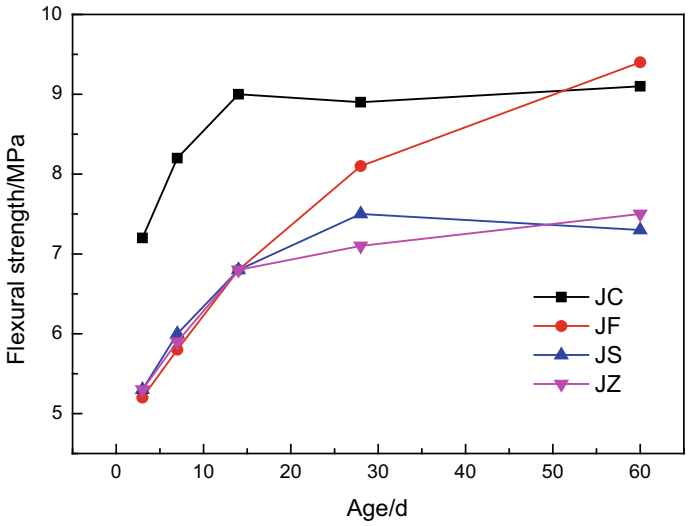

Fig. 4 Flexural strength

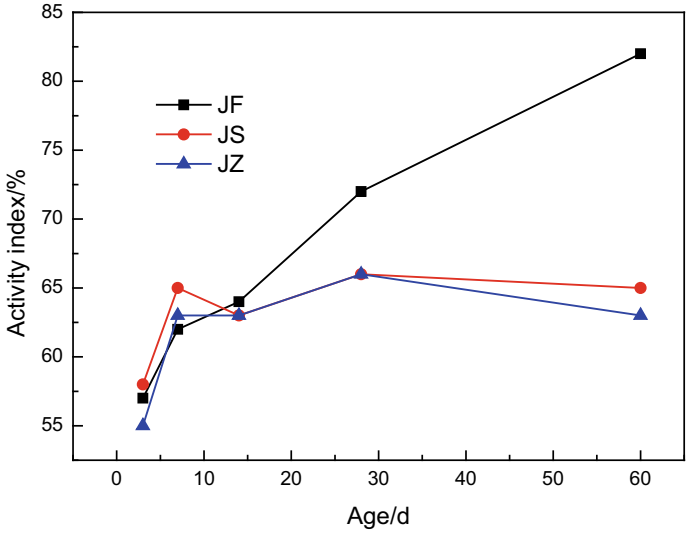

Fig. 5 Activity index

with the development of age are basically consistent. The reason may be that the filling effect and the crystal nucleus effect of the three admixtures play a major role in the early hydration stage, resulting in little difference in compressive and flexion strength of the three cemels before the age of 14d. However, after the age of 14d, the pozzolash effect of the admixtures begins to play a role, and more C-S-H gels are generated by the second hydration reaction, contributing to the strength. Due to the high activity index of fly ash and stronger pozzolash effect, more hydration products are generated in the later stage of hydration, while the low activity index of iron tailings and limestone powder belong to inert admixture, which is also consistent with the test results of the strength growth characteristics of the three admixtures (Fig. 6).

3.3 Comparison of Effects of Different Mineral Admixtures on Concrete Properties

C30–C40 strength grade concrete was selected, and three admixtures with equal mass of 60 kg fly ash, limestone powder and iron tailings fine powder were added respectively. In the test, the water-binder ratio and water consumption were fixed. In order to meet the workability requirements, the water-reducing agent content was changed to adjust the output slump of concrete in each test group within the range of 200 ± 30 mm.

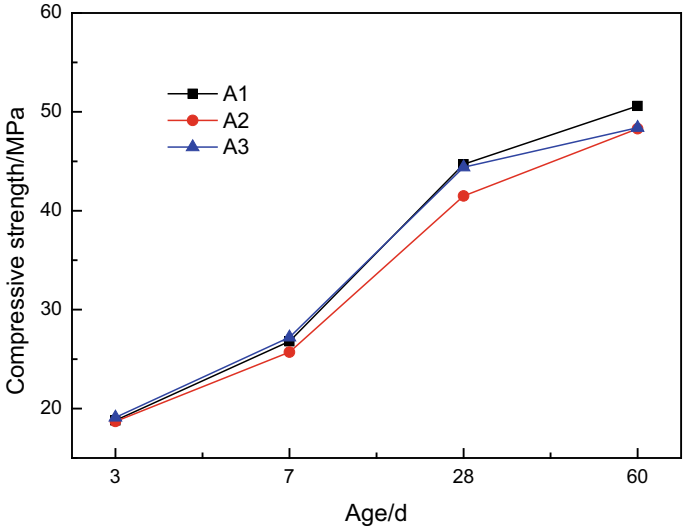

Fig. 6 C30 concrete under the same curing conditions

Influence of admixture type on compressive strength of concrete

The concrete with different water-binder ratio, different curing methods and different admixtures was cured to 3, 7, 28 and 60 days respectively, and the curve of compressive strength change with age was obtained, as shown in Figs. 7, 8, 9, 10 and 11.

The performance of compressive strength of concrete with different types of admixtures is inconsistent, mainly because the activity of the three admixtures is quite different. Combined with the data curve in Fig. 6, it can be seen that the activity of iron tailings fine powder and limestone powder is close to that of fly ash, and the activity index of both are inert admixtures, which only play the role of micro-aggregate filling in cement slurry, and their contribution to concrete strength is relatively limited. The strong pozzolanic effect of fly ash will generate more hydration products in the hydration reaction process, and combined with the dense filling effect on the particle structure of the cementing material, the compressive strength of concrete mixed with fly ash will increase more.

Influence of type of admixture on shrinkage performance of concrete

C35 concrete with three different admixtures in Table 4 was selected as the test ratio, and the non-contact method was used to measure the shrinkage and deformation properties of concrete specimens after hardening under unconstrained and specified temperature and humidity conditions. The shrinkage rate of three kinds of admixture concrete at different ages is shown in Fig. 12.

According to the change curve of concrete shrinkage rate shown in the figure, the shrinkage rate of the three kinds of admixture concrete increases with the extension

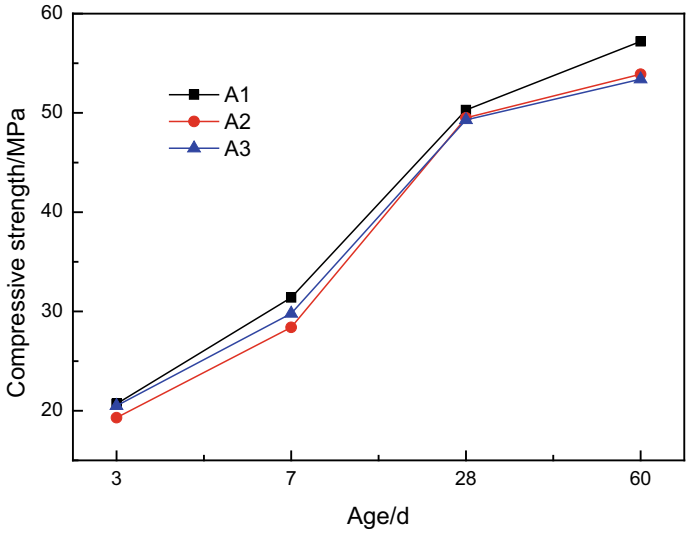

Fig. 7 C30 concrete under standard curing

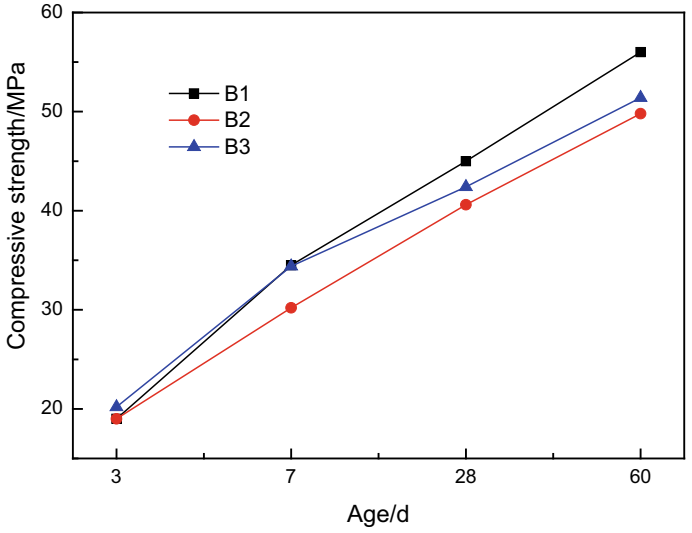

Fig. 8 C40 concrete under the same curing conditions

of curing age. Compared with fly ash concrete, the addition of limestone powder and iron tailings fine powder has a better inhibition effect on the self-shrinkage of concrete, and its self-shrinkage value at 12d age is 0.057% and 0.04%, respectively. It is only 50% and 35% of the shrinkage of fly ash doped concrete. This may be due to the fact that the hydration reactivity of limestone powder and iron tailings fine powder

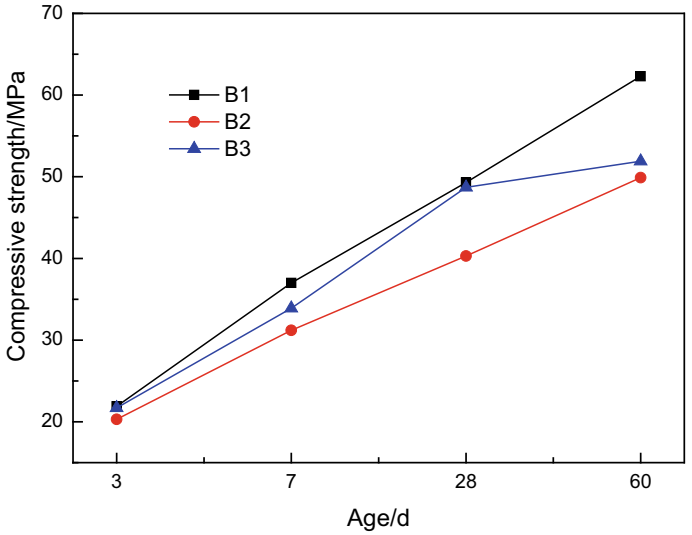

Fig. 9 C40 concrete under standard curing

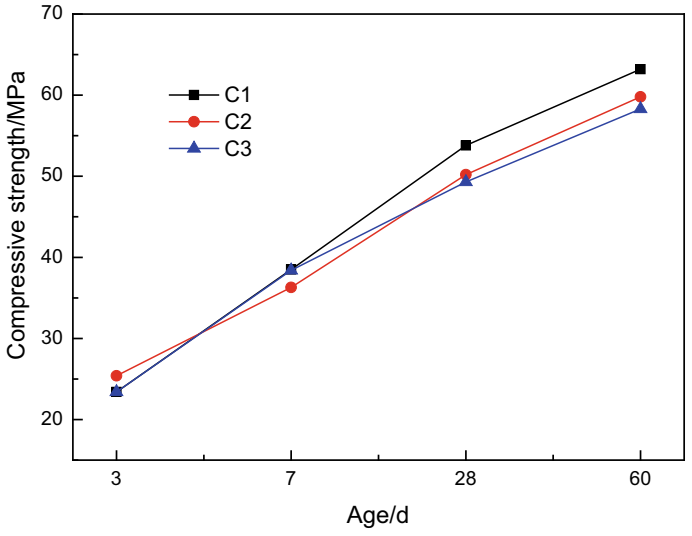

Fig. 10 C50 concrete under the same curing conditions

is lower than that of cement, fly ash and other cementing materials. After replacing cement of equal quality, with the development of curing age, most of the fine powder particles of limestone powder and iron tailings do not react with water, but stably exist in the void structure of cement slurry in the form of inert filler. Its volume

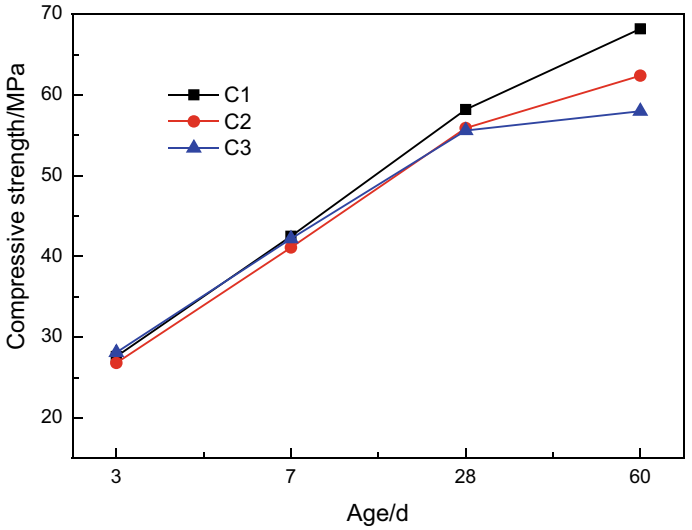

Fig. 11 C50 concrete under standard curing

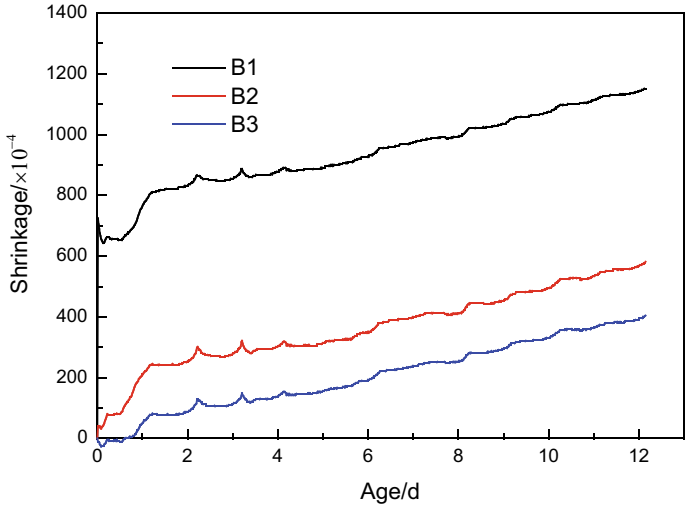

Fig. 12 Shrinkage rate of concrete

does not change, which is conducive to improving the self-shrinking performance of concrete.

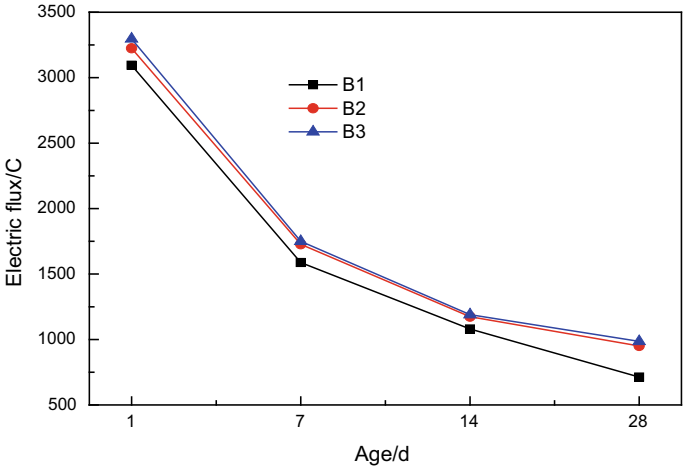

Fig. 13 Electric flux of concrete

Influence of the type of admixture on the chloride ion penetration resistance of concrete

In the test, C35 concrete with three different admixtures in Table 4 was selected as the test ratio, and the electric flux method was used to evaluate the chemical damage resistance and permeability resistance of hardened concrete. The electric flux values of three kinds of admixture concrete at different ages are shown in Fig. 13.

It can be seen from the law of numerical changes in Fig. 13 that the electric flux of C35 strength grade concrete prepared with different types of admixtures decreases with the increase of age. The electric flux values of the concrete mixed with limestone powder and iron tailings have little difference at each age, while the electric flux values of the concrete mixed with fly ash at each age are lower than the first two, and the electric flux values of the three are 951C, 986C and 713C at the age of 28d. According to JGJ/T 193 evaluation standard, the electric flux results of three different admixtures are divided into "Q-iv" grade, that is, the electric flux is in the range of "500C $\leq$ Q < 1000C". The results show that the chloride ion penetration resistance of the concrete prepared with iron tailings is equivalent to that of the concrete mixed with fly ash and limestone powder, and can meet the application requirements of the concrete's chloride ion erosion resistance.

3.4 SEM Microscopic Analysis

In order to further analyze the influence of three different admixtures on the concrete microstructure, SEM photos and EDS spectra of C35 concrete samples doped with fly ash, limestone powder and iron tailings micro-powder were selected after 28d

hydration and magnified by 5000 times. See Fig. 14 for the photos of the microstructure analysis of concrete with different types of admixtures.

As can be seen from Fig. 14a, the concrete doped with fly ash has more C-S-H gels in clusters and a small amount of sheet $Ca(OH)_2$, which is because the secondary hydration reaction of fly ash consumes a large amount of $Ca(OH)_2$ in the system. In Fig. 14b, c, it can be seen that there are a large number of plate-like $Ca(OH)_2$ crystals and a small amount of granular C-S-H gel in the concrete mixed

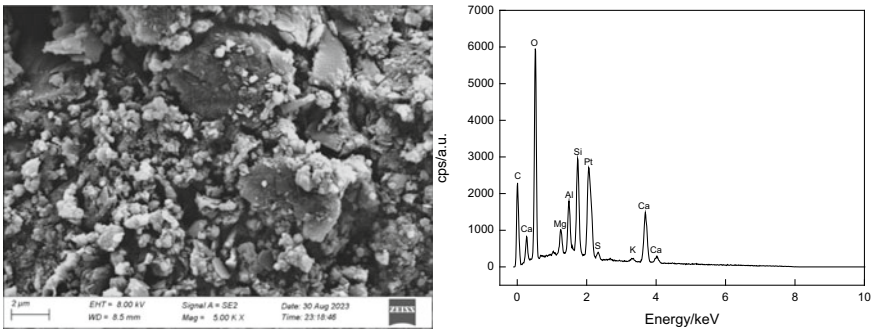

(a) fly ash concrete

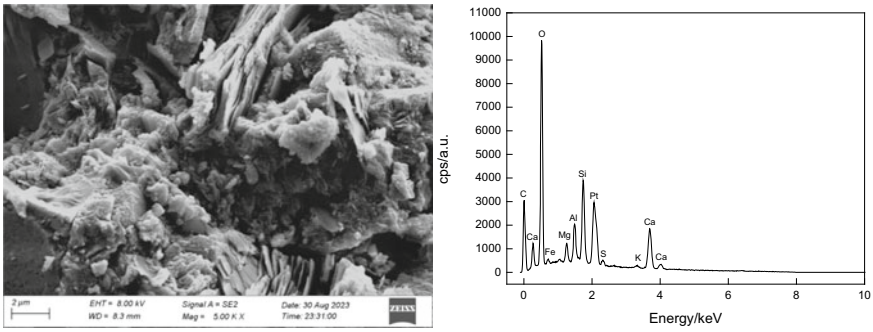

(b) limestone powder concrete

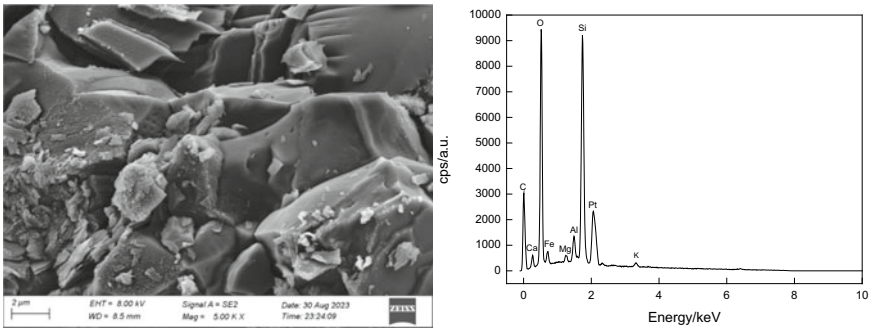

(c) iron tailings micro-powder concrete

Fig. 14 SEM photos and EDS spectra of the sample after 28 days of hydration

with limestone powder and iron tailings fine powder, and the amount of hydration products generated is not enough to fill the internal pores, and the overall structure is relatively loose. The microstructure analysis shows that fly ash has pozzolanic effect, which can promote the hydration of cement, and it also has micro-aggregate effect, which has more advantages in enhancing the density of structure. Similar to iron tailings, limestone powder only has weak hydration reactivity, and when added to the system, it mainly plays the role of particle filling, so the dense filling effect on the structure is not as good as fly ash, which is also consistent with the macro performance of concrete.

4 Conclusion

(1) The chemical composition of iron tailings is similar to that of fly ash, and the main chemical composition is SiO_2, which belongs to siliceous powder and has certain alkali-silicon activity, and can be used as mineral admixtures in concrete.
(2) Under the condition that the initial fluidity of cement mortar is the same by changing the admixture content, the 1, 2 and 3 h flow loss of cement mortar of iron tailings and fly ash is similar, but greater than that of cement mortar with limestone powder; For the same amount of iron tailings, fly ash and limestone powder, the compressive and folding strength of the three camels is basically similar before the age of 14d, while the strength of the camels with fly ash increases greatly at the age of 28d and 56d, and is higher than the other two. The activity index of each age is consistent with the change of strength.
(3) Under the same age and curing conditions, the relationship between the compressive strength of C30–C40 concrete mixed with three different admixtures is as follows: the compressive strength of fly ash concrete is the highest, the compressive strength of iron tailings powder is the second, and the compressive strength of limestone powder concrete is the lowest; Under the same curing age and the same mix ratio, the strength of concrete under standard curing conditions is generally higher than that under the same curing conditions, and all meet the design requirements of different grades of concrete strength.
(4) The non-contact shrinkage test of concrete shows that the shrinkage rate of concrete mixed with fly ash is the highest, followed by that of limestone powder, and that of iron tailings is the lowest, which has good anti-shrinkage performance.
(5) Compared with limestone powder and fly ash concrete, the 28d electric flux value of the concrete doped with iron tailings is in a lower range, and it has good chloride ion penetration resistance.
(6) Combined with the microscopic scanning electron microscopy image analysis, it can be seen that the internal hydration product structure of the concrete with iron tailings micro-powder and limestone powder is not as dense as that of fly ash concrete, which is mutually confirmed with the macro performance.

Acknowledgements This paper is one of the phased achievements of the general project 《Application of iron tailings stone powder in wet mixed mortar in Zhashui area》 (BF202101), a fund of Zhongjian Western Construction North Co., Ltd.

References

1. Ronghang G, Jinjin H (2021) Recycling and utilization of waste concrete [J]. Sichuan Cem 277(9):282–283
2. Li J, Kun T (2021) Experimental study on the effect of replacing fly ash with tuff powder on the performance of hydraulic concrete at Plateau [J]. Hydropower New Energy 35(11):6–11
3. Glotov VE, Jiri C, Glotova LP, et al (2021) Causes and environ-mental impact of the gold-tailings dam failure at Karamken, the Russian Far East [J]. Eng Geol 245(6):236–247
4. Lu C, Chen H, Fu L et al (2021) Progress in the preparation of new building materials from iron tailings at home and abroad [J]. Mater Rev 35(05):5011–5026
5. Gu X, Ai Y, Zhao Y et al (2023) Status of resource utilization of iron tailings [J/OL]. Chin J Nonferrous Metals 12(9):1–29
6. Zhou JM, Dang Z, Cai MF et al (2007) Soil heavy metal pollution around the dabaoshan mine [J]. Pedosphere 17(5):588–594
7. Lu HJ, Qi CC, Chen QS, et al (2021) A new procedure for recycling waste tailings as cemented paste backfill to underground stopes and open pits [J]. J Clean Prod 188(9):601–612
8. Zhang Y, Liu B, Gu X et al (2022) Mechanical activation mechanism of multicomponent admixture of iron tailings [J]. J Shenyang Univ Technol 44(01):95–101
9. Zhang S, Xue S, Lin X, et al (2006) Current situation and comprehensive utilization of iron tailings resource [J]. J Min Sci 42(4):403–408
10. (2020) Effect of different fineness iron tailing powder on properties of cement-based materials [J]. J Xi'an Univ Arch Technol (Nat Sci Ed) 52(2):241–247
11. Song S, Chen H (2020) Effect of iron tailings fine powder on properties of low clinker cementative concrete [J]. Bull Silic 39(8):78–98
12. Zhang H, Ji T, Liu F et al (2020) Mechanical properties of ultra-high performance concrete mixed with iron tailings powder under different curing systems [J]. J Fuzhou Univ (Nat Sci Ed) 48(1):90–97
13. Huang Z, Hou Y, Song S (2020) Effect of iron tailings fine powder on shrinkage and durability of concrete [J]. Concrete 367(5):56–59
14. Huang K, Zhang X, Lu D, Xu N, Gan Y, Han X, Liu Y (2021) The role of iron tailing powder in ultra-high-strength concrete subjected to elevated temperatures [J]. Adv Civ Eng 11(8):202
15. Zhou S, Liu J (2021) Experimental study on the mechanical properties of C40 self-compacting solid ferrous tailings concrete [J]. IOP Conf Ser: Earth Environ Sci 546(4):38–42
16. Xuan L, Huixin L (2021) Study on preparation and hydration products of micro-powder cementing material of iron tailings [J]. J Shangluo Univ 35(6):31–34+47
17. Jingjing H, Renwei Z, Yongxin D et al (2021) Cementing property and microstructure analysis of iron Tailings [J]. J Lanzhou Inst Technol 28(4):60–64
18. Yang M, Sun J, Dun C, Duan Y, Meng Z (2021) Cementitious activity optimization studies of iron tailings powder as a concrete admixture [J]. Constr Build Mater 12(4):265
19. Cheng Y, Huang F, Li W et al (2016) Test research on the effects of mechanochemically activated iron tailings on the compressive strength of concrete [J]. Constr Build Mater 118:164–170

Study on Smoke Control of Tunnel Fire Under the Synergistic Effect of Longitudinal Ventilation and Top Exhaust System

Guanghui Yao, Chenchen Liang, Mengyi Xu, and Zhongyuan Yuan

Abstract In order to establish a smoke-free and secure evacuation environment in long tunnels during fire incidents, while ensuring efficient utilization of fan equipment. We focus on the critical situation where smoke is just able to be completely discharged from the vent under the combined system of longitudinal ventilation and top exhaust. We establish a full-scale three-dimensional numerical computational model using FDS to investigate the impact of various factors on the critical complete exhaust volumetric flow rate of the exhaust system, including the heat release rate (HRR), the location of the longitudinal fire source, and the length of the exhaust vent. The findings indicate that an increase in heat release rate leads to a higher critical complete exhaust volumetric flow rate. Additionally, as the fire source moves away from the vent, there is a decrease in critical exhaust rate. Moreover, increasing the length of the smoke vent tends to initially increase and then decrease the critical exhaust rate. This study aims to provide guidance on determining the appropriate design values for exhaust volumetric flow rate in combined exhaust systems within long tunnels.

Keywords Tunnel fire · Combined smoke extraction · Smoke control · Longitudinal ventilation · Top smoke extraction

1 Introduction

As a mountainous and densely populated country, China has made significant progress in constructing mountain tunnels [1], including numerous lengthy ones. However, due to their unique narrow and elongated structure, tunnels often pose

G. Yao · C. Liang · M. Xu · Z. Yuan (✉)
School of Mechanical Engineering, Southwest Jiaotong University, Chengdu 610031, Sichuan, China
e-mail: zhongyuan.yuan@home.swjtu.edu.cn

G. Yao
e-mail: YaoGuanghui@my.swjtu.edu.cn

G. Mei et al. (eds.), *Advanced Construction Technology and Research of Deep-Sea Tunnels*, Lecture Notes in Civil Engineering 490,
https://doi.org/10.1007/978-981-97-2417-8_26

a high risk of causing substantial casualties and economic losses in the event of a fire [2]. Smoke caused by tunnel fires poses the greatest threat to individuals trapped inside [3–5]. How to scientifically design the smoke exhaust system to reduce casualties and property losses is a key issue in tunnel construction and operation. According to relevant norms [6], the longitudinal smoke exhaust distance of mountain tunnels is not more than 5 km, and the longitudinal smoke exhaust distance of municipal tunnels is not more than 3 km. Therefore, the integration of longitudinal ventilation system and top exhaust system can be considered for the evacuation of smoke in lengthy tunnel. Extensive research has been conducted by numerous researchers and scholars on this combined smoke exhaust method. Ingason and Li [7] conducted small-scale experiments to investigate the smoke control effects of single and two vents in a top exhaust system in the presence and absence of longitudinal air velocity, respectively. Chen et al. [8] modified the dimensionless return smoke length model developed by Li [9], and developed a predictive model of return smoke lengths for a top exhaust system with vents above the fire source and a longitudinal ventilating system in concert. Tang et al. [10] found that compared with other locations, the mechanical smoke exhaust system has the most significant effect on the velocity of the smoke front when the fire source is directly below the ceiling exhaust vent. Wang et al. [11] built a full-size numerical simulation with FDS to investigate the effect of different smoke exhaust strategies (varying longitudinal and exhaust air velocities) on a coupled system of longitudinal and shaft ventilation. It can be seen that the coupling of longitudinal and top exhaust systems has received much attention in recent years, but the focus is still on the prediction of returning smoke [12–14]. In fact, the smoke returns to the upstream of the fire and spreads downstream across the vent, still posing a threat to the escape route of personnel. The actual project is more concerned about the setting of the exhaust volumetric flow rate so that the smoke can be completely eliminated to create a good escape environment. However, the relevant norms [6] states that there's no recognized value for smoke volume in centralized smoke exhaust tunnels. In this paper, the study focuses on the complete exhaust volumetric flow rate. The critical longitudinal ventilation velocity is set as the velocity of longitudinal ventilation, and the minimum volume flow rate of the exhaust vent required for effective containment of smoke between the fire source and the exhaust vent is defined as the critical complete volume flow rate. Furthermore, this study investigates various factors such as heat release rate (HRR), fire source location, and ventilation vent size to determine their influence on the critical exhaust rate. This research aims to provide scientific and rational foundations for determining the combined smoke exhaust system volume in engineering design.

2 Model Building

In this paper, a full-size tunnel model of a mountain tunnel is established using FDS, as shown in Fig. 1. The tunnel section consists of a semicircle with a radius of 6 m and a rectangle with a height of 1.4 m. The tunnel is 2500 m long and 12 m wide.

The smoke vent is located in the central axis of the tunnel ceiling, with its inner edge is 320 m away from the entrance of the tunnel, and the width of the vent is fixed at 5 m. The vent is set in seven different lengths: 1, 3, 5, 7, 10, 13, and 15 m. N-heptane is used to simulate the fire source with heat release rate of 5 MW, 10 MW and 30 MW respectively. The fire source is located at the bottom of the tunnel along its longitudinal axis as shown in Fig. 2. The temperature probes were positioned at intervals of 0.5 m along the longitudinal direction, specifically 20 cm below the tunnel ceiling. There are four different locations for the fire source. The tunnel wall material is set as "concrete" with a thickness of 0.5 m. The boundary between the tunnel exit and the calculation area is set as "open". At the entrance of the tunnel, "supply" is used to introduce wind into it while "exhaust" at the vent facilitates smoke evacuation. The initial ambient temperature is set at 25°C with an ambient pressure of 101325 Pa, and a simulation time of 600 s.

The prerequisite for conducting numerical simulation calculations is an in-depth analysis of the impact of grid size on the resulting outcomes. As specified in the FDS User's Guide [15], the grid size is intricately linked to the characteristic diameter of the fire source. The term "characteristic flame diameter D^*" is defined as follows:

$$D^* = \left(\frac{\dot{Q}}{\rho_\infty c_p T_\infty \sqrt{g}} \right)^{\frac{2}{5}} \tag{1}$$

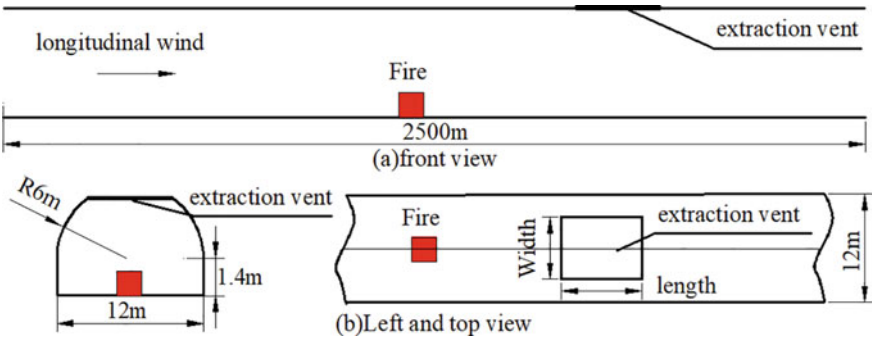

Fig. 1 Schematic of the model

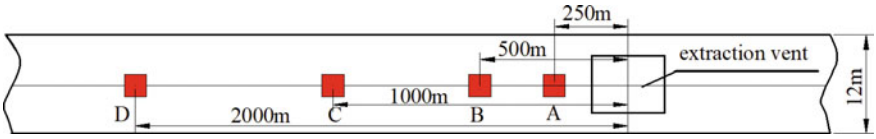

Fig. 2 Schematic of fire source location

Fig. 3 Grid-independent verification

where $\dot{Q}$ is the rate of heat release from the ignition source, kW; ρ_∞ is the density of ambient air, 1.2 kg/m^3; c_p is the specific heat of air, 1 kJ/(kg·K); T_∞ is the ambient air temperature, 293 K; g is the acceleration of gravity, 9.81 m/s^2.

Taking the heat release rate of the fire source as an example of 10 MW, as illustrated in Fig. 3, which presents the simulation results of the longitudinal temperature distribution of the smoke under varying grid sizes of the model, it can be observed that, as the grid size decreases from 0.088 D^* to 0.072 D^*, the accuracy is incrementally improved. Moreover, the calculated results for the grid sizes of 0.072 D^* and 0.062 D^* remain virtually unchanged. To balance the accuracy of the results and the computational cost, it is more rational to select the grid size of 0.072 D^* for the subsequent three-dimensional simulation of the tunnel fire.

The 1:10 scaled-down model tunnel test was conducted to validate the numerical model. Figure 4 shows the actual view of the model tunnel platform. The dimensions of the model tunnel are 5 m in width, 12 m in height, and 12 m in length. The selected fire source had a heat release rate of 5.68 kW and was positioned in the longitudinal center of the tunnel. The smoke vent measured 0.1 m in length and 0.5 m in width,

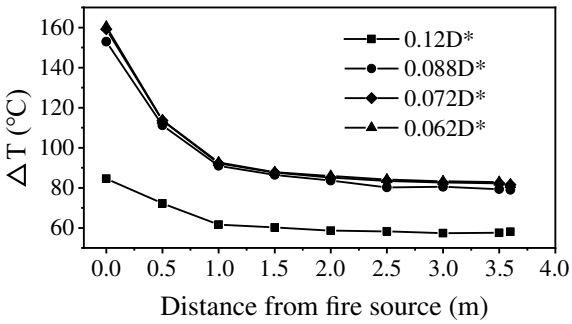

Fig. 4 Model tunnel table view

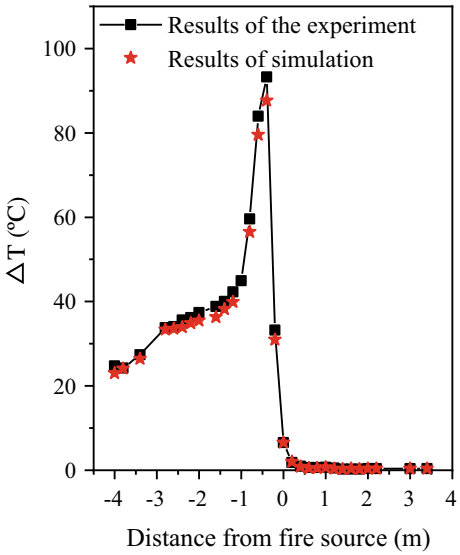

Fig. 5 Comparison of numerical simulation results with model test results

located 3 m away from the source of fire, while the longitudinal wind speed was 0.62 m/s. The exhaust volumetric flow rate was set at 180m^3/h. Thermocouples were used to measure the temperature and were placed at 0.2 m intervals along the tunnel, with measurement points located 2 cm below the tunnel ceiling. The ambient temperature during testing was maintained at 35 °C. It can be observed from Fig. 5 that the longitudinal temperature distribution obtained from numerical simulation results closely aligns with the experimental data, with a maximum error within 20%. This demonstrates that the proposed model is capable of accurately simulating and calculating tunnel fires.

The study investigates the critical complete exhaust volumetric flow rate in tunnel fires under the synergistic effect of longitudinal ventilation and top smoke exhaust, considering factors such as fire source heat release rate, fire source location, length of the smoke exhaust vent, and specific simulation conditions shown in Table 1.

3 Results and Discussion

The critical complete exhaust volumetric flow rate, as defined in this paper, refers to the volumetric flow rate of smoke exhaust that allows for complete discharge from the smoke vent without any downstream spreading through the vent when there is no smoke return. The simulation results are summarized in Table 2.

Table 1 Simulation conditions

HRR/MW	Location of fire	Length of the vent/m
5	A	1/3/5/6/7/10/13/15
	B	1/7/15
	C	7/15
	D	7/15
10	A	1/7/15
	B	7
	C	7
30	A	1/7/15
	B	1/7/15

Table 2 Summary of simulation results

HRR /MW	Longitudinal Vertical /m·s^{-1}	Fire location	Length of the smoke vent /m	Smoke extraction /m^3·s^{-1}
5	2.71	A	1/3/5/6/7/10/13/15	235/237/241/243/245/247/243/235
		B	1/7/15	220/230/221
		C	7/15	217/210
		D	7/15	204/198
10	3.28	A	1/7/15	312/321/318
		B	7	302
		C	7	287
30	4.3	A	1/7/15	514/527/519
		B	1/7/15	489/504/490

3.1 Influence of the Heat Release Rate on the Critical Complete Exhaust Volumetric Flow Rate

The impact of the heat release rate of the fire source on the critical complete exhaust volumetric flow rate is illustrated in Fig. 6. From the diagram, it can be observed that an increase in the heat release rate corresponds to a rise in the critical complete exhaust volumetric flow rate. This can be explained by the force exerted on the smoke vent. As shown in Fig. 7, the smoke below the vent is mainly subject to the vertical inertia force generated by the smoke exhaust and the horizontal inertia force caused by the superposition of the longitudinal forced airflow and smoke heat pressure. On the one hand, when increasing the heat release rate of the fire source, it leads to an elevation in the temperature of the smoke below the vent. Consequently, this results in an augmented thermal buoyancy of the smoke near the exhaust vent. On the other hand, as indicated in Table 2, an increase in heat release rate corresponds to a higher

critical wind speed for longitudinal ventilation. This leads to an escalation in the horizontal inertia force induced by longitudinal wind. Therefore, both the horizontal inertia force caused by longitudinal wind and smoke thermal buoyancy intensify with higher heat release rates. To counterbalance this surge in horizontal inertial force, a larger exhaust inertial force is required to prevent smoke from crossing over the vent. This can only be achieved by increasing the volume of exhaust. Therefore, the critical volume of smoke exhaust at the critical wind speed increases with an increase in the heat release rate. Furthermore, in the actual tunnel project, once the vent setting is established, the critical exhaust volumetric flow rate for complete smoke extraction under varying heat release rates can be determined. As a result, a corresponding decrease in the critical exhaust volumetric flow rate can be achieved when the heat release rate is reduced, thereby avoiding unnecessary waste caused by excessive volume.

Note: ρ_s is the density of smoke, kg/m^3; V_s is the exhaust volumetric flow rate at the vent, m^3/s; l is the length of the vent, m; w is the width of the vent, m; u_h is the average velocity of smoke when there is no smoke exhaust, m/s; A is the cross-sectional area of smoke, m^2.

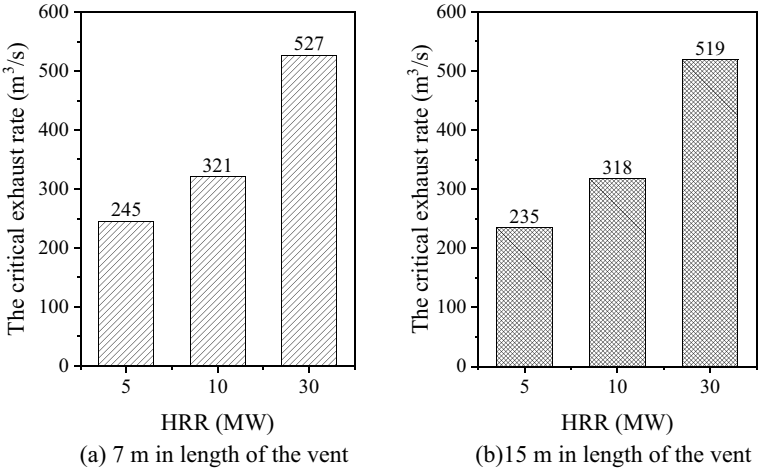

Fig. 6 Effect of HRR on critical complete exhaust volumetric flow rate

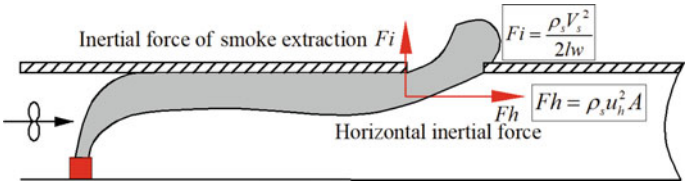

Fig. 7 Schematic diagram of smoke force analysis underneath the smoke vent

3.2 *Influence of the Location of Fire Source on the Critical Complete Exhaust Volumetric Flow Rate*

Figure 8 illustrates the critical exhaust volumetric flow rate for complete smoke exhaust under four fire source positions (A, B, C, and D) with a heat release rate of 5 MW, longitudinal wind speed at its critical velocity, and vent lengths of 7 m and 15 m. It can be observed from the figure that as the longitudinal position of the fire source increases from the vent distance, the critical complete exhaust volumetric flow rate also increases. This can be attributed to the fact that an increased distance results in a longer smoke flow path towards the vent, causing a decrease in temperature below it As indicated by Fig. 7, this reduction leads to a decrease in horizontal inertial force due to hot smoke buoyancy, thereby the inertial forces required for critical smoke evacuation can be reduced accordingly. Consequently, the critical complete exhaust volumetric flow rate is also reduced. Through the above analysis, it becomes evident that the critical complete exhaust volumetric flow rate increases proportionally with the longitudinal fire source location moving away from the vent. It is important to note that while the critical complete exhaust volumetric flow rate decreases as the vent spacing increases, excessively large spacing results in an elongated fire source section, which hinders safe personnel evacuation. Therefore, careful consideration should be given to determining the optimal smoke exhaust vent spacing, which will be further studied in future work.

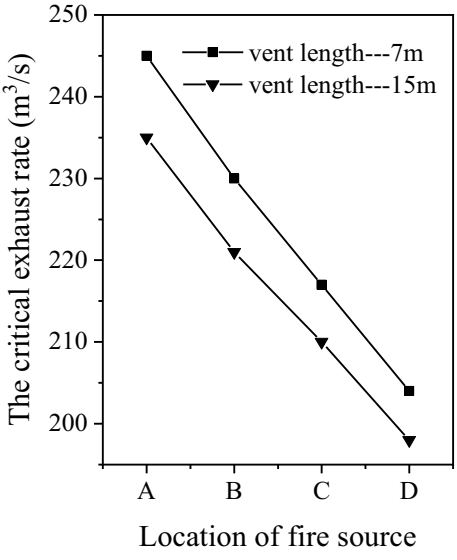

Fig. 8 Influence of fire source location on critical complete exhaust volumetric flow rate

3.3 Influence of Smoke Vent Length on the Critical Complete Exhaust Volumetric Flow Rate

Taking the case where the heat release rate of the fire source is 5 MW and the longitudinal wind speed is at its critical level as an example, Fig. 9 illustrates the impact of smoke vent length on the critical complete exhaust volumetric flow rate in tunnel fires under the combined influence of longitudinal wind and top smoke venting. It can be observed that, for a fixed heat release rate, increasing the length of the vent initially leads to an increase in critical complete exhaust volumetric flow rate, followed by a decrease. This occurs because as the length of the smoke vent gradually increases, it results in an increased area at its mouth and a reduced wind speed for smoke exhaust; consequently weakening inertia force during smoke exhaust. Although increasing the length of the vent does not significantly affect horizontal inertia force, it becomes necessary to increase smoke exhaust capacity in order to ensure complete discharge. When the length of the vent exceeds 10 m, due to its larger size, smoke can directly enter and exit through the vent without easily overflowing. This facilitates effective smoke exhaust and reduces requirements for critical exhaust volumetric flow rate. Therefore, we observe an increasing trend followed by a decreasing trend in critical complete exhaust volumetric flow rate with longer lengths of vent. This suggests that during actual tunnel operation, the exhaust volumetric flow rate can be suitably diminished in accordance with the vent length without necessitating waste. Furthermore, when adjusting the exhaust volumetric flow rate based on specific vent dimensions is infeasible, it can be set to the maximum value corresponding to the pertinent firepower (e.g., the exhaust volumetric flow rate corresponding to a 10-m-long vent under this working condition). This ensures comprehensive smoke discharge from any vent within the 1–15 m range.

4 Conclusions

In this paper, a full-size tunnel model is established using FDS and three-dimensional numerical calculation methods are employed to investigate and analyze the variations in the critical complete exhaust volumetric flow rate at the exhaust vent of a tunnel fire under the combined influence of longitudinal ventilation and top smoke extraction, considering various factors. The key findings obtained from this study are as follows:

(1) When the vent size and fire source location are fixed, an increase in heat release rate leads to a corresponding increase in the critical exhaust volumetric flow rate required for complete ventilation. Therefore, the critical complete exhaust volume flow rate at varying heat release rates can be determined accurately in actual tunneling projects, ensuring both efficient smoke evacuation and the prevention of unnecessary waste resulting from excessive exhaust volume flow rates.

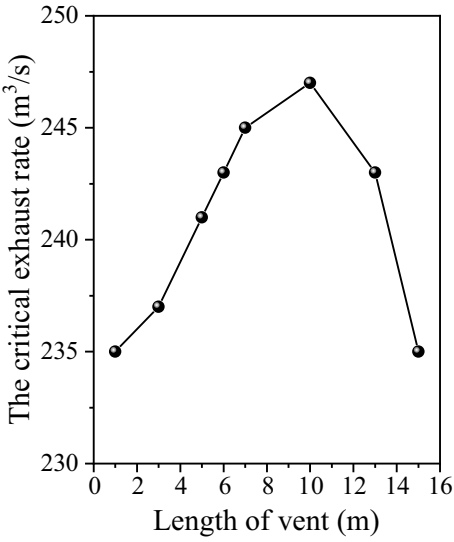

Fig. 9 Effect of different vent lengths on complete exhaust volumetric flow rate

(2) In cases where the vent size and the power of the fire source remain constant, as the distance between the fire source and vent location increases, there is a decrease in the critical complete exhaust volumetric flow rate. It should be noted that although increasing vent spacing leads to a reduction in the critical complete exhaust volumetric flow rate, excessively large spacing can elongate the fire source section, impeding safe personnel evacuation. Therefore, careful consideration must be given to determining optimal smoke exhaust vent spacing.
(3) The critical complete exhaust volumetric flow rate increases when the length of the vent is less than 10 m and decreases when it exceeds 10 m, while keeping the heat release rate and location of the fire source unchanged. The findings indicate that during the tunnel operation, the exhaust volumetric flow rate can be appropriately reduced in accordance with the vent length, thereby eliminating the need for waste. Moreover, when it is impracticable to adjust the exhaust volumetric flow rate based on specific vent dimensions, it can be set to the maximum value corresponding to the relevant fire power (the exhaust volumetric flow rate corresponding to a 10-m-long vent under these working conditions). This approach ensures complete smoke discharge from any vent within the 1–15 m range.

The present study primarily focuses on a specific vent width for research and analysis, neglecting factors associated with it. These aspects will be further explored in future research, enhancing the practicality of the findings. Additionally, an investigation is being conducted to integrate theoretical concepts and derive a predictive formula for the critical complete smoke exhaust volume. This aims to develop a universally applicable equation that offers direction for tunnel smoke exhaust.

Acknowledgements The author would like to express gratitude to Mengyi Xu for her assistance in the experiments.

References

1. Ji J, Tan T, Gao Z, Wan H, Zhu J, Ding L (2019) Numerical investigation on the influence of length–width ratio of fire source on the smoke movement and temperature distribution in tunnel fires. Fire Technol 55(3):963–979
2. Yao YZ, Li YZ, Cheng XD (2019) Numerical study on overall smoke control using naturally ventilated shafts during fires in a road tunnel. Int J Therm Sci 140
3. Fan JY, Zhao XL, Zhu YL, Zhao XL, Feng W (2021) Study on the longitudinal ceiling temperature distribution induced by double pool fires in a tunnel. Int J Therm Sci 168(1)
4. Yousefi M, Yousefi M, Safikhani H, Inthavong K, Bamdad K (2021)Study of the critical velocity of the tunnels using an analytical approach. Fire Saf J 123
5. Xu Z, Zhou D, Tao H, Zhang X, Hu W (2022) Investigation of critical velocity in curved tunnel under the effects of different fire locations and turning radiuses. Tunn Undergr Space Technol 126
6. Unit China Merchants Chongqing Transportation Research and Design Institute Co. (2014) Guidelines for Design of Ventilation of Highway Tunnels. People's Transportation Press Co
7. Ingason H, Li YZ (2011) Model scale tunnel fire tests point extraction ventilation. J Fire Prot Eng 21(1):5–36
8. Chen LF, Hu LH, Tang W, Yi L (2013) Studies on buoyancy driven two-directional smoke flow layering length with combination of point extraction and longitudinal ventilation in tunnel fires. Fire Saf J 59:94–101
9. Li YZ, Lei B, Ingason H (2011) Study of critical velocity and back layering length in longitudinally ventilated tunnel fires. Fire Saf J 45(6–8):361–370
10. Tang F, He Q, Mei FZ, Wang Q, Zhang H (2021) Effect of ceiling centralized mechanical smoke exhaust on the critical velocity that inhibits the reverse flow of thermal plume in a longitudinal ventilated tunnel. Tunn Undergr Space Technol 82:191–198
11. Wang MN, Guo XH, Yu L, Zhang YT, Tian Y (2021) Experimental and numerical studies on the smoke extraction strategies by longitudinal ventilation with shafts during tunnel fire. Tunn Undergr Space Technol 116
12. Hong Y, Kang JH, Fu CJ (2022) Mixed ventilation approach combined with single-shaft complementary system for highway tunnels. Fire Saf J 127
13. Yang D, Dong S, He M, Zhang Z, Ji W (2020) Experimental study on the performance of hybrid ventilation system combining forced longitudinal flow and shaft natural ventilation in tunnels. Tunn Undergr Space Technol 103:103491
14. Jiang XP, Qiao YF, He ZH (2019) On the back-layered smoke flow in the lateral points of the smoke extraction tunnels. J Saf Environ 18(6):2177–2182
15. Mcgrattan KB, Mcdermott RJ, Weinschenk CG, Forney GP (2016) Fire dynamics simulator, user's guide. Nist Special Publication

Influence of 3% Barium Chloride as a Retarder on the Setting Time of Geopolymer Cement and Compressive Strength of Geopolymer Concrete

Conghui Liu and Meichun Zhu

Abstract Addressing the issue of short setting time in geopolymer cement, this study focuses on common retarders in engineering, and explores the effect of retarders in alkali activated geopolymer cement systems, including the impact on the solidification time of geopolymer cement and the impact on the strength of geopolymer concrete after adding aggregates to prepare concrete. Using 1 and 3% Sucrose, Borax and barium chloride as retarders, comparative experiments were conducted to determine the setting time of geopolymer cement and the compressive strength of geopolymer concrete. Results indicate that, compared to Sucrose and Borax, barium chloride exhibited the most effective retarding effect on the setting time of geopolymer cement, with initial and final setting times reaching 265 and 420 min, respectively. Whatsmore, at concentrations ranging from 1 to 3%, sucrose, borax, and barium chloride as retarders had a minimal impact on the compressive strength of geopolymer concrete. This research provides a reference basis for the effectiveness and applicability of retarders in engineering applications.

Keywords Geopolymer cement · Geopolymer concrete · Retarder · Barium chloride · Setting time · Compressive strength

1 Introduction

With cement being the world's second-largest consumable material in industrial production, its high energy consumption and significant industrial CO_2 emissions pose challenges in meeting the needs of green ecological engineering construction. Geopolymer cement, an eco-friendly and low-carbon cementitious material, has been increasingly emphasized to promote carbon dual-carbon strategies and facilitate low-carbon development [1]. Widely applied in construction, subways, bridges, tunnels, and water conservancy, geopolymer [2].

C. Liu · M. Zhu (✉)
School of Civil Engineering, Shanghai Normal University, Shanghai, China
e-mail: zhumeichun@shnu.edu.cn

G. Mei et al. (eds.), *Advanced Construction Technology and Research of Deep-Sea Tunnels*, Lecture Notes in Civil Engineering 490,
https://doi.org/10.1007/978-981-97-2417-8_27

Geopolymer cement is produced from amorphous aluminosilicate solid waste materials with alkaline activators. It has been proven to possess mechanical properties and durability comparable to ordinary Portland cement (OPC) [3]. However, geopolymer cement still suffers from the drawback of short setting time, hindering its extensive application in engineering [4]. Therefore, the incorporation of a certain amount of retarder is necessary to control the setting time. Previous research has indicated significant variations in the effects of traditional cementitious retarders on the setting time of alkali-activated cementitious materials [5]. Moreover, the influence of retarder performance on concrete specimens remains understudied, necessitating further research on whether the addition of retarders affects the compressive strength of geopolymer concrete [6]. Therefore, there is a lack of exploration into the optimal retarder for a specific fixed mix proportion of geopolymer cement with alkali-activated materials.

This study primarily focuses on slag-fly ash concrete and cement, through experiments, aims to explore a suitable retarder that effectively prolongs the setting time of geopolymer cement while minimally affecting the workability and compressive strength of the concrete.

2 Experiment

2.1 Materials

The materials used in this study are detailed as follows: (1) Slag, provided by Longze Purified Water Materials Co., Ltd., Gongyi City, China, with a density of 3100 kg/m^3; (2) Fly ash, provided by Henan Borun Foundry Materials Co., Ltd., China, with a density of 2550 kg/m^3; (3) Solid activator with a purity of over 95% NaOH; (4) Liquid activator, sodium carbonate, prepared by blending sodium hydroxide and water glass, produced by Qingdao Yousuo Chemical Technology Co., Ltd., China. The specific composition of water glass is shown in Table 1.

Table 1 Composition of water glass

Component name	Content
Sodium oxide/w/%	8.82
Silicon dioxide/w/%	28.03
Module	3.28

2.2 Experimental Design

Experimental Equipment

The experimental equipment used in this study includes a ring knife, 100 cm*100 cm mold, cement slurry mixer, cement mortar mixer, humidity curing box, penetration tester, electronic scale, electro-hydraulic servo universal testing machine, vibration table, etc.

Experimental Procedure

The experimental design procedure of this study is as follows, ensuring the prolongation of the setting time of geopolymer concrete while maintaining its strength. The specific process flowchart is shown in Fig. 1.

Step 1: Determine the mix proportion of geopolymer cement for this experiment.

Step 2: Prepare geopolymer cement test blocks. Prepare the control group geopolymer cement test blocks and prepare experimental group geopolymer cement test blocks with 1% sucrose, 1% borax, 1% barium chloride, 3% sucrose, 3% borax, and 3% barium chloride as retarders, then place them in a humidity curing box for setting.

Step 3: Determine the initial and final setting times of each test block to understand the impact of different types and proportions of retarders on the setting effect of geopolymer cement.

Step 4: Prepare geopolymer concrete test blocks using geopolymer cement as a binder material. The control experiment method is adopted. Prepare geopolymer cement according to the mix proportion in Step 1, then add aggregates in a certain proportion, mix the aggregates with the binder material thoroughly, and pour the mixture into the mold to form the control group geopolymer concrete test blocks and geopolymer concrete test blocks made with 1% sucrose, 1% borax, 1% barium chloride, 3% sucrose, 3% borax, and 3% barium chloride as retarders.

Step 5: Demold the test blocks after 12 h of setting, then perform high-temperature curing, and conduct compressive strength tests on the geopolymer concrete test blocks to investigate the impact of retarders on the compressive strength.

Step 6: Draw conclusions and identify the most effective retarder that effectively prolongs the setting time of geopolymer cement and minimally affects the workability and compressive strength of the concrete.

Fig. 1 Experimental design flowchart

Table 2 Geopolymer cement mix designs

Component	Density (kg/m^3)
Slag	168
Fly ash	252
Sodium hydroxide	12.15
Water glass	45
Water 153.6	153.6

2.3 Experimental Mix Design

In this experiment, the precursor materials of geopolymer cement are slag and fly ash, with a mass ratio of 2:3. Sodium hydroxide and liquid sodium silicate are used as activators. The specific mix ratios of each material in geopolymer cement are shown in Table 2. Considering the feasibility of the candidate materials as retarders, this experiment employs the materials and proportions of retarders at 1% and 3%, namely, barium chloride [7], sucrose [8], and borax [9].

2.4 Sample Preparation

Preparation of Geopolymer Cement

Before preparing the sample, prepare a sodium silicate solution according to the design concentration, and then cool it to room temperature for later use. Subsequently, the retarder is added to the prepared solution to obtain a mixed solution of the retarder and activator. Then, slag, fly ash, and solution are mixed using a cement sand mixer. These test samples are named Z1, Z2, Z3, Z4, Z5, Z6, and Z7, respectively. The types and proportions of retarders in different geopolymer cement test blocks are shown in Table 3. After mixing, inject the slurry into the circular test mold, use the vibration method to remove bubbles, and place it in a moisture curing box for curing. It should be noted that the entire process was carried out in a room with a room temperature of 23 °C [10].

Preparation of Geopolymer Concrete

The aggregates for geopolymer concrete in this study are 5–10 mm crushed stone, 10–20 mm crushed stone, and river sand. The specific proportions of cementitious materials and aggregates are shown in Table 4. The specific preparation process is as follows: after the production of geopolymer cement is completed, a retarder and aggregate are quickly added, and then mixed to prepare geopolymer concrete. Next, quickly place the concrete into a 100 * 100 * 100 mm cube mold, named L1, L2, L3, L4, L5, L6, L7 (Table 5). To reduce test errors and ensure accuracy, each group of concrete test blocks has the same three blocks (Fig. 2), and the average compressive strength of each group of three test blocks is taken [11]. The materials and dosage of

Table 3 Types and proportions of retarders in different geopolymer cement test blocks

Group	Retarder	Proportion (%)
Z1	/	/
Z2	Sucrose	1
Z3	Sucrose	3
Z4	Borax	1
Z5	Borax	3
Z6	Barium chloride	1
Z7	Barium chloride	3

Table 4 Test plan for mix proportion of geopolymer concrete (kg/m^3)

Component	Density
Geopolymer cement	630
Crushed stone (5–10 mm)	240
Crushed stone (10–20 mm)	842
River sand	777

Table 5 Types and proportions of retarders in different geopolymer concrete test blocks

Group	Retarder	Proportion (%)
L1	/	/
L2	Sucrose	1
L3	Sucrose	3
L4	Borax	1
L5	Borax	3
L6	Barium chloride	1
L7	Barium chloride	3

retarder for each test block are shown in Table 5. Subsequently, the mold is placed on a vibration table to temporarily damage the flocculent structure of the concrete, reducing its viscosity and increasing the fluidity of the cement slurry in the concrete, thereby reducing the pores in the concrete test block [12] (Fig. 3).

2.5 Determination of Setting Time

To investigate the effect of retarders on the initial setting time, the initial setting time of the test block was measured. As the initial setting approaches, place the test block under the test needle and lower it until it comes into contact with the surface of the cement paste. After tightening the screw, it suddenly relaxes and the test needle sinks vertically and freely into the cement slurry. Observe the reading of the pointer

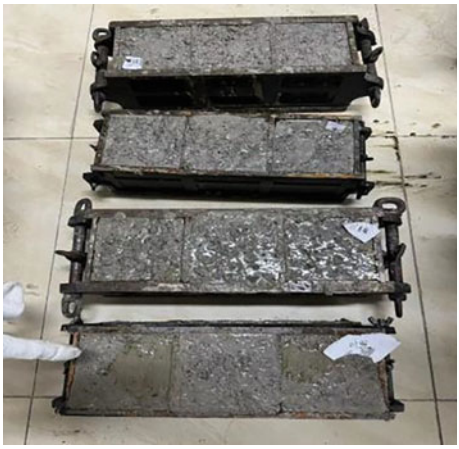

Fig. 2 Geopolymer concrete test block before demolding

Fig. 3 Excluding bubbles

when the test needle stops sinking. When the test needle sinks to a distance of 4 ± 1 mm from the bottom plate, it indicates that the cement has reached its initial setting state [13], as shown in Fig. 4. After measuring the initial setting time, immediately remove the test mold and slurry from the glass plate in a translational manner, flip it 180°, and then place it in a moisture curing box to continue curing. Insert a circular attachment at the bottom of the test needle, and the measurement method for the final setting time is consistent with the measurement method for the initial setting time. The difference is that when the test needle sinks 0.5 mm into the specimen, that is, when the circular attachment cannot leave any marks on the specimen, the cement reaches the final setting state, as shown in Fig. 5 [14].

Fig. 4 Measure the initial setting time

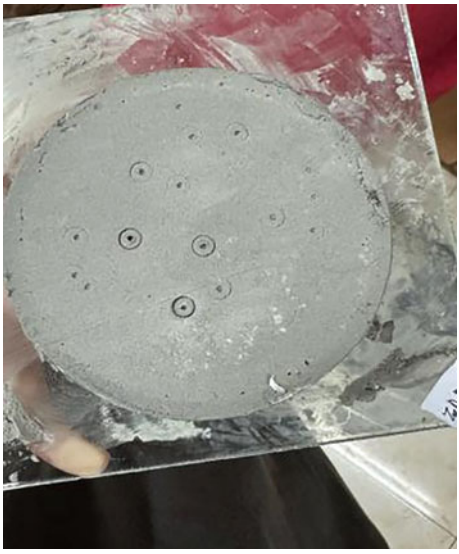

Fig. 5 The test block reaches the final setting state

2.6 Testing of Compressive Strength

To investigate the effect of retarders on the compressive performance of geopolymer concrete specimens, the compressive strength of the specimens was tested. Leave the prepared concrete test block groups L1, L2, L3, L4, L5, L6, and L7 standing for

12 h before demolding, and wrap them with cling film before quickly placing them in a high-temperature curing box for 24 h, as shown in Fig. 6. The cured geopolymer concrete test blocks were placed into an electro-hydraulic servo universal pressure testing machine for pressure testing, as shown in Fig. 7. After completing the test, directly use the screen display pressure testing machine to read the data [15].

Fig. 6 High temperature curing

Fig. 7 Pressure test

3 Results

3.1 Results and Analysis of the Influence of Initial Setting Time

Table 6 shows the initial setting time of each test block group, and it can be seen that the barium chloride −3% group has the longest initial setting time of 228 min, which is 128 min longer than the control group and has a significant positive impact. Compared to the control group, the saccharose -1% group only extended the initial setting time by 9 min, which had a smaller impact. Figure 8 shows the percentage increase in initial setting time of each effective group compared to the control group, with a significant retardation effect of 3% concentration of barium chloride, an increase of 341.7%.

3.2 Results and Analysis of the Effect of Final Setting Time

Table 7 shows the final setting time of each test block group, and it can be seen that the barium chloride -3% group has the longest final setting time of 420 min, which is 290 min longer than the control group. Figure 9 shows the percentage increase

Table 6 Initial setting time of each group of test blocks group

Test block group	Initial setting time (min)
Z1	60
Z2	69
Z3	144
Z4	168
Z5	206
Z6	228
Z7	265

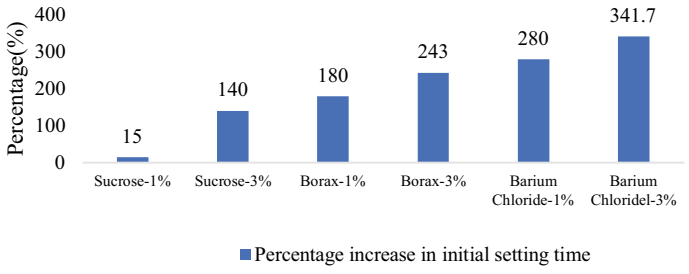

Fig. 8 Percentage increase in initial setting time of each effective group

Table 7 Final setting time of each group of test blocks

Group	Final setting time (min)
Z1	130
Z2	148
Z3	280
Z4	297
Z5	345
Z6	380
Z7	420

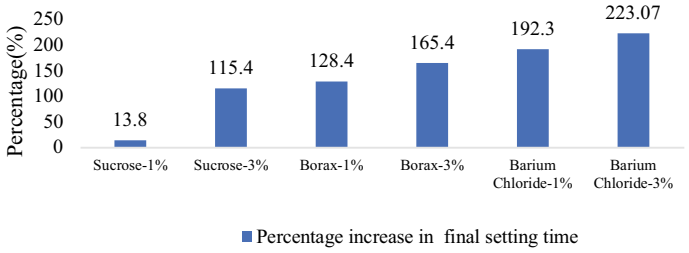

Fig. 9 Percentage increase in final coagulation time for each effective group

in initial setting time of each effective group compared to the control group, with a significant retardation effect of 3% concentration of barium chloride, an increase of 341.7%.

3.3 Compressive Strength Results

Table 8 shows the compressive strength of the concrete test block group. Overall, compared with the control group, adding 1–3% sucrose, borax, and barium chloride retarders does not have a significant impact on the compressive strength of geopolymer cement. Among them, the average compressive strength of the 3% borax experimental group L5 decreased by 11.2% compared to the control group L1. However, the average compressive strength of the 3% barium chloride experimental group L7 was 29.85 N/mm^2, Compared to the control group, only decreased by 4.3%.

Table 8 Average compressive strength of each group of concrete test blocks

Group	Average compressive strength (N/mm^2)
L1	31.18
L2	29.98
L3	29.88
L4	28.57
L5	27.69
L6	30.18
L7	29.85

4 Conclusions

In response to the impact of retarders on the initial setting time and compressive strength of geopolymer cement, this study selected three types of retarders: sucrose, borax, and barium chloride, and set corresponding proportions. Through indoor experiments, the influence of these retarders on the setting time of geopolymer cement was explored. The conclusion drawn is as follows:

(1) Compared to sucrose and borax, the geopolymer cement with barium chloride as a coagulant has the longest setting time. When the dosage is 1%, the initial setting time and final setting time of geopolymer cement can reach 228 and 380 min, respectively. When the dosage is 3%, the initial setting time and final setting time of geopolymer cement can reach 265 min and 420 min, respectively.
(2) Compared to barium chloride −1%, barium chloride −3% has a better retarding effect. The percentage increase in initial and final retarding time is 341.7 and 223.7, respectively, which are 61.7 and 30.77% higher than barium chloride −1%.
(3) In the six groups of test blocks, the effects of 1% and 3% concentrations of retarders on setting time were not the same, and the retarding effects of sucrose, borax, and barium chloride all became stronger with the increase of proportion.
(4) There are differences in the impact of different types of retarders and their dosage on the compressive strength of geopolymer concrete. When the dosage is 1% −3%, retarders such as sucrose, borax, and barium chloride do not have a significant negative impact on their compressive strength.

References

1. Yifan G, Tao G, Zhaofeng L, Zhihao Z, Jian Z (2022) Mechanism of retarder on hydration process and mechanical properties of red mud-based geopolymer cementitious materials. Constr Build Mater 356:129306
2. Jixiang W, Han L, Ze L, Dongmin W (2020) Setting controlling of lithium slag-based geopolymer by activator and sodium tetraborate as a retarder and its effects on mortar properties. Cem Concr Compos 110:103598
3. Bernal SA, Provis JL, Walkley B et al (2013) Gel nanostructure alkali-activated binders based on slag and fly ash, andffects of accelerated carbonation. Cem Concr Res 53(1):27–144
4. Sasaki K, Kurumisawa K, Ibayashi K (2019) Effect of retarders on flow and strength development of alkali-activated fly ash/blast furnace slag composite. Constr Build Mater 216:337–346
5. Tennakoon C, Nicolas RS, Sanjayan JG, Shayan A (2016)Thermal effects of activators on the setting time and rate of workability loss of geopolymers. Ceram Int 42(16):19257–19268
6. Andersen MD, Jakobsen HJ, Skibsted J (2003) Incorporation of aluminum in the calcium silicate hydrate (C-S-H) of hydrated Portland cements: a high-field 27Al and 29SiMAS NMR investigation. Inorg Chem 42(7):2280–2287
7. Cong XEM (2019)Low field NMR relaxation as a probe to study the effect of activators and retarders on the alkali-activated GGBFS setting process. Cem and Concr Compos 104
8. Assi LN, Deaver E, Ziehl P (2018) Using sucrose for improvement of initial and final setting times of silica fume-based activating solution of fly ash geopolymer concrete. Constr Build Mater 191:47–55
9. Kai-Tuo W, Li-Qiu D, Xue-Sen L, Yan H, Xue M (2017) Preparation of drying powder inorganic polymer cement based on alkali-activated slag technology. Powder Technol 312:204–209
10. Lateef NA, Edward D, Paul Z (2018) Using sucrose for improvement of initial and final setting times of silica fume-based activating solution of fly ash geopolymer concrete. Constr Build Mater 191:47–55
11. Dali B, Lynsdale CJ, Milestone NB, Hassani N, Ramezanianpour AA (2011)Effect of type, form, and dosage of activators on strength of alkali-activated natural pozzolans. Cem Concr Compos 33:251–260
12. Atis CD, Bilim C, Çelik Ö, Karahan O (2009) Influence of activator on the strength and drying shrinkage of alkali-activated slag mortar. Constr Build Mater 23(1):548–555
13. Myers RJ, Bernal SA, Provis JL, Gehman JD, Van Deventer JSJ (2015) The role of Al in cross-linking of alkali-activated slag cements. J Am Ceram Soc 98(3):996–1004
14. Blaise NB, Ndigui B, Emmanuel Y, Rodrigue CK, Robert N (2019) Effect of limestone dosages on some properties of geopolymer from thermally activated halloysite. Constr Build Mater 217:28–35
15. Falini G, Gazzano M, Ripamonti A (1996) Magnesium calcite crystallization from water-alcohol mixtures. Chem Commun 9:1037–1038

Study on the Effect of Uniform Corrosion on the Durability of Corrugated Web-Concrete Combination Box Girders with Steel Base Plate

Kaihui Zhang

Abstract In order to study the effect of uniform corrosion on the durability of steel bottom plate corrugated web-concrete composite box girder, this new type of steel-concrete composite structural girder bridge is analysed by using the time-varying reliability as the durability index. The static loading test is carried out on the steel bottom plate corrugated web-concrete composite box girder before and after corrosion, the mid-span deflection and stress before and after corrosion are calculated, and the time-varying reliability is used to calculate the reliability index of the composite box girder. The results show that under static loading, the mid-span deflection of the model test beam increases with the increase of load. The stress values before and after corrosion do not differ much when the load is small, and there is a significant difference in the stress values of the steel bottom plate with the increasing load. According to the relevant codes and using the primary second-order method of moments, the time-varying reliability indexes under different t moments are calculated by Matlab software.

Keywords Steel-substrate corrugated web-concrete composite structural box girder · Mid-span deflection and stress · Time-varying reliability · Durability

1 Introduction

The traditional waveform steel web combined box girder whose concrete bottom plate is easy to be tensile cracked and other problems under the action of positive bending moment, which seriously affects the durability and service life of the bridge [1, 2]. Conventional corrugated steel web combined box girder in the positive moment under the action of the concrete bottom plate is prone to tensile cracking disease [3]. Domestic experts and scholars have improved the traditional corrugated web combination box girder by replacing the concrete bottom plate of the traditional

K. Zhang (✉)
Colleague of Civil Engineering, Lanzhou Jiaotong University, Lanzhou 730000, China
e-mail: zhang2781268085@qq.com

G. Mei et al. (eds.), *Advanced Construction Technology and Research of Deep-Sea Tunnels*, Lecture Notes in Civil Engineering 490,
https://doi.org/10.1007/978-981-97-2417-8_28

corrugated web combination box girder with a steel plate. The advantages of the respective material properties of steel and concrete in steel–concrete combined girder bridges are fully utilized [4, 5]. As a result, a new type of steel–concrete combined structure is formed—steel bottom plate waveform web—concrete combined box girder.

The steel base plate corrugated web-concrete combined box girder has high load carrying capacity and seismic performance. In order to ensure its safe and long-lasting operation, durability analysis is needed [6, 7]. Zhang [8] and others proposed an analytical method that can accurately analyze the vertical bending mechanical properties of corrugated web steel box girders; Gan [9] established the elastic control differential equations of this type of box girder to study its damage mechanism; Chen [10] analyzed the changes in stress and stiffness of the box girder of the combined structure, which is positively significant for the promotion and development of this type of box girder structure in the future. However, none of the existing studies have deeply analyzed the durability performance of this type of combined box girder. As the bridge is exposed to the atmospheric environment for a long time, then the bridge tends to suffer from uniform corrosion, and its de-icing salt corrosion problem is the most serious. As a new type of combined structure newly proposed in recent years, corrosion on the corrugated web steel bottom plate combined box girder in the durability performance of the impact of the study has not. In view of this, it is of great significance to carry out the research on the effect of uniform corrosion on the durability of new steel-hybrid composite structure girder bridges in this paper. In view of this, this paper carries out static loading test on steel bottom plate corrugated web-concrete composite box girder, and analyzes the durability based on the time-varying reliability, which is a certain guidance for the design of this kind of structure.

2 Durability Index of Combined Box Girder

By establishing the durability limit state objective, the influence of corrosion on the durability of steel base plate waveform web-concrete combined box girder is analysed, so as to put forward the measures to improve the durability of combined box girder and ensure the normal use function of combined box girder. In this paper, the functional equation constructed by deflection and stress of the combined box girder is taken as the structural functional equation of the normal use limit state. Under the existing external and internal factors, the reliability equations of different times are established by combining the time-varying reliability with the changes of structural deflection and stress after corrosion, and referring to the Steel Structure Design Standard (GB 50017-2017) [11].

2.1 Structural Deflection Time-Varying Reliability Assessment Model

The structural functional equations for the normal service limit state can be constructed from the deflections:

$$Z(t) = [f]_{\max} - f \tag{1}$$

formula: $[f]_{\max}$ is the structural deflection limit value specified in the code.

Assumptions $[f]_{\max}$ and f all obey normal distribution, and the time-varying reliability index of the member is obtained from the primary second-order method of moments:

$$\beta = \frac{\overline{[f]_{\max}} - \overline{f}}{\sqrt{\delta^2_{[f]_{\max}} + \delta^2_f}} \tag{2}$$

Formula: $\overline{[f]_{\max}}$ is $[f]_{\max}$ average value; $\overline{f}$ is f average value; $\delta_{[f]_{\max}}$ is $[f]_{\max}$ standard deviation; δ_f is f standard deviation.

2.2 Structural Stress Time-Varying Reliability Assessment Modeling

Structural functional equations for normal service limit states can be constructed from the stresses:

$$Z(t) = [\sigma] - \sigma \tag{3}$$

Formula: $[\sigma]$ is the structural stress limit value specified in the code, σ is the value of stress obtained from the test.

Hypothesis $[\sigma]$ and σ all of them obey normal distribution, and the time-varying reliability index of the member is obtained by the primary second-order method of moments:

$$\beta = \frac{\overline{[\sigma]} - \overline{\sigma}}{\sqrt{\delta^2_{[\sigma]} + \delta^2_\sigma}} \tag{4}$$

Formula: $\overline{[\sigma]}$ is $[\sigma]$ average value; $\overline{\sigma}$ is σ average value; $\delta_{[\sigma]}$ is $[\sigma]$ standard deviation; δ_σ is σ standard deviation.

3 Uniform Corrosion on Steel Bottom Plate Wave Web Combined Box Girder Model Test Research

3.1 Test Overview

With a span of 30 m steel base plate waveform web-concrete combination box girder as a structural prototype, according to the similarity theory to do 1:9 scaled model.

The span of the box girder is L = 3.4 m, the height of the girder is 0.4 m, the width of the top plate is 1 m, the thickness is 0.05 m, the width of the bottom plate is 0.58 m, and there is a cross partition at the pivot point, L/4 and in the middle of the span, and the material of the girder is C50 concrete; the web plate is made of corrugated steel plate with a thickness of 3 mm, and the bottom plate is made of flat steel plate with a thickness of 5 mm, and the material of the girder is Q345 steel plate; and the web and the top plate adopt the buried type of shear connectors. The test beams are shown in Figs. 1 and 2.

The centralized symmetric loading was carried out on the test beams before and after corrosion respectively, and the test beams were preloaded before the test with

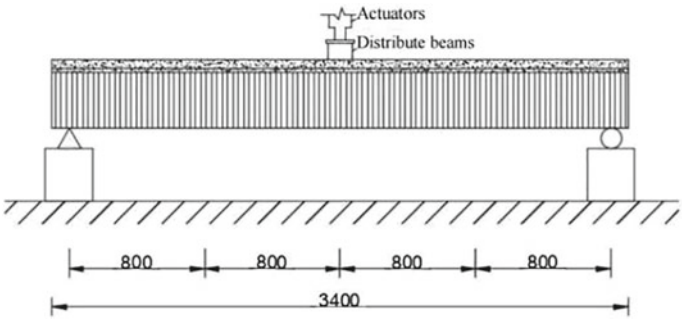

Fig. 1 Elevation of the test beam (mm)

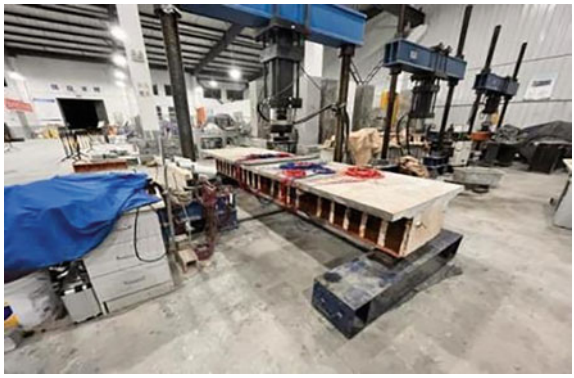

Fig. 2 Test beam loading device

two load levels of 4 and 8 kN. In this paper, the maximum load applied during the symmetric loading stage was 80 kN, and the test loading was divided into 8 levels of loading, with each level of loading in increments of 10 kN. After the loading readings were stabilized for 2 min, the corresponding actual load, deflection and stress–strain data were recorded. The loading process utilizes the structural laboratory to load the model test beams with reaction frames and jacks, and the loading process is controlled by pressure sensors, the corresponding strain data are recorded regularly by the static data acquisition system, and the vertical displacements are recorded by the percentile meter.

The model test beams were immersed in a chloride salt solution with a concentration of 6% for 517 days, and the corrosion conditions are shown in Figs. 3 and 4.

Fig. 3 Uniform corrosion of the web

Fig. 4 Uniform corrosion of the base plate

3.2 Analysis of Static Test Results

Load-mid-span vertical displacement analysis

The values of load-vertical displacement in the span cross-section of the model test beam before and after corrosion are shown in Table 1, and the change rule of load-vertical displacement in the span cross-section of the model test beam before and after corrosion is shown in Fig. 5.

The mid-span deflection of the model test beam increases with increasing load during loading. The mid-span deflections before and after corrosion do not differ much when the load is small, and the difference between the mid-span deflections before and after corrosion is larger as the load keeps increasing. When the load is 10 kN, the mid-span displacement of the model beam after corrosion increases by 13.89% compared with that before corrosion. When the load increases to 80kN, the mid-span displacement of the model beam after corrosion increases by 20.52% compared with that before corrosion. It can be seen that uniform corrosion has

Table 1 Vertical displacement values in span before and after corrosion

Value of vertical displacement in span before corrosion								
Load (kN)	10	20	30	40	50	60	70	80
Deflection (mm)	0.36	0.75	1.10	1.45	1.76	2.04	2.35	2.68
Value of vertical displacement in span after corrosion								
Load (kN)	10	20	30	40	50	60	70	80
Deflection (mm)	0.41	0.82	1.25	1.66	2.01	2.41	2.85	3.23

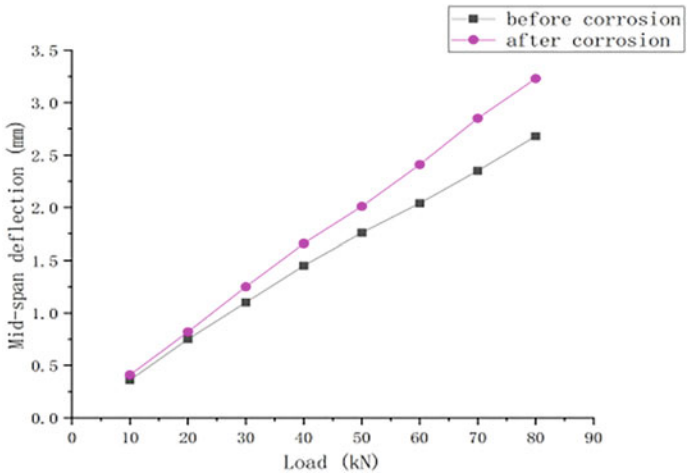

Fig. 5 Load-mid-span vertical deflection curve

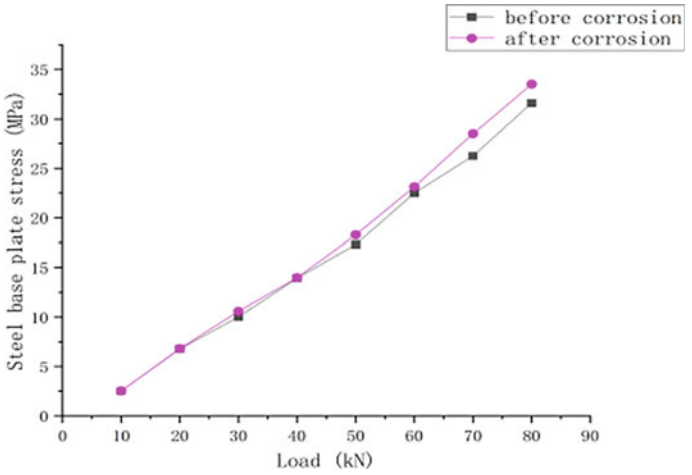

Fig. 6 Load-stress curve

a significant effect on the durability of steel base plate corrugated web-concrete combination box girders.

Positive stress analysis of steel base plate

The stress values of strain gauges numbered D6 in the steel base plate before and after corrosion of the model test beam for each load level are shown in Fig. 6.

The stress values before and after corrosion do not differ much when the load is small, and there is a significant difference in the stress value of the steel base plate with the increasing load; when comparing the 80kN load, it is found that the stress of the steel base plate after corrosion differs by 5.93% compared with the stress before corrosion. It can be seen that uniform corrosion has little effect on the stresses in the box girders of the combined structure.

4 Based on the Time-Varying Reliability of the Bridge Durability Analysis

According to the Unified Standard for Reliability Design of Highway Engineering Structures (JTG 2120–2020) [12], the load carrying capacity limit state target reliability index of highway bridges is 5.2. The time-varying reliability index at different t moments is calculated by Matlab software using the primary second-order method of moments, and is shown in Fig. 7.

As can be seen from Fig. 7, The time-varying reliability indexes calculated based on stress and deflection do not differ much. The time-varying reliability index based on deflection of the uncorroded test beam is 10.9, and the time-varying reliability

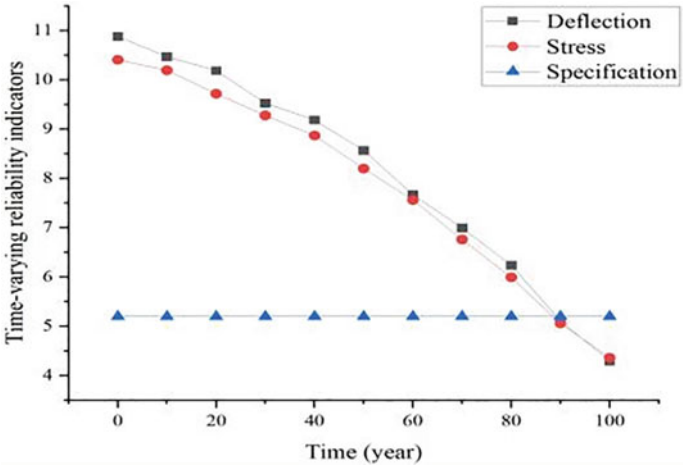

Fig. 7 Time-varying reliability index under deflection and stress

based on stress is 10.4, with a difference of 4.8%; in the uniform corrosion state, the reliability index of the composite box girder shows a decreasing trend, and when the composite box girder serves in this environment for 89 years, the reliability index is less than 5.2 stipulated in the specification, and at this time, the structure will be invalidated.

5 Conclusion

(1) With reference to the specification and existing literature, the functional equations constructed by deflection and stress of the combined box girder are taken as the structural functional equations of the limit state of normal use at different t moments.
(2) The model test beam before and after corrosion was subjected to static loading test, and the test loading was divided into 8 levels of loading, with each level of loading in increments of 10kN, and the maximum load of loading was 80kN.
(3) Under static loading, the deflection and stress were all roughly linear, and the mid-span deflection and stress before and after corrosion did not differ much when the load was small, and with the increase of load, the deflection and stress before and after corrosion had a significant difference.
(4) In the uniform corrosion state, the reliability index of the combined box girder shows a decreasing trend, when the combined box girder serves in this environment for 89 years, its reliability index is less than the specification of 5.2, at this time the structure will fail.

References

1. Zhang ZC, Wang GH, Fan J et al (2021) Self-oscillation characteristics of continuous beams with steel box combination with equal cross-section corrugated web. J China Railw Sci 42(04):51–59
2. Zhang ZC, Wang GH (2019) Influence of fold effect on mechanical properties of new combined box girder. J Railw Sci Eng 16(10):2491–2496
3. Kövesdi B, Jáger B, Dunai L (2016) Bending and shear interaction behavior of girders with trapezoidallycorrugated webs. J Constr Steel Res 121(6):383–397
4. Xiao L., Wen Z.Y.,et al.(2021) Research progress of steel-hybrid composite structure bridges in 2020.J. Journal of Civil and Environmental Engineering (in Chinese and English).43(S1): 107–119.
5. He L.X.,Song L.,(2014)Application of steel-mixed combined beam bridge.J.Northern Transportation.(7): 1–5.
6. Yan L,Wang Y.Y.,Li P.J., et al.(2023) Time-varying seismic resilience analysis of coastal bridges by considering multiple durability damage factors.J. International Journal of Structural Integrity.14(4).
7. He W.,Sun X.,Li C.,(2020)Research on Durability Evaluation Method of Bridge Slings Based on Set Pair Analysis.J. IOP Conference Series: Earth and Environmental Science.474(7).
8. Zhang ZC, Jin XJ, Gan YN (2019) Vertical bending mechanical properties of corrugated web steel box combination girders. J China Railw Sci 40(06):52–59
9. Gan YN, Wang GH, Zhang ZC et al (2023) Study on damage mechanism and design problems of improved simply supported combined box girder. J Railw 45(09)
10. Chen PF (2021) Study on fatigue damage and modeling test of corrugated web steel bottom plate combined box girder. Lanzhou Jiaotong University
11. GB 50017-2017 steel structure design standard
12. JTG 2120-2020 Unified standard for structural reliability design of highway engineering

Study on the Influence of Burner Size on the Maximum Temperature Rise of Smoke Flow Induced by Double Tunnel Fires

Youming Shu, Na Meng, and Shenghao Zhang

Abstract Based on FDS, numerical simulations were carried out to investigate the maximum temperature rise of smoke flow induced by double fires in a tunnel with natural ventilation. A full-scale model tunnel was established. The influence of 4 different sizes of double fire sources on the maximum temperature rise under the ceiling is studied when the distance between fire sources is 0 ~ 2 m. Results found that the maximum temperature rise decreases with the increase in burner separation distance and also decreases with the increasing burner size. Based on the model for the highest temperature for the ceiling-jet of one fire source, a new expression considering the burner size and the burner distance was put forward to predict the maximum temperature rise for double fire sources in tunnel fire, which can well correlate the numerical results.

Keywords Tunnel fire · Double fires · Burner size · Separation distance · Maximum temperature rise

1 Introduction

A fire in a tunnel is among the most terrifying transportation mishaps. Because tunnels are long, narrow, closed and have few escape routes, a fire in tunnel could pose a significant risk to the lives of the trapped individuals. At the same time, the high temperature will also damage the structure of the tunnel, leading to serious property damage. Therefore, in order to minimize casualties and economic losses, early monitoring and alarming of tunnel fires and effective control of smoke are very necessary.

Temperature is an extremely important factor in studying tunnel fires. It can be reference for the design of automatic fire alarm system and fire extinguishing system

Y. Shu · N. Meng (✉) · S. Zhang
College of Safety and Environmental Engineering, Shandong University of Science and Technology, Qingdao 266590, Shandong, China
e-mail: mengna@sdust.edu.cn

G. Mei et al. (eds.), *Advanced Construction Technology and Research of Deep-Sea Tunnels*, Lecture Notes in Civil Engineering 490,
https://doi.org/10.1007/978-981-97-2417-8_29

in tunnels. Currently, numerous scholars have conducted research on the highest temperature in tunnels. However, most of these researches have been confined to scenarios involving a single fire source. The impact of factors such as the heat release rate of the fire source, the velocity of longitudinal ventilation, and the parameters of the fire source on the highest temperature have been examined. In 1972, Alpert [1] investigated experimentally the variation of the highest ceiling temperature when there is no accumulation of smoke in the tunnel and established a prediction model. In 2003, Kurioka et al. [2] designed fire experiments in five model tunnels to study the highest temperature. A model for the highest temperature was established using both theoretical and experimental data analysis. Hu et al. [3] established Kurioka's maximum temperature correction model considering the tunnel slope factor through small-size experiments. Li et al. [4] found that Kurioka's model is no longer applicable when wind speeds are low. Therefore, Li et al. designed two tunnel model test platforms to investigate the variation of highest smoke temperature at different longitudinal ventilation rates. Jiang et al. [5] investigated the variation rule of the maximum temperature rise through full-size tunnel fire experiments, and verified the existing highest temperature rise prediction model. Wang [6] designed fire experiments in tunnels with different slopes, and studied the change of the maximum temperature by changing the tunnel slope.

The above studies consider single fire scenarios in tunnels and do not consider multiple fires scenarios. According to the survey results of tunnel fires [7], the proportion of fires caused by vehicle collisions in tunnels is as high as 81%. Vehicle collisions can easily lead to multiple fires accidents, which increases the scale of the fire as well as the hazards significantly. For example, in 2014, in Shanxi Yanhou tunnel 2 trucks collided and led to a fire in the tunnel. It spread rapidly, igniting vehicles around it, and resulting in 40 fatalities and 12 injuries [8]. It can be seen that the hazards caused by dual fires in tunnels are more serious. For dual source fire scenarios, scholars have also carried out corresponding researches. Xu [9] studied the impact of separation distance between the double fires on the combustion characteristics of dual fires through numerical simulation and model experiments, and established a prediction model for the maximum temperature of the smoke below the ceiling. Xu [10] conducted deep research to investigate the correlation between the maximum ceiling temperature and the separation distance between the two fires during longitudinal ventilation, and based on earlier studies, they added the influence factor of the separation distance between the two fires to create a new maximum temperature prediction model. Zhou et al. [11] investigated the effects of fire source spacing as well as the distance between the wall and two fire sources on the maximum smoke temperature by means of small-size experiments and established a maximum temperature prediction model by introducing the above two factors on the basis of previous studies. Chen [12] investigated the impact of the separation distance between the two fires on the maximum temperature in the case of longitudinal ventilation by means of small-size experiments, and a model for the highest temperature below the tunnel ceiling was established by theoretical analysis. Wan et al. [13] investigated the variation of the highest temperature of the smoke below the ceiling for double fire sources

with different sizes under natural ventilation through small-size experiments, and developed a prediction model for the highest temperature below the ceiling.

The interactions between two fires makes the combustion of two fires much more complicated than that of one fire. The current researches [9–13] on the highest temperature rise of smoke from double fire sources mainly take into account the impact of separation distance between the two fires, lateral position of the double fires, and longitudinal ventilation speed on the highest temperature of the smoke. However, previous studies on the maximum temperature of tunnel ceilings lacked consideration of the size of the fire source. Therefore, this article combines the factors influencing the maximum temperature of tunnel ceilings in previous studies and introduces the size parameter of the fire source to establish a highest temperature model.

2 Numerical Simulation

2.1 Physical Modeling

In this paper, numerical simulations are carried out using the fire dynamics software FDS (Fire Dynamics Simulator), whose effectiveness in the study of tunnel fires has been widely verified [14]. FDS is developed from a CFD analysis program specifically for simulating fire smoke dispersion. This software employs numerical methods to solve the Navier–Stokes equations for low-velocity, thermally-driven flows, with a focus on smoke motion and heat transfer processes due to fire.

As seen in Fig. 1, referring to specifications for design of highway tunnels [15], a full-size model tunnel of 80 m in length, 10 m in width, and 5.5 m in height is constructed using FDS. The model tunnel has a rectangular cross-section and is configured with two open ends to replicate a fire scenario with natural ventilation. Considering that the temperature is highest in the area directly above the fire source during combustion, thermocouples are set up according to the location of the fire source and the content of the study. A set of thermocouples with a 0.125 m longitudinal spacing is positioned in the longitudinal center and 0.1 m below the tunnel ceiling. The tunnel wall material is set as "concrete". 20 °C and 101 kPa of pressure are the beginning conditions inside the tunnel.

Double fire sources are installed along the tunnel longitudinal centerline, with the heat rate of a single fire source set to be 1.0, 1.25, and 1.5 MW. The fire source has

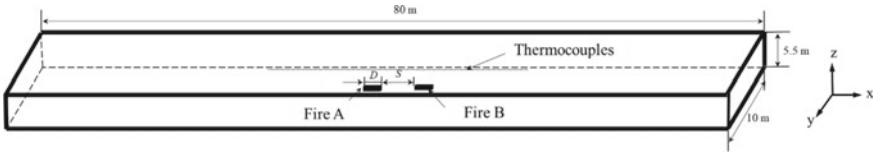

Fig. 1 Schematic diagram of tunnel model

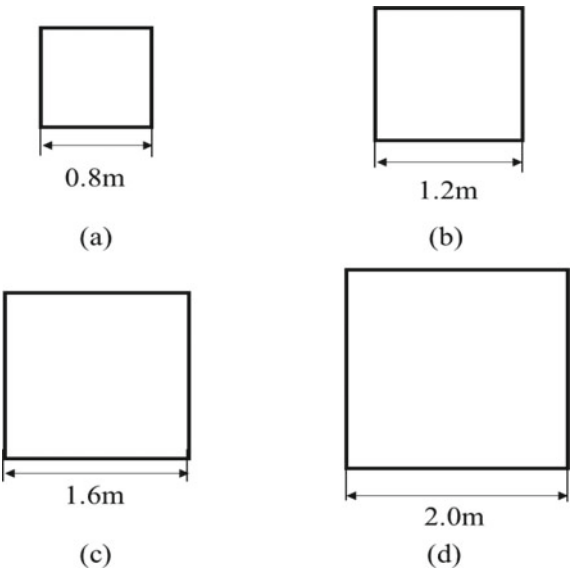

Fig. 2 Burner surface in four different sizes (Top view)

Table 1 Fire simulation table

Test number	Heat release rate/MW	Fire size/m	Separation distance/m
1–28	1.0 + 1.0	0.8, 1.2, 1.6, 2.0	0, 0.25, 0.5, 0.75, 1, 1.5, 2
29–56	1.25 + 1.25	0.8, 1.2, 1.6, 2.0	0, 0.25, 0.5, 0.75, 1, 1.5, 2
57–84	1.5 + 1.5	0.8, 1.2, 1.6, 2.0	0, 0.25, 0.5, 0.75, 1, 1.5, 2

a square surface with four side lengths of 0.8 m, 1.2 m, 1.6 m, and 2.0 m (refer to Fig. 2) and a height of 0.5 m. This study carried out a total of 84 tests by changing the heat release rate of the sources, the size of the fires, and separation distance between the two fires, as shown in Table 1. The simulation time for each test was set to be 200 s, and at this time the fire smoke could reach a stable state.

2.2 Grid System

The precision of the numerical simulation results will depend on the grid size. In this paper, we refer to the user manual of FDS to determine the grid size depending on the calculation outcomes of the characteristic diameter of the fire source [16] according to Eq. (1).

$$D^* = \left(\frac{\dot{Q}}{\rho_0 c_p T_0 \sqrt{g}}\right)^{2/5} \tag{1}$$

Table 2 Selection of grid size

Gird system	Grid size in near-fire region	Grid size in other regions
1	0.125 m × 0.125 m × 0.125 m	0.25 m × 0.25 m × 0.25 m
2	0.15 m × 0.15 m × 0.15 m	0.15 m × 0.15 m × 0.15 m
3	0.25 m × 0.25 m × 0.25 m	0.25 m × 0.25 m × 0.25 m
4	0.5 m × 0.5 m × 0.5 m	0.5 m × 0.5 m × 0.5 m

where D^* is the characteristic diameter of the fire source, m; $\dot{Q}$ is the heat release rate, kW; ρ_0 is the density of air, kg/m^3, as 1.204 kg/m^3; c_p is the constant pressure specific heat capacity of air, kJ/(kg·K), generally 1.005 kJ/(kg·K); T_0 is the ambient temperature, K, in this paper as 293 K; g is the acceleration of gravity, m/s^2, as 9.81 m/s^2.

For the fire scenario in this paper when the minimum heat release rate of the fire source is 1.0 MW, the characteristic diameter of the fire source D^* is calculated by Eq. (1) to be 0.96 m. According to the grid size formula proposed by Mcgrattan et al. [16], the model can accurately restore the fire scenario if the ratio of the characteristic diameter of the fire source to the grid size is between 4 and 16. Therefore, the numerical simulation results are more reliable when the grid size is between 0.06 and 0.24 m. For grid sensitivity analysis, four different grid systems were selected, as shown in Table 2.

Figure 3 gives the temperature comparison between the four grid systems when the fire source size is 1.2 m, the separation distance between the two fires is 0 m, and the heat release rate of a single fire source is 1.0 MW. As the point of origin, we choose the center between the two fire sources. The comparison reveals that the difference in longitudinal temperatures is small for grid system 1, 2 and 3. When the grid size is increased to 0.5 m, the temperature difference between grid system 4 and grid system 1, 2 and 3 is larger. Grid system 1 has been selected for this study in order to obtain precise results.

We consult earlier studies [17] to guarantee the accuracy of the experimental data. The sensitivity test is conducted using four alternative grid systems, as indicated in Fig. 3. In the study conducted by Huang et al. [17], a tunnel model with a width of 10 m and a height of 5 m was used, exhibiting great similarity with the model used in this paper. To assure the accuracy of the results of the numerical simulation, a grid system that is similar to that used in their study is used in this paper.

3 Simulation Results and Discussion

Figure 4 depicts the change of the smoke maximum temperature with respect to the distance between fires for different fire sizes under conditions of natural ventilation when the heat release rate of a single fire source is 1 MW, 1.25 MW, and 1.5 MW, respectively. It can be seen from Fig. 4.

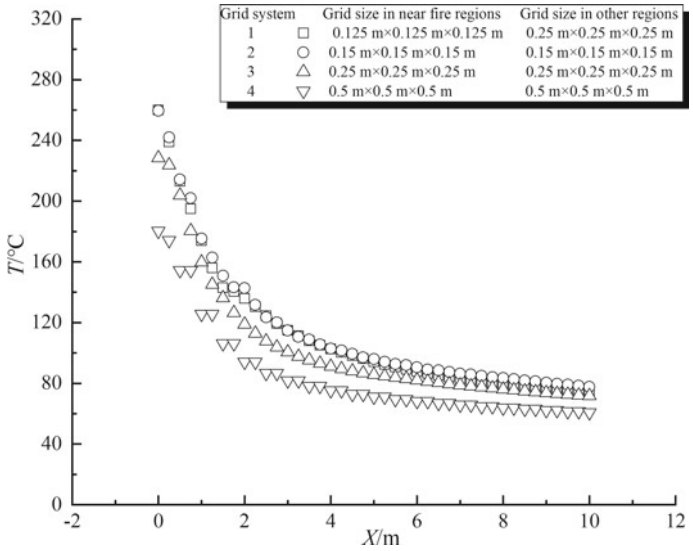

Fig. 3 Distribution of the ceiling smoke longitudinal temperature using various grid sizes

(1) With increasing fire separation and a constant fire size, the maximum smoke temperature drops. The primary reason for this is that when the two fires are farther apart, there is less contact between the two fire sources and more entrainment of the fire plume, which lowers the maximum temperature.
(2) The maximum temperature of the smoke decreases with the increase in the fire source size under fixed fire source spacing. The primary reason for this is that as the total heat release rate of the fire source remains constant, the heat release rate per unit area of the fire source decreases as the fire source area increases, and the flame height decreases accordingly, which leads to a decrease in the temperature of the fire plume ceiling jet.

Considering the effect of fire source size on the maximum temperature of the smoke, we try to introduce the fire source size as well as the fire spacing parameter to predict the maximum temperature. According to the research by Alpert [1] on the maximum temperature of smoke under an open ceiling, the maximum temperature of the smoke induced by a single fire ceiling jet was proportional to the 2/3 power of the heat release rate of the fire source and inversely proportional to the 5/3 power of the distance from the surface of the fire source to the ceiling, as shown in Eq. (2).

$$\Delta T_{\max} \propto \frac{\dot{Q}^{2/3}}{H_{ef}^{5/3}} \tag{2}$$

The maximum smoke temperature for double tunnel fires drops with increasing fire separation and gradually drops with increasing fire source size. This article investigates the highest smoke temperature under weak plume conditions based on Alpert's

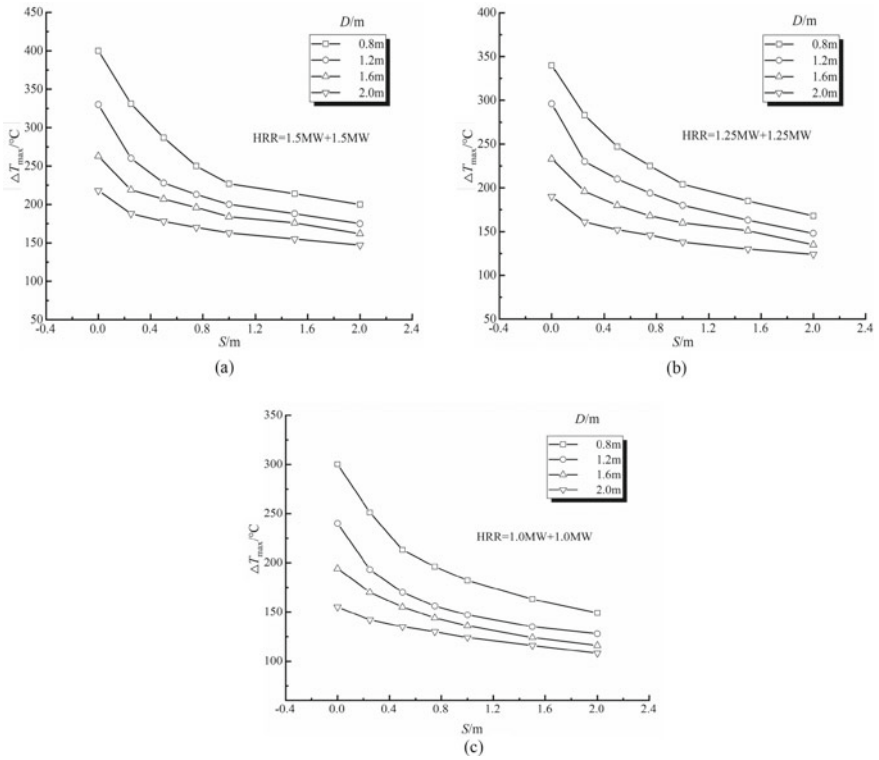

Fig. 4 Variation of maximum temperature rise with fire spacing for fire sources of different sizes

research on the maximum ceiling temperature. The maximum smoke temperature for fire sources of four different sizes is correlated using Eq. (2), and the results of the fitting are displayed in Fig. 5.

The expressions related to the maximum temperature of the smoke for four different fire sizes are given in Fig. 5, and based on the equations in Fig. 5, an expression for the maximum temperature for different fire sizes was established in the following Eq. (3).

$$\Delta T_{\max} = k \frac{\dot{Q}^{2/3}}{H_{ef}^{5/3}} \tag{3}$$

As can be seen in Fig. 5, the coefficient k is related to the fire source spacing and fire source size. The expression for the relationship between k and fire source size and fire source spacing is established from the fitting results as shown below:

$$k = \alpha e^{(-0.88S)} + 9.21 \tag{4}$$

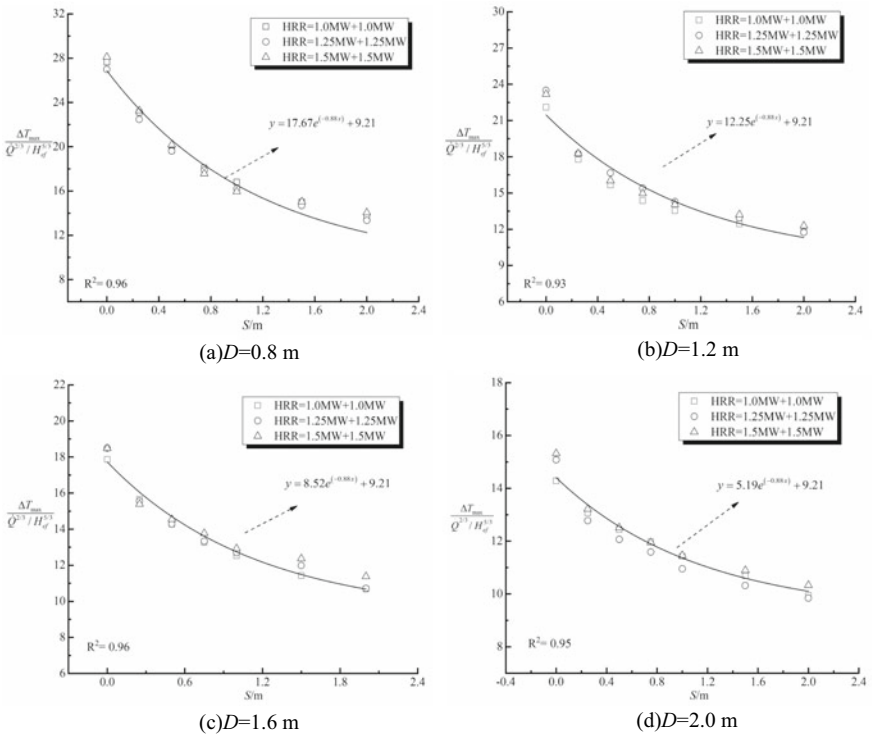

Fig. 5 Correlation of maximum temperature rise with fire spacing and fire size

Combined with Fig. 5 and the expression for the coefficient k, the value of the coefficient α decreases as the fire source size increases. Figure 6 illustrates the correlation between the coefficient α and the size of the fire source, as seen by Eq. (5) below.

$$\alpha = -10.29D + 25.31 \tag{5}$$

Substituting Eqs. (4) and (5) into Eq. (3), the maximum temperature for fires of different sizes at different spacings can be expressed by Eq. (6):

$$\frac{\Delta T_{\max}}{\dot{Q}^{2/3}/H_{ef}^{5/3}} = (25.31 - 10.29D)e^{-0.88S} + 9.21 \tag{6}$$

Therefore, the maximum temperature for fires in different sizes and at different fire spacings can be expressed as follows:

$$\Delta T_{\max} = \left[(25.31 - 10.29D)e^{-0.88S} + 9.21\right]\dot{Q}^{2/3}/H_{ef}^{5/3} \tag{7}$$

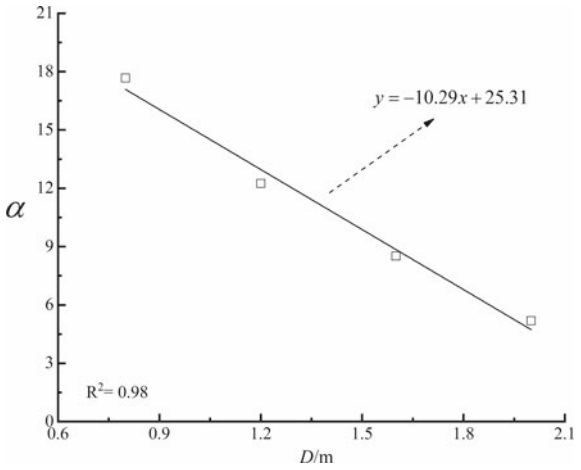

Fig. 6 Correlation of the coefficient α for fire sources of different sizes

As illustrated in Fig. 7, the numerical simulation results of the maximum temperature are compared to the highest temperature predicted by Eq. (7). According to the research results, the prediction model created in this article is able of accurately predicting the highest temperature for two fires with various sizes.

This article assumes a fire scenario when two vehicles collide at the tunnel longitudinal centerline. The model may not be applicable when the lateral position of the fire source changes. In addition, only the two-source fire scenario is considered in this paper, and further expansion of the fire will consider a multiple-source fire scenario. In future work, the effect of the number and location of fire sources on the maximum ceiling temperature could be considered.

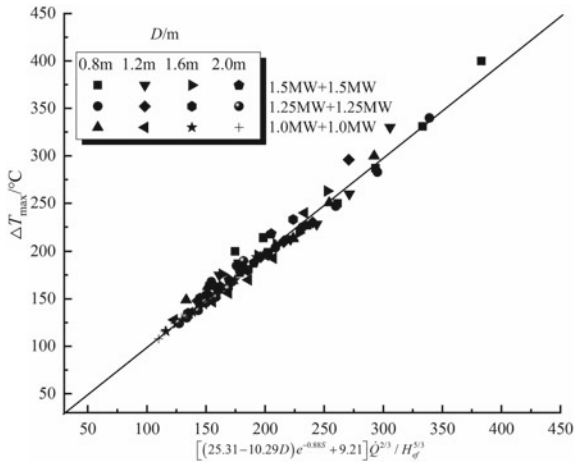

Fig. 7 Comparison between model predictions and results from numerical simulation (Eq. (7))

4 Conclusions

Studying the highest temperature of double fires is crucial for the safety and design of tunnels. This study uses numerical simulations to investigate the impact of fire source sizes on the highest smoke temperature for double tunnel fires. The study takes into account various fire source heat release rates, different fire source sizes, and different fire source separation distances. These are the primary conclusions:

(1) The maximum temperature gradually drops with increasing fire source size and decreases with increasing fire source separation while the fire source heat release rates are fixed.
(2) Combined with previous research on maximum ceiling temperatures, a maximum temperature rise prediction model considering the fire source heat release rates, fire source sizes, and fire source separation distances was established. Furthermore, when compared with the prediction model, the study's results revealed a strong correlation. This study is of great significance for the parameter setting of temperature alarms in tunnels and the evacuation of personnel.

Acknowledgements This research was funded by the National Natural Science Foundation of China (Grant No. 51974175).

References

1. Alpert R (1972) Calculation of response time of ceiling-mounted fire detectors. J Fire Technol 8:181–195
2. Kurioka H, Oka Y, Satoh H et al (2003) Fire properties in near field of square fire source with longitudinal ventilation in tunnels. J Fire Saf J 38:319–340
3. Hu L, Chen L, Wu L et al (2013) An experimental investigation and correlation on buoyant gas temperature below ceiling in a slopping tunnel fire. J Appl Therm Eng 51:246–254
4. Li Y, Lei B, Ingason H (2011) The maximum temperature of buoyancy-driven smoke flow beneath the ceiling in tunnel fires. J Fire Saf J 46:204–210
5. Jiang Y, Li L, Liao S et al (2015) Full scale tests on maximum smoke temperature rise in an urban tunnel. J Eng Thermophys 36:2287–2292
6. Wang J (2017) Maximum smoke temperature and gas temperature decay near the tunnel ceiling in sloped tunnel fire. J Build Energy Environ 36:25–29
7. Zhang S, Ma Z, Xu C (2008) Traffic accidents distribution law in freeway tunnel. J Chang'an Univ 4:74–78
8. Guo B, Han L, An C et al (2023) Research status and prospect of safety risk and disaster prevention and evacuation in large highway tunnel. J Water Resour Hydropower Eng 54:327–332
9. Xu H (2020) Experimental and numerical simulation study on combustion characteristics of tunnel fires on the basic of two fire sources interaction. Soochow University, Suzhou
10. Xu C (2023) Study on smoke diffusion law of tunnel double-ignition source fire under longitudinal ventilation. Anhui University of Science and Technology, Huainan

11. Zhou Y, Chen F, Geng Z et al (2021) Experimental study on the characteristics of temperature distribution of two pool fires with different transverse locations in a naturally ventilated tunnel. J Tunn Undergr Space Technol 116:104095
12. Chen R (2021) Study on the characteristics of flame morphology and ceiling temperature in tunnels with dual fire sources. Southwest Jiaotong University, Chengdu
13. Wan H, Xiao Y, Wei S et al (2022) Performance of ceiling jet induced by dual unequal strong plumes in a naturally ventilated tunnel. J Appl Therm Eng 211:118447
14. Liang Y, Liu Q, Xu Z et al (2023) Study on the influence of exhaust vent size on smoke spread characteristics of the lateral smoke exhaust system in underwater tunnels. J Saf Environ 23:748–755
15. CMCT (2014) JTG D70/2-2014 Specifications for design of highway tunnels. China Communication Press, Beijing
16. Mcgrattan K, Mcdermott R, Hostikka S et al (2010) Fire dynamics simulator (version 5) user's guide. NIST Special Publication, Gaithersburg
17. Huang P, Ye S, Xie J et al (2023) Study on the maximum and longitudinal distribution of ceiling gas temperature in a naturally ventilated tunnel: the effect of longitudinal fire location. J Int J Therm Sci 185:108037

Study on Permeability Performance and Prediction Model of Coal Gangue Pervious Concrete

Junwu Xia, Zhichun Zhu, Enlai Xu, and Linli Yu

Abstract To expand the in-situ utilization of coal gangue in mining area and meet the demand of "sponge city", the permeability coefficient, total porosity and effective porosity of coal gangue pervious concrete (CGPC) in different mixtures were deeply explored. The results show that the permeability coefficient of CGPC can reach 1.5 ~ 2 mm/s. In general, the permeability coefficient and porosity of CGPC increase as the aggregate particle size and designed porosity increase. Effective porosity is the key factor affecting the permeability coefficient of CGPC. More importantly, the prediction model of permeability coefficient of CGPC is established based on the mix proportion, providing a theoretical reference for the application of CGPC in pervious pavement of mining areas.

Keywords Coal gangue pervious concrete · Permeability coefficient · Effective porosity · Prediction model

1 Introduction

China is rich in coal resources, a large number of solid waste-coal gangue will be produced in the process of coal mining. About 7 billion tons of coal gangue accumulated in mining areas, resulting in the land occupation, environmental pollution and even geological disasters [1–3]. Thus, the utilization of coal gangue in situ has

J. Xia
Jiangsu Design Institute of Geology for Mineral Resources (Testing Center CNACG), Xuzhou 221006, China

CNACG Key Laboratory of Mineral Resources in Coal Measures, Xuzhou 221006, China

J. Xia · Z. Zhu · L. Yu (✉)
China University of Mining and Technology, Xuzhou 221116, China
e-mail: cumt_yulinli@cumt.edu.cn

E. Xu
Shandong Vocational University of Foreign Affairs, Weihai 264504, China

G. Mei et al. (eds.), *Advanced Construction Technology and Research of Deep-Sea Tunnels*, Lecture Notes in Civil Engineering 490,
https://doi.org/10.1007/978-981-97-2417-8_30

become an urgent issue to be solved. Many studies indicate that the most effective way to use coal gangue is to replace ordinary gravel for the preparation of green concrete [4, 5]. On the other hand, the urbanization of concrete impervious roads leads to the un-recycling of water, causing the urban waterlogging. With the development of the "sponge city" concept, permeable concrete pavement can realize the recycling of water resources [6, 7]. Liu et al. [8] substituted 3%, 6%, 9% and 12% cement with fly ash to prepare pervious concrete, and the results showed that the addition of fly ash reduced the strength of pervious concrete at 28d in the early stage but increased the strength at 150d in the later stage. Tan et al. [9] found that iron tailing can be used as a substitute for coarse aggregate to prepare pervious concrete, and the permeability coefficient is up to 3.2 mm/s. Many scholars have carried out certain research on different types of pervious concrete, including pervious concrete modified fly ash [10], pervious recycled concrete [11], iron tailing pervious concrete [9] and so on, but there is no report on the study of coal gangue pervious concrete (CGPC).

Therefore, this study investigates the variation in the permeability coefficient and porosity of CGPC. More importantly, it delves into the correlation between the permeability coefficient and effective porosity, establishing a prediction model for the permeability coefficient in CGPC based on the mix proportion.

2 Experimental Program

2.1 Materials

The raw materials used for preparing CGPC include coal gangue coarse aggregate, cement, water, and permeable agent. The cement used in the experiment is P.O 52.5 ordinary Portland cement, meeting the Chinese standard GB175-2020. The coal gangue used is from Zhang Shuanglou Coal Mine in Xuzhou, Jiangsu. Its main chemical composition is as shown in Table 1. By crushing and sieving, four particle sizes of coal gangue coarse aggregate (4.75 ~ 9.5mm, 9.5 ~ 16mm, 16 ~ 19mm, 19 ~ 26.5mm) are obtained. The basic physical properties measured according to the Chinese standard GB/T14685-2011, as presented in Table 2. The permeable agent is from Jiangsu Guangda Ecological Engineering Technology Co., Ltd. The water used for the experiment is regular tap water.

Table 1 Chemical components of coal gangue

Chemical component	SiO_2	Al_2O_3	CO_3	Fe_2O_3	K_2O	CaO	Na_2O	MgO	Others
Content (%)	61.69	19.11	5.83	4.16	3.04	2.35	2.28	0.64	0.90

Table 2 Basic physical properties of coal gangue coarse aggregate

Particle size (mm)	Bulk density (kg/m^3)	Apparent density (kg/m^3)	Void ratio (%)	Moisture content (%)	Water absorption ratio (%)	Elongated particle content (%)
4.75 ~ 9.5	1350	2150	37.2	0.6	2.2	7.1
9.5 ~ 16	1470	2660	44.7	1.1	2.0	2.7
16 ~ 19	1440	2210	34.8	0.5	1.8	2.5
19 ~ 26.5	1410	2080	32.2	0.8	1.8	5.6

2.2 Sample Preparation

The influence of three factors aggregate particle size (A), w/c ratio (B), and designed porosity (C) on the permeability performance of CGPC is considered, as shown in Table 3. The mix design for CGPC is calculated by considering the volume of pervious concrete as a combination of raw materials and designed porosity, as shown in Formula (1). Given the designed porosity and the information about the w/c ratio and the closely packed porosity of coarse aggregates, the quantities of each component can be determined by substituting them into the formula:

$$\frac{M_G}{\rho_g}+\frac{M_C}{\rho_c}+\frac{M_W}{\rho_w}+P=1 \tag{1}$$

where M_G, M_C, M_W is the mass of coal gangue coarse aggregate, cement and water per unit volume (kg/m^3), respectively; ρ_g, ρ_c, ρ_w is the apparent density of coarse aggregate, cement and water of coal gangue(kg/m^3), respectively; P is the designed porosity (%). The mass of coarse aggregates per unit volume is determined based on Formula (2):

$$M_G=\alpha\cdot\rho_G \tag{2}$$

where α is the correction factor for the amount of coarse aggregates, a dimensionless parameter, taken as 0.98; ρ_G is the closely packed density of coal gangue coarse aggregates (kg/m^3). The mix designs for each group of CGPC, calculated using Formulas (1) and (2), are shown in Table 3.

The HJW-60 concrete mixer is used to prepare CGPC in the experiment. The sequence is as shown in Fig. 1. Finally, the mixture is poured into the 100 mm × 100 mm × 100 mm mold by three times, inserted into shape, and the top surface is smoothed with a scraper. After 24 h, the specimens were demolded and placed in a standard curing room (at 20 ± 2°C and 95 ± 5% relative humidity) for 28 d. After curing, the basic properties of the specimens were tested.

Table 3 Test design and mix proportion

Group	Aggregate size (mm)	W/C ratio	Designed porosity (%)	Coal gangue coarse aggregate (g)	Cement (g)	Water (ml)	Permeable agent (g)
A1	4.75 ~ 9.5	0.27	20	12,700.80	2991.41	807.68	95.73
A2	9.5 ~ 16	0.27	20	13,829.76	4186.51	1130.36	133.97
A3	16 ~ 19	0.27	20	13,547.52	2615.51	706.19	83.70
A4	19 ~ 26.5	0.27	20	13,265.28	2197.95	593.45	70.33
B1	9.5 ~ 16	0.25	20	13,829.76	4332.74	1083.18	138.65
B2	9.5 ~ 16	0.27	20	13,829.76	4186.51	1130.36	133.97
B3	9.5 ~ 16	0.29	20	13,829.76	4049.82	1174.45	129.59
B4	9.5 ~ 16	0.31	20	13,829.76	3921.78	1215.75	125.50
C1	9.5 ~ 16	0.27	16	13,829.76	4834.52	1305.32	154.70
C2	9.5 ~ 16	0.27	18	13,829.76	4510.51	1217.84	144.34
C3	9.5 ~ 16	0.27	20	13,829.76	4186.51	1130.36	133.97
C4	9.5 ~ 16	0.27	22	13,829.76	3862.50	1042.87	123.60
C5	9.5 ~ 16	0.27	24	13,829.76	3538.49	955.39	113.23

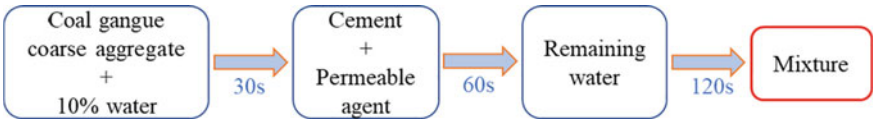

Fig. 1 Preparation process of CGPC

2.3 Test Methods

Permeability coefficient. In accordance with the Chinese standard CJJ/T135-2009, this paper measures the permeability coefficient of CGPC with the fixed water level, as shown in Fig. 2.

First, use Vaseline to smear the side of the test block and wrap it with PVC film to prevent side seepage; Then put the test block into the steel mold, and fill the edge gap with cement; Next, assemble the upper and lower parts of the device into a whole, set up the inlet pipe and outlet, and begin testing the permeability coefficient. During the test, the water head in the container maintains a height of 150 mm. Once the water level stabilizes, measure the water level difference (H) using a steel ruler. Measure the amount of water outflowed in t seconds, and after repeating the measurement three times, take the average value as Q. Then the permeability coefficient of CGPC is calculated as follows:

Fig. 2 Porosity test

$$K_T = \frac{QL}{AHt} \cdot \frac{\eta_T}{\eta_{15}} \tag{3}$$

where KT is the permeability coefficient of pervious concrete specimen at a water temperature of T °C (mm/s); Q is the volume of water seeping out in t seconds (m^3); L is the thickness of the specimen (mm); A is the surface area of the specimen's top surface (mm^2); H is the water level difference (mm); t is the during time (s); ηT and η15 is the temperature T and 15 °C relative viscosity of water, dimensionless parameters. The results are the average value of three identical test blocks.

Porosity. Porosity test refers to the measurement of the total porosity and effective porosity. Referring to the ASTM C1754/C1754M-2012 standard, the volume method was used to determine the total porosity. The testing setup is as shown in Fig. 3.

The testing procedure for total porosity is as follows: (1) Place the test specimen in an oven at 110 ± 5 °C for continuous drying for 24 h. After drying, remove the specimen and weigh its mass, denoted as *A*. (2) Measure and calculate the volume with a steel ruler, denoted as *V*. (3) Using a suspension basket, immerse the test specimen in water, allowing it to float up and down 10 times. Once no more air bubbles emerge, weigh the specimen's mass in water, denoted as *B*. (4) The total porosity ρ can be calculated using the following formula:

$$\rho = 1 - \frac{A - B}{\rho_w \cdot V} \tag{4}$$

The testing procedure for effective porosity is similar to that of the total porosity testing in the initial steps (1) and (2). After drying and measuring the mass and volume, the test specimen is soaked for 48 h to saturate it with water. Then, the specimen is removed and allowed to drain for approximately 2 min. After draining, surface moisture is wiped off, and the mass is measured again, denoted as C.

Fig. 3 Porosity test

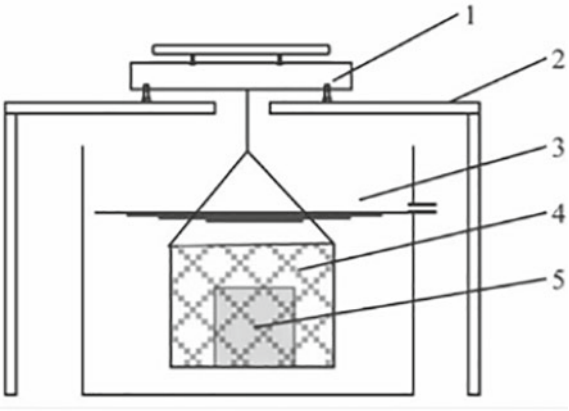

1--Electronic scale 2--Holder

3--Water storage 4--Hanging basket

5--Specimen

To calculate the effective porosity ρ_e, you can substitute these values into the appropriate formula.

$$\rho_{\mathrm{e}} = \rho - \frac{\mathrm{C} - \mathrm{A}}{\rho_{\mathrm{w}} \cdot \mathrm{V}} \tag{5}$$

3 Results and Discussion

3.1 Permeability Coefficient

The permeability coefficient represents the amount of water that passes through within a unit of time. Calculated through permeability tests, the permeability coefficients for various groups are shown in Fig. 4. It can be observed that with an increase in aggregate particle size, the overall trend of CGPC changes from decreasing to increasing. For group A1, even though the 4.75 ~ 9.5 mm aggregate has a higher bulk density, its surface mortar thickness is smaller, and it has more internal porosity, resulting in a permeability coefficient of 1.67 mm/s, slightly higher than the 1.58 mm/s for group A2. In Fig. 4b, within the range of w/c ratios from 0.25 to 0.29, there is not a significant change in the permeability coefficient of CGPC. However, when the w/c ratio increases from 0.29 to 0.31, the permeability coefficient drops rapidly

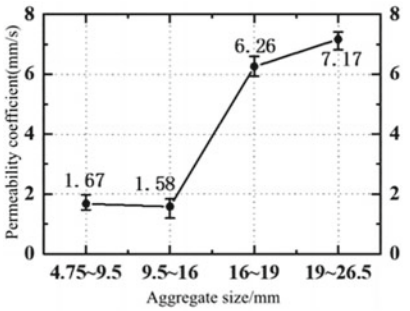

(a) The influence of aggregate size on permeability coefficient.

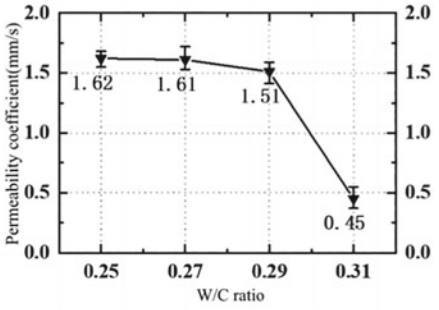

(b) The influence of W/C ratio on permeability coefficient.

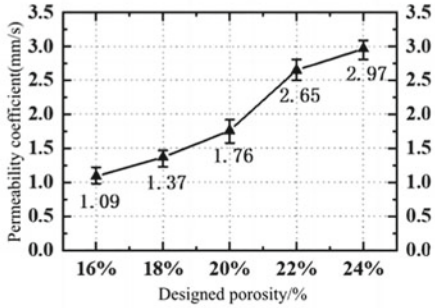

(c) The influence of designed porosity on permeability coefficient.

Fig. 4 Permeability coefficient of CGPC in different groups

from 1.51 mm/s to 0.45 mm/s. The primary reason is that some mortar flows to the bottom, preventing the formation of connected pores and resulting in a decrease in the permeability coefficient. From Fig. 4b, it can be observed that as the designed porosity increases, the permeability coefficient gradually increases. The permeability coefficients of groups C2, C3, C4, and C5 increase by 25.64%, 61.47%, 143.12%, and 172.48% compared to group C1. A higher designed porosity leads to larger internal pores, resulting in a higher permeability coefficient.

3.2 Porosity

The porosity is divided into total and effective porosity, to evaluate the permeability performance of CGPC. The porosity for different aggregate particle sizes, w/c ratios, and designed porosity groups are shown in Fig. 5. The figure illustrates that there is a good correlation between the total porosity and effective porosity. The effective proportion for each group is shown in Table 4. From Fig. 5a, it can be observed that as the aggregate particle size increases, both total porosity and effective

porosity decrease at first and then increase. Table 4 shows that the effective proportion increases gradually with the increase in aggregate particle size, from 47.40% for A1 to 79.80% for A4. Additionally, from Fig. 5b and Table 4, it can be seen that as the w/c ratio increases, both total porosity and effective porosity, along with the effective proportion, generally decrease. When the w/c ratio increases from 0.29 to 0.31, the total porosity decreases by 30.82%, the effective porosity decreases by 82.42%, and the effective proportion rapidly drops from 59.20 to 15.20%. In Fig. 5c, with the designed porosity increases, both the total and effective porosity of CGPC increase, along with the effective proportion.

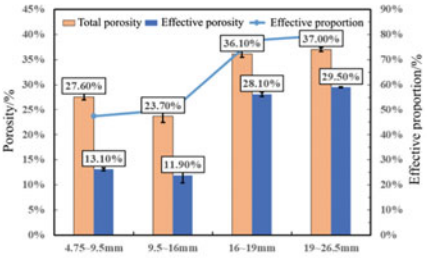

(a) The influence of aggregate size on porosity.

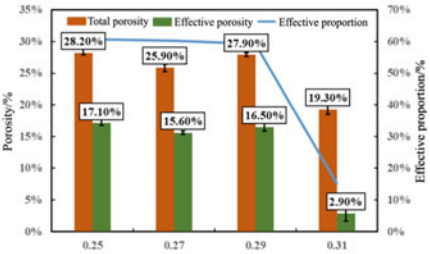

(b) The influence of W/C ratio on porosity.

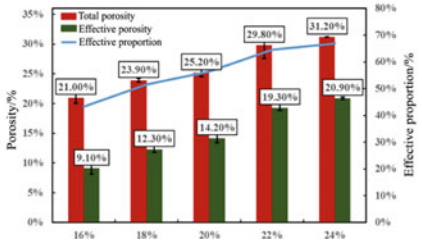

(c) The influence of designed porosity on porosity.

Fig. 5 Porosity of CGPC in different groups

Table 4 Effective pore/total pore ratio of CGPC in different groups

Group	Effective proportion (%)	Group	Effective proportion (%)	Group	Effective proportion (%)
A1	47.40	B1	60.70	C1	43.30
A2	50.10	B2	60.30	C2	51.60
A3	77.70	B3	59.20	C3	56.40
A4	79.80	B4	15.20	C4	64.60
				C5	66.80

3.3 Relationship Between Permeability and Porosity

It is evident that side pores are sealed. Effective pores are the connected pores that enable permeability. Therefore, there is a close relationship between the permeability coefficient and the effective porosity of CGPC. The correlation coefficients between permeability coefficient and porosity under different groups are calculated, as shown in Fig. 6. The figure demonstrates that the change in permeability coefficient and effective porosity for CGPC follows a similar curve, with correlation coefficients R > 0.99.

Additionally, it's observed that there is a clear functional relationship between the permeability coefficient and effective porosity, as shown in Fig. 7. A regression fit is used to establish the relationship between the permeability coefficient of CGPC and the effective porosity:

$$K = 0.3977e^{9.6789\rho_e} \tag{6}$$

where K is the permeability coefficient of CGPC (mm/s); ρ_e is the effective porosity (%). As shown in Fig. 7, the test data points are distributed on both sides near the

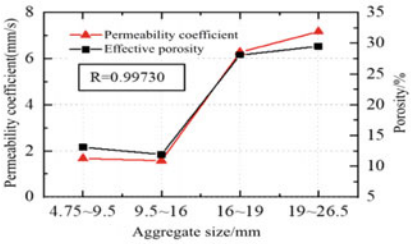

(a) Correlation between permeability coefficient and effective porosity among different aggregate sizes.

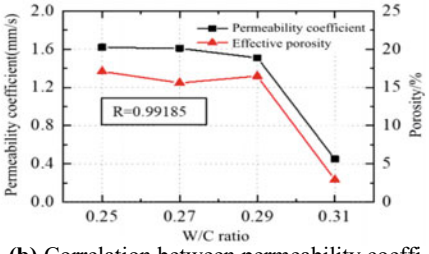

(b) Correlation between permeability coefficient and effective porosity among different W/C ratio.

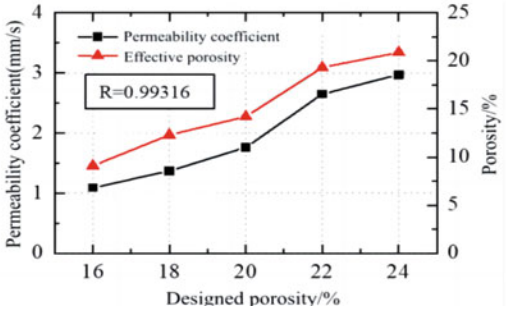

(c) Correlation between permeability coefficient and effective porosity among different designed porosity.

Fig. 6 Correlation between permeability coefficient and effective porosity

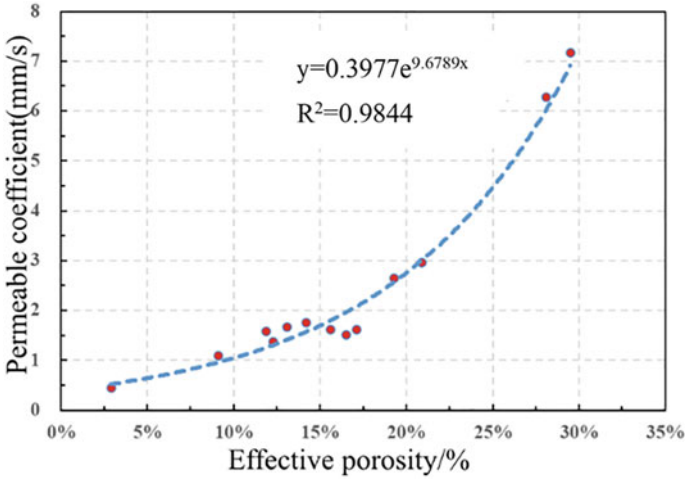

Fig. 7 Regression curve of effective porosity and permeability coefficient

fitting curve, and the correlation coefficient R^2 is 0.9844, indicating a good fitting effect.

4 Prediction Model of CGPC

From the previous analysis, it is clear that the permeability coefficient of coal gangue concrete is closely related to aggregate particle size, w/c ratio, and designed porosity. Therefore, to better guide real-world projects, this study takes 9.5-16mm coal gangue coarse aggregate as a reference and uses the w/c ratio, and designed porosity as independent variables to establish a model for the permeability coefficient. The experimental data is subjected to binary surface fitting. The formula takes the form:

$$K = ax_1 + bx_2 + cx_1^2 + dx_2^2 + ex_1x_2 + f \tag{7}$$

where K is the permeability coefficient; x_1, x_2 is the w/c ratio and designed porosity, respectively; a, b, c, d, e, f is the coefficients to be determined. The values for these coefficients, obtained through data fitting, are shown in Table 5, resulting in the formula:

$$\begin{aligned} K = {} & 144.90538x_1 - 221.60461x_2 - 435.22126x_1^2 \\ & +315.45521x_2^2 + 445.62063x_1x_2 + 1.90161 \end{aligned} \tag{8}$$

The correlation of each parameter is close to 1, indicating a good correlation. As shown in Fig. 8, the predictive model aligns well with the experimental results. The

Table 5 Binary nonlinear fitting coefficient of permeability coefficient

Coefficient	Value	Standard error	t	Probability > |t|	Correlation
a	144.90538	65.91388	2.1984	0.05914	0.99999
b	−221.60461	68.97046	−3.21304	0.01237	0.99997
c	−435.22126	141.6571	−3.07236	0.01529	0.99996
d	315.45521	108.83438	2.89849	0.01994	0.99975
e	445.62063	291.21876	1.53019	0.1645	0.99998
f	1.90161	13.02013	0.14605	0.88749	0.99997

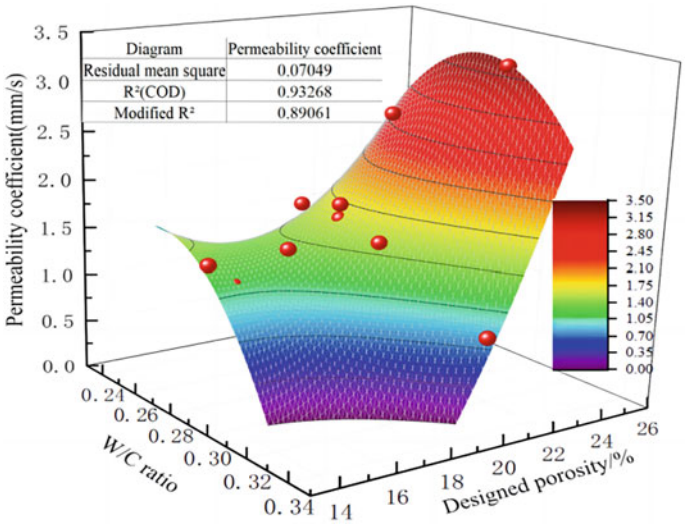

Fig. 8 Regression curve of effective porosity and permeability coefficient

permeability coefficient prediction model for CGPC holds significant importance for its application.

5 Conclusion

(1) The permeability coefficient of CGPC can meet the requirements of 1.5 ~ 2 mm/s. With the increase of aggregate particle size and designed porosity, the permeability coefficient generally shows an upward trend, improving the permeability performance.

(2) There is a positive correlation between the total porosity and the effective porosity of CGPC. In general, the larger the aggregate particle size and designed porosity, the larger the total porosity and effective porosity, and the larger the effective proportion of CGPC.
(3) Effective porosity is the key factor affecting the permeability coefficient of CGPC. The relationship between the permeability coefficient and effective porosity of CGPC is obtained.
(4) The prediction model of permeability coefficient of CGPC is established, in good agreement with the experimental results.

Acknowledgements This study was supported by the National Natural Science Foundation of China (No. 52074270) and the CNACG Key Laboratory of Mineral Resource in Coal Measures (No. KFKT-2020-4).

References

1. Caneda-Martínez L, Sánchez J, Medina C, Isabel Sánchez De Rojas M, Torres J, Frías M (2019) Reuse of coal mining waste to lengthen the service life of cementitious matrices. Cem Concr Compos 99:72–79
2. Li J, Wang J (2019) Comprehensive utilization and environmental risks of coal gangue: a review. J Clean Prod 239:117946
3. Hao Y, Guo X, Yao X, Han R, Li L, Zhang M (2022) Using Chinese coal gangue as an ecological aggregate and its modification: a review. Materials 15(13):4495
4. Yu L, Xia J, Xia Z, Chen M, Wang J, Zhang Y (2022) Study on the mechanical behavior and micro-mechanism of concrete with coal gangue fine and coarse aggregate. Constr Build Mater 338:127626
5. Gao S, Zhang S, Guo L (2021) Application of coal gangue as a coarse aggregate in green concrete production: a review. Materials 14(22):6803
6. Zhou J, Zheng M, Zhan Q, Zhou R, Zhang Y, Wang Y (2023) Study on mesostructure and stress–strain characteristics of pervious concrete with different aggregate sizes. Constr Build Mater 397:132322
7. Cai J, Liu Z, Xu G, Tian Q, Shen W, Li B et al (2022) Mix design methods for pervious concrete based on the mesostructure: progress, existing problems and recommendation for future improvement. Case Stud Constr Mater 17:e1253
8. Liu H, Luo G, Wang L, Gong Y (2019) Strength time-varying and freeze-thaw durability of sustainable pervious concrete pavement material containing waste fly ash. Sustain Basel 11(1):176
9. Tan Y, Zhu Y, Xiao H (2020) Evaluation of the hydraulic, physical, and mechanical properties of pervious concrete using iron tailings as coarse aggregates. Appl Sci 10(8):2691
10. Kamisetty A, Gandhi ISR, Kumar A (2023) Combined effect of fly ash and fiber on spreadability, strength and water permeability of foam concrete. J Build Eng 78:107607
11. Mitrosz O, Kurpińska M, Miśkiewicz M, Brzozowski T, Abdelgader HS (2023) Influence of the addition of recycled aggregates and polymer fibers on the properties of pervious concrete. Materials 16(15):5222

Experimental Study on the Influence of Erosive Solution on Unconfined Compressive Strength of Fiber Reinforced Cemented Soil

Lina Xu, Tatenda Kelvin Gomba, Lei Niu, and Daohan Song

Abstract Many erosive environments, such as acidic or various salts, can cause damage to structures like roads, tunnels, and buildings. Various tests were conducted to investigate how the strength of cemented soil is affected by different soaking periods, types of saline solutions, and fibers. Samples including and excluding basalt fibers were tested in water, acid, and salt solutions for 1, 8, 19, 39, and 54 days. The results show that the strength of cemented soil soaked in clear water gradually increases with the increase of maintenance days, which is the development law of strength of cemented soil. As the soaking time increases, the unconfined compressive strength of soil samples soaked in acidic and salt environments gradually decreases. The addition of fiber to cemented soil slightly increases its strength compared to soil without fiber in the same solution concentration. This suggests that fiber has a distinct role in protecting cemented soil from erosion caused by erosive solutions.

Keywords Soaking time · Cemented soil · Basalt fiber · Erosive solution

1 Introduction

Enhancing the durability and efficiency of the sub-grade soil is attainable through the stabilization process. This has been proven to be a highly successful approach in achieving this goal. Given the unfavorable characteristics of soils, geotechnical engineers are constantly researching various methods that are cost-effective and meet the bearing capacity to stabilize such soils. Two methods, mainly mechanical and chemical, are usually adopted by geotechnical engineers to improve the stability of the soil.

L. Xu
School of Transportation Science and Engineering, Jilin Jianzhu University, Changchun, Jilin, China
e-mail: xulina@jlju.edu.cn

T. K. Gomba · L. Niu (✉) · D. Song
School of Civil Engineering, Jilin Jianzhu University, Changchun, Jilin, China
e-mail: niulei2016@163.com

G. Mei et al. (eds.), *Advanced Construction Technology and Research of Deep-Sea Tunnels*, Lecture Notes in Civil Engineering 490,
https://doi.org/10.1007/978-981-97-2417-8_31

Relevant research on fibers and improved stability of soils include the following: Shao et al. [1] investigated the cement soil's strength properties in saliferous and acidic-alkalescent environments and achieved precise outcomes. Liu et al. [2] experimented with the effects of corrosion on cemented soil's mechanical properties.. Chen et al. [3] examined the impact of sodium sulfate solution on the shear strength of cemented soil. Zhang and Li [4] researched the effects of salt lake solution on the strength of expansive soils. Hui et al. [5] experimented to study the compressive strength of basalt Clay soil reinforced with fiber. Chen et al. [6] analyzed the influence of fiber length and content on the durability of granite residual soil when reinforced with glass fiber and basalt fiber. Through my research, I have analyzed the influence of fiber length and content on the durability of granite residual soil when reinforced with glass fiber and basalt fiber. Lee et al. [7] examined the Macroscopic Bonding Principles and Microscopic Bonding Methods of Glass Fiber-Modified Loess. Ding et al. [8] conducted research on how the mechanical properties of cement-stabilized clay and polypropylene fiber are affected by freeze–thaw cycles.. In all the above-mentioned papers, it is shown that fibers increase the strength of soil significantly.

Using cement and lime to stabilize soil is a standard method that dramatically improves soil properties rapidly and significantly by reducing plasticity and eliminating swelling in soil [9, 10]. Because of their economic benefits, some researchers have used recycled basanite and coal ash as binders to stabilize expansive soil. However, the use of such materials is questionable due to their sustainability. Pore solution concentration, ion type, and pH value highly affect shrink-swell soil strength. Changes in pore solution result in macroscopic and mechanical properties. Soil strength improvement has been shown to combat these changes effectively. The mechanism of the effects of the type of solute and concentration in the pore water of expansive soil on the physical and mechanical properties of soil [11]. Therefore, it requires urgent investigation, considering potential geotechnical engineering issues such as geological hazards and soil slope stability.

This study investigated how saline solution and hydrochloric acid (HCL) affected the engineering characteristics of fiber-reinforced cement soil. To achieve this objective, cemented soil with basalt fiber and without fiber were soaked in different concentrations of salt and HCL solution (0.1, 0.3, and 0.5 mol/L) under different soaking times. An analysis was conducted on the impact of soaking time, fiber, solution type, and concentrations on the compressive strength of soil blocks.

2 Materials and Method

2.1 Materials

For this project, the soil that was tested had been gathered from a construction site located in Jilin Province's Changchun City, which is situated in China. The liquid and plastic-limited water content of the soil is 41% and 25%, respectively. Basalt

Fig. 1 Specimens cured in water

fiber is used to reinforce the soil samples. The cement utilized is Ordinary Portland Cement with a rating of P.O. 42.5.

2.2 Preparation of Specimen

A cube test block measuring 70.7 mm × 70.7 mm × 70.7 mm was prepared according to the specifications of the 'Cement Soil Mix Design Specification' (JGJ/T 233–201). The block was mixed manually, loaded into a mold, and vibrated before being cured naturally for 1 day. It was then watered and covered with plastic film for 3 days before mold removal. The specimens were submerged in room temperature water for 28 days, as depicted in Fig. 1.

2.3 Test Design

Na_2SO_4 and HCl solutions with 0.1, 0.3 and 0.5 mol/L concentrations were prepared, respectively. The prepared test blocks were put into the prepared solution and soaked for 1, 8, 19, 39, 54, and 60 days, respectively. The unconfined compressive strength of cemented soil was then tested. The test scheme is shown in Table 1.

Table 1 Test scheme

Fiber	Water	HCl or Na_2SO_4 solutions (mol/L)		
		0.1	0.3	0.5
1 (With fiber) (days)	1, 8, 19, 39, 54 and 60	1, 8, 19, 39, 54 and 60	1, 8, 19, 39, 54 and 60	1, 8, 19, 39, 54 and 60
0 (Without fiber) (days)	1, 8, 19, 39, 54 and 60	1, 8, 19, 39, 54 and 60	1, 8, 19, 39, 54 and 60	1, 8, 19, 39, 54 and 60

3 Results and Discussion

3.1 The Effect of Soaking Time on Compressive Strength.

Figure 2 displays the results of measuring the compressive strength of soil that was soaked in distilled water. Two types of soil were tested: one with fiber and one without.

The gradual increase of maintenance days is observed to have a positive impact on the unconfined compressive strength of test blocks soaked in clear water, as illustrated in Fig. 2. This is in line with the typical development law of cemented soil strength. The presence or absence of fiber in the cemented soil does not seem to have much effect on its strength.

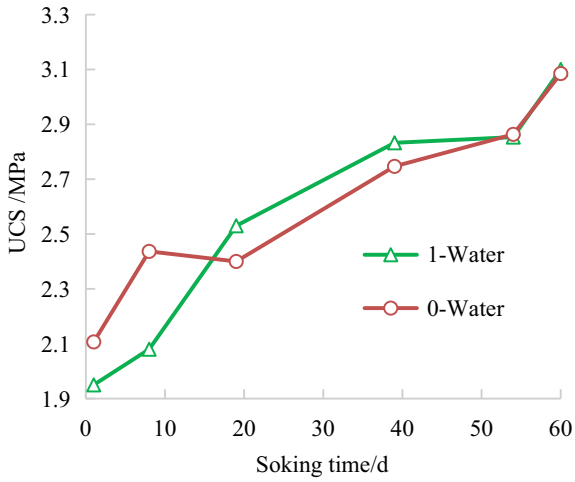

Fig. 2 The relationship between compressive strength and soaking time of blocks in water

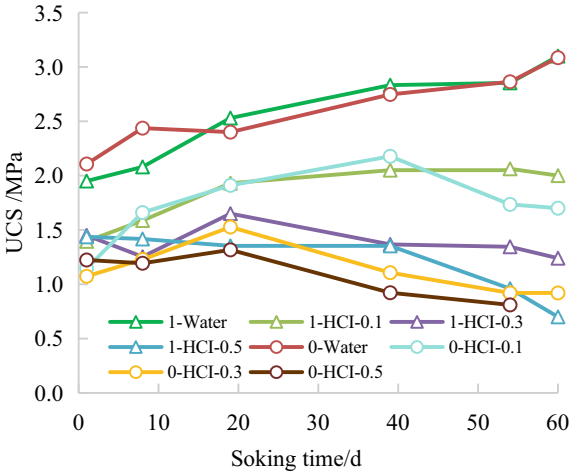

Fig. 3 The correlation between the compressive strength of cemented soil and the number of days it is soaked in an acidic environment (HCI)

3.2 The Impact of HCL on the Strength of Materials Under Unconfined Compression.

Figure 3 shows the strength curves of test blocks soaked in HCl solution at concentrations of 0.1, 0.3, and 0.5 mol/L for 1 day, 8 days, 19 days, 39 days, 54 days and 60 days, respectively.

The compressive strength of test blocks soaked in acid is significantly lower than that of clear water. The strength of the samples submerged in an acidic environment declined as the duration of submersion increased. In the same concentration of the solution, the strength of cemented soil with fiber added is slightly higher than that without fiber, indicating that fiber plays a specific role in the resistance of cemented soil to acid solution erosion. Figure 4 shows the relationship between the stress and strain of cemented soil in HCL solutions.

3.3 Influence of Salt on the Compressive Strength

The concentration of Na_2SO_4 solution is depicted in the strength curves of the samples shown in Fig. 5. 0.1, 0.3, and 0.5 mol/L for 1 d, 8 d, 19 d, 39 d, 54 d, and 60 d, respectively. With the increase in soaking days, the strength of the samples showed a downward trend. With the increase of salt concentration, the unconfined compressive strength of basalt fiber cemented soil gradually decreases, especially at the concentration of 0.5 mol/L, the cemented soil with fiber added experienced 39 days, while the soil–cement without fiber added experienced only 19 days, and the failure occurred, as illustrated in Fig. 6.

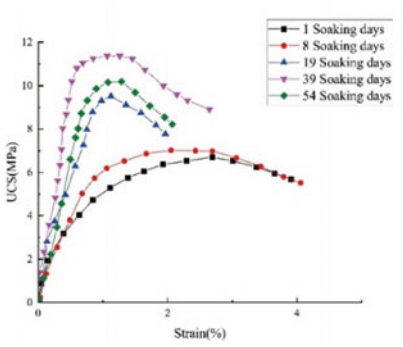

(a) 0-HCL-0.1

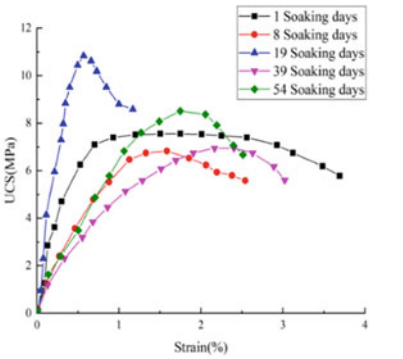

(d) 1-HCL-0.3

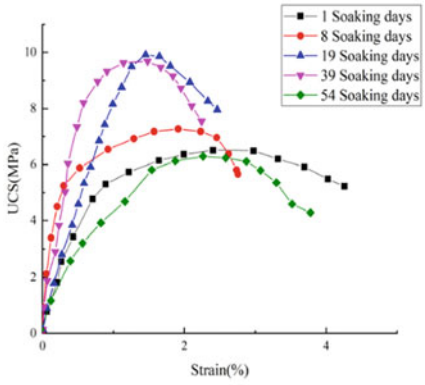

(b)1-HCL-0.1

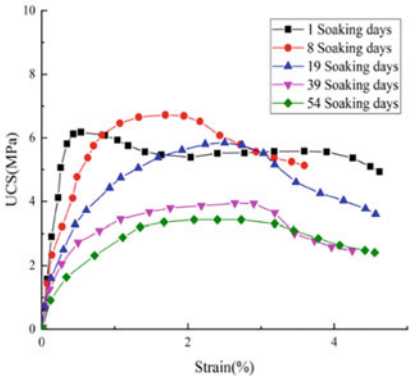

(e) 0-HCL-0.5

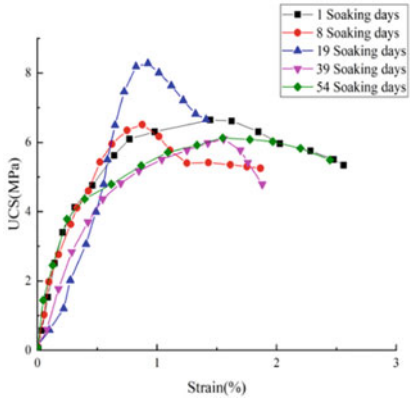

(c) 0-HCL-0.3

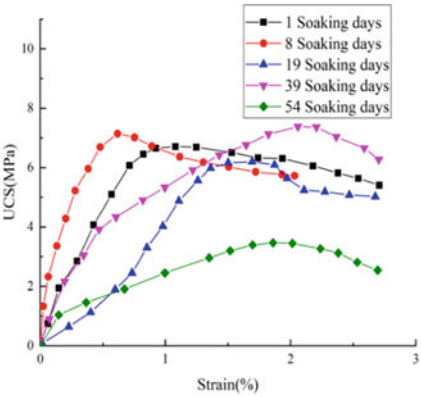

(f) 1-HCL-0.5

Fig. 4 Stress–strain curve

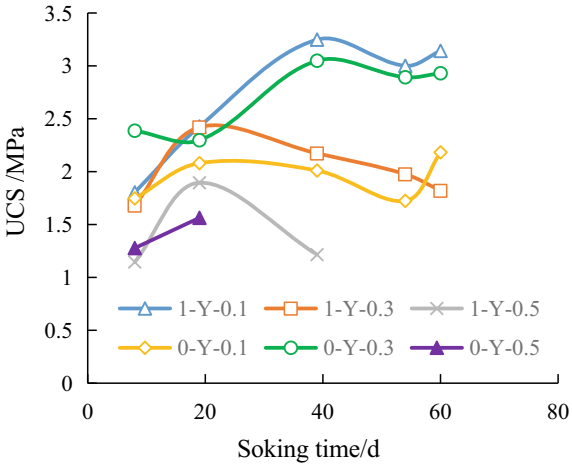

Fig. 5 Relationship between unconfined compressive strength of basalt fiber reinforced cemented soil and soaking days in saline environment

Fig. 6 Test block after soaking

4 Conclusion

Different soaking time cycles and unconfined compression tests were performed on basalt fiber-stabilized cemented clayey soil, and the effects of different soaking times on stress–strain behaviors and unconfined compressive strength were analyzed and discussed. The main findings of this study can be summarized as follows:

(1) It can be concluded that samples soaked in water retained most of their properties and strength, the longer the samples were soaked, the weaker they became.
(2) The unconfined compressive strength of the test blocks soaked in acidic environment gradually decreases with the increase of soaking time, and the strength of cemented soil with fiber is slightly higher than that without fiber in the same

concentration of the solution, indicating that fiber plays a specific role in the resistance of cemented soil to acid solution erosion.

(3) With the increase of salt concentration, the strength of basalt when subjected to compression without confinement. Fiber-reinforced cemented soil gradually decreases, especially at the concentration of 0.5 mol/L, the fiber-reinforced cemented soil experienced 39 days, while the reinforced cemented soil experienced only 19 days.

(4) The incorporation of basalt fiber in clay soil has been found to be a highly effective method of enhancing the compressive strength of the soil. (UCS).

Acknowledgements This study received funding from the Jilin Provincial Department of Science and Technology, with grant number 20220203063SF".

References

1. Shao GH, Yang WM (2007) Strength characteristics of cement soil in saliferous and acidic-alkalescent environments. J Nanjing For Univ 132(06):73–76
2. Liu QS, Qu JW, Liu ZP, He J (2014) Experimental studies of mechanical properties of cemented soil under corrosion influence. J Rock Soil Mech 35(12):3377–3384
3. Chen SL, Zhang JY, Ning BK, Yang YL, Wei X, Wu YH (2015) Experimental study of sodium sulfate solution effect on the shear strength of cemented soil. J Adv Sci Technol Water Resour 35(06):82–85
4. Zhang SW, Li DD (2022) The effects of salt-lake salt solution on the strength of expansive soils. J Geofluids 2022
5. Hu GH, Xu N, Fu JY, Xiang C, Yang C (2015) Experimental study on the unconfined compressive strength of basalt fiber-reinforced clay soil. J Adv Mater Sci Eng 2015
6. Chen WJ, Zhao J, Fan LT, Li J, Yuan BX (2022) The effect of length and content of fiber on glass fiber and basalt fiber-reinforced granite residual soil. J Adv Civil Eng 2022
7. Li L, Ye WJ, Bai Y, Wu YT (2022) Macroscopic mechanical properties and microscopic bonding mechanisms of glass fiber-modified loess. J Adv Mater Sci Eng 2022
8. Ding MT, Zhang F, Ling XZ, Bo L (2018) Effffects of freeze-thaw cycles on mechanical properties of polypropylene fiber and cement stabilized clay. J Cold Reg Sci Technol 154:155–165
9. Aldaood A, Bouasker M, Almukhtar M (2014) Impact of freeze–thaw cycles on mechanical behaviour of lime stabilized gypseous soils. J Cold Reg Sci Technol 99:38–45
10. Xu LN, Ding X, Sun S, Gu H, Niu L, Chen Y (2023) Experimental study on the influence of Snow-melting agents on the fiber-reinforced cemented soil under freezing-thawing cycles. J Adv Mater Sci Eng 2022
11. Huang W, Wang SJ, Cheng MS (2018) Effect of dry wet cycle on cement modified expansive soil under erosion environment. J Bull Chin Ceram Soc 37(2):649–659

Experimental Research on Dry Shrinkage Property of High Performance Concrete

Tao Ge and Han Wu

Abstract In order to reveal the durability of high-performance concrete in underground engineering, 10 different mix ratios of dry shrinkage tests were conducted on high-performance concrete used in an underground civil air defense project. After three days' age, we dismantle the mold and measure the base length. And then, make test-pieces stay in water at 20 ± 3 °C to test the first, seventh and fourteenth day's length. After that, we move the test-pieces in the drying chamber to measure the twenty-eighth and ninetieth day's length. We reach the impact of every aggregate dosage on concrete's expansion and shrinkage rate. And we analysis high performance concrete's crack resistance. At last, we reach the best mix proportion in the construction and dry shrinkage property, and summarize some necessary measures to prevent or reduce concrete shrinkage cracks.

Keywords High performance concrete · Dry shrinkage test · Crack resistance

1 Introduction

The application of high-performance concrete in modern large and medium-sized engineering is very extensive. Professor Wu Zhongwei's definition of High performance concrete (HPC) is a new type of high-tech concrete, which is made using modern concrete technology on the basis of significantly improving the performance of ordinary concrete. It is designed with durability as the main indicator and focuses on durability, construction, applicability, strength Key guarantees for volume stability and economy [1]. One of the important indicator in the high performance concrete's durability is dry shrinkage (expansion) and crack resistance, which is particularly important in the underground engineering like civil air defense engineering and subway engineering. And domestic scholars have also conducted extensive research

T. Ge (✉) · H. Wu
Aeronautics Engineering CollegeAir Force Engineering University, Xi'an 710038, China
e-mail: getaoge@163.com

G. Mei et al. (eds.), *Advanced Construction Technology and Research of Deep-Sea Tunnels*, Lecture Notes in Civil Engineering 490,
https://doi.org/10.1007/978-981-97-2417-8_32

on related content in these years [2–6]. This article attempts to draw meaningful conclusions through experiments.

2 Dry Shrinkage Test

The concrete's dry shrinkage is related to its component, which mainly includes cement, fly ash, slag and water-cement ratio. Twelve different mix proportions' HPC specimens are designed and the raw materials for each cubic meter of concrete are shown in the Table 1. The A100 is the reference concrete and the A110 is a reference concrete which adds HLC anti crack and anti-seepage agent. The test is mainly about ten mix proportion HPC from A111 to A136.From the first table, we can get twelve types mix proportion HPC which is the Table 2.

When we determine C30 pumping concrete water cement ratio and the influence of raw materials such as cement, sand and gravel, and additives on the work ability and mechanical properties of concrete, we use ordinary silicon 32.5 cement, first grade ash, slag powder, river sand and crushed stone HLC anti crack and anti-seepage agent to test C30 pumping concrete's comprehensive performance such as work ability, physical and mechanical properties, volume stability and durability. We use that to determine the optimal mix ratio of concrete and ensure the service life of civil air defence engineering concrete exceed a hundred years.

The comprehensive performance test of C30 high-performance pumped concrete shows the concrete mix ratio in Table 1.

In the table, the A100 is the reference concrete and it's water-cement ratio is 0.43; the A110 is reference concrete which add HLC anti crack and anti-seepage agent, and

Table 1 C30 HPC mix ratio

Number	Amount of raw materials used per cubic meter of concrete(kg/m^3)							
	Cement	Fly ash	Slag	Sand	Fine crushed stone	Small gravel	Water	HLC
A100	368	–	–	764	632	516	158	–
A110	334	–	–	747	591	484	156	29
A111	266	114		718	592	484	157	33
A112	229	152	–	700	579	473	157	33
A121	214	–	164	713	588	482	156	33
A122	132	–	246	708	584	480	156	33
A131	215	62	103	721	595	488	157	33
A132	190	76	114	708	584	478	156	33
A133	154	115	115	714	590	482	158	33
A134	153	77	153	716	591	484	158	33
A135	116	116	154	706	583	477	159	33
A136	116	77	193	713	588	482	159	33

Table 2 The test result of C30 high-performance pumped concrete

Number	Concrete expansion, shrinkage rate(%)				
	Stay in water 1d	Stay in water 7d	Stay in water 14d	Stay in air 28d	Stay in air 90d
A100	0.0005	−0.0003	−0.0004	−0.0133	−0.0197
A110	0.0009	0.0058	0.0063	−0.0082	−0.0217
A111	0.0256	0.0336	0.0332	0.0186	0.0076
A112	0.0069	0.0130	0.0154	−0.0001	−0.0124
A121	0.0136	0.0151	0.0136	−0.0008	−0.0106
A122	0.0324	0.0349	0.0363	0.0214	0.0111
A131	0.0161	0.0203	0.0175	0.0028	−0.0115
A132	0.0269	0.0331	0.0350	0.0234	0.0117
A133	0.0278	0.0363	0.0358	0.0236	0.0133
A134	0.0217	0.0305	0.0324	0.0175	0.0033
A135	0.0324	0.0463	0.0469	0.0382	0.0272
A136	0.0335	0.0573	0.0580	0.0499	0.0382

it's ware-cement ratio is 0.43; A111 is a concrete with a single addition of 28% fly ash and the ware-cement ratio of it is 0.38; A112 is a concrete with a single addition of 37% fly ash and the ware-cement ratio of it is 0.38; A121 is a concrete with a single addition of 40% slag powder and the ware-cement ratio of it is 0.38; A122 is a concrete with a single addition of 60% slag powder and the ware-cement ratio of it is 0.38; A131 is a double mixed concrete with 15% fly ash and 25% slag micro powder and the ware-cement ratio of it is 0.38; A132 is a double mixed concrete with 18% fly ash and 28% slag micro powder and the ware-cement ratio of it is 0.38; A133 is a double mixed concrete with 28% fly ash and 28% slag micro powder and the ware-cement ratio of it is 0.38; A134 is a double mixed concrete with 18% fly ash and 37% slag micro powder and the ware-cement ratio of it is 0.38; A135 is a double mixed concrete with 28% fly ash and 37% slag micro powder and the ware-cement ratio of it is 0.38; A136 is a double mixed concrete with 18% fly ash and 46% slag micro powder and the ware-cement ratio of it is 0.38.

3 Concrete Shrinkage Test

Dry shrinkage (expansion) test of C30 high-performance pumped concrete refer to the "Highway Civil Testing Regulations" (JTGE40-2007) for testing. After three days' age, we dismantle the mold and measure the base length. And then, make test-pieces stay in water at 20 ± 3 °C to test the first, seventh and fourteenth day's length. After that, we move the test-pieces in the drying chamber to measure the twenty-eighth and ninetieth day's length.

The detection results are shown in Table 2, and the analysis of the result is shown in Figs. 1,2 and 3.

From the experimental results, it can be seen that after adding HLC anti crack and anti-seepage agent, strengthening wet curing can slow down the occurrence of early shrinkage cracking in concrete. But the shrinkage rate of concrete is still relatively high, which is comparable to the concrete specimens. Without HLC anti crack and anti-seepage agent.

From Fig. 1, it can be seen that after adding high-quality fly ash to replace some cement in the concrete, the early expansion rate of the concrete increases, and the corresponding dry shrinkage rate of the concrete decreases, but the decrease rate of

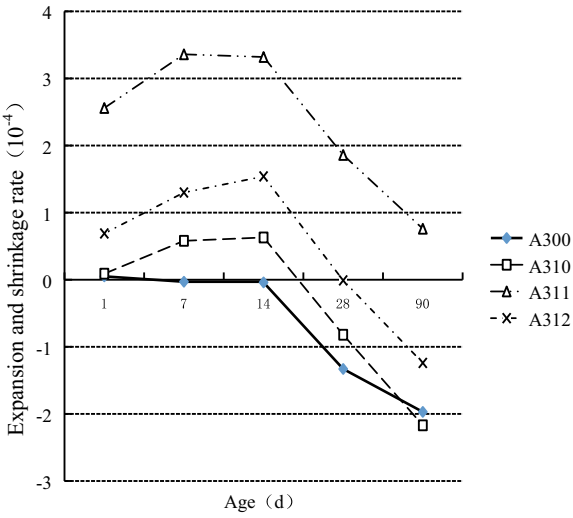

Fig. 1 The influence of fly ash content on the expansion and dry shrinkage rate of concrete

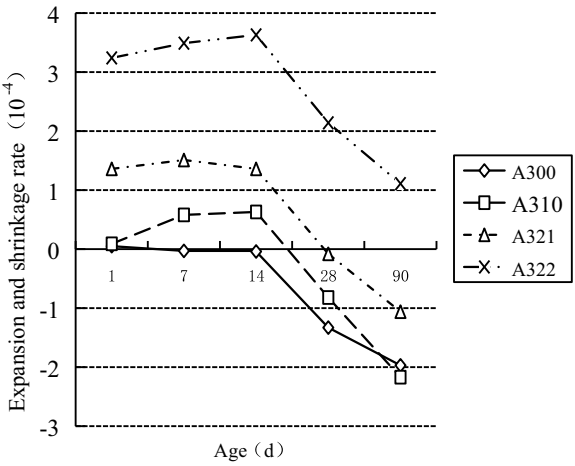

Fig. 2 Effect of slag content on concrete expansion and shrinkage rate

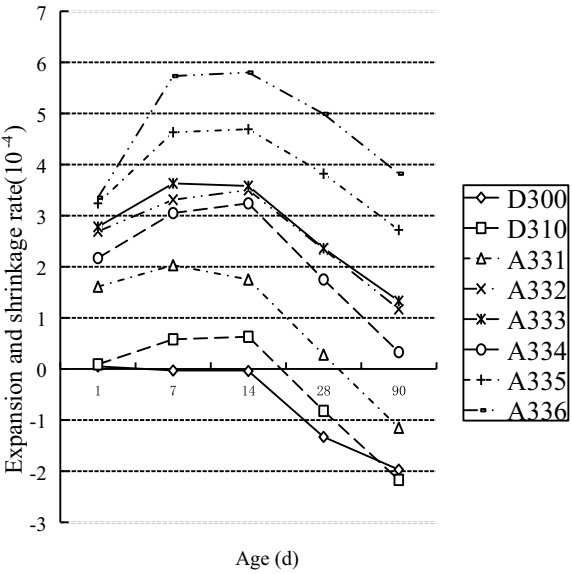

Fig. 3 Effect of dual dosage of admixtures on the expansion and shrinkage rate of concrete

dry shrinkage rate is consistent with the benchmark concrete added with HLC anti crack and anti-seepage agent. The addition of high-quality fly ash is beneficial for slowing down the occurrence of early shrinkage cracking in concrete. The continued increase in fly ash content (from 28 to 37%) is not conducive to improving the early cracking resistance of concrete.

From Fig. 2, it can be seen that after adding slag powder to replace some cement in concrete, the early expansion rate of concrete increases, and increases with the increase of slag powder content, but the rate of decrease in dry shrinkage is consistent with the reference concrete. The experimental results show that adding an appropriate amount of slag powder can slow down the occurrence of early shrinkage cracking in concrete.

From Fig. 3, it can be seen that after using double fly ash and slag micro powder to replace some cement in concrete, the early expansion rate of concrete increases, and increases with the increase of double admixture content. However, the rate of decrease in dry shrinkage is also consistent with the reference concrete. The experimental results show that an appropriate amount of dual admixtures can slow down the occurrence of early shrinkage cracking in concrete.

4 Analysis of Concrete Crack Resistance

4.1 Analysis of Concrete Expansion Mechanism

The early expansion mechanism of concrete mixed with HLC crack resistance and anti-seepage agent is the formation of ettringite, namely, trisulfide calcium sulphoaluminate ($C_6A\overline{S}_3H_{32}$), at the initial stage of cement hydration. When this mineral is formed, its solid phase volume increases by 1.27 times. Ettringite begins to form in the first hour of cement hydration, and then its quantity increases in the first day. When the original sulfate is consumed, in the case of insufficientsulfate, ettringite will dissolve and react with $Al(OH)_3$ to convert into single sulfur type calcium sulphoaluminate ($C_4A\,\overline{S}H_{12}$), and the solid volume will not increase when the single sulfur type calcium sulphoaluminate is formed. Which phase is stable depends on the sulfate concentration in the pore solution, and monosulfide type calcium aluminate is stable at low sulfate ion concentrations [7].

The amount of ettringite in concrete gel is determined by the content of effective aluminate, sulfate and calcium ions in concrete binding materials. Research has shown that large expansion occurs only when $Ca(OH)_2$ is fully supplied. When $Ca(OH)_2$ is insufficient, the expansion of hydrated calcium sulfoaluminate is very small and does not develop into a solid matrix [8].

The chemical composition of the cementitious material used for C30 pumping concrete in underground civil air defense engineering is as follows.

The chemical composition testing results of 32.5 ordinary silicon cement used are shown in Table 3.

The results of the chemical composition detection of Grade I ash used are shown in Table 4.

The chemical composition testing results of the slag powder used are shown in Table 5.

After replacing 28% cement with Grade I ash, the content of effective Al2O3 in the cementitious material decreases, the proportion of ettringite converted into single sulfur calcium sulphoaluminate decreases, and the early expansion of concrete

Table 3 Chemical composition test results of Tianbao 32.5 ordinary silicon cement

Testing items	SiO_2	Al_2O_3	CaO	MgO	TiO_2	Fe_2O_3	MnO	Na_2O	Ka_2O	SO_3	Loss on ignition
Content (%)	25.63	8.27	53.36	2.73	0.50	3.22	0.16	0.00	0.62	1.69	3.62

Table 4 Chemical composition test results of Nanre grade I ash

Testing items	SiO_2	Al_2O_3	Fe_2O_3	TiO_2	MgO	CaO	SO_3	Loss on ignition
Content (%)	50.24	33.12	4.01	1.39	0.92	5.18	0.46	1.45

Table 5 Chemical composition test results of slag powder

Testing items	SiO_2	Al_2O_3	Fe_2O_3	CaO	MgO	TiO_2	MnO	SO_3	Loss on ignition
Content (%)	32.05	15.59	0.84	37.28	10.18	0.86	0.43	0.89	1.88

increases. With the replacement amount of fly ash increases to 37%, although the effective Al_2O_3 content in the cementitious material decreases more, the content of $Ca(OH)_2$ in the gel pore decreases significantly, which may be the main reason for the reduction of the early expansion amount of concrete, which is lower than the expansion amount of 28% cement concrete specimens replaced by fly ash.

After using slag powder to replace part of cement, as slag powder is mixed with 3%$CaSO_4 \cdot 2H_2O$, the content of calcium sulfate in the cementitious material is sufficient, and the content of calcium oxide is rich, so the content of ettringite in the gel is more, and the early expansion of concrete specimens is larger, and with the increase of slag powder replacing cement, the early expansion of concrete increases. Based on the same reasons mentioned above, the early expansion rate of concrete increases with the addition of fly ash and slag micropowder to replace some cement, and increases with the increase of the amount of double admixtures.

4.2 Analysis of Concrete Crack Resistance

Under constrained conditions, cracks occur in concrete when the sum of dry shrinkage strain, self generated volume shrinkage strain, chemical reduction strain, carbonization shrinkage strain, and temperature difference shrinkage strain exceeds the ultimate tensile rate of the concrete. It is very difficult to improve the ultimate tensile rate of concrete, so the measure to improve the crack resistance of concrete is to reduce temperature difference and concrete shrinkage [9, 10].

Due to the fact that autogenous shrinkage of concrete mainly occurs 14 d before hydration, ensuring 14 d of wet curing after concrete formation can eliminate most of the shrinkage deformation of concrete. At the same time, strengthening wet curing is conducive to the full formation and stability of ettringite, the source of concrete expansion. And through 14 d of sufficient moisture curing, the temperature difference and shrinkage deformation of concrete can be reduced.

The measurement results of dry shrinkage strain of concrete with different mix ratios are shown in Figs. 2 and 3. When measuring the shrinkage strain of concrete, it already includes the autogenous shrinkage strain, chemical shrinkage strain, and carbonization shrinkage strain of concrete.

From the comparison between the shrinkage strain of concrete and the ultimate tensile rate of concrete, it can be seen that the absolute value of the 28 d shrinkage strain of the benchmark concrete without the addition of HLC crack resistance and anti-seepage agent and active admixture is greater than the ultimate tensile rate of

the concrete, indicating that even if early water saturation curing is strengthened, the concrete is still prone to shrinkage cracks.

After adding HLC anti crack and anti-seepage agent, the absolute value of the 28 d dry shrinkage strain of concrete is less than the ultimate tensile rate of concrete at 28 d, which can meet the anti crack requirements without the influence of temperature difference shrinkage strain. However, the absolute value of dry shrinkage strain in the later stage of concrete is relatively large, and shrinkage cracks may still occur under constrained conditions.

After adding an appropriate amount of high-quality fly ash and slag micro powder, the absolute values of dry shrinkage strain of concrete at 28 and 90 d are less than the ultimate tensile rate of concrete at 28 d. Without considering the influence of temperature difference shrinkage strain, the concrete can meet the crack resistance requirements. If the influence of temperature difference shrinkage strain of concrete is considered, the cracking resistance performance of A111 single mixed 28% fly ash concrete, A132 double mixed 18% fly ash + 28% slag powder concrete, A133 double mixed 28% fly ash + 28% slag powder concrete, and A134 double mixed 18% fly ash + 37% slag powder concrete is better. Replacing cement with a certain amount of fly ash and slag powder in concrete can also reduce the hydration heat of concrete, reduce the temperature difference and shrinkage strain of concrete, and improve the crack resistance of concrete.

A122 single addition of 60% slag micro powder concrete, A135 double addition of 28% fly ash + 37% slag micro powder concrete, and A136 double addition of 18% fly ash + 46% slag micro powder concrete. Due to the high early expansion rate of the concrete, under constrained conditions, the compressive stress of the concrete is relatively high. At this time (4–5d), the compressive strength of the concrete is still low, and the concrete may experience expansion and cracking damage, but it cannot play a crack resistance role. Taking A135 double mixed 28% fly ash + 37% slag micro powder concrete as an example, the expansion rate of the concrete after 5 d of water addition is about 0.046%. The compressive modulus of the concrete is calculated at 30.0 GPa, and the compressive stress of the concrete is about 12–15 MPa, which is close to the stress zone of concrete compressive crack propagation.

5 Conclusion

(1) Adding high-quality fly ash and slag powder in moderation is beneficial for improving the workability of concrete. However, when the amount of slag micro powder and double fly ash plus slag micro powder is too large (greater than 60%), the delayed setting time of concrete is too long, which is not conducive to normal construction of concrete.

(2) From the perspective of improving the crack resistance of concrete, it is advisable to choose A111 single mixed 28% fly ash concrete, A132 double mixed 18% fly ash + 28% slag micro powder concrete, A133 double mixed 28% fly

ash + 28% slag micro powder concrete, and A134 double mixed 18% fly ash + 37% slag micro powder concrete.

(3) Ensuring 14 d of wet curing after concrete formation is a necessary measure to prevent and reduce concrete shrinkage cracks.

References

1. Wu Z, Huizhen L (1999) High performance concrete. China Railway Press, Beijing, pp 1–5
2. Changxu J, Xingang W, Kai W et al (2006) Analysis and research on durability of concrete used in underground engineering structure. J Wuhan Univ Technol 28(8):43–45
3. Luo Q, Li Z, Fu L et al (2023) Study on durability of ultra-high performance concrete in urban underground environment. Synth Mater Aging Appl 52(02):51–54
4. Wang F, Wang S, Wang J et al (2020) Experimental study on durability of high-performance concrete. Concrete (04):107–109
5. He L (2021) Practice on durability of concrete structures in underground engineering of rail transit. Eng Technol Res 6(03): 168–169.
6. Chen T (2010) Multiple factors and attribute prediction study of durability life on underground concrete structurese. Concrete 08:45–47
7. Sommer H (1998) Durability of high performance concrete. Science Press, Beijing, pp 95–107
8. Barnes P (1991) Structure and properties of cement. China Architecture & Building Press, Beijing, pp 227–306
9. Zebin X, Xiaohu Y, Dong Y (2023) Study on durability of asphalt concrete containing acidic aggregate. Yangtze River (02):200–204, 209
10. Luo Q, Li Z, Fu L etc (2023) Study on durability of ultra-high performance concrete in urban underground environment. Synth Mater Aging Appl (02):51–54

Experimental Study on the Influence of Expansion Agents and Fibers on the Dry Shrinkage Performance of Concrete

Tao Ge and Han Wu

Abstract In order to study the influence of expansion agents and fibers on the dry shrinkage of concrete, this paper designed and implemented dry shrinkage tests on plain concrete and various fiber reinforced concrete after adding expansion agents, as well as dry shrinkage tests on concrete with different lengths and types of fibers added. The mechanism of the influence of fibers and expansion agents on the dry shrinkage performance of concrete was revealed. The experimental results show that expansion agents have an improvement effect on the dry shrinkage performance of various types of concrete, while fibers have varying effects on the dry shrinkage of concrete due to their length and equivalent diameter. The research results have guiding significance on how to improve the dry shrinkage performance of concrete.

Keywords Expansion agent · Fiber · Concrete · Dry shrinkage

1 Introduction

The crack resistance of concrete has always been a technical challenge of concern. Cracks can accelerate concrete carbonization and steel corrosion, and create a vicious cycle, seriously damaging the safety and durability of concrete structures [1–4]. There are many factors that can cause concrete cracks, but most of them are related to shrinkage. Controlling shrinkage will be an important measure to prevent concrete cracks [5–7].

The cracking of concrete has always been a key factor in its structural life and durability, and is also a technical challenge. Cracks in concrete can usually be divided into load induced cracks and non load induced cracks. As for non load cracks, they mainly include various shrinkage cracks, including plastic shrinkage cracks, temperature shrinkage cracks, dry shrinkage cracks, self shrinkage cracks, and carbonization

T. Ge (✉) · H. Wu
Aeronautics Engineering CollegeAir Force Engineering University, Xi'an 710038, China
e-mail: getaoge@163.com

G. Mei et al. (eds.), *Advanced Construction Technology and Research of Deep-Sea Tunnels*, Lecture Notes in Civil Engineering 490,
https://doi.org/10.1007/978-981-97-2417-8_33

shrinkage cracks. To avoid the occurrence of non load cracks, in addition to strengthening early maintenance and controlling hydration heat, measures should also be taken to limit and compensate for shrinkage. The main purpose of adding expansion agents to concrete is to reduce and compensate for shrinkage, especially for concrete with high crack resistance requirements, which generally requires the addition of expansion agents. In steel fiber reinforced concrete, in order to fully encapsulate steel fibers and maximize their performance, it is necessary to increase the amount of cementitious materials, which will inevitably lead to significant shrinkage. Therefore, it is necessary to study the effect of expansion agents on the performance of steel fiber reinforced concrete. The purpose of this part of the experiment is to analyze the effect of expansion agents on the performance of concrete and determine whether it is still necessary to add expansion agents in steel fiber reinforced concrete.

The shrinkage of concrete can be divided into plastic shrinkage, temperature shrinkage, self shrinkage, drying shrinkage, and carbonization shrinkage. For ordinary concrete structures, due to the use of lower amounts of cementitious materials and the limited size of components, the influence of temperature shrinkage is relatively small. The common destructive factors are mainly dry shrinkage and plastic shrinkage. The influence of fibers (mainly hybrid fibers) and expansion agents on the dry shrinkage of concrete has also been studied by many scholars [8–10]. This article studies the effects of fibers (polypropylene fibers, steel fibers, and hybrid fibers) and expansion agents on the dry shrinkage of concrete from the perspectives of limiting shrinkage and compensating shrinkage.

2 Experimental Design and Mix Proportion

The effect of expansion agents on the dry shrinkage of concrete: Adding expansion agents to plain concrete, polypropylene fiber concrete, and hybrid fiber concrete, testing the effect of expansion agents on the dry shrinkage of these three types of concrete;

1. The effect of steel fiber content on concrete shrinkage: Add 32 and 64 kg m^{-3} steel fibers (with a length of 15 mm) to the concrete, and test their impact on concrete shrinkage;
2. The effect of steel fiber type on concrete shrinkage: The influence of different steel fibers on concrete shrinkage was tested by adding 64 kg m^{-3} of 15 mm long steel fibers and 30 mm long steel fibers to the concrete.

Test using 100 mm × 100 mm × 515 mm. After the specimen is formed and removed, its initial length is measured, and then the specimen is sent to the standard curing room for immersion curing for 7 days, and then moved to the constant temperature and humidity chamber to measure its 7d Free expansion rate, and finally its corresponding strain is measured at the specified age. The mix proportions tested in this article are shown in Table 1.

Table 1 Test mix proportions for dry shrinkage of concrete

Number	Polypropylene fibers	Steel fibers			water	cement	fly ash	sand	Gravel	expander	Water reducing agent (kg m^{-3})
		30.5 mm	30 mm	15 mm							
S1	0	0	0	0	155	274	84	771	1160	0	2.162
S2	0	0	0	0	155	244	84	771	1160	30	1.432
S3	0.9(P2)	0	0	0	155	274	84	771	1160	0	2.758
S4	0.9(P2)	0	0	0	155	244	84	771	1160	30	1.432
S5	0.9(P2)	0	0	0	155	244	84	771	1160	30	1.432
S6	0.9(P1)	0	0	0	155	244	84	771	1160	30	1.432
S7	0.9(P1)	32	32	0	165	300	84	861	1096	0	5.376
S8	0.9(P1)	32	32	0	165	270	84	861	1096	30	2.758
S9	0	0	0	32	165	270	84	861	1096	30	2.586
S10	0	0	0	64	165	270	84	861	1096	30	2.758
S11	0	0	64	0	165	270	84	861	1096	30	2.758
S12	0	32	0	32	165	270	84	861	1096	30	2.758

3 Dry Shrinkage Test Results and Analysis

3.1 Effects of Expansion Agents on the Dry Shrinkage of Concrete

In the experiment, the effects of expansion agents on the dry shrinkage of plain concrete (S1 group), polypropylene fiber concrete (S3 group), and hybrid fiber concrete (S7 group) were tested. The results are shown in Figs. 1, 2, and 3, respectively. The horizontal coordinate "7w" in the figure represents day 7 of immersion curing, while the rest represents the curing time in a constant temperature and humidity chamber.

From Figs. 1, 2, and 3, it can be seen that the addition of expansion agents reduces the drying shrinkage of concrete at various stages, especially in the early stages. Among them, the expansion agent has a significant effect on reducing shrinkage of plain concrete and hybrid fiber concrete, and the dry shrinkage can be reduced by about 30% at day 60. The principle is that after adding an expansion agent to the concrete, a chemical substance with expansion properties is generated, which improves the compactness of the matrix and fills, blocks, and seals the pores of the concrete, preventing the migration of water, thereby compensating for and reducing the drying shrinkage of the concrete itself.

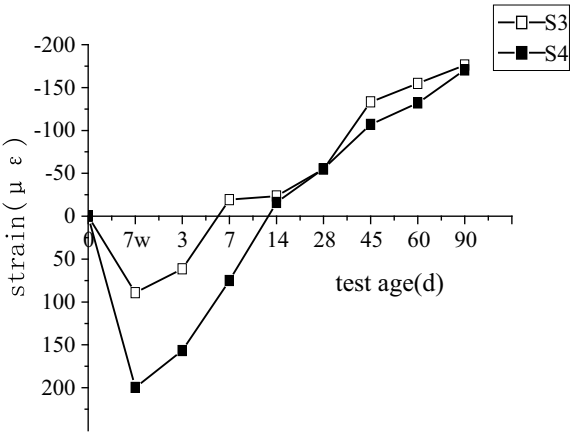

Fig. 1 Effects of expansion agent on dry shrinkage of ordinary concrete

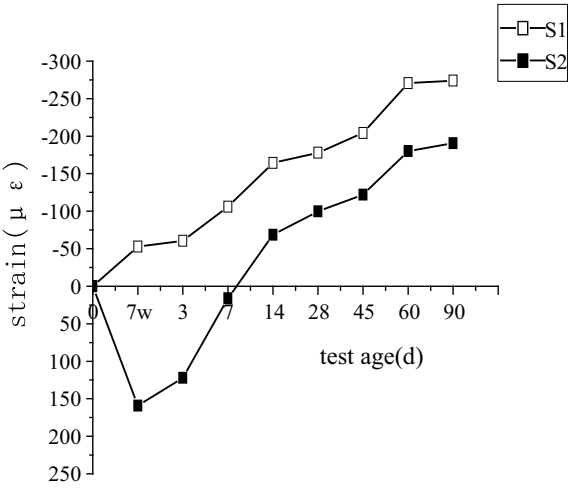

Fig. 2 Effects of expansion agent on the dry shrinkage of polypropylene fibers concrete

3.2 The Effects of Steel Fibers Content on the Dry Shrinkage of Concrete

In the experiment, the effect of steel fibers (with a length of 15 mm) mixed with 32 and 64 kg m^{-3} on the dry shrinkage of concrete was tested, as shown in Fig. 4. From Fig. 4, it can be seen that the addition of steel fibers does not reduce the dry shrinkage of concrete, but instead increases it. However, the dry shrinkage of concrete mixed with 64 kg m^{-3} steel fibers is smaller than that mixed with 32 kg m^{-3}. Under certain water cement ratio conditions, the dry shrinkage of concrete is closely related to its pore structure. Due to the high density and equivalent diameter of steel fibers, the number of steel fibers per unit mass is relatively small. A single length of steel fibers is difficult to improve the pore structure of concrete, and even has certain

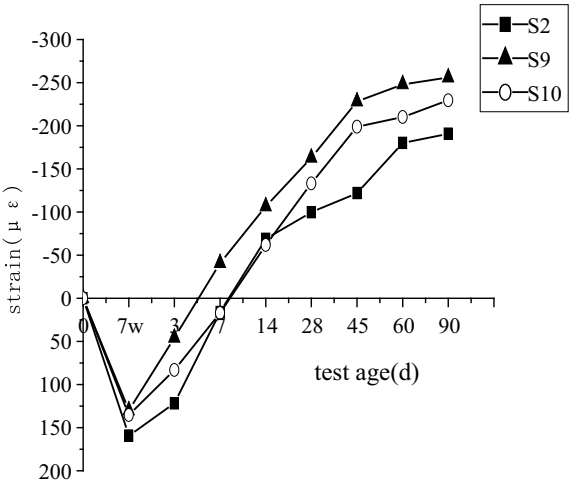

Fig. 3 Effects of expansion agent on dry shrinkage of hybrid fibers reinforced concrete

adverse effects (related to the quality of vibration forming), thereby increasing the dry shrinkage of concrete. This fully indicates that steel fibers cannot effectively reduce the dry shrinkage of concrete.

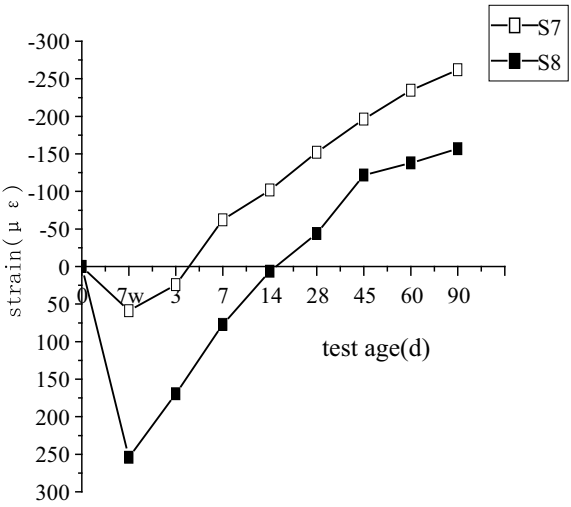

Fig. 4 Effects of steel fibers content on concrete dry shrinkage

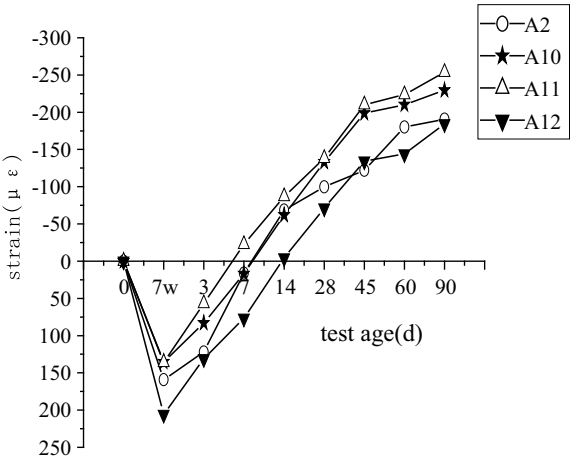

Fig. 5 Effects of steel fiber types on concrete dry shrinkage

3.3 The Influence of Steel Fibers Types on the Dry Shrinkage of Concrete

Under a certain amount of steel fiber, the influence of different steel fibers on the dry shrinkage of concrete was tested, as shown in Fig. 5. From Fig. 5, it can be seen that after adding 64 kg m^{-3} of 15 mm long steel fibers and 30 mm long steel fibers, namely S10 and S11 groups, the dry shrinkage of concrete is also greater than the reference group S2. Among them, the ability of 15 mm long steel fibers to limit dry shrinkage is better than that of 30 mm long steel fibers. The main reason is that the equivalent diameter and length of steel fibers with a length of 15 mm are relatively small, and there are more fibers per unit volume, which is beneficial for improving the pore structure of concrete.

When two types of steel fibers are mixed with 32 kg m^{-3} each, the dry shrinkage ratio of concrete in reference group A2 is slightly smaller, with a decrease of nearly 20% in dry shrinkage after 60 days. The reason is that hybrid steel fiber fibers can improve the pore structure of concrete at different scales, especially under the synergistic effect of expansion agents, which can refine the pore size, reduce water leakage, and thus reduce dry shrinkage.

3.4 The Effect of Hybrid Fibers on the Dry Shrinkage of Concrete

To better limit and reduce the dry shrinkage of concrete, polypropylene fibers and composite steel fibers were mixed and added, and the dry shrinkage results are shown in Fig. 6. From Fig. 6, it can be seen that mixed fiber concrete (S8 group) has the smallest dry shrinkage. The 60 day shrinkage of the S8 group decreased by

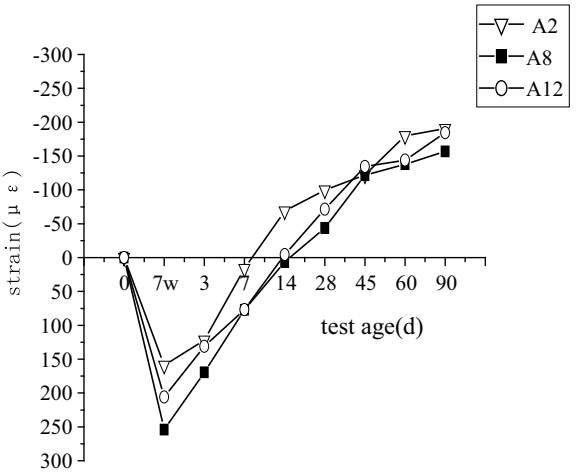

Fig. 6 The effects of mixed fibers on the dry shrinkage of concrete

23.5% compared to the reference group S2, which fully demonstrates the composite effect between different fibers. Mixing polypropylene fiber and composite steel fiber can improve the pore structure of concrete at different scales and levels in three-dimensional space, refine the size of pores, improve the uniformity of concrete, and effectively prevent the escape of water. Meanwhile, polypropylene fibers and steel fibers with different elastic moduli can better disperse capillary shrinkage stress, prevent local stress concentration, and reduce dry shrinkage.

In this part of the experiment, the mechanical properties, fracture mechanical properties, and dry shrinkage properties of hybrid fibers were mainly compared and studied. Experiments have shown that hybrid fibers have better performance than pure steel fibers or polypropylene fibers. However, it is not that polypropylene fibers and any volume fraction of steel fibers have good reinforcement effects, but rather that there is an optimal volume addition. When 0.9 kg/m^3 polypropylene fiber is mixed with 0.8% volume fraction composite steel fiber, it has better comprehensive performance. The effect of hybrid fibers on improving the compressive strength of concrete is not significant, but the improvement of flexural strength, splitting tensile strength, and initial crack strength is more prominent, which can be increased by about 26%, 13%, and 25%, respectively. In terms of dry shrinkage, expansion agent JM—III can effectively reduce the dry shrinkage of concrete, with a 60 day dry shrinkage reduction of about 30%. The effect of a single variety of steel fibers on reducing concrete shrinkage is not significant, which is consistent with the research results in the first part. However, steel fiber composites with different lengths effectively reduce the dry shrinkage of concrete, with a reduction of nearly 20% after 60 days. Hybrid fibers, especially polypropylene fibers and composite steel fibers, have the best effect in reducing dry shrinkage, with a 60 day dry shrinkage reduction of about 23.5%.

Expansion agents can effectively reduce the dry shrinkage of concrete, but compared to concrete with expansion agents, the addition of steel fibers (with a

volume content of less than 1.5%) cannot effectively reduce the dry shrinkage of concrete, and even if there is some inhibition, the effect is relatively limited. The effect of Shanghai Becarte steel fiber on limiting dry shrinkage is better than Jiangxi Guomao steel fiber.

In order to meet the requirements of good process performance, mechanical performance, and anti shrinkage performance, the technology of adding expansion agents and steel fibers should be used. The volume content of steel fiber should be controlled at around 1.0%, the length should be controlled at around 30 mm, and the maximum particle size of coarse aggregate should be less than 20 mm. Medium sand should be used, and high-efficiency additives should be used.

4 Conclusion

(1) Expansion agents can effectively reduce the dry shrinkage of plain concrete or fiber reinforced concrete, with a 60 day dry shrinkage reduction of about 30%.
(2) The effect of reducing concrete shrinkage with a single variety of steel fibers is not significant. However, steel fiber composites with different lengths effectively reduce the dry shrinkage of concrete, with a reduction of nearly 20% after 60 days.
(3) Hybrid fibers, especially polypropylene fibers and composite steel fibers, have the best effect in reducing dry shrinkage, with a 60 day dry shrinkage reduction of about 23.5%.

References

1. Jia H, Yan G, Yan G (2005) Study on corrosion of reinforcement in concrete. China Saf Sci J (5):56–59
2. Zhou X, Peng J, Yang J (2009) Study-I of corrosive crack width on reinforcement concrete cover. J Foshan Univ (Nat Sci Edn) (1):59–62
3. Li Y, Zhang Z, Lin D etc (2022) Analysis of the influence of reinforcement corrosion expansion on cracking of concrete cover. J Railway Eng Soc (5):73–79
4. Hao T, Qiao T, Luminescence etc (2022) Review on shrinkage and cracking of concrete. Concrete (12):22–28
5. Liu W (2011) Prevention and Treatment of Cracksin Concrete. Coal Technol (3):134–136
6. Zhang Y, Li Q (2010) Analysis about concrete cracks and study on the preventive and repairing measures. Concrete (12):137–140
7. Yu C (2009) Problem and prevention of cracks in concrete construction. Coal Technol (8):101–103
8. Hao J, Yu H, Zhou P etc (2007) Effect of expansion agent, fiber and their combination on drying shrinkage of concretes with high content mineral admixtures. J Civil Eng Manage (4):40–44
9. Shi J (2013) Effect of concrete admixtures on concrete shrinkage and cracking. Develop Guide Build Mater 11:47–48

10. Zhang Y (2022) Experimental study on shrinkage and cracking performance of hybrid fiber self compacting concrete. Master's thesis, North China University of Water Resources and Hydropower, Zhengzhou City, pp 21–33